ENGINEERED NANOSTRUCTURES FOR METAL ENHANCED FLUORESCENCE APPLICATIONS IN THE NEAR-INFRARED

Jing Sheng Pang

Department of Materials

Imperial College London

This thesis is submitted in fulfilment of the requirements for the degree of Doctor of Philosophy (PhD), Imperial College London

Declaration of Originality

I declare that this work is my own and that any references to other work are appropriately referenced. Some of the work in this thesis has been published in the following journal article.

Fang Xie, Jing S. Pang, Anthony Centeno, Mary P. Ryan, D. Jason Riley, and Neil M. Alford, Nanoscale control of Ag nanostructures for plasmonic fluorescence enhancement of near-infrared dyes, **Nano Research** 2013, 6(7): 496–510.

Declaration of Copyright

Abstract

Recent advancements in fabrication techniques allow construction of nanostructures with well-defined features in nanometres scale. Tiny nanostructures that have features below the resolution of optical diffraction limit can now be made in the laboratory. The specific properties of those nanostructures with specific properties made from variety of materials allow us to study and explore many different properties that have never been observed while they are in bulk. One such phenomenon is localised surface plasmon resonance effect, which is exhibited by certain materials when in nanometric size. Their peculiar interaction with light is in such a way that the optical properties such as reflection and transmission deviate from typical characteristics and change according to the material involved and their shapes. Furthermore, this effect could also enhance the electric field in a specific area of the structure.

This thesis is motivated by the attractiveness of the tunability of localised surface plasmon resonance and aims at exploring those properties by fabricating multiple types of nanostructures through a low-cost and versatile technique called nanosphere lithography. By improving the technique and combining with other fabrication techniques (such as oxygen plasma etching and argon ion milling), a large variety of nanostructures with hexagonal lattice like as nanocones, nanopencils, and nanofins arrays have been successfully created. Among them, three main types of nanostructure were selected for detailed study: nanotriangle, nanodisc, and nanohole-disc arrays. The distance between the adjacent nanoparticles were changed in those structures and strong interparticle coupling behaviours were observed as the distance between them becomes shorter.

Current portable biosensing devices for in vitro studies are limited by the sensitivity limit of the detector, the poor quality of emitters and the size of the devices. In this thesis, the application of localised surface plasmon resonance for near infrared in vitro biosensing is explored. This is achieved through a mechanism called metal enhanced fluorescence. The techniques take advantage of the high electrical field strength and the resonance condition of the plasmon to enable a fluorophore to achieve brighter emission. The greater the resonance and electrical field are, the greater the emission amplification would be. Such effect makes it highly attractive for near infrared in vitro studies, which benefits from high optical penetration of common biology components such as water and lipids, but suffer from poor emission of existing fluorophores. Thus, enhancement of the emission signals through metal enhance fluorescence mechanism is an attractive route to obtain better signal to noise ratio in medical diagnostic, and improve detectability while at the same time reduce the need of a high sensitivity detector which can be costly and large in size. The three chosen nanostructures, i.e. nanotriangular arrays, nanodisc arrays and nanohole-disc arrays have shown marked enhancement in the emission of attached fluorophores up to 83x, 235x, and 411x respectively, making them highly attractive nanostructures for such application.

This work is dedicated to my family and my parents, Johnny Pang and Chai See Ngoh for their endless support and love; my wife Do Anh Thu, for her continuous care, love and companionship through good and bad times.

This work is also dedicated to the loving memory of my pets, Rocky, Richy, Bobo, and Billy as my lovely companions and sharing so many memories together.

Acknowledgements

I have learnt many things and discovered new knowledge while researching and developing plasmonic nanostructures for different applications. It has been a wonderful experience not only because the science is fundamentally intriguing but also thanks to family and friends who have given me constant support in times of good and bad.

I would like to thank my supervisors Dr Fang Xie and Prof Mary Ryan for sharing their knowledge and experience on doing good research. They have taught me how to approach science differently and allows me to learn about the community in a wider context. Their commitment to high quality scientific research have always inspired me. They are also very willing to listen and understand my ideas and let me explore it. Moreover, they are not just supervisors to me but also have become friends of mine. They have given me many valuable mentoring and made a big difference to my life in the college.

Prof Neil Alford has always been helpful and genuinely supportive; willing to share his long-standing experience and guide young researchers like myself toward our goals. Busy as he is as head of department, he remains very approachable and allocate his time for us. When there is a problem, he would provide profound help and advice until a solution is found.

I would also like to thank Dr Peter Petrov for his help at the beginning of my PhD work and for maintaining the Thin Film Laboratory every day to ensure it is in working condition. Together with my close friends Dr Kevin Zou Bin, Dr Tianle Wang, Evgeniy Donchev, we have created many unforgettable memories inside the lab. Those jokes, story-telling, and singing has always warmed my heart.

Dr Anthony Centeno, who have been supporting our research by doing a lot of modelling and discussing many interesting mechanisms behind the plasmonic phenomena. I remember many of those coffee time discussions and am always fascinated by his knowledge. I have always enjoyed my time with him.

Daniel Darvill, who joined our research group in my second year in PhD. I thoroughly enjoyed working with him, we had so much fun exchanging crazy ideas and discussing science in details. He is also a very friendly and charismatic person that seems to know everyone in the department.

Dr Peter Gammon was a post-doc in our research group when we were working on rectenna project. Although he only worked with us for a short time, I have learned many interesting thingsworks on semiconductors. He also gave me some personal guidance from time to time. Now he is based in Warwick University and continues to come visit us from time to time.

Dr Lefteris Danos, Liping Fang who have helped me many times for doing fluorescence lifetime research study in Southampton University and have always been very welcoming. Dr Jeremy Ball for my time in doing some measurements in London Southbank University. Those coffee and ginger cookies were very delicious.

Russell Stracey and Michael Lennon from workshop have always understood my designs and produced great quality products. Dr Mahmoud Ardakani and Ecaterina Ware for their constant effort in ensuring the scanning electron microscope always in the best working condition.

Thanks to this PhD research, I have also made many good friends and we shared a wonderful time together. Friends in LCN, Giuseppe, Sima, Romi, Monica, Ruth, Leo, Basma and many more with whom we shared many up and down moments. Ross, who always bakes scrumptious cakes every Thursday.

I would like to take this opportunity to give my heartfelt thanks to my family and pets who have always been so understanding and have always given me constant support especially when I was having rough time in my research. Their warm and loving nature have always a motivation for me to be positive toward life.

Last but not least, I would like to give my utmost thanks and appreciation to Do Anh Thu, who is not only being a loving companion but also the closest friend I could ever wish for, and who always supports, and looking after me.

Table of Contents

List of Figures

List of Tables

Abbreviation

bBSA	biotinylated Bovine Serum Albumin
C2C	centre to centre distance
EELS	Electron Energy Loss Spectroscopy
EOT	Extraordinary Optical Transmission
LSPR	Localised Surface Plasmon Resonance
MPTMS	(3-Mercaptopropyl)triethoxysilane
Ni	Nickel
NIR	Near Infrared
NIR-I	650 - 950 nm
NIR-II	1000 - 1359 nm
NSL	Nanosphere Lithography
PS	Polystyrenes
RIS	Refractive index sensing
RIU	Refractive index unit
SA-AF	Streptavidin-Alexa Fluor
SDS	Sodium dodecyl sulphate
SEM	Scanning Electron Microscope
Si	Silicon
SPP	Surface Plasmon Polariton
UV	Ultraviolet
VIS	Visible

Chapter 1

Introduction

Figure 1 A picture of a 50 nm thick Au nanodisc arrays plasmonic substrate. The material is made up of gold, but does not reflects gold colour at all.

Chapter 1 Introduction

In general, the definition of light is classified as part of the electromagnetic radiation that we see every day. What we see is actually not the light itself but the interaction of light with the matter around it. The colour we see is a result of loss or emission of energy in the visible spectrum (approx. 400 to 700 nm). Light can also be diffracted, or refracted. The colour of a rainbow is one typical example of splitting of light in the water molecules in the sky.

The understanding of interaction of light with matter allows us to design and apply the mechanism into applications. Thus, it is necessary to properly understand how the light interacts with the matter, and then design structures that allows optimum conversion of light into the specific application.

Advancement in nanotechnology allows us to create nanoscale structures. As the size of the metal is reduced to much smaller than the wavelength of the incoming light, a localised collective oscillation of electrons occur in metals. This is now commonly known as localised surface plasmon resonance. This phenomenon has opened diverse opportunities in technology advancement, ranging from arts, science, medical, and engineering.

In this thesis, a specific application of localised surface plasmon resonance in biosensing is explored. In biosensing, fluorophores are the fluorescing agent. It usually comprise of organic molecules that absorb light follow by reemission of light at longer wavelength. When compatible fluorophores are attached to these plasmonic metal nanostructures, they can couple together and enhances the fluorescing intensity known as metal enhanced fluorescence. This greatly enhancing the detectability of the fluorophores emission, especially at near-infrared region at which the water window are located, but suffers poor detection sensitivity with currently available technology.

Nanostructures for biosensing were fabricated based on nanosphere lithography, a versatile method that can generate large variety of nanostructure arrays and can be combined with many other nanofabrication methods to produce complex structures. A straightforward nanotriangle together with more complex nanodisc, nanoholes, and nanodisc-holes arrays were produced. Their optical properties were characterised. In biosensing application, fluorophores were applied to those structures to demonstrate and compare the strength of metal-enhanced fluorescence. Three orders of magnitude increased in emission of applied near-infrared fluorophores have been observed, providing one step closer in realisation of practical application of plasmonic NIR biosensing detection.

This thesis will first introduce the general overview of nanostructures produced by nanolithography (chapter 2), followed by application of metal nanoparticles for biosensing (chapter 3). Fabrication methods in this work are described in chapter 4. Properties of the nanoparticle structures produced by nanosphere lithography are discussed in chapter 5. Their associated application in metal

enhanced fluorescence can be found in chapter 6. Finally, the thesis is concluded in chapter 7 with some outlook based on the work shown in this thesis.

Chapter 2

Optical Properties of Metal Nanoparticles

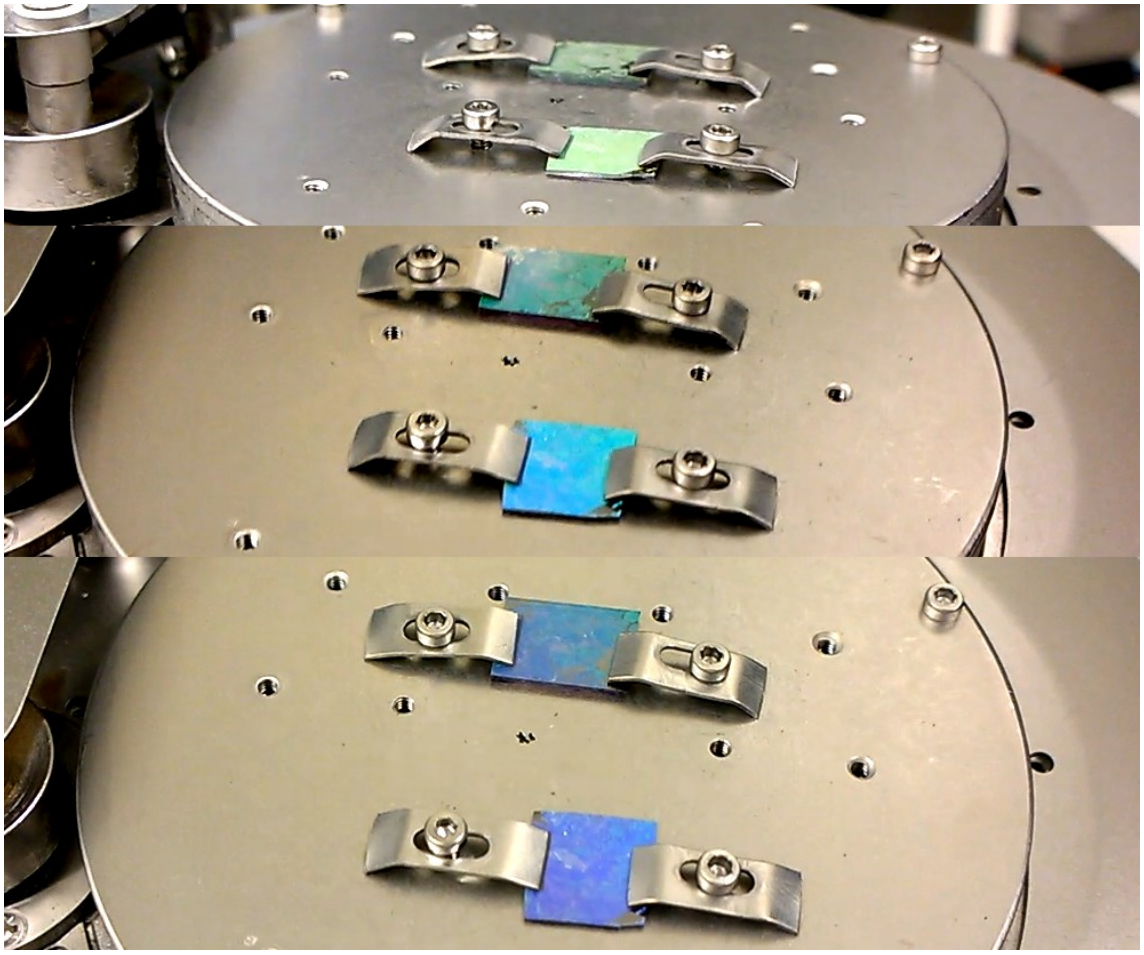

Figure 2 Nanodisc arrays as seen from different angles shows different colour of reflection.

Chapter 2 Optical Properties of Metal Nanoparticles

The word metal origins from Greek "μέταλλον"- *métallon*, meaning "mine, quarry, metal and mineral"[1]. Some of the common properties associated with metals are ductility, shiny, and have good electrical and thermal conductivity. The recent advancement in nanotechnology revealed even more fascinating properties when metals are in nanometer scale. Solutions and solids containing metal nanoparticles such as gold, silver, and copper display beautiful color under illumination owing to a property known as localised surface plasmon resonance (LSPR). Under photo-excitation, the electrons in the conduction bands undergo collective oscillation and result in absorption of energy from the incoming photon in the optical wavelength, thus producing the vibrant color from those metal nanoparticles. The Lycurgus cup is one of the excellent examples, crafted by Romans in the fourth century. The color changing property when illuminated at different angles is due to the gold and silver nanoparticles embedded in the cup. Of course, back then they did not know it was due to the embedded nanoparticles.

Figure 2-1 The Lycurgus Cup made by Romans in the fourth century. Light illumination from the front (left) and from the rear (right) results in two very different colours. (Reprinted with permission from British Museum.)

The exciting properties of those nanoparticles are not limited to aesthetic purpose. Their usage have now extended widely into many different areas such as lighting[2], solar cells[3–5], sensors[6–9], nonlinear optics[10], printing[11] and also extended from semi-classical to forefront research in quantum computing[12,13]. The study of interaction between metal nanoparticles in response to the electromagnetic radiation is now termed plasmonics. This chapter will explain the fundamental of localized surface plasmon resonance and surface plasmon polariton, the basis on which this project relies.

2.1 From bulk metals to nanoparticles – A look at their change in optical property

In metals, the atoms are surrounded by delocalised outer electrons. These free moving electrons not only contribute to the high thermal and electrical conductivity in the metals, but also their optical response. A free-electron metal is one such that the most of the electronic and optical properties are due to the conduction electrons alone. The response of the metal to the electromagnetic waves is described by its wavelength dependent dielectric function, $\varepsilon(\omega) = \varepsilon_1(\omega) + i\varepsilon_2(\omega)$. (Note that dielectric function is also known as relative permittivity). The real term, ϵ_1, is related to the polarizability of the metal and the imaginary term, ε_2, is related to the absorption.

A simple approach to understand the optical phenomena is to use Drude-Lorentz-Sommerfeld model[14]. Although the effect of crystal lattice and the influence of the nearby electrons are ignored, this approach provides a good approximation to help understanding the optical properties of the metals. The metal atom can be considered as a fixed positive ionic core surrounded by a cloud of negatively charged electrons. If a tiny displacement of the overall electron cloud occurs with respect to the ionic core, it would form a plasma state. A Coulomb force will pull the electrons to restore the system back to equilibrium. A continuous perturbation to the plasma state can be caused by external field such as incoming light beam, leading to a resonance condition. In bulk metal, assuming the thermal motion of the electrons is insignificant, this resonance condition occurs at volume plasmon frequency, ω_p:

$$\omega_p^2 = \frac{n_e e^2}{\varepsilon_0 m^*} \qquad \textit{Equation 2-1}$$

where n_e is the number density of the electrons, e is the charge of an electron, $\epsilon_0$is the permittivity of the free space, and m^* is the effective mass of the electrons in the system. Incoming radiation with frequency less than the volume plasmon frequency will be effectively screened by the induced motion of the electrons and reflected, thus the shiny reflection seen on the metal surface. Above this frequency, the electrons in the bulk metal are unable to keep up with the frequency of the incoming radiation and therefore transmitted. Under this model, the dielectric constant can be written as

$$\varepsilon(\omega) \approx 1 - \frac{\omega_p^2}{\omega^2 + i\Gamma\omega} \qquad \textit{Equation 2-2}$$

where Γ is the relaxation constantly associated with the damping of the oscillation due to the scattering event. Mathematically, it is related to the electron mean free path, l, and Fermi velocity by $\Gamma = v_f/l$. For $\gg \Gamma$, the real part and the imaginary part can be written as

$$\varepsilon_1(\omega) \approx 1 - \left(\frac{\omega_p}{\omega}\right)^2 \; ; \varepsilon_2(\omega) \approx 1 - \frac{\omega_p^2}{\omega^3}\Gamma \qquad \textit{Equation 2-3}$$

The real part of the equation shows that the resonance condition occurs when $\omega = \omega_p$. Another common form to write the dielectric constant is to relate it susceptibility, χ, to give $\varepsilon(\omega) = 1 + \chi^{DS}(\omega)$, where χ^{DS} denotes the free-electron Drude-Sommerfield susceptibility.

So far, the approach above treats the optical property purely from conduction electrons alone. However, all the electrons at the core of the atom also influence the dielectric constant. For instance, metals which undergo interband transition, an additional susceptibility term due to interband transition, $\chi^{IB} = \chi_1^{IB} + i\chi_2^{IB}$, will have to be considered. The complex part becomes large around the frequency at which the interband transition occurs and is related to dissipation of energy. As such, the complex dielectric function becomes $\varepsilon(\omega) = 1 + \chi^{IB}(\omega) + \chi^{DS}(\omega)$. For metals such as Au and Al, this becomes very important as the transition occurs around 520 nm and 830 nm, respectively, falling within the optical spectrum of interest. For this reason, Al is a good candidate for UV region, and Au is good for NIR region for biosensing applications.

Another physical effect worth considering is the penetration depth of electromagnetic radiation into the metal[14]. The radiation can only penetrate into a certain depth due to energy dissipation in the metal. Skin depth, δ_s, is the distance at which the amplitude of the incoming electric- or magnetic field reduced by a factor of 1/e. This value can be estimated from optical absorption coefficient, k, of the metals through $k = 2/\delta_s$. Therefore, depending on the metal nanoparticle size, the electric field felt across the whole particle could be different.

2.2 Localized Surface Plasmon Resonance – Isolated case

Unlike bulk metal, when the size of metal particles is much smaller than the wavelength of the incoming light, the electric field surrounding the nanoparticles can be taken as constant. The interaction between the nanoparticle and the light is now governed by electrostatic rather than electrodynamics. This is also known as quasistatic approximation. Figure 2-2 below illustrates the effect of electric field of the light affecting the electron cloud of spherical metal nanoparticles. The displacement of the electron clouds causes charge to distribute around the nanoparticles and form a dipole electric moment. Since the electric field oscillates as the light propagates, the displacement of charge on the nanoparticles is also displaced in the collective manner. As the charge remains localised to the surface of the metal nanoparticles, this mechanism is termed localised surface plasmon resonance (LSPR).

The induced electric field generated by a metal nanosphere can be calculated using the Maxwell equation with appropriate boundary conditions[14,15]. Assuming the incoming electric field, $\boldsymbol{E}_o$, is in the x direction, the induced dipole electric field outside the sphere is

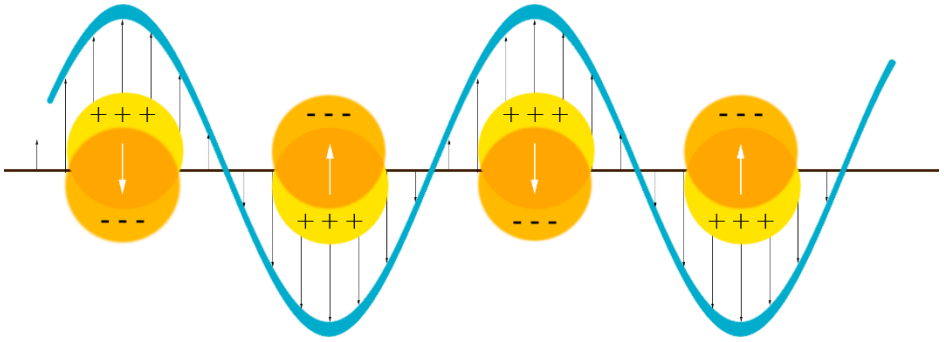

Figure 2-2 Dipole moment generated on the metal nanoparticles by the electric field of the incoming light.

$$\boldsymbol{E}_{induced\ dipole} = \alpha \boldsymbol{E}_o \left[\frac{\hat{x}}{r^3} - \frac{3x}{r^5}(x\hat{x} + y\hat{y} + z\hat{z})\right] \qquad \textit{Equation 2-4}$$

where $\hat{x}$, $\hat{y}$, and $\hat{z}$ are the Cartesian unit vector, r is the distance from the centre of the sphere, and α is the dipole polarizability:

$$\alpha = 4\pi g_d a^3 \qquad \textit{Equation 2-5}$$

with

$$g_d = \frac{\varepsilon_i - \varepsilon_m}{\varepsilon_i + \chi\varepsilon_m} \qquad \textit{Equation 2-6}$$

where a is the diameter of the sphere, ε_i and ε_m are the dielectric constant of the metal and the medium it is in respectively, g_d is the assymetriocal term for dipole, and χ is shape dependent parameter which equals to 2 for a sphere and can be larger (smaller) than 2 for prolate or oblate shape along major axis[16] (minor axis) (please be aware that this is not the electrical susceptibility in this equation). Note that the dielectric constant ϵ remains a phase dependent value. From the equations above, we can see that for a sphere the resonance occurs when $|\epsilon_i + 2\varepsilon_m| = \left[\varepsilon_{i,1}(\omega) + 2\varepsilon_m\right]^2 + \left[\varepsilon_{i,2}(\omega)\right]^2 = minimum$. Since the dielectric constant of the medium is usually positive, this means that the conditions for resonance to occur is (1) real part of the metal dielectric constant is negative at that frequency, and (2) $\varepsilon_{i,1}(\omega) = -2\varepsilon_m$ provided $\varepsilon_{i,2}(\omega)$ is small and does not vary much around the resonance wavelength. Further detail analysis will show that $\varepsilon_{i,1}(\omega)$ determines the location of the plasmonic peak and also influences the width. A steep $\varepsilon_{i,1}(\omega)$ will gives a narrow resonance peak and a flat $\varepsilon_{i,1}(\omega)$ will produces a broad peak. As for $\varepsilon_{i,2}(\omega)$, it is responsible for energy loss in the material and if this value is sufficiently large, it may smear out the resonance peak. An ideal lossless plasmonic material will have negative $\varepsilon_{i,1}$ and $\varepsilon_{i,2} = 0$.

Using Equation 2-3 from a free-electron model, the LSPR condition and assuming $\varepsilon_m = 1$ (i.e. in a vacuum space), the nanoparticles LSPR frequency is related to the volume plasma frequency by

$$\omega \approx \frac{\omega_p}{\sqrt{3}}$$ *Equation 2-7*

Within the wavelength window of interest, other than dipole mode, higher order mode could also arise. A similar treatment can also be applied to derive equations to find contribution of quadrupole mode outside the sphere:

$$\boldsymbol{E}_{induced\ quadrupole} = -\beta \boldsymbol{E}_o \left[\frac{x\hat{\boldsymbol{x}} + z\hat{\boldsymbol{z}}}{r^5} - \frac{5z}{r^7}(x^2\hat{\boldsymbol{x}} + y^2\hat{\boldsymbol{y}} + xz\hat{\boldsymbol{z}})\right]$$ *Equation 2-8*

where $\beta = g_q a^5$ is quadrupole polarizability with $g_q = \frac{\varepsilon_i - \varepsilon_m}{\varepsilon_i + 3\varepsilon_m/2}$. Note that for dipole (Equation 2-4), the electric field decay as a function of approximately $1/r^3$. As for quadrupole, although the influence of the sphere size on the polarizability is two order of magnitude stronger, the effect of the electric field decay is also two order of magnitude faster (i.e.$\propto 1/r^5$). Thus, at spatial distance of less than the square of the radius of the sphere, the quadrupole field is likely to be dominant. With further increase in distance, the field by the dipole mode is stronger (see appendix 4.2). When considering the application of LSPR, it is therefore important to consider the spatial distance as the near-field electric field enhancement has a limited spatial distance.

The interaction between those metal nanoparticles and the incoming light results can result in absorption of energy by the nanoparticles (generation of heat) or elastic scattering of light back to the space (change of light direction). In optics, those are commonly expressed in term of absorption σ_{abs} and scattering cross-section σ_{sca}, which is derived through calculations of intensity of a parallel beam incident on the nanoparticles. For dipole of a metal sphere[17,18]:

$$\sigma_{abs} = k\ Im[\alpha] = 4\pi k a^3\ Im[g_d]$$ *Equation 2-9*

$$\sigma_{sca} = \frac{k^4}{6\pi}|\alpha|^2 = \frac{8\pi}{3}k^4 a^6\ |g_d|^2$$ *Equation 2-10*

where $k = 2\pi/\lambda$. Since most measurement systems measure the intensity loss of incoming light after passing through a sample, the light intensity loss due to both absorption and scattering are not measured independently. The sum of absorption and scattering cross-section is known as extinction cross-section:

$$\sigma_{ext} = \sigma_{abs} + \sigma_{sca}$$ *Equation 2-11*

$$\sigma_{ext}(\omega) = 9\frac{\omega}{c}\varepsilon_m^{3/2} V_0 \frac{\varepsilon_{i,2}(\omega)}{\left|\varepsilon_{i,1}(\omega) + 2\varepsilon_m\right|^2 + \varepsilon_{i,2}(\omega)^2}$$ *Equation 2-12*

where $V_0 = 4\pi R^3/3$ is the volume of the sphere. Note that this equation only account for the dipolar effect.

To evaluate the optical cross-section against the actual physical geometrical cross-section of the sphere, a dimensionless optical efficiency is used:

$$Q_{ext} = \frac{\sigma_{ext}}{\pi a^2}\,;\, Q_{abs} = \frac{\sigma_{abs}}{\pi a^2}\,;\, Q_{sca} = \frac{\sigma_{sca}}{\pi a^2} \qquad \textit{Equation 2-13}$$

Insert Equation 2-9 and Equation 2-10 into Equation 2-13, then we get

$$Q_{abs} = 4ka\ Im\,[g_d]$$
$$Q_{sca} = \frac{8}{3}k^4a^4|g_d|^2 \qquad \textit{Equation 2-14}$$

Also note that the efficiency of scattering scales rapidly with a^4. This presents a problem in identifying small particles from background with larger particle sizes. By changing the property of the LSPR of the metal nanoparticle, the optical efficiencies can be tuned and it is possible to achieve absorption efficiency larger than 1[19,20], i.e. more energy is being absorbed per unit area. This is beneficial for applications such as where the heat energy absorbed is used to convert to other useful energy form such as electricity for solar cell or water splitting.

2.2.1 *Mie Theory and Computer Simulation*

The approach so far is based on quasi-static approach. However, it is only valid for spheres and ellipsoids that are much smaller than the incident wavelength (below 100 nm)[17]. Phase retardation effects (i.e. phase variation felt and induced across the resonating particle) that occur in larger particles which results in excitation of higher order modes were not considered. Thus quasistatic approaches serve as a first rough estimation only and a general solution is needed to extend considerably to account for larger particle sizes and particle size distribution. This was accomplished by Gustav Mie in 1908 within the frame of electrodynamics[21,22]. Ever since, the Mie theory has been widely accepted to simulate optical properties of electrically neutral clusters of coated spheres and spheroids of size ranging from a few nanometres to micrometres. It has also been extended to other shapes such as spheroids, ellipsoids and core -shell particles. Even so, the shapes that the Mie theory can be modified and applied to are limited, and it provides no insight into materials properties. In order to simulate nanoparticles in complex geometries and the matrix of particles arrays, numerical calculations are often applied and compared with experimental results. Currently, common choices of numerical calculations are discrete dipole approximation (DDA)[23], and finite-difference time-domain method (FDTD)[24]. In addition, computer modelling can also draw electric field map which helps understanding the detailed mechanism and planning better complex structures strategically. Details of numerical approach are beyond the scope of this thesis.

2.2.2 *Materials*

The wavelength at which the plasmonic resonance will occur is determined by the dielectric constant of the materials of choice, i.e. the wavelength at which $\varepsilon_{i,1}(\omega) = -2\varepsilon_m(\omega)$ provided $\varepsilon_{i,2}(\omega)$ is very small and does not vary much in the region of resonance. For this reason, gold (Au), silver (Ag), and aluminium (Al) have been popular choices for plasmonic research in visible wavelength because their real part of dielectric constants are negative, satisfying part of the requirements for LSPR. Figure 2-3 shows the dielectric constant of Au, Ag, and Al. We can also see that Al has a negative ϵ_1 values further down in UV, and therefore being a good choice for plasmonic applications in UV region. Similarly, for Ag, and Au which are good candidates for the visible spectrum up to near infra-red (NIR).

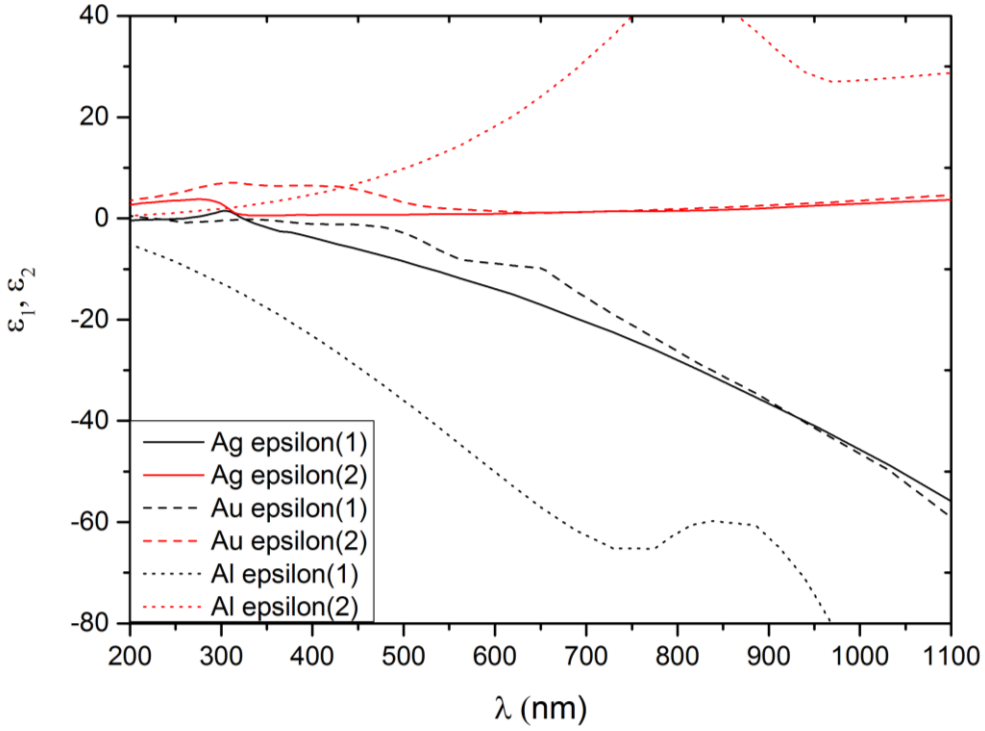

Figure 2-3 Real ϵ_1 and complex ϵ_2 part of complex permittivity $\tilde{\epsilon}$ for Ag, Au, and Al[25].

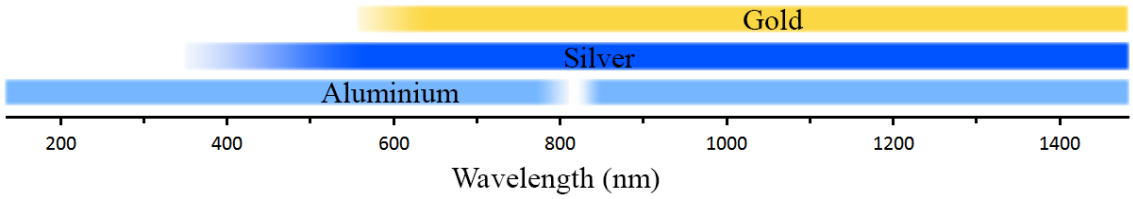

Figure 2-4 Schematic diagram showing the overlapping and region at which different metals (Au, Ag, Al) resonate. The small white regions in the aluminium range around 827 nm is due to interband transition.

The other important consideration is the wavelength at which the interband absorption occurs. Interband absorption causes non-radiation damping in the system and generate heat which could be useful in thermoelectric application but not in applications that requires radiative decay such as biosensing. Table 2-1 lists the location at which the interband absorption occurs for different materials.

It is also possible to observe this wavelength from the dielectric function of the materials where a sudden peak occurs in $\varepsilon_{i,2}$ (or trough in $\varepsilon_{i,1}$). The physics behind the interband excitation can also differ from one material to another. For Al, the interband excitation only presents within a narrow wavelength where the conduction electrons transit into another conduction band. For Au and Ag, it involves transition of electrons in the D orbitals.

Table 2-1. List of threshold energy and associated wavelength at which interband absorption occurs for different materials.

Material	Threshold Energy [eV]	Equivalent value in wavelength [nm]
Al	1.5[26]	827
Ag	3.86 – 3.9[27–29]	318 – 321
Au	2.3 – 2.45[28,30,31]	506 - 521

Chemical properties is another consideration. Au, a noble metal, is highly attractive because of resistance against corrosion and oxidation in air. Ag, will undergo sulfidation in air to form a layer of silver sulphide and has shown to change resonance peak[32] and degrades plasmonic properties. Similarly, Al gets oxidised in air[33]. However, Au is incompatible with the silicon semiconductor industry and is also expensive compared to Ag and Al.

Since in principle, the plasmonic resonance can occur when $\varepsilon_{i,1}$ is negative, other materials that fit these criteria at the wavelength of interests are being considered. Approaches to find those alternative materials include increasing the doping level in semiconductors to make them more metal-like[34] (such as transparent conductive oxide), looking at different alloys[34] such as TiN[35], and carriers concentration in graphenes[34,36]. Graphene is especially of huge interest because it has a very high Q-factor, as it is significantly less lossy than traditional plasmonic materials. Figure 2-5 shows a wide range of alternative conductive materials that could be used in visible, infrared, and microwave which was drawn up by Tassin *et al.*[37].

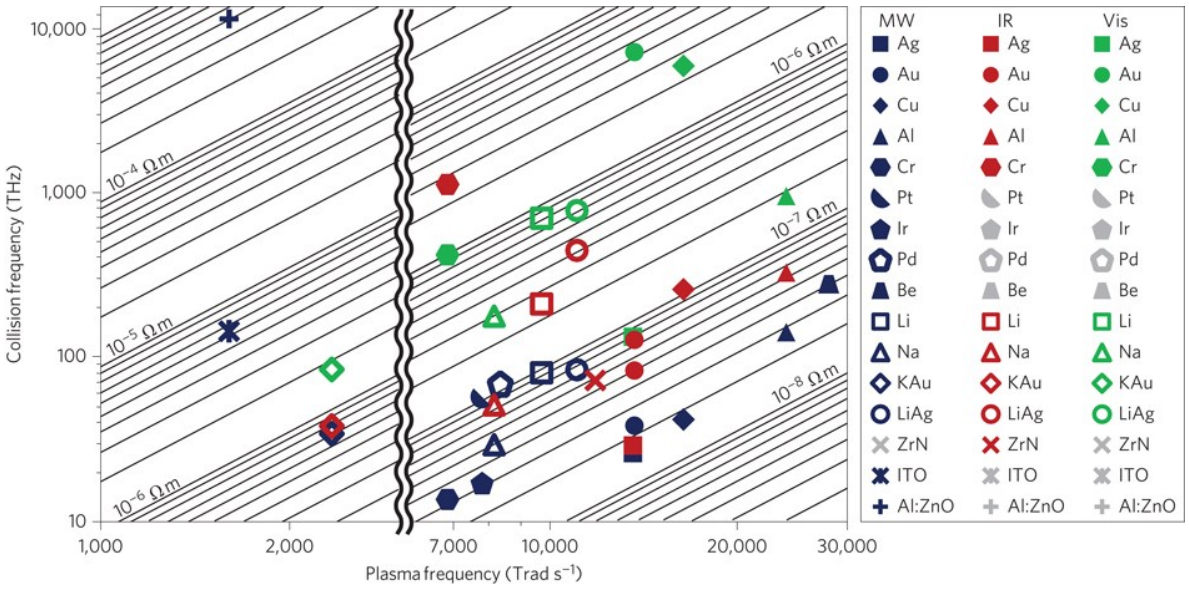

Figure 2-5 The different symbols indicate different materials (see key). The collision frequency takes into account all scattering from the conducting electronic states (electron–phonon scattering, interband transitions and so on) and therefore depends upon frequency. Blue symbols indicate material properties at microwave (MW) frequencies, red symbols in the infrared (IR, 1.55 μm), and green symbols in the visible (Vis, 500 nm). Oblique lines indicate a constant real part of the resistivity and therefore equal loss performance in metamaterials [37]. (Reprinted from ref 37 2012 with permission from Nature Publishing Group.)

2.2.3 *Size and Shape*

The extreme sensitivity of LSPR to the particle size and shape makes it an attractive research subject because the resonance wavelength can be tuned to fits a specific wavelength of interest. From Equation 2-9 and 2-10, the absorption and scattering cross-section of the sphere is directly related to its size with scattering becomes dominant as the size increases. For gold nanoparticles it is found that below ca. 20 nm, absorption channel is dominant. As the size increases, the scattering becomes dominant[38]. Simulation based on the Mie theory[39] and experiment results[15,40,41] showed that increasing the size also causes red-shifting and broadening the LSPR spectrum due to phase retardation effects and presents of higher order mode. The strength and the distance of the induced electric field also increased when the particle gets larger (see Equation 2-5).

For asymmetrical shaped particle, the effects LSPR resonancebecomes more complex. Some additional parameters to consider are the axis at which the size increases, and the direction and polarisation of the incident light. For instance, nanopillar has two axes – height and diameter. Under broadband illumination at normal incidence with unpolarised light, increasing in height results in blue-shift of the resonance peak instead until the height is comparable to the diameter[42]. Similar effect has also been observed for other shapes such as naontriangles, increasing in lateral dimension causes a red-shift in the resonance peak, while increasing the height results in blue-shift[43,44]. Figure 2-7 illustrates a simplified explanation of this phenomenon using a nanopillar as an example (adapted from Henson *et*

Figure 2-6 Solutions containing gold or silver nanoparticles of different nanoparticle sizes. From left to right: 80 nm Ag sphere, 20 nm Ag sphere, 40 nm Au sphere, 12 nm Au sphere, 200 nm Ag sphere, 120 nm Ag nanoplates, and 60 nm Ag nanoplates.. (Reprinted with copyright permission from nanoComposix.com.)

al. [42]). The incident light induced electric moment across one side of the pillar to the opposite side. As the height of the nanopillar is increased there is an increased concentration of displaced charge on both sides, but the distance between the two sides remains the same since the diameter is kept constant. Therefore a stronger restoring force is required, leading to a shorter resonance wavelength. In this example, it is assumed that the total height of the nanopillar remains within a quarter of the incoming wavelength in dimension so that electric field is uniform and phase retardation effect is insignificant. However, if the length is sufficiently long to cause phase retardation between the top and the bottom of the pillar, it will also cause a blue shift due to excitation of higher order plasmonic mode. Furthermore, if there are other nanoparticles around this nanopillar, increased in height also increased the coupling between these nanoparticles which also causes a blueshift in resonance wavelength. Note that due to the symmetry of this nanopillar, incoming light of any polarisations will produce the same result as long as the direction of the light is the same as the axis of symmetry.[43,44]

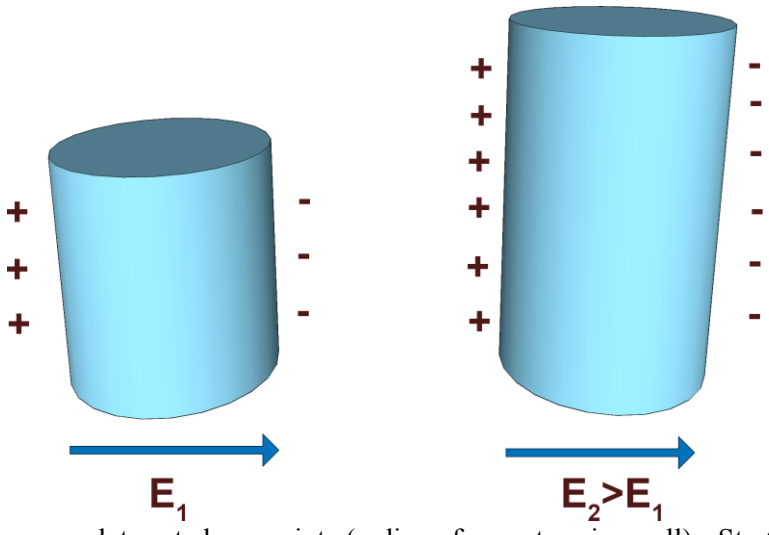

Figure 2-7 A simplified illustration of the phase retardation effect on two nanopillars with same diameters but different heights.

Shape also plays an important role in electric field enhancement. One of the properties of irregular shaped isolated conductor is that the charge accumulates at sharp points (radius of curvature is small). Strategically design structures with sharp edges can lead to dramatic improvement in local electric field enhancement, also known as "lightning

rod effect". Figure 2-8 shows electrodynamics calculated extinction efficiency and electric field contour map for Ag of same volume but in different shapes[45]. Regions of high electric field (so called "hot spots") show up as red color on the map. Other than major change in the extinction spectrum across different shapes, a tremendous increased of electric field enhancement is found at the sharp edges. With this objective in mind, highly complex asymmetrical structures such as nanorice[46], nanocrescent[47–49], and nanostars[50–52] become a subject of huge interest.

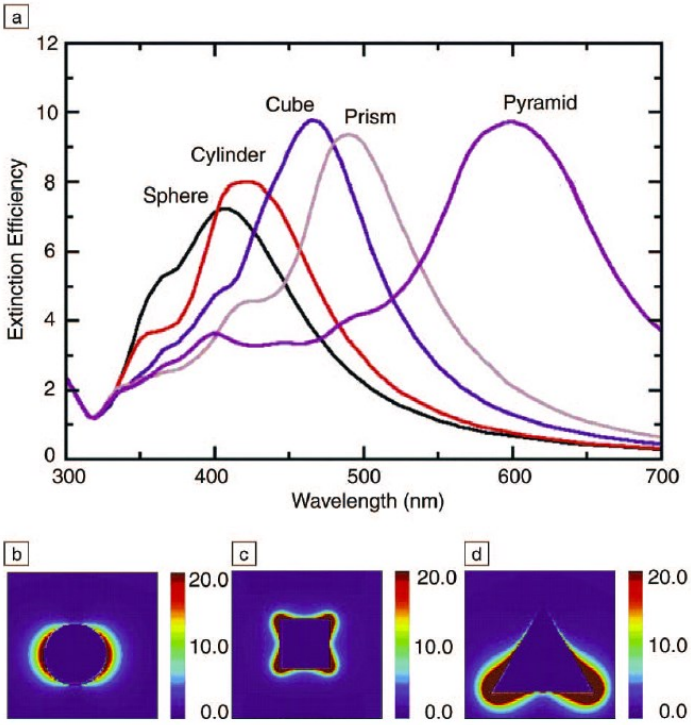

Figure 2-8 (a) Extinction efficiency of silver nanoparticles in Vacuum with same volume as of a 50 nm radius sized sphere but different shapes. The simulated electoral field contour map for corresponding (b) sphere, (c) cube, and (d) pyramid at resonance wavelength with peak value $|E|^2$ of 54, 745, and 9770, respectively[45]. (Reprinted from Ref 45 with permission from Cambridge University Press)

The physical properties such as roughness and polycrystallinity also affects the LSPR property by increasing the damping due to electron scattering rates, especially when the nanoparticles are in nanometres scale. Deposited metals through physical vapour deposition are usually polycrystalline[53,54]. Thermal annealing of the element allows it to dewet and decreases the roughness and polycrystallinity have shown to have significant effect due to change of dielectric response[55,56]. Other effect such as temperature is also found to change the LSPR peak[41,57] due to thermal expansion and also increase of carrier mobility at higher temperature.

2.2.4 *Dielectric medium*

The medium surrounding the nanoparticle also affects its LSPR. In section 2.2.2, it is mentioned that the interband transition could affect the choice of material. Conversely, with the same material at hand it is possible to shift away the resonance peak from the interband transition by choosing an appropriate embedding medium. The dielectric constant of the surrounding medium determine the value ϵ_m and therefore the wavelength at which the resonance occurs. Medium with higher dielectric function will causes further redshift to the resonance peak.

Refractive index sensing (RIS) is one such application that exploits the property of the sensitivity of the LSPR structure against the surrounding medium[58–60]. Nanoparticle with larger aspect ratio and sharper edges were also found to be much more sensitive, similar to phenomena seen to the electric field enhancement as described in section 2.2.3. Thus, without a sophisticated and expensive equipment such as electron energy loss spectroscopy (EELS) to measure the actual electric field enhancement by the nanoparticle at nanoscale, it is still possible to estimate the overall electric field enhancement effect of the nanoparticle in the micro scale through RIS testing.

The dielectric medium also affects the local electric field strength generated by the nanoparticle in resonance mode. From Equation 2-4, it was shown that the electric field generated is related to the dielectric medium. In a medium with higher dielectric constant, other than redshift to match the resonance condition, the numerator in the equation also gets larger and results in larger local electric field.

In most practical case, the nanoparticles are not embedding in vacuum but in solutions or deposited on a substrate such as glass or silicon. In latter case, the nanoparticles are exposed to two different dielectric medium, i.e. the substrate and air or solution. Since the induced electric moment is affected by the surrounding medium, an asymmetrical electric field is generated across the nanoparticle. It is found that the electric field at the interface of air/substrate/nanoparticle most likely to produce the largest electric field enhancement[61,62]. In addition, different dielectric medium shifts the peaks differently. A simple qualitative approach to estimate the redshift is by using effective medium approximation[33,63–67] by taking the average refractive index of the surrounding medium. This approach was found to give qualitative information but tended to deviate from the real values when the nanoparticle are complexed. For instance, it is found the effective medium model underestimated the substrate effect[64]. More detail estimation can be done by using Bruggeman model, Yamaguchi method which includes dynamic depolarisation effect or through calculation intensive Maxwell Garnet theory. However, they require more rigorous calculation and do not guarantee good results for semi-continuous and continuous film.

Metals such as Au and Ag do not bond well to the substrates such as glass and silicon. An additional adhesion layer such as titanium (Ti) and chromium (Cr) are usually applied to promote the binding of the metals to the substrate. Depending on the choice of materials and thickness, those adhesive layer could significantly damp the resonance mode and reduce the full benefit of the LSPR property[68]. A common molecular linker (3-mercaptopropyl)trimethoxysilane (MPTMS) was found to be a good replacement for metal adhesive layer without observable damping and resonance peak shifting[69].

2.3 Coupled Arrays

So far, the scenario above are all based on isolated metal nanoparticles, meaning there is no near-field and far-field interaction between the particles. However, in many cases the particles do influence each other and result in interesting change of properties. When the gap between plasmon particles becomes small enough that an intense electric field enhancement is generated at the gap between them. This electric field enhancement can be even stronger than the lightning rod effect generated on sharp metal tip. In addition, plasmon particles in specific geometries also give rise to other phenomena such as near-field focussing[70], Fano resonance (spectral overlapping of bright mode and destructive mode, causing light confinement)[71,72], magnetic plasmon propagation[73], and optical near-field energy transfer[74]. Coupled arrays could also suppress radiative damping, leading to increase in Q factor[75]. Thus, by arranging the specific geometries of the nanoparticles, it is possible to design the structures with plasmonic properties to suit different applications. This leads to investigation into the potential of coupled nanoparticles, a certain geometry arrangement or large arrays. We will begin with cluster of particles, follow by large 1-D, and 2-D arrays. Some recent works on 3-D arrays will also be discussed briefly.

2.3.1 *Clusters*

When a nanoparticle is in LSPR mode, it also generates a near field profile around it. This can influence other nearby nanoparticles provided the distance is sufficiently close. The particles are said to be coupled when this occurs and formed a new hybrid mode[76–78]. A good detail discussion of hybridisation theory can be found in review article written by Halas and Nordlander group[78]. It has been reported coupling can occur when the distance between the nanoparticles are less than 2.5 to 5 times the size of the nanoparticles[67,79,80].

In this chapter, the cluster is defined as plasmon nanoparticles deposited in a specific group arrangement such as dimer[23,79,81], pentamer[76], heptamer[82–84] (seven particles) or even complex chrysene and triphenylene structures[73] in such a way that the interaction is within the cluster itself. The most basic cluster will be a dimer made of same material and geometry. Since dimer has two axes of symmetry (parallel and perpendicular to the particle axis), incident light on these two different axes produce different LSPR mode. Polarisation along the particle axis results in dipole mode on both nanoparticles in the same direction, whereas polarisation along the perpendicular axis results in dipoles mode on each nanoparticle undergoing phase retardation effect and facing the opposite directions (i.e. out of phase)[85] as this is more energy favourable configuration (Figure 2-9).

Jain *et al*. fabricated gold nanodisc dimer and showed that for light polarisation along the particle axis, the magnitude of plasmon wavelength shift decays nearly exponentially as the nanoparticles are further apart[86,87]. They found that a universal exponential decay length of 0.2 units of

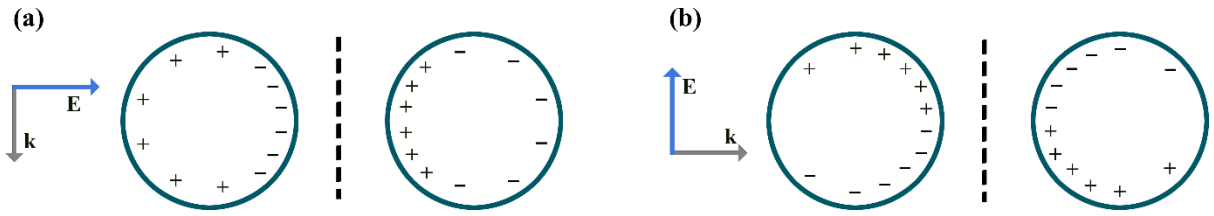

Figure 2-9 Charge distributions in a dimer experiencing excitation at two different polarisation direction indicated by the wavevector k and associated electric field E: (a) along and (b) perpendicular to the interparticle axis.

the particle diameter irrespective of the diameter, shape, metal type, and dielectric medium. The sensitivity to the surrounding dielectric medium also improved as the interparticle distance was closer[88].

A study by Kinnan *et al.* also showed that dielectric medium, a measure of how much energy is stored by external field, improved the coupling strength due to larger particle polarizability which in turn lead to stronger local electromagnetic field and facilitates interaction between neighbouring nanoparticles in larger distance[89]. In addition, as the nanoparticles get nearer, results showed that there is a much more intense electric field generated at the gap between the two particles when comparing to the maximums generated by an isolated identical particle. Studies of variety of dimers in different shapes such as nanotriangles[23] and nanorings[81] also showed similar results except some additional effect due to asymmetrical configuration.

Naturally, it is even more interesting by increasing the number of particles and in different geometrical arrangement. It was found that increasing the number of nanoparticles along the particle axis can cause complex oscillations of peak wavelengths due to the collective phase retardation introduce by the adjacent nanoparticles[90].

Bigger cluster size such as pentamer[91,92], heptamer[82–84], and other oligomer clusters[82] were also fabricated aiming to obtain Fano resonance mode[72,92,93]. This resonance mode occurs when the sharp subradiant and broad superradiant mode interacts and overlaps in energy. The coupling between these two modes allows transfer of energy to another and give rise a characteristic asymmetric line-shape. Application for such unique characteristic leads to even higher sensitivity to dielectric medium and electromagnetically induced transparency[94]. Furthermore, the polarisation direction was found to be able to select the Fano resonance mode at different axis of symmetry[91].

2.3.2 *Arrays*

In arrays, although some properties remain similar to clusters some additional properties arise and become prominent in arrays. Krenn *et al.*[95] found that in one-dimensional nanoparticle chain where the nanoparticles are close to each other, the highest local electric field generated was not on the nanoparticle but the gap between them, similar to case in dimer.

Grating effect

When designing arrays of particles, it is worth considering grating effect as it changes the extinction profile and could also induce damping. Figure 2-10 illustrates three main domains in grating. The domain exists in the plasmonic arrays depends on the interparticle distance along the axis, d, the LSPR wavelength λ_{LSPR}, the critical grating constant, c_{crit}, and the effective refractive index n_{eff}.

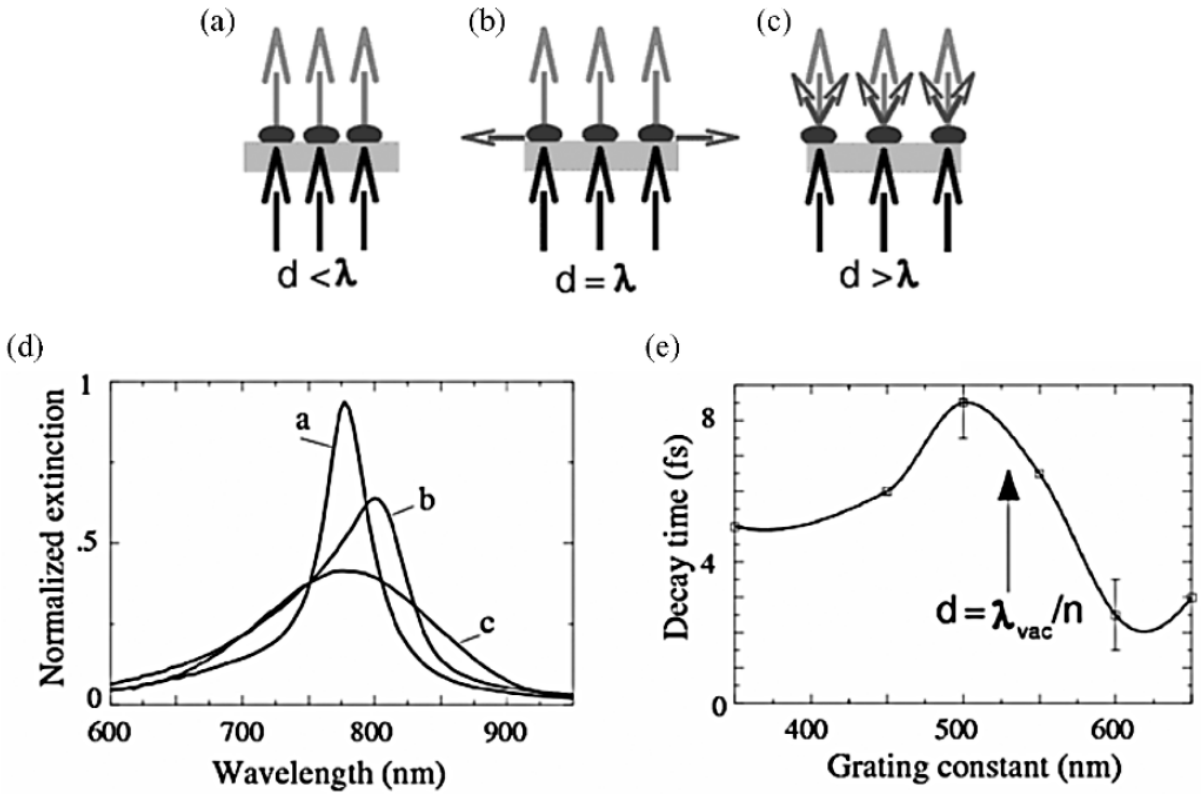

Figure 2-10 (a)-(c) illustrate different domains of grating orders. (d) Extinction spectra of (a) – (c) for square lattice arrays with oblate gold nanoparticles of diameter 150 nm and height 14 nm on glass substrate[96]. (Reprinted from ref 96 with permission from Springer.)

a. Zeroth order grating: $d < \lambda_{LSPR}/n_{eff}$

   When the interparticle distance is smaller than the LSPR wavelength, light scattering is mostly prohibited and the system is predominantly in transmission mode. As such this mode is referred to as radiative mode.

b. First order grating: $d = \lambda_{LSPR}/n_{eff} = c_{crit}$

   When the LSPR wavelength is equal to the interparticle distance in the grating, a cross over between zeroth and first order grating occurs. The interparticle distance at which this occurs is also known as critical grating constant,c_{crit}. Since first grating occurs at wavelength below λ_{LSPR}, this distorts the Gaussian emission shape and produce an asymmetrical emission profile instead. First and higher order grating is also referred as evanescent mode.

c. Higher order grating: $d > \lambda_{LSPR}/n_{eff}$

As the interparticle distance gets larger, higher order grating exists over the whole spectra range, producing multiple scattering mode and results in broader and weaker shape.

Since light scattering is relevant to damping, suppression of damping by having higher grating orders reduces surface plasmon damping and leads to a narrower and sharper extinction spectra[96].

Salerno *et al.*.[97] constructed one-dimensional arrays gold nanodisc chains with distance large enough to avoid spectral shift due to coupling. They showed that as the distance between the nanoparticles decreases from a large distance, the resonance wavelength for polarisation along the particle axis remain fairly constant but a huge variation is seen for polarisation at perpendicular axis. This variation is contributed by grating effect, giving rises to red shift of the wavelength whenever the grating order switches from evanescent to propagating nature[98]. Grating effect also occurs for well-ordered 2D arrays[98–100] with the benefit of additional polarisation directions depending on the symmetry of the nanoparticle arrangement. For instance, a rectangular lattice will have two polarisation direction to achieve grating effect in two perpendicular axes.

Height

It remains possible to change the resonance wavelength and the electric field profile around the nanoparticles in 2-D arrays by changing the height of each nanoparticles. Experiment and simulation by Henson *et al.* showed that increasing the height blue shifts the resonance wavelength, increases the scattering to absorption ration, and also increases the electric field strength[42]. Note that this is similar to isolate LSPR case. However, it is interesting to note that when the interparticle coupling becomes stronger, the electric field penetrate into the substrate reduced and more localised at the regions between nanoparticles.

Homogeneous vs non-homogeneous 2D array structure

In this project, nanosphere lithography is chosen as the nanoscale patterning technique as it is low-cost and can cover larger surface area than e-beam. However, nanosphere lithography which is based on self-assembly mechanism often comes with imperfections such as inhomogeneous particle distribution and random arrangements. Even so, coupling can still occur in random distribution provided the nanoparticles are close enough[101]. However, Nishijima *et al.* demonstrated that a high degree of randomness could results in significant deviation in spectrum[102] due to wide distribution of nanoparticles at different coupling distance and thus strength. Since coupling changed the resonance wavelength, this inevitably affect the overall extinction spectra. On the other hand, simulation shows that such randomness improved the overall electric field intensity due to intense field generated by some of the particles that become very close together when compared to perfect square lattice. Since the improvement is due to the occurrence of some nanoparticles become very close together in their work, it is worth mentioning that if all nanoparticles were very close together in a perfect square lattice, then

the overall field enhancement would still be higher than that non-homogeneous array. In addition, polarisation direction may also become unimportant in random arrays[103].

2.4 Nanoholes and Surface Plasmon Polariton (SPP)

LSPR is only a subcategory of plasmonic. There are also delocalized plasmons that propagate between interfaces of a dielectric medium and metal, known as surface plasmon resonance (SPP). Figure 2-11 illustrates the propagation of SPP along a metal-dielectric interface and the decay of electric field strength away from the interface. Unlike LSPR, generation of SPP requires a more stringent requirement - the energy and momentum of the incident light to match with the SPP in order to fulfil conservation law[17]. As such, a coupler such as a prism or a grating is usually required to excite SPP mode[17].

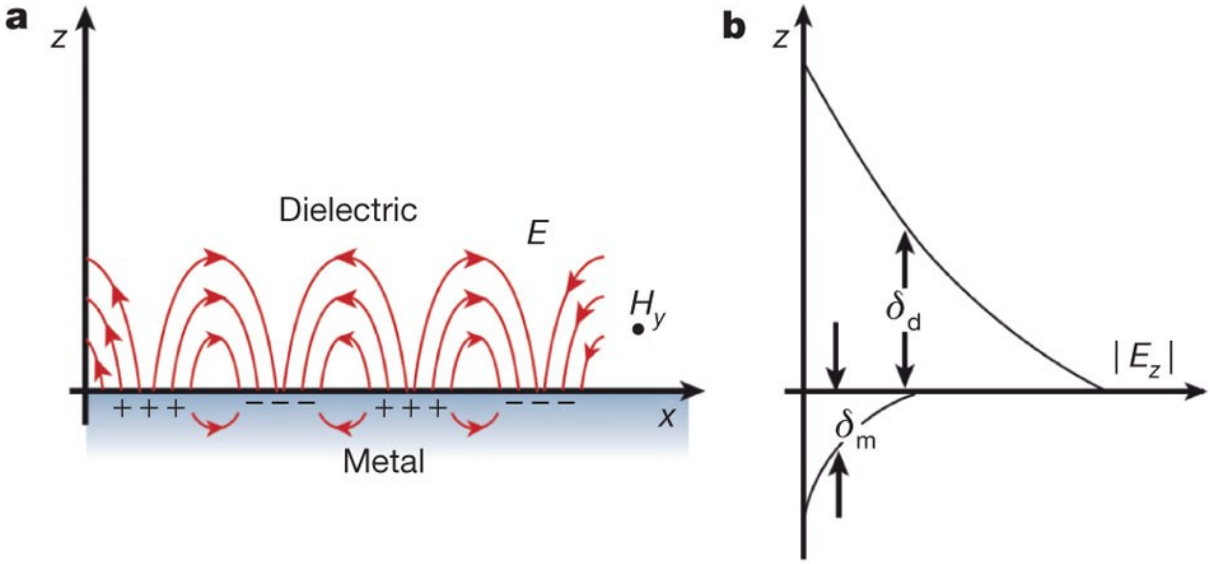

Figure 2-11 (a) Illustration of SPP excited between a dielectric and metal interface. The electric field is plotted in the z-x axis. H_y indicates the direction of the magnetic field (i.e. into the plane). (b) Skin depth of the electric field in the dielectric δ_d and metal δ_m in the z-axis[104]. (Reprinted from ref 104 with permission from Nature Publishing Group.)

Interestingly, it was discovered that SPP can also be generated through nanohole structures without any coupler. Figure 2-12 shows an example of Au nanohole arrays deposited on Pyrex substrate[105]. This simplifies the fabrication requirement while allowing utilization of the SPP property. Another interesting property found on nanohole arrays is the transmission efficiency is larger than unity at the resonance wavelength when normalized to the area of the hole, a phenomenon now commonly referred as extraordinary optical transmission (EOT) first discovered by Ebbessen *et al.*[106]. In their experiment, they measured absolute transmission efficiency greater than 2 at the maxima, more than twice the flux of light passing through the hole than through the air. Some additional properties of the nanohole array they found are: (1) Intensity of the arrays scale linearly with the surface area of the holes. (2) Position of the transmission peak is scale with periodicity of the arrays, independent of the

metals tested (Au, Ag, and Cu). (3) Width of the peaks are strongly dependent on the aspect ratio of the thickness to the hole diameter. Excitation along the long axis is also suggested to be similar to case in LSPR nanoparticle, where resonance at long axis has larger oscillation strength and at lower resonance energy (i.e. longer wavelength). (4) Spectra is significantly different between square and triangular lattice. Experiments by other research groups also shown that spectra and light transmittance are strongly dependent on the shape of the nanohole and polarization direction[107–110]. This polarization dependency allows specific transmittance mode to be selected, which is advantageous in applications such as an on-off switch like a filter[111,112].

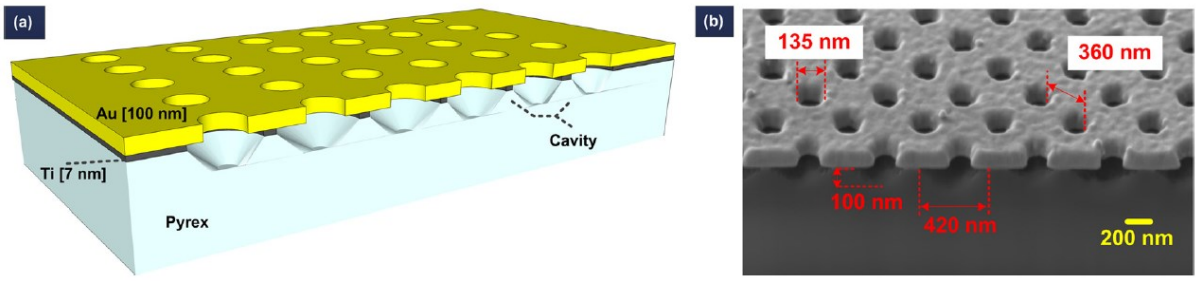

Figure 2-12 A (a) 3-D schematic and (b) SEM view of Au nanohole array in square lattice on Pyrex substrate. There is a cavity beneath each of the nanohole to focus and enhance the electric field around the rim of the nanoholes[105]. (Reprinted from ref 105 with permission from AIP Publishing LLP.)

The plasmonic wavelength in ordered nanohole arrays for square and hexagonal arrays can be calculated from the following equations[113]:

$$\lambda_{SPP}(i,j) = \sqrt{\frac{\varepsilon_i \varepsilon_m}{\varepsilon_i + \varepsilon_m}} \frac{P}{\sqrt{i^2 + j^2}} \qquad \textit{Equation 2-15}$$

$$\lambda_{SPP}(i,j) = \sqrt{\frac{\varepsilon_i \varepsilon_m}{\varepsilon_i + \varepsilon_m}} \frac{P}{\sqrt{i^2 + ij + j^2}} \qquad \textit{Equation 2-16}$$

where P is the periodicity and $\lambda_{SPP}(i,j)$ is the plasmonic wavelength for Bragg resonance orders i,j. It can be seen that the dependency on the geometries, materials, and surrounding medium are similar to LSPR. This implies SPP arise from nanohole arrays also has high tunability. In addition, the EOT is not strictly limited to ordered arrays but also disordered arrays[114].

As for the electric field generated in the nanohole arrays, Correia-Ledo *et al.* found that electric field hot spot depends on the ratio of diameter to periodicity (D/P)[115]. A transition region at D/P between a values of 0.75 to 0.60 was observed. At high D/P ratio above the transition period, the electric field propagates along the top of the metallic network. In the transition region, the electric field slowly becomes localized around the rim of the nanoholes. Further decrease in D/P ratio resulted in electric confinement inside the nanoholes.

3-D Structure

A 2-D plasmonic structure on a substrate is limited by the surface area and parameters to optimize the plasmonic properties. Although the height of the particles gives rise to another parameter to control the plasmonic effect, it remains very limited. Thus, a 3-D plasmonic structure is highly sought after as it adds an additional geometrical parameter in third dimensions, providing more variety of new structures better plasmonic effects. For instance, combining LSPR and SPP type structures altogether could combine the plasmonic effects arrive from both type of system and therefore further improve their application in the system. An example of 3-D structure worth mentioning is a "disk-coupled dots-on-pillar antenna arrays" array fabricated by Zhou *et al.*[116] (Figure 2-13). Essentially, it is a structure comprise of gold nanohole arrays in square lattice, nanodisc at the center of each nanohole and tiny gold nanoparticles between the nanoholes and nanodiscs. Such structure has the combined properties of both LSPR and SPP. Although nanohole SPP is typically known to be much weaker in electric field enhancement when compared to LSPR based structure, in this case their enhancement has convoluted together and become much stronger than the nanostructure based on the individual LSPR and SPP alone with the same geometry. Furthermore, the close distance between the SPP and LSPR nanostructure also give rise to very strong interparticle coupling. The result is a tremendous enhancement in electric field which was harvested to enhance fluorescence emission, a phenomenon known as metal-enhanced-fluorescence emission (MEF, see chapter 3), one of the highest ever recorded to date. Furthermore, this type of plasmonic substrate also has a full surface coverage, meaning that there will be enhancement effect throughout the whole area. Although the plasmonic hot spots may be concentrated at specific regions, the overall average enhancement per area remains higher than usual LSPR and SPP structures alone. Similar structures nanocap-nanohole coupled structures were also made by Wen *et al*. and it was shown that the electric field distribution and enhancement are highly sensitive to the gap[117].

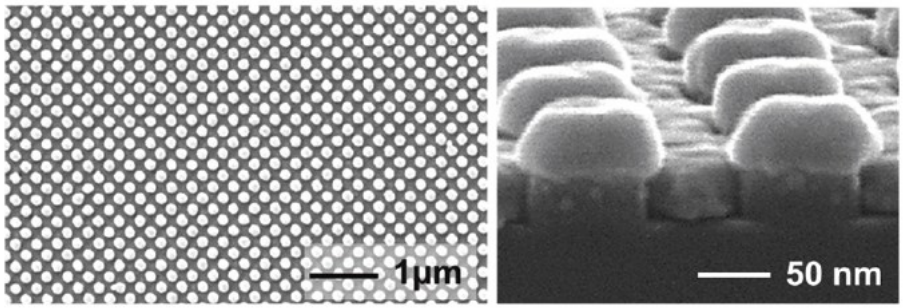

Figure 2-13 Scanning electron microscope images of D2PA structure from top view (left) and cross-section view (right)[116]. (Reprinted from ref 116 with permission from American Chemical Society.)

With the improvement in our current nanofabrication techniques, fabrication of 3D complex structures have become more reachable. More research should be focusing on 3D complex plasmonic structures on different surfaces for different applications for giant electromagnetic field enhancement.

2.5 Conclusion

A basic understanding of LSPR and SPP is necessary to provide a strategy roadmap and design criteria to optimize structures to suits a specific application. This chapter reviews general concepts of LSPR and SPP and their potential applications. Figure 2-14 shows a number of different parameters that influence LSPR properties and Figure 2-15 shows a mind map of different applications based on LSPR and SPP properties. However, full potential of those plasmonic properties has yet to be explored and an optimum structure for every different applications has yet to be found. For example, a recent study by Atwater group[12] shows that surface plasmon can play the same role as the photon in quantum phenomena. In particularly, they observed unambiguous two-photon quantum interference between plasmons, with the same visibility and mutual coherence time as in the photonic scenario. This is an important breakthrough if plasmonic structures are to be employed in quantum information applications, which typically require indistinguishable particles. In printing, the nanoscale features and optical properties of clustered plasmonic structures open up a new strategy to overcome current industrial print resolution at sub ~10,000 dots per inch (d.p.i.). To demonstrate this feasibility, Yang group used nanoimprint technology to fabrication nanohole-disk plasmonic structures with a pitch of 250 nm and printed images at optical resolution limit of ~ 100,000 d.p.i[11].

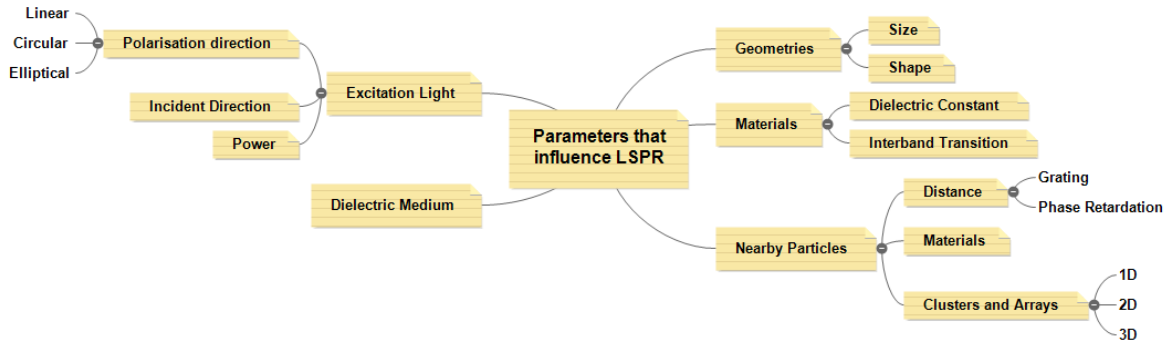

Figure 2-14. A mind map showing different parameters that influences the LSPR.

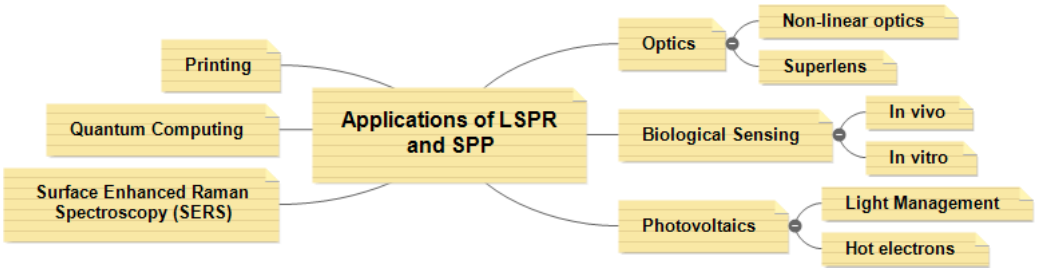

Figure 2-15 This mind map summarise the extend of LSPR and SPP applications in different fields mentioned in literature review in this chapter.

Recent advancement in nanofabrication technique allows further manipulation and control of material geometries in nanoscale, enabling optimization of 3-D structures for myriad of applications. In this project, a low cost, versatile nanofabrication is used to fabricate large variety of nanoscale

structures such as nanotriangles, nanodisc arrays, and a novel nanohole-disc arrays structure. The topography and optical properties of those structures are shown in chapter 5.

In the next chapter, the application of LSPR and/or SPP in biosensing through a mechanism called metal-enhanced fluorescence (MEF) will be introduced. This method enables a tremendous enhancement in fluorescence emission from fluorophores and improves the current detection limit. This will benefit us to have an earlier diagnosis of cancer.

Chapter 3

Application of Plasmonic in Biosensing

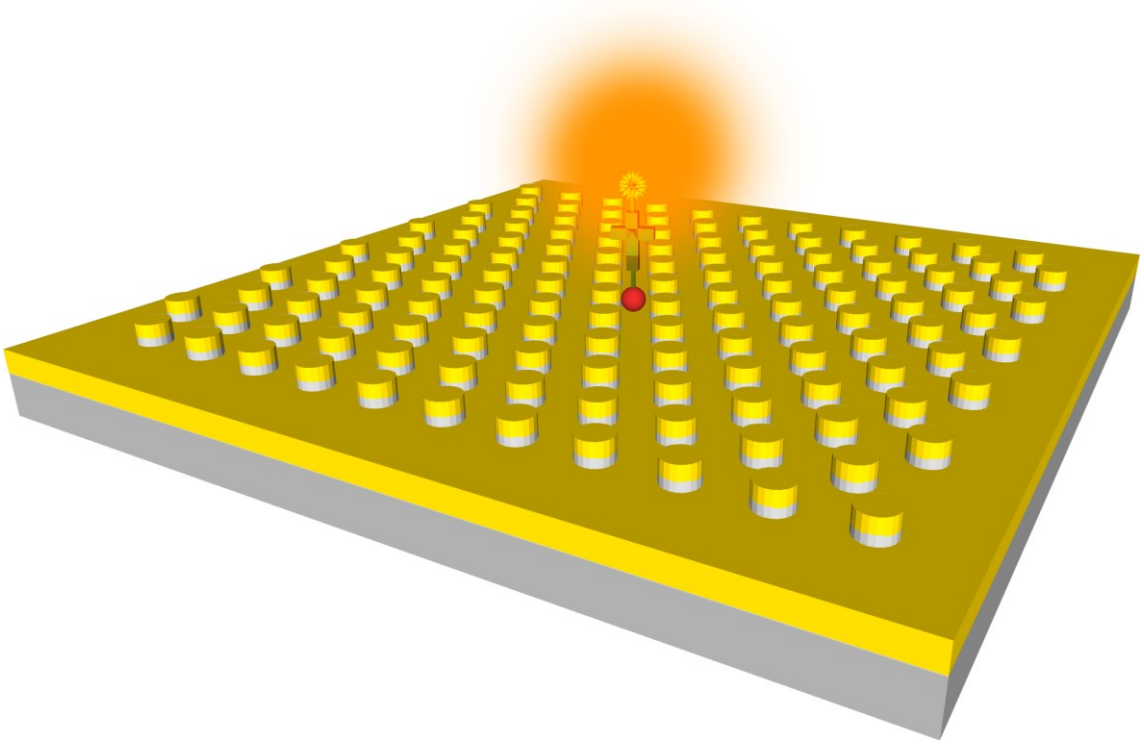

Figure 3 Illustration of enhanced fluorescence from a fluorophore attached onto a nanohole-disc arrays plasmonic substrate.

Chapter 3 Application of Plasmonic in Biosensing

Biosensors are devices incorporating a biological element for measuring and detecting wide spectrum of analytes. First basic concept of biosensor was revealed by Leyland C. Clark in 1962, described as "enzyme electrode". In the last few decades, there has been rapid development in biosensors[118,119] for medical diagnosis, pharma and food process control, environment monitoring[120], and security[121,122].

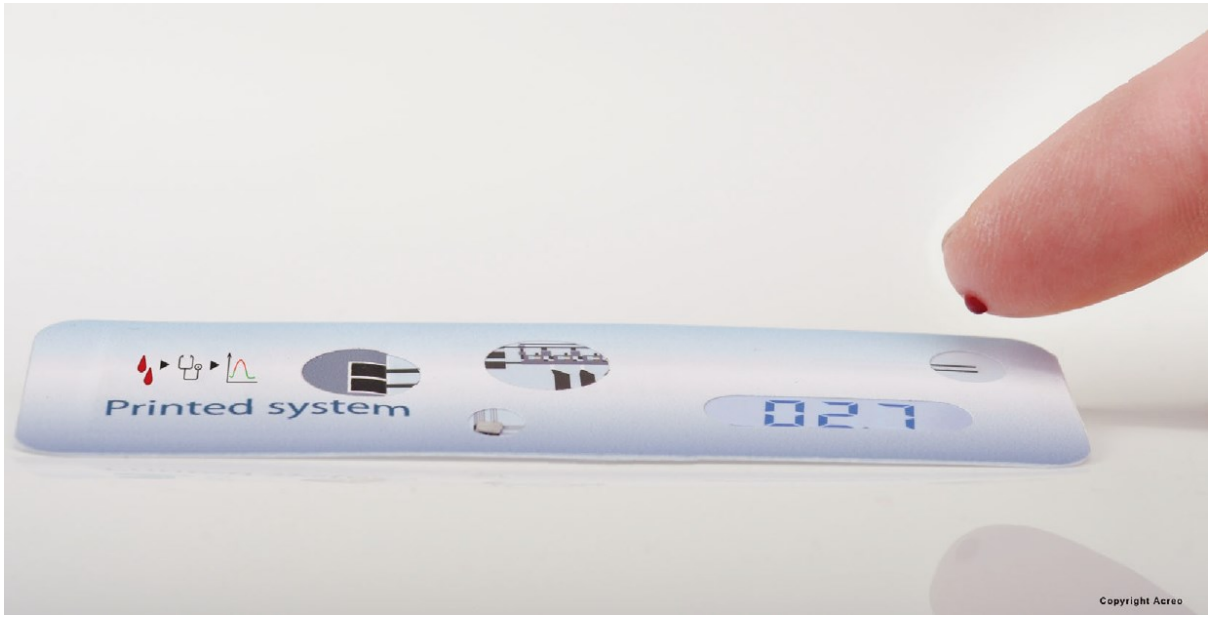

Figure 3-1 An illustration of an all printed disposable biosensor being developed by Acreo[121]. (Reprinted from ref 121 with permission from Royal Society of Chemistry.)

In particular, applications in healthcare receive most of the attention and investment. There are two broad categories of instrumentation[121]: (1) sophisticated expensive laboratory equipment that is capable of accurate analysis in short time; (2) portable, and user friendly devices designed for general publics. In an attempts to lower the cost of those devices, various innovations have been made but the early stage of biosensors relied on SPP technology and were not very successful. Later, a notable revolutionary discovery of LSPR gave promising roadmap for highly sensitive with lower fabrication cost.

The measurement can be classified into *in vivo* (in a living organism) or *in vitro* (elsewhere outside living organism). *In vivo* method allows direct observation of the object of interest such as tumor[123] and vasculature imaging[124] in the body which helps determine the affected location. However, such method can be very challenging as living organism are a complex system containing many different type of biological and chemical components such as genes, proteins, organics and inorganics compounds. Those additional components can complicate the study and making the investigation difficult. On the other hand, *in vitro* method allows simplification of the system or disease under study by performing the study outside their normal complex biological context, reducing the extra unknown parameters that could be introduced by other components exists inside the living organism.

Nevertheless, both methods are affected by intrinsic fluorescence property possessed by some biological tissues, known as autofluorescence. Coincidentally, the autofluorescence is in the visible wavelength makes detection and imaging in visible wavelength ambiguous and presents a major problem. Solutions are to either increase the biomarker emission intensity or avoiding measurement at wavelength that autofluorescence emits.

Near-infrared light (NIR-I) between 700 – 900 nm is referred as the first "biological window" because light can penetrate biological tissues more efficiently as these tissues scatter and absorb less light at these wavelength[125–127]. Furthermore, autofluorescence from the tissues is relatively low in this region[128–130] when compared to optical wavelength. Above this wavelength, absorption by water and lipids become significant. At longer wavelength, a second NIR window (NIR-II) exists between 1000 – 1400 nm. This region has shown to be able to provide a better signal contrast and signal-to-noise ratio[131,132] than NIR-I (Figure 3-2). Simulation also showed that quantum dots that emits light at 1320 nm improved the signal quality by over 100-fold when compared to one that emits at 850 nm[133]. Thus, structures and materials that photoluminescence at NIR-II makes them a much more promising candidates for biological imaging than NIR-I.

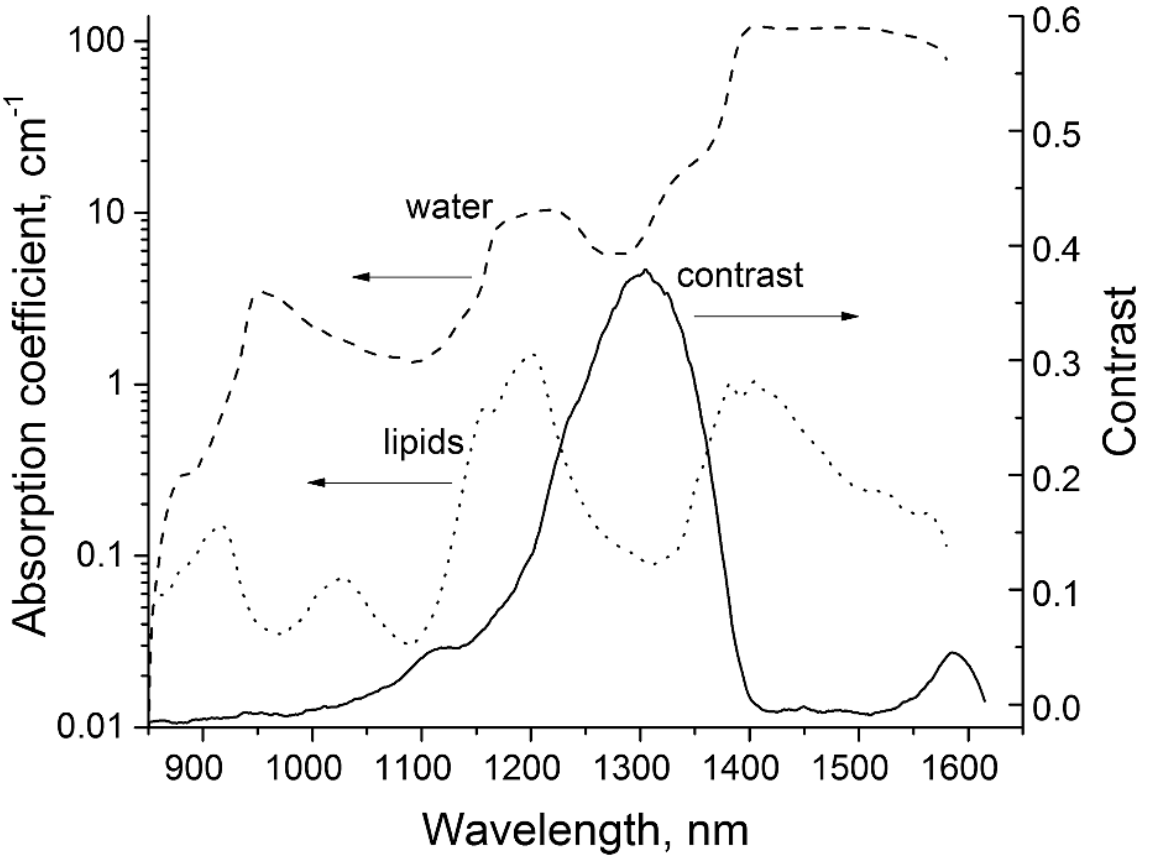

Figure 3-2 Absorption spectra for water, lipids, and the signal contrast between them at NIR region[132]. (Reprinted from ref 132 with permission from SPIE.)

However, fluorescence dye at NIR-II dyes remain uncommon and suffers problems such as low quantum yield, photostability, and biocompatibility. Therefore, even with high promising results speculated from theoretical calculation, detection and imaging at NIR-II window remain difficult due to intrinsic problem with current existing NIR-II dyes. As such, research and development to obtain more reliable and higher quality NIR-II dyes is a huge interest to the industry[134–138]. An alternative solution which is perhaps faster and cheaper, is to couple fluorophores with plasmonic structures to achieve a mechanism known as metal-enhanced-fluorescence (MEF). It has been shown successfully that MEF can tremendously improve the photostability, quantum yield and the emission of fluorophores in visible and NIR-I regions. This chapter aims to introduce the mechanism and properties of MEF together with some state-of-the-art in the literature. The results that demonstrate the potential of MEF in NIR-II region can be found in chapter 6 of this thesis.

3.1 Fluorescence

Fluorescence is one of the luminescence process. It involves three main stages as illustrated in the simplified Jablonski diagram shown in Figure 3-3: (1) Incoming photons with higher energy are first absorbed by the fluorophores and excited to higher electronic state. (2) The excited state exist for a finite time while undergoing a non-radiative internal relaxation process before reaching the lowest excited state. (3) The system then de-excites back to ground state through emission of light with energy equal to the difference between the two states, this process is also known as spontaneous emission.

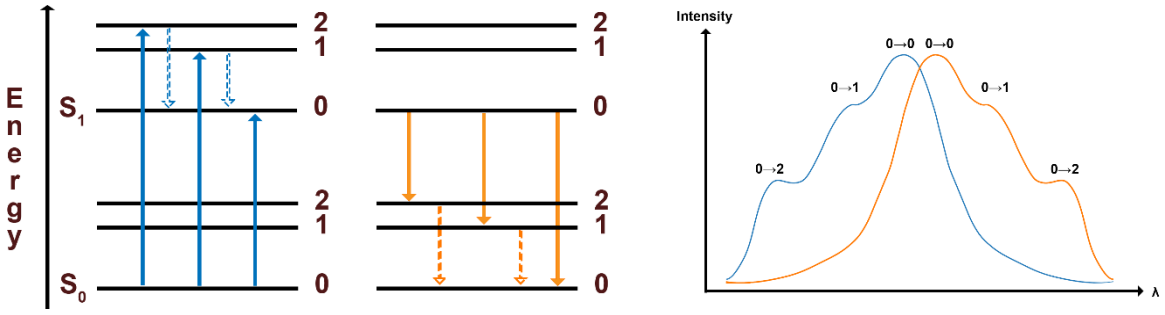

Figure 3-3 (Left) A Jablonski diagram showing three main processes involved in fluorescence mechanism. The vertical exists resembles the energy level of the states.S_1 is the singlet higher electronic state, and S_0 is the ground state. Orange solid and dash lines resemble emission by photon emission and internal relaxation, respectively. (Right) An example of a fluorophore absorption and emission spectra based on Frank-Condon principle. Blue solid lines and dash lines resemble excitation by energy absorption and internal relaxation, respectively.

The efficiency of a fluorophore, also known as quantum yield (Q_0), is defined by ratio of number of photons emitted to the number of photons absorbed (Equation 3-1). Alternatively, it can also expressed in term of intrinsic radiative decay rates (Γ_0) and non-radiative decay rates (k_{nr}) as shown in Equation 3-2 for a fluorophore.

$$Q_0 = \frac{number\ of\ photons\ emitted}{number\ of\ photons\ absorbed} \qquad \textit{Equation 3-1}$$

$$Q_0 = \frac{\Gamma_0}{\Gamma_0 + k_{nr}} \qquad \textit{Equation 3-2}$$

The lifetime (τ) of the fluorophore is the average length of time the fluorophore spending at the excited state prior to return back to ground state. It is related to the decay rates and quantum yield through the following expressions:

$$\tau_0 = \frac{1}{\Gamma_r + k_{nr}} = \frac{Q_0}{\Gamma} \qquad \textit{Equation 3-3}$$

3.1.1 *Rules*

The fluorescence mechanism also tends to follow a few rules. Note that there are cases where exception to those rules occurs.

Mirror Image Rule

The absorption spectrum and the emission spectrum are typically a mirror image of one another. This reason is that the same transitions are involved in both absorption and emission process and similarities in vibronic states in ground states and excited states. According to Frank-Condon principle, those electronic transitions are vertical, thus an excitation where, say, the zeroth ground state to second vibronic levels in excited is the largest, then reciprocal relaxation from zeroth excited states back to second vibronic ground state is also most probable[139].

Stokes Shift of Fluorescence Emission

This phenomena is named after Sir G. G. Stokes who made his discovery in 1852[140]. Analysis on the Jablonski diagram also implies energy loss during the relaxation process, therefore the emitted spectrum are usually at a longer wavelength than the absorption spectrum. Generally, this is due to (1) non-radiative decay to the lowest excited states before emission, and (2) the emission of photon usually leaves the fluorophores at highest vibronic level at ground state S_0. Polar fluorophores in polar solvent produced largest stoke shift whereas in viscous or glassy media typically blueshifts. The latter is because the fluorophores relaxes on much faster timescale than the time for solvent molecules to re-orientate.

Kasha-Vavilov Rule on Quantum Yield

According to Kasha-Vavilov rule, the quantum yield of the fluorophore is generally independent of the excitation wavelength provided it is within the absorption window. This is because when the fluorophore is excited to higher electronic states, internal relaxation occurs very rapidly and decay into

the lowest vibronic level of excited state S_1 before decay back to highest vibronic level at ground state S_0.

3.1.2 *Spontaneous Emission*

The emission of light in fluorescence is a spontaneous emission process by which a quantum system such as atom, molecules, and in this case the fluorophore emitter in an excited states undergoes a transition to a lower energy state associated with release of a photon with energy equivalent to the energy difference between the higher and lower energy states. In 1946, Purcell discovered that the spontaneous emission depends on both the emitter itself and its surrounding environment[141]. This means that the emitter and the environment cannot be considered as a separate entities because they interact and modify each other. Therefore, we need to consider the system with the emitters and the surrounding environment as a whole.

In ground state where there is no photon in the system, a quantized of energy $E_{vac} = {}^1/_2\,\hbar\omega$ exists due to the random fluctuations of the electric field known as the vacuum field. This state can interact with an isolated emitter in an exited state and make it de-excite into a lower energy level. The corresponding radiative transition rate γ from initial state $|i>$ and final state $|f>$ can be calculated based on base on Fermi's Golder Rule[142–144]:

$$\Gamma = \frac{2\pi}{\hbar^2}\left|< f\left|\hat{\boldsymbol{\mu}}\cdot\hat{\boldsymbol{E}}\right|i>\right|^2\rho(\omega) \qquad \textit{Equation 3-4}$$

where $\hat{\boldsymbol{\mu}}$ and $\hat{\boldsymbol{E}}$ are the electric dipole and electric field operators evaluated at the emitter position, and $\rho(\omega)$ is the frequency dependence final photonic density of states. The matrix element in this equation take into accounts the quantum mechanical properties of the emitters while $\rho(\omega)$ reflects the influence of the environment. For a ground state in vacuum field $\hat{\boldsymbol{E}}_{vac}$ and by consider averaging over all possible directions, the transition matrix then becomes

$$\left|< f\left|\hat{\boldsymbol{\mu}}\cdot\hat{\boldsymbol{E}}_{vac}\right|i>\right|^2 = \frac{1}{3}\mu_{if}^2 E_{vac}^2 \qquad \textit{Equation 3-5}$$

where μ_{if} is the square modulus of the electric dipole moments of the transition, i.e.

$$\mu_{if} = -e < i|\boldsymbol{r}|f > \qquad \textit{Equation 3-6}$$

Here, e is the electron charge and $\boldsymbol{r}$ is the position operator.

The $\rho(\omega)$ in vacuum in Equation 3-4 can be calculated EM modes within a cube of volume V:

$$\rho(\omega) = V\rho_0 = V\frac{\omega^2}{\pi^2 c^3} \qquad \textit{Equation 3-7}$$

where ρ_0 is the magnitude of the local density of states for vacuum, defines as the number of final states (modes) per unit volume with frequency ω. The value of E_{vac} can also be calculated by equating the electromagnetic energy in a volume V to the zero point energy:

$$\int \varepsilon_0 E_{vac}^2 dV = \frac{\hbar\omega}{2}$$

$$\therefore\ E_{vac} = \sqrt{\hbar\omega/2\varepsilon_0 V} \qquad \textit{Equation 3-8}$$

Note that ε_0 is the permittivity of free space and not to be confused with dielectric function defined in previous chapter.

Equation these equations above, we obtain the decay rate of an isolated emitter in vacuum

$$\Gamma_0 = \frac{1}{\tau_0} = \frac{\mu_{if}^2 \omega^3}{3\pi\varepsilon_0 \hbar c^3} \qquad \textit{Equation 3-9}$$

In the next section, we look at the effect of plasmonic metal, which becomes the environment that influences fluorophore emitters and modifies the decay rates.

3.2 Metal Enhanced Fluorescence (MEF)

Fluorophores can interact with surface plasmon resonance of metal and produce brighter emission through a mechanism commonly known as metal enhanced fluorescence (MEF). This is also sometimes referred to metal induced fluorescence enhancement (MIFE)[145] and plasmon enhanced fluorescence (PEF)[146,147] in some literatures.

3.2.1 *Mechanism*

There are two main processes that give rises to MEF: (1) External electric field that influence the molecules, and (2) the emission of radiation influenced by local field environment. When a fluorophore is in the vicinity of a plasmon resonating nanoparticle, the fluorophore will experience the electric field generated by the nanoparticle. Those enhanced electric field increase the amount of energy absorbed by the fluorophore known as excitation enhancement. The rate of the enhanced excitation (E_{ex}) is related by the following equation[148]:

$$E_{Ex} = \frac{|\boldsymbol{E}(x_d, \lambda_{ex}) \cdot \boldsymbol{p}|^2}{|E_i|^2} \qquad \textit{Equation 3-10}$$

where $\boldsymbol{E}(x_d, \lambda_{ex})$ is the electric field at the position and wavelength of excitation, p is the emitters (fluorophore in this case) orientation, and E_i is the incident free space electric field without the presence of the nanosphere. Sergei *et al.* shows a direct correlation of the strength of the plasmonic generated

electric field strength with the excitation enhancement by using two different lasers with slightly different wavelengths. In their experiment, they showed that the fluorescence emission intensity improved by a factor of 2.5 when the electric field generated is also increased by about 2.5 times[149].

As mentioned earlier, the discovery of Purcell effect shows that lifetime of an excited atomic state depends not only on the atom but also the surrounding environment[141]. A similar situation occurs when an emitter is placed inside a cavity. However, photons can only decay into certain final states supported by the cavity involved. For example, for an emitter near a LSPR nanoparticles, the final density of states $\rho(\omega)$ will have a peak maximum at the resonance wavelength as this provides a strong and new decay channel to the emitter[142].

Consider a cavity that only support one mode of frequency at ω_c with Lorentzian lineshape, the desity of state $\rho(\omega)$ can be described as

$$\rho(\omega) = \frac{2}{\pi} \frac{\Delta\omega}{4(\omega - \omega_c)^2 + \Delta\omega^2} \qquad \textit{Equation 3-11}$$

where $\Delta\omega$ is the width of the local density of state maximum at $\omega = \omega_c$. If an emitter is inside this cavity and has an electronic transition at $\omega_0 = \omega_c$, then the density of state at this frequency becomes

$$\rho(\omega_0) = \frac{2Q}{\pi\omega_0} \qquad \textit{Equation 3-12}$$

where $Q = \omega_c / \Delta\omega$ is the quality factor.

For a weakly coupled system, the cavity and emitter can be isolated into two different entities and the transition matrix can be calculated using Equation 3-5 and Equation 3-8, yielding

$$\left| < f \left| \hat{\boldsymbol{\mu}} \cdot \hat{\boldsymbol{E}} \right| i > \right|^2 = \beta^2 \frac{\mu_{if}^2 \hbar\omega}{2\varepsilon_0 V} \qquad \textit{Equation 3-13}$$

where β is the coefficient that takes into account the orientation of the dipole emitter with respect to the electric field

$$\beta = \frac{|\boldsymbol{\mu} \cdot \boldsymbol{E}|}{|\boldsymbol{\mu}||\boldsymbol{E}|} \qquad \textit{Equation 3-14}$$

For an emitter that is parallel in the cavity, $\beta = 1$, and for randomly distributed orientation, $\beta^2 = 1/3$. Same as before for an emitter in ground state, the decay rate of the emitter placed in an emitter Γ_{cav} can be calculated using Equation 3-4, Equation 3-12 and Equation 3-13, we arrive with the following equation

$$\Gamma_{cav} = \beta^2 \frac{2\mu_{if}^2}{\varepsilon_0 \hbar} \frac{Q}{V} \qquad \textit{Equation 3-15}$$

By comparing the decay rate in cavity and in free space, it allows us to determine if the coupled system enhanced or quenched the emitter:

$$\mathrm{F_P} = \frac{\Gamma_{cav}}{\Gamma_0} = \frac{\tau_0}{\tau_{cav}} = \frac{3}{4\pi^2} Q \left(\frac{\lambda^3}{n^3 V}\right) \qquad \textit{Equation 3-16}$$

Here, we have used $c/\omega = n(2\pi/\lambda)$, where n is the refractive index of the cavity. The factor F_P is also known as Purcell factor. For $F_P > 1$, the spontaneous emission decay rate is enhanced. If the value is less than 1, then the cavity is quenching the emission. From this equation, we can also see that the Purcell factor is proportional to the quality factor of the cavity, and inversely proportional to the mode volume. Despite poor quality factor in typical plasmonic system ($Q \approx 10 - 100$), the highly reduced mode volume of LSPR enables very strong enhancement of the decay rates, given by the factor λ^3/n^3V in the equation[142].

The explanation above are for weakly coupled system in term of a quantum mechanics system, where there is no strong perturbation of the electric field into the emitter and the lifetime of the LSPR is very short compare with the inverse of the spontaneous decay rate of the isolated emitter. If the system is strongly coupled (in term of quantum mechanics system), the photons remain in the cavity for a long time, undergoes multiple absorption and reemission process before radiate out from the system. In this case, the emitter and the environment must be considered as one single entity and a full quantum electrodynamics analysis is required. However, the strong coupling mode mentioned here is not to be confused with the term strong coupling mode used throughout in this thesis which arise from the interparticle plasmonic effects.

Similarly in MEF, the electromagnetic coupling between the fluorophore and the nanoparticle plasmon also causes an increase in radiative decay rate of the molecule at the emission wavelength or decreases the decay rate if quenching occurs. This emission enhancement introduces new radiative and non-radiative decay rates ($\Gamma_{m,r}$ and $\Gamma_{m,nr}$), and modifies both the quantum yield and lifetime of the fluorophore. Equation 3-2 and Equation 3-3 then become[118,150,151]:

$$Q_m = \frac{\Gamma_{m,r} + \Gamma_{0,r}}{\Gamma_{m,r} + \Gamma_{0,r} + \Gamma_{m,nr} + \mathrm{k}_{nr}} \qquad \textit{Equation 3-17}$$

$$\tau_m = \frac{1}{\Gamma_{m,r} + \Gamma_{0,r} + \Gamma_{m,nr} + \mathrm{k}_{nr}} \qquad \textit{Equation 3-18}$$

where Q_m is the modified quantum yield due to MEF, the subscript m represents modified term due to the plasmon coupling. The ability to modify the quantum yield of the fluorophores is an important benefit for MEF because fluorophores with poor quantum yields can be improved externally through coupling with plasmon resonance generated by the metal. Consequently, this leads to emission enhancement:

$$E_{Em} = \frac{Q_m}{Q_0} \qquad \textit{Equation 3-19}$$

Together, the new excitation and decay rate increased the rate of total fluorescence emission (E_F), and is related by the following relationship:

$$E_F = E_{Ex} E_{Em} \qquad \textit{Equation 3-20}$$

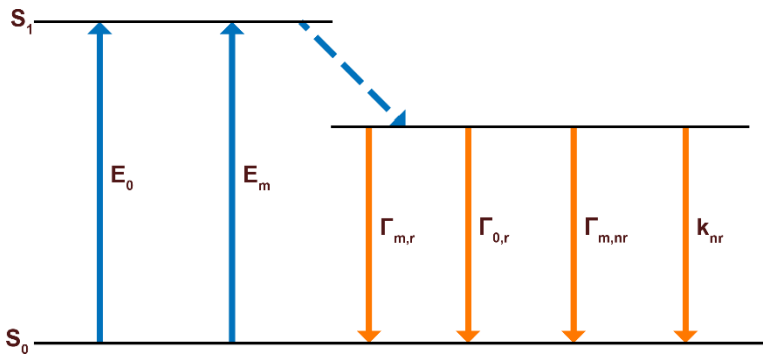

Figure 3-4 A simplified Jablonski diagram showing the additional decay routes, $\Gamma_{m,r}$ and $\Gamma_{m,nr}$, when experiencing MEF.

It is worth emphasising that from the above equations, the MEF primarily due to (1) electric field enhancement which boosts the excitation rate of the fluorophores, and (2) the addition of new radiative decay channels that improves the emission rates and quantum yields. In the case where the fluorophore has intrinsic high quantum yield, the emission enhancement will not be significant.

For optical measurements, the enhancement (E_F) of a single fluorophore emitter can be written as[152]

$$E_F = {(S_{MEF} P_0)}/{(S_0 P_{MEF})} \qquad \textit{Equation 3-21}$$

where S_{MEF} and S_0 are the fluorescence intensity with and without MEF respectively, P_{MEF} and P_0 are the laser excitation power used for fluorophore with and without MEF respectively which acts as a correction factor. The laser excitation plays a role here because higher laser excitation power implies higher rate of photon excitation with same wavelength. Consequently, the fluorophore experience greater rate of excitation-emission cycle, provided that the laser excitation does not saturate the population of the excited state. For direct comparison, the excitation power are usually kept constant in experiments and this equation simplifies to

$$E_F = S_{MEF}/S_0 \qquad \textit{Equation 3-22}$$

For large area of nanostructures covered with a monolayer of conjugated fluorophores, it becomes necessary to consider the effect of potential emission from the conjugated proteins, and also the difference in surface area available for fluorophores attachment. As such, the fluorescence enhancement factor in the nanostructure need to be modified as[150]

$$E_F = \frac{(S_{MEF,fluorophores} - S_{MEF,protein})}{(S_{0,fluorophores} - S_{0,protein})} \frac{C_{o,fluorophores}}{C_{MEF,fluorophores}} \quad \text{Equation 3-23}$$

where the subscript represents (substrate type, emitter). For instances, $S_{MEF,fluorophores}$ is the emission signal from the MEF conjugated fluorophores attached on plasmonic nanostructure. $S_{0,protein}$ is the emission signal from the protein attached on bare substrate without the plasmonic nanostructure. The surface area correction factor,C, allows one to adjust for the differences in the total amount of emitters deposited on various surfaces. It can be calculated based on the surface area difference between bare substrate and plasmonic nanostructured surfaces.

3.2.2 *Criteria*

There are a few parameters that need to be considered when engineering MEF based biosensors.

Spectral Overlap

The optical spectrum indicates wavelength at which the metal nanoparticles resonate, which also implies the location at which the strongest electric field generated. If there are very little spectra overlapping between the fluorophore and the metal, then one would expect insignificant enhancement effect from SPR[147]. Thus, it is important to have both the excitation and emission spectra of the fluorophore fall within the SPR extinction spectrum, ideally around the maximum peak.

Even when the spectra are completely overlapped, it has also been observed that the brightest fluorescence is when the fluorophore emission peak is at longer wavelength (i.e. lower energy) relative to the LSPR scattering peak[153,154]. Ginger *et al.* interpreted this could be due to both the radiative and nonradiative decays are enhance at resonance. However, when at slightly longer wavelength than the resonance peak the nonradiative decay rate decreases faster than radiative decay rate. Therefore, higher fluorescence enhancement is located at longer wavelength from the LSPR peak. Lakowicz *et al.* also had the similar interpretation through optical spectra[155]. The nonradiative decay and radiative decay are related to absorption and scattering of the nanoparticles, respectively. Since scattering peak is usually at longer wavelength than absorption, fluorophore emission at slightly longer wavelength allows greater scatter scattering efficiency while reduced absorption. Similar results were also obtained by Novotny group[156].

Location of 'Hot Spots'

The enhanced electric field generated by SPR are not uniform throughout the surface. Since MEF is highly dependent to the enhanced electric field, the fluorophores should all be located at region of 'hot spots' where electric field generated are the highest. In an experiment performed by Yuan *et al.*.,[157] a large variation of fluorescence enhancement value has been shown when a single dye molecule to diffuse slowly to different location of nanorods. Structures such as nanostars, which has multi high

density of sharp points could be beneficial where most of the surface is covered by the spikes. However, the measurement performed on a single molecule would require time consuming process and expensive equipment. Practical measurements are performed on large area and covered the locations where there is no MEF effect. Therefore, the enhancement factors obtained from experiments are typically an average value which is much lower than the maximum fluorescence intensity obtained at the hot spots.

Metal-Fluorophore Distance

It is widely recognised that the MEF is highly dependent on the distance between the fluorophores and the metal nanoparticles. Quenching occurs when the fluorophores are too close to the metal and facilitate nonradiative energy transfer and dissipation of energy in the fluorophore-metal system[147,155]. At distance below the optimum enhancement, the enhancement factor follows a r^{-6} dependency[120,158–160]. Whereas when the distance gets further away, the dipole near-field of the SPR drops $\propto 1/r^3$ (or $1/r^5$ for quadrupole) and thus weakened the enhancement. However, an optimum distance appears to depend on the surrounding medium and the plasmonic structures (Table 3-1). For example, metal core surrounded by silica shell appears to require much larger separation from the fluorophore to achieve maximum fluorescence emission. In comparison, fluorophore-metal distance of around 10 nm appears to work well for most of the nanoparticles with substrate below and spacer at the top.

Recent results from Geddes group[167] suggested that the decreased in fluorescence intensity as the spacer thickness increased (silicon dioxide SiO_2 in this case) results from the drop of electric field intensity at the surface of the spacer. Li group[120] also revealed a very interesting result when determining the optimum distance for silver nanoparticles (Ag NPs) of different sizes. It was shown that the optimum distance does depend on the size of the Ag NPs. For small Ag NPs, a maximum enhancement is found at 10 nm but the enhancement factor is smaller than larger Ag NPs due to modest electric field generated around the Ag NPs. Maximum enhancement factor is found at larger size and the optimum distance also decreases. They attributed this to less quenching from larger size nanoparticles as the majority of the extinction is scattering.

Type of Resonance Mode

Since larger metal nanoparticles can generate higher order resonance mode and cover large wavelength range, it is possible to multiplex with different fluorophores at different wavelengths. Although in general dipole mode typically generates higher electric field enhancement, Okada *et al.*[10] showed that in nanoprism the electric field generated by quadrupole is around 70% strength of those from dipole. Van Duyne group also showed that the RIS, which is an indication of the LSPR generated electric field strength, the dipole is more sensitive than quadrupole mode[65]. In addition, semi-qualitative estimation (without taking electromagnetic retardation and higher order interactions) shows that dipole electric field decays at a rate of $1/r^3$ whereas quadrupole decays much faster at a rate proportional to $1/r^5$, thus would require a shorter fluorophore-metal distance for MEF. Dipole resonance also covers much

larger wavelength range thus support wider operation bandwidth. On the other hand, quadrupole mode requires more energy to excite, hence falls in to shorter wavelength, which makes it less ideal for NIR fluorophores.

Plasmonic Structure	Spacer Material	Dye	Optimum Distance (nm)	Groups
Ag islands	BSA-Avidin	Cy3, Cy5	9	Lakowicz[161]
	PSS & PAH	Sulforhodamine B	9	Lakowicz[162]
	Stearic acid	Nitrobenzoxadiazole	Direct contact with metal structure.	Lakowicz[163]
	Stearic acid	Sulforhodamine B	10	Lakowicz[164]
	Oligonucleotide	Cy5, Cy5.5	8.3-13	Lakowicz[165]
	DNA	FAM (VIS)	2	Geddes[166]
	SiO2	Eosin (VIS)	1-3	Geddes[167]
Ag nanosphere	DNA	6-carboxyfluorescein	10 for 36 nm	Li[120]
			13 for 89 nm	
			7.5 for 199 nm	
	SiO_2	Fluorescein isothiocyanate	21	Xu[168]
		FAM, CYe	25	Gerritsen[169]
Au nanosphere	SiO_2	FAM, CYe	25	Gerritsen[169]
Au nanorods	Polyelectrolyte (polyallylamine hydrochloride and polystyrene sulfonate)	LS288 (NIR)	4	Singamaneni[147]
	DNA	Rhodamine	16	Keating[170]
Ag nanorods	DNA	Rhodamine	8.6	Keating[170]

Table 3-1 Optimum distance for MEF for different plasmonic structures by different research groups.

Nevertheless, the potential of quadrupole mode should not be neglected. In reality, the actual contribution of the quadrupole in optical measurements are hard to distinguish from dipole as the spectrum are usually a combination of both or even other higher resonance order. If the electric field enhancement is to be determined experimentally, it would requires techniques such as electron energy loss spectroscopy (EELS) which is very time consuming and expensive. As such, a computational analysis is often applied to understand the physical phenomena. A simulation on nanotube by Zhou *et al.*[171] showed that the contribution to scattering and electric field enhancement by quadrupole component can become increasing dominant and even shadow the dipole mode when the nanoparticle

size increases. This suggests that the size and shape of the nanoparticles could be tuned to harvest the potential of the quadrupole mode.

As introduced in the chapter 2, the LSPR of a nanoparticle can couple with another nearby nanoparticle when they are within certain distance. This results in a massive increased in electric field enhancement confined in the space between the two nanoparticles. Xie *et al.* showed that on both gold[148] and silver[150] nanotriangle arrays, reduced tip to tip distance between the nanotriangles improved the MEF significantly. This attests the fact that the interparticle coupling effect is another strategy in improving MEF ability with huge potential.

3.2.3 *Recent development*

Since the discovery of MEF, it has been receiving huge attentions and soon becomes a very active research field. Leading by recent technology push from advancement in nanofabrication and characterisation techniques, various fabrication techniques, materials, and structures have been explored progressively to obtain better MEF structures. Figure 3-5 shows the exponential growth of publications related to this research area and forecasts that strong upward trends will continue in the near future.

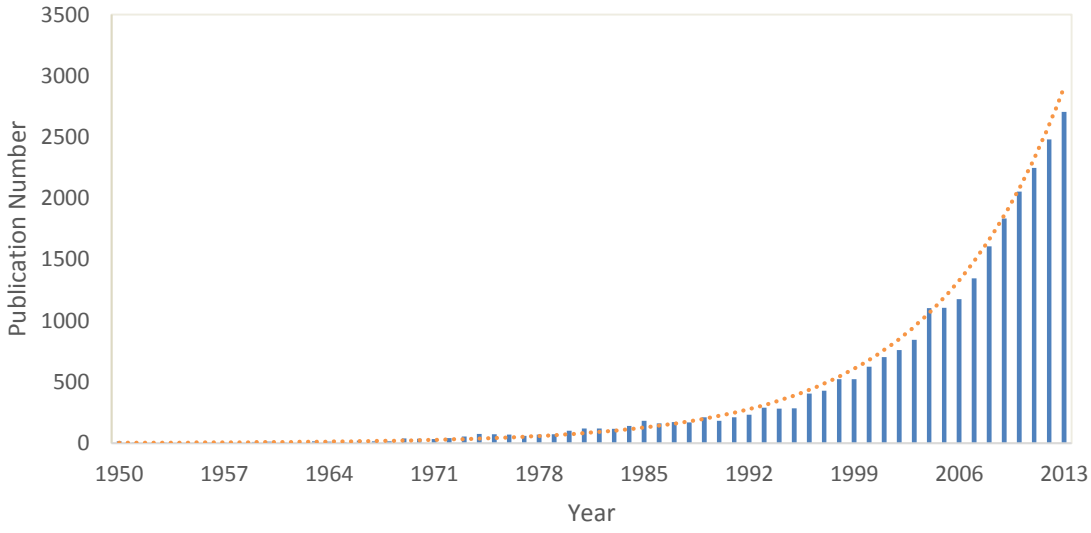

Figure 3-5 Number of publications related to metal enhanced fluorescence by year (Source: Scopus database).

Table 3-2 list some examples of recent development in this field. Gold and silver are the primary candidates of interest due to their SPR in visible and NIR regions. Regardless, both metals can offer large enhancement factors and the signal is usually homogeneous throughout the substrate, which is important for biosensing and bioimaging applications[172].

Geometries	Type of SPR	Fluorophore	Enhancement Factor
Ag islands thin film	LSPR	Eosin (Vis) FAM (Vis)	9[167] 360[166]
Au islands thin film	LSPR	Single wall carbon nanotubes (NIR-II)	10[173]
Au colloids	LSPR	Epicocconone (deep blue)	15[174]
SiO2 Core-Au Shell	LSPR	IR800 (NIR-I)	40[175]
Au Core-Silver Shell	LSPR	Fluorescein isothiocyanate (FITC)	13[145]
Ag Core-SiO2 Shell	LSPR	BHHCT-Eu-DPBT (Vis)	120[176]
Au Core- SiO2 -Au Shell (nanomatryoshkas)	LSPR	CY7 & IR800 (NIR-I)	16[177]
Au nanorods	LSPR	IR800 (NIR-I)	9[175]
Ag nanorods	LSPR	Cy5 (Vis)	23[178]
Au bowtie nanoantenna	LSPR	TPQDI (Vis)	1340[152]
Ag nanotriangle arrays	LSPR	AF790 (NIR-I)	5 to 83[150]
Au nanotriangle arrays	LSPR	AF790 (NIR-I)	36 to 69[148] depending on interparticle coupling
Au nanocylinder arrays	LSPR	CdSe core-ZnS shell (Vis)	26[179]
Au 50 nm nanohole arrays **Au 100 nm nanohole arrays**	SPP	Alexa 647 (Vis) Oxazine 720 (NIR-I)	10[180] 82[181]
Au Klarite-thin Ag SERS substrate	LSPR, SPP	Alexa 647 (Vis)	50[182]
Gold nanoantenna-dots arrays	LSPR, SPP	IgG (NIR-I)	7400[116]

Table 3-2 Some examples of published results based on different type of structures for MEF.

Note that the table is not an exhaustive list of best enhancement factor obtained for a specific structure. In addition, although the approach toward getting a quantitative value for fluorescence enhancement is similar, comparison between similar structures could be misleading due to difference in experiment setup and structure configurations. For instances, the protein, fluorophores, and the fluorophore-metal distances varies from experiment to experiments and may not have been optimised. Therefore table 3-2 serves as a guideline toward analysing the trend in optimising SPR substrates for MEF.

From table 3-2, it can be deduced that research is progressively towards more complex structures which require advance fabrication techniques such electron beam and nanoimprint technology in order to obtain higher enhancement factors. One of the examples is the single molecule fluorescence enhancement through the hot spot generated in a gold bowtie nanoantenna fabricated by e-beam lithography to achieve 1340 times enhancement[152]. Another example is to structure that

combines both SPP and LSPR mode by Chou group[116] using nanohole, nanodots, and nanodiscs arrays together. With precise fabrication to achieve optimise interparticle distance between the metals and structures, this plasmonic structure benefits from a combination of three plasmonic enhancement effects – interparticle coupling, nanohole SPP, and nanodisc LSPR. The result is a remarkable enhancement factor over 7400 times, the highest value obtained to date. However, the fabrication of the structure relied on nanoimprint technology which is expensive and time consuming.

Advancement in biosensors has achieved considerable success and related products are emerging in the market. But it still remains a challenge to develop cheaper, more reliable, and more efficient biosensors. MEF based technology has proven to be a very promising route in helping to achieve these goals.

3.2.4 *Chapter Summary*

MEF is a highly versatile technique that the shape and size can be tuned systematically to enhance the fluorophore of interest, allowing a lower detection limit and earlier diagnosis. However, although the application of LSPR and SPP has been widely explored, the technology still faces many challenges and the best structure to match each different fluorophore remains to be discovered. This project aims to provide methods to fabricate plasmonic substrate based on LSPR and SPP that are highly sensitive using a low-cost versatile method base on nanosphere lithography. Nanotriangle, nanodisc, and nanohole-disc arrays were produced based on low cost, versatile modified nanosphere lithography technique. Our results showed that interparticle coupled gold nanostructures were able to produce MEF of over two orders of magnitude.

Chapter 4

Fabrication Methods

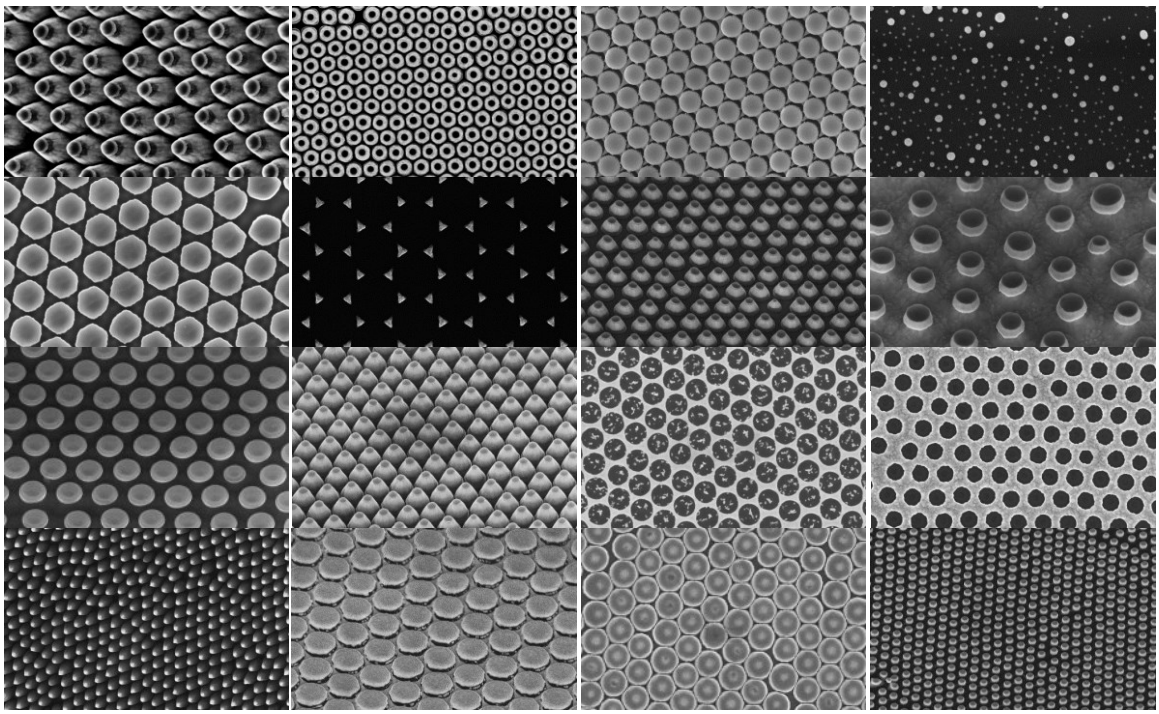

Figure 4 Different type of nanostructures developed through the course of this project.

Chapter 4 Fabrication Methods

Localised surface plasmon resonance is highly sensitive to the geometries of the nanoparticles and the surrounding materials. Therefore, well-defined patterned structures are essential for interacting with light through LSPR of nanoparticles. It is crucial not only to fabricate structure in nanometres regime but also ensure the shapes of the nanoparticles are precisely controlled. This chapter represents the development and optimisation of fabrication method for the new plasmonic systems developed later in the thesis. In particular, the capability to control three important geometry parameters: (1) shape, (2) size, and (2) the separation distance between the nanoparticles. The aim is to have a full design space to allow us to build variety of plasmonic systems. To aid understanding the challenge and recent development in the nanofabrication technology, this chapter begins with a brief review of state-of-the-art literature followed by my results.

Recent advancement in nanofabrication techniques has overcome the optical diffraction limit challenged by photolithography. Electron beam lithography is a highly advanced technique which is widely used by high tech industrial manufacturers such as Intel, and some research institutes. Instead of using optical light source, the wavelength of electron beam is much smaller than light, allowing sub-10 nm resolution in patterning. The main drawbacks of this technique are small active area, time consuming, and high cost. Nanoimprint lithography is another common method in producing well-defined nanostructures. It is considerably cheaper than e-beam lithography and has ability to cover a larger area of surface. A mask must be used to stamp onto a substrate with imprint resist coated. Since the mask is expensive to produce and has to be pre-patterned, it lacks the versatility in producing variety of shapes and structures. In this project, a large area, versatile approach in fabricating nanoscale structures called nanosphere lithography is employed. Being a very low-cost technique while also can be modify and combine with other nanofabrication technique easily and does not require any expensive equipment and chemicals, it becomes a very attractive method to fabricate many different type of nanostructures and is actively in use by many academic researchers worldwide.

Nanosphere lithography is essentially a patterning technique using spherical nanosphere such as polystyrenes and silica as a mask. When those spheres self-assemble onto a surface, they form two dimensional hexagonal close pack arrays (Figure 4-1). Metal can then deposit through the interstices of the spheres. Nanotriangular arrays are formed if the metal is deposited at normal incidence angle (Figure 4-7b). Other alternative shapes have also been extensively explored by varying the metal deposition angle[183,184]. The resulting features includes crescent moon[47–49], nanorings[47,185,186], nanobars[185], and even some arbitrary shaped structures[187] through clever exploration of nanospherical lens effect arise from those nanospheres. Additional shapes such as nanoholes can be made by expose the polystyrene spheres to oxygen plasma[150,188]. 3D structures such as nanodisc arrays can also be fabricated by incorporation of ion milling process. Other sophisticated three-dimensional structure has

also been demonstrated through nanosphere lithography techniques. Figure 4-3 illustrates a variety of three-dimensional hollow nanostructures developed by Zhang *et al.*[189]. Proven to be cost effective and to have the ability to manufacture large variety of structures, it is a highly popular technique.

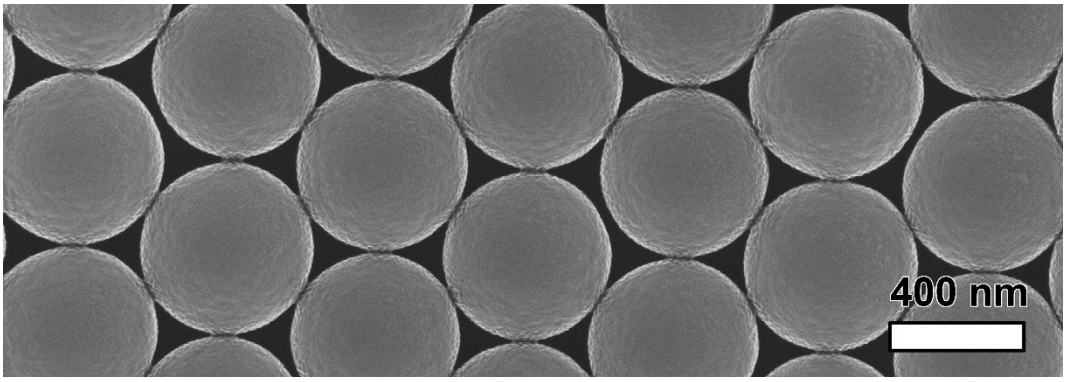

Figure 4-1 Top view of a HCP structures formed by self-assembled PS nanospheres with 500 nm diameters on a silicon substrate.

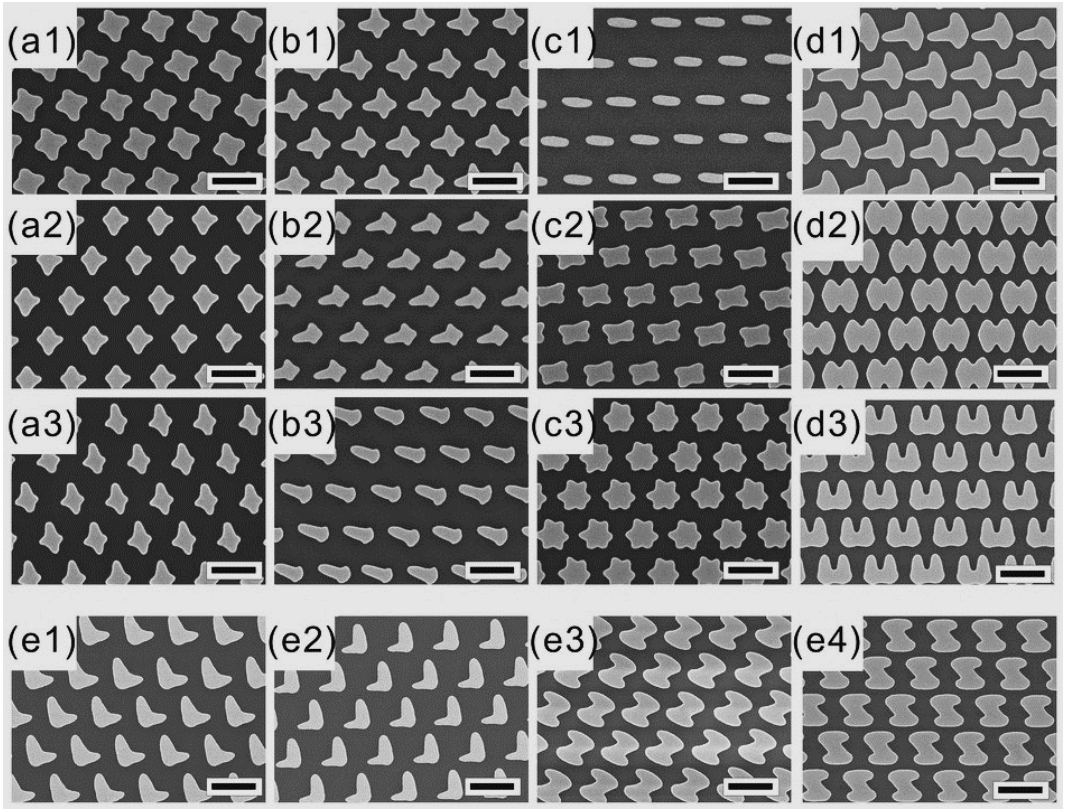

Figure 4-2 A large variation of nanostructures produced by Chang et al.. through exploring the nanospherical lens effect from PS monolayer[187]*. (Reprinted from ref 187 with permission from Nature Publishing Group.)*

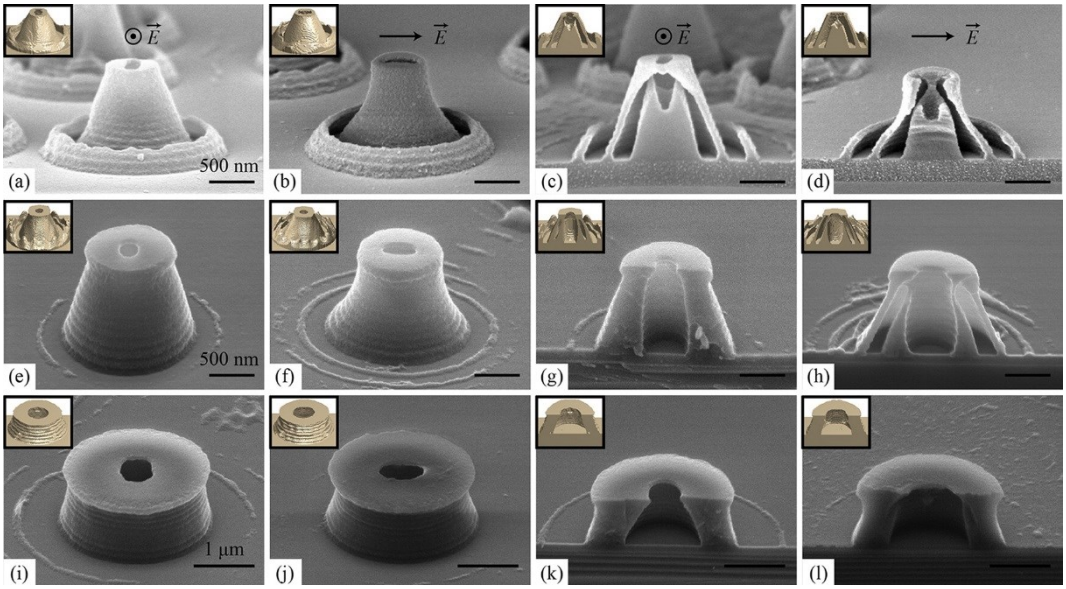

Figure 4-3 Three dimensional complex hollow nanostructures fabricated through light scattering by nanosphere into photoresist[189]. (Reprinted from ref 189 with permission from American Chemical Society.)

4.1 Nanosphere Lithography

Nanosphere lithography (NSL) was also known as "natural lithography" [44] or colloidal lithography[150]. The original works date back to 1980s when "naturally" self-assembled polystyrene latex nanospheres were used as a mask for contact imaging with visible light in 1981 by Fischer and Zingsheim[190]. Later on, Deckman and co-workers demonstrated this polystyrene monolayer can also work as a mask for metal deposition and etching[191]. Further works were performed by Richard Van Duyne's group who extended the application of NSL by incorporating the idea of double layer polystyrene mask and angle resolved metal deposition to deposit wider range of possible periodic particle arrays[16,43–45,66,183,192–195]. Currently, NSL is widely accepted as an inexpensive and high throughput technique to fabricate controllable shape, size and interparticle spacing nanoparticle structures for wide range of applications[196–204].

Like other self-assembly methods, the typical challenge associated with NSL technique is the formation of defects such as voids between the monolayer grains, dislocation, aggregation, and crystallinity. To circumvent such problems, many fabrication methods have been explored, ranging from drop casting[205–207], spin coating[194,208–210], vertical deposition[211], and air-water interface transfer[212–215]. Currently, a large area substrate deposition in cm coverage has been made possible (see Figure 4-5) but a defect free monolayer grain size remains usually in millimetre regime.

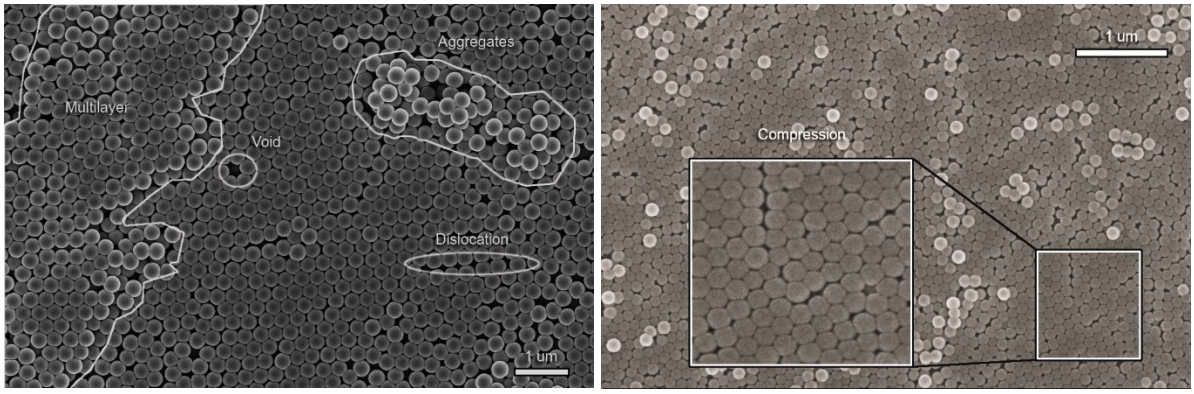

Figure 4-4 SEM images of 290 nm (left) and 120 nm (right) sized PS deposited on silica substrates demonstrating different type of defects found on NSL deposited substrate.

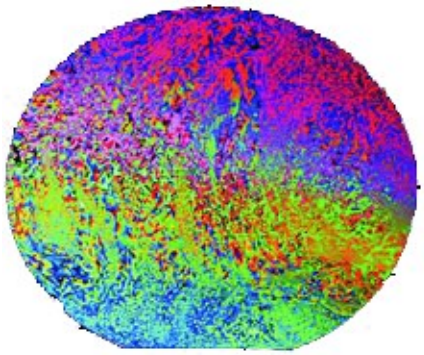

Figure 4-5 A full coverage of binary PS (50 µm and 1 µm) deposited using Langmuir trough method on a six inch silicon substrate. The defects can still be seen throughout different area of the substrate[216]. (Reprinted from ref 216 with permission from Advanced Functional Materials.)

4.2 Improved NSL monolayer Fabrication Techniques

High quality nanosphere mask are important in ensuring reproducibility of quality data. NSL is based on self-assembly of the nanosphere onto substrates to produce hexagonal closed pack patterned. In this project, an improved fabrication of NSL technique based on air-water interface method was developed based on previous work by Xie *et al.*.[148]. Due to the use of water buffer and angular transfer of the PS monolayer, this technique is termed water buffer based transfer NSL, or alternatively "fishing" technique. A detailed standard operating procedure listing each step in this method can be found in appendix. In brief, a 10% weight polystyrene solution (purchased from Bangs Laboratories Inc., USA.) is first mixed with equal volume of absolute ethanol, which helps suspending the PS nanosphere onto the water-air surface. This solution is then spread across a clean and UV-ozone treated silicon substrate held in an angle to form a first self-assemble PS monolayer. It was found that this method reduces the amount of aggregation of the PS on the transfer silicon substrate. The transfer substrate was allowed to dry slowly while partially immersed in water. Next, this PS coated silicon transfer substrate was slided into ultrapure deionised water at a small angle to the water surface slowly to form a PS monolayer. Aggregation of dried PS on the transfer substrate was found to sink into the water while good quality PS monolayer formed on top of the water bath, thus further improve the PS monolayer formation. These steps can be repeated several times until the PS covers approximately 70% area of the water surface. A few µl drops of 2% sodium dodecyl sulphate (SDS, surfactant) were then applied on top of the surface to promote compactness of the monolayer while also sinking PS aggregation into the water. Finally,

sample substrates were slided underneath the PS monolayer that is suspending on the water surface, and lifted up slowly as horizontally as possible to deposit monolayer of PS onto the sample substrate. The speed and angle is crucial to prevent disturbance on the water surface which may cause shockwave throughout the water bath, which will damage the quality of the PS monolayer. The samples are then dried slowly in atmosphere at approximately 30° to facilitate further self-assembly of PS grains on the surface while drying.

In order to have good quality PS coverage, it is necessary to ensure all the samples are cleaned as dust particles can promote nucleation of PS and disrupt the pattern. The microscope glass and silicon substrates were all pre-cleaned by sonication in acetone, isopropanol, and deionised water for a duration of 5 minutes each. It was found that the substrate with good hydrophilicity property helps promote larger PS monolayer coverage and reduce grain defects. To make the substrates hydrophilic, substrates were exposed to UV-ozone plasma which removes hydrocarbons with nanometres thickness on the substrate surface[217] for at least 5 minutes.

Depending on the types of nanostructures required, the processing steps and parameters in the fabrication can be altered and combined with other nanofabrication techniques. For example, while the centre-to-centre pitch distance is determined by the size of the PS, the individual size of each PS can be reduced by treating the deposited PS with a controlled oxygen plasma process. This modified PS mask can then be used to fabricate arrays of nanodisc or nanoholes depending on the type of substrate used. In this project, different sizes of PS in combination with oxygen plasma, argon ion milling, and metal deposition were explored to produce wide range of results. Figure 4-6 shows a schematic workflow to produce a few different types of nanostructures, note that it is not an exclusive list of possible nanostructures that NSL's capability.

To allow an acceptable quality and reproducible results, the conditions for deposition monolayer mask (based on different PS sizes, size reduction rate by oxygen plasma, precise metal deposition in angle, and etching parameters of ion milling process) are all thoroughly investigated before the technique are combined to form a desired structure.

The most basic structure is nanotriangular arrays, produced by deposition of metal through the interstices of the PS mask followed by PS mask removal (Figure 4-7b). The size, and the distance between adjacent nanotriangles depend on the diameter of the surrounding PS (Figure 4-7a). For metal deposited at normal incident angle to the mask and substrate, the perpendicular bisector, a, and the interparticle spacing, d_{ip}, can all be calculated knowing the diameter, D, of the PS[44]:

$$a = \frac{3}{2}\left(\sqrt{3} - 1 - \frac{1}{\sqrt{3}}\right) D \approx 0.233\, D \qquad \textit{Equation 4-1}$$

$$d_{ip} = \frac{1}{\sqrt{3}} D \approx 0.577\, D \qquad \textit{Equation 4-2}$$

Similarly, the area of the triangle,A, can also be calculated as follow:

$$A = \frac{D^2}{16}\left(4\sqrt{3} - 2\pi\right) \approx 0.04\, D^2 \qquad \textit{Equation 4-3}$$

As can be seen from the equations 4-1 to 4-3, the size and spacing scale linearly with the diameter of the sphere. However, the actual geometry of the nanotriangle deposited can be different from the calculation above. As the thickness of the deposited metal increases, the interstices also gets smaller as the surface of the PS also being covered by the metal. Thus, the resulting nanotriangle resembles more of a prism with larger base and smaller truncated top.

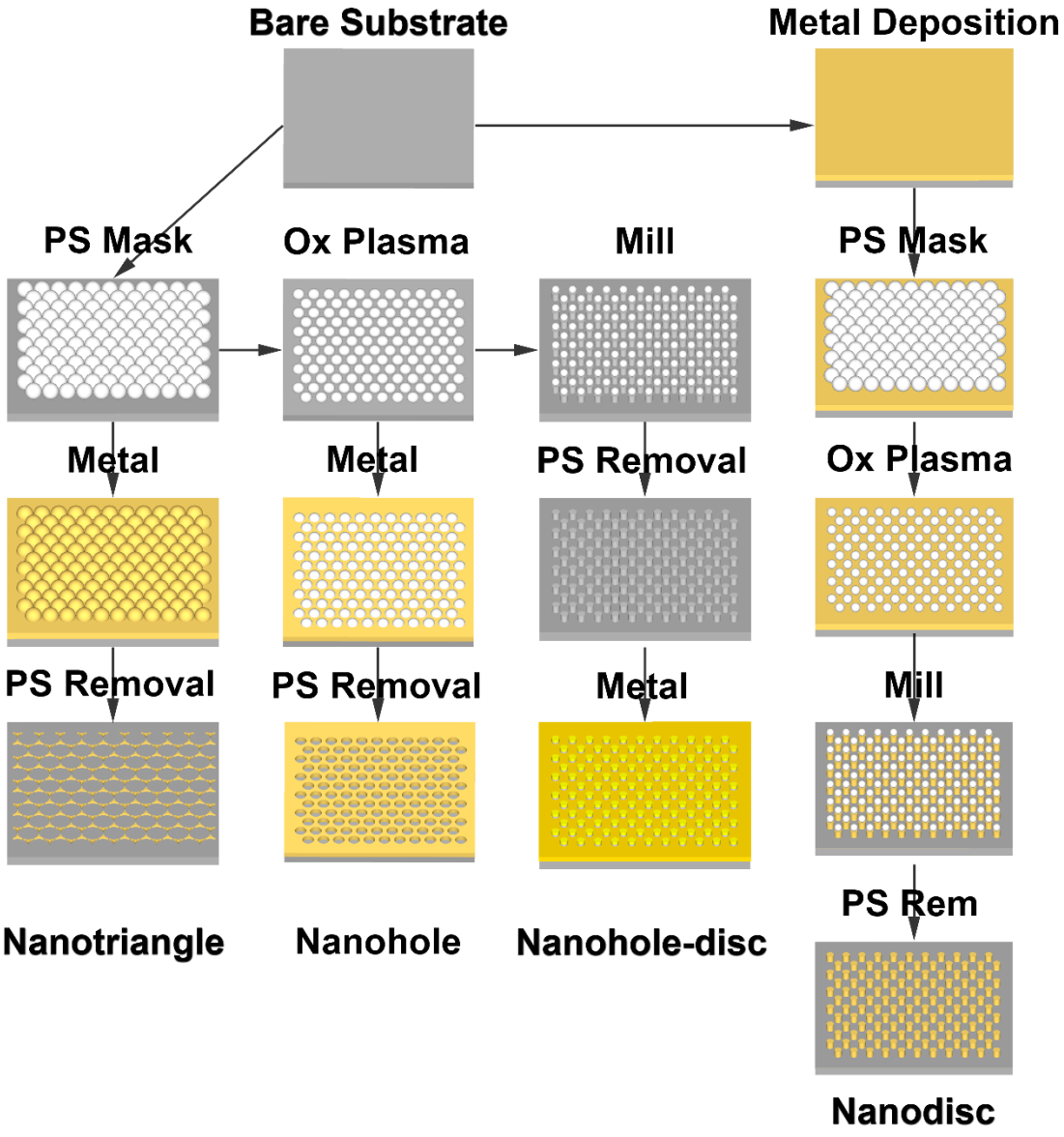

Figure 4-6 Schematic workflow of fabricating few different nanostructures by combining nanosphere lithography with metal deposition, oxygen plasma, and argon ion milling.

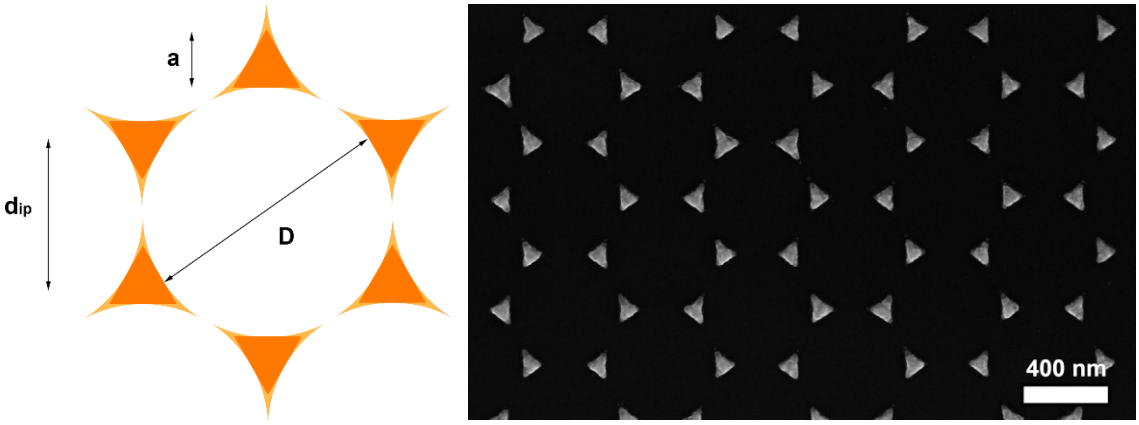

Figure 4-7 (a) Dimension of nanotriangle fabricated through NSL method. (b) Top view SEM image of a 75 nm thick silver nanotriangular arrays based on 500 nm sized PS fabricated using the improved NSL recipe.

With the ability to control the size and distance between the PS, a large variation of the structures were successfully fabricated in this project (Figure 4). Those structures were achieved through combination of metal deposition, oxygen plasma process and angular argon ion-milling process. Among those structures, nanodisc and nanohole-disc arrays are particularly interesting as it allows characterisation of interparticle coupling effect and also exhibits remarkable electric field enhancement.

4.3 Metal deposition

Metal was deposited through magnetron sputtering or e-beam evaporation in a custom made *Mantis* deposition system. Magnetron sputtering produces low roughness and very uniformly thin film. It is selected when a full coverage of metal on a substrate is required. On the other hand, E-beam evaporation produces a more directional metal deposition, thus making it suitable for deposition of metal through interstices between PS to produce sharp features. In addition, to ensure the sharpness of the feature is not degraded, the stage rotation is disabled and samples are located directly above the thermal evaporator. Figure 4-7b shows the nanotriangular arrays produced using the optimised setting.

It is worth noting that the top view of PS monolayer seems acceptable from the SEM images, however the mask quality can only be accessed after deposition of nanotriangular arrays by metal evaporation where a more stringent requirement of well-packed PS is requited to achieve good quality. Figure 4-8 illustrates defects found after PS removal where nanotriangles joined up together to form a larger and undesirable nanostructures which could resonates at unintended wavelength. In addition, the maximum height of nanotriangle is limited by the PS size. If the metal deposition between the top surfaces of the PS connect to the nanotriangle below, the PS will be very difficult to remove. As a general guide, the maximum allowed metal thickness is slightly less than half of the PS diameter.

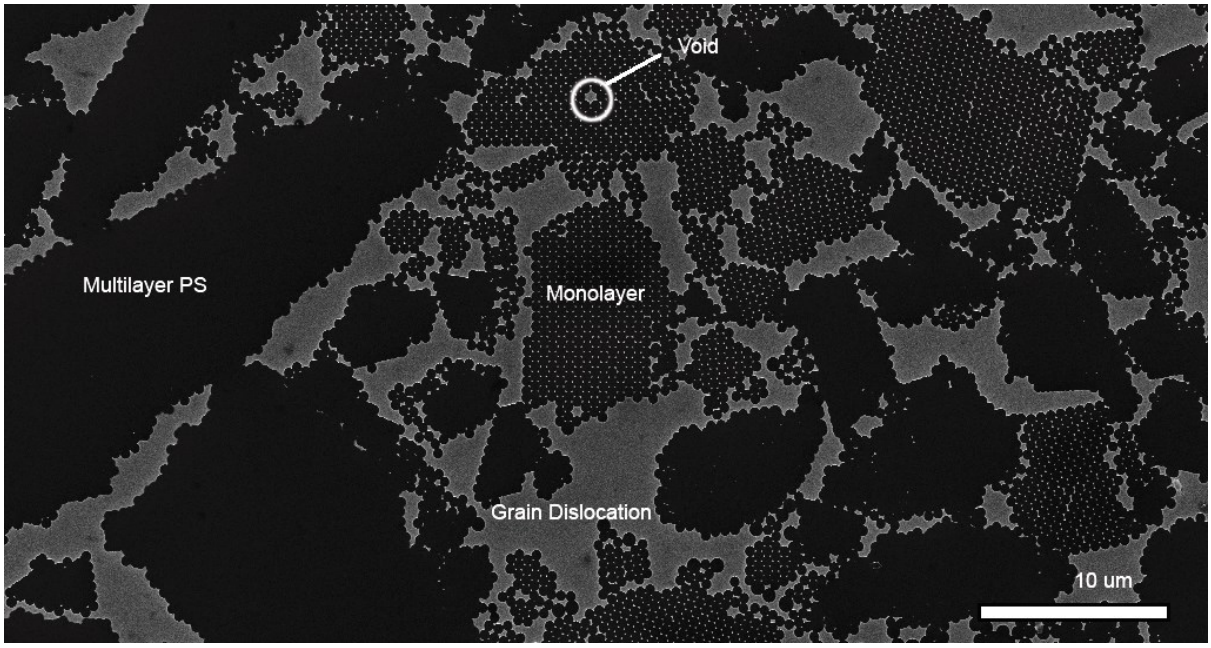

Figure 4-8 Large area SEM scan of an defective area of sample after metal deposition and PS removal showing different types of defect cause by imperfection of PS monolayer.

Since metal atoms may arrive at substrate with excess energy, they are able to diffuse. Hence, the actual size and shape of the metal nanotriangle on the substrate surface can also be different from the calculated geometry. This is due to the wetting property of substrate and the diffusion of the evaporated metal. Chan *et al.* reported that their aluminium nanotriangle was larger due to wetting on glass substrate[16]. Here, we limit our metal deposition rate to be around 0.1 – 0.5 Å/s to reduce the diffusion effect. **Error! Reference source not found.** compares the measured to the calculated anotriangle's size deposited in this project and it was found that they are within a good agreement.

Table 4-1: In-plane edge width, a (tip to tip dimensions) of 75 nm thick silver nanotriangle deposited through various PS monolayer of various sizes.

PS Size	**290**	**500**	**620**
a (measured)	72	118	137
a (calculated)	68 ± 7	117 ± 12	144 ± 14

Challenges arise when fabricating nanohole-disc arrays which require the metal deposition angle to align perfectly with the normal (perpendicular) axis. A 10° deviation of the thermal evaporator source from the normal axis of the substrate holder was sufficient to cause the top metal nanodisc connected to the bottom nanohole arrays, which affect the generation of LSPR mode. The stage was modified to compensate the tilting of the thermal evaporator to compensate this deviation and nanohole-disc arrays are successful fabricated. Figure 4-9 illustrates the modification on the substrate holder and the nanodisc arrays produced.

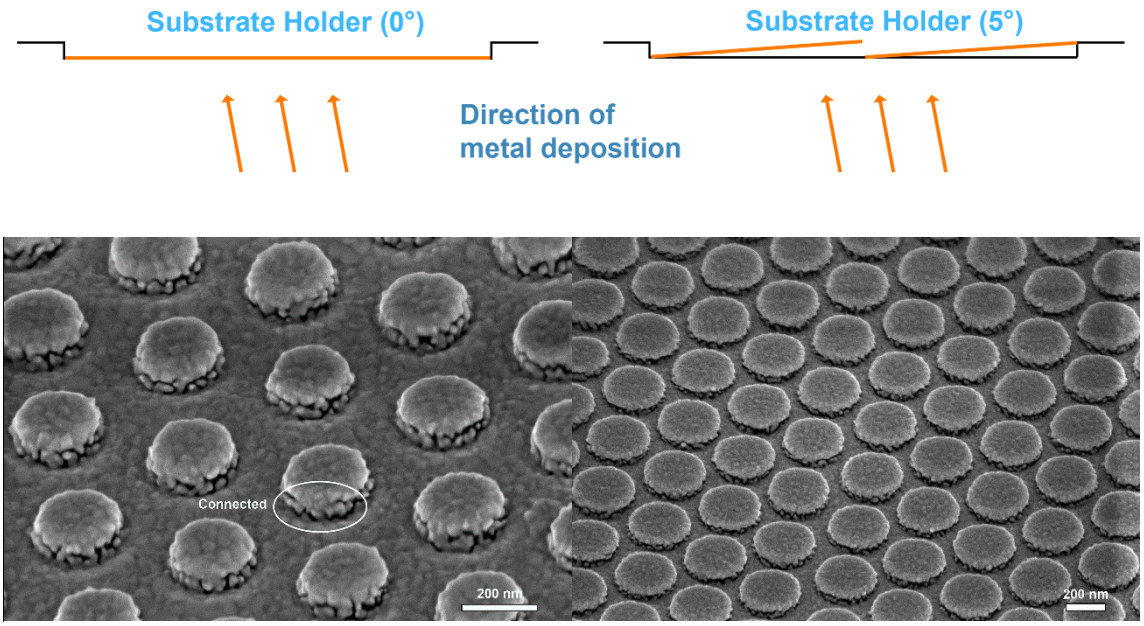

Figure 4-9 Initial (top left) and modified (top right) stage to compensate the angle deviation between the evaporator source and substrate plane. SEM images of nanodisc structures before (bottom left) shows a small connection point formed between the nanodisc and nanohole arrays. After (bottom right) stage modification, the nanodiscs are isolated from the nanohole at all sides. Scale bar: 200 nm.

4.4 Polystyrenes Sphere Reduction by Oxygen Plasma

One of the benefits of using PS NSL is that the distance between the PS and the size of the individual PS can be controlled independently. Exposure of polymer to plasma and ion bombardment can cause breakage of polymer backbone, side chain scissioning and depolymerisation by insertion of peroxo-radicals into the backbone[200,218]. The initial PS diameter determines the centre-to-centre distance and remains unchanged after oxygen plasma process, whereas the individual size of the PS nanosphere can be reduced to desired size by exposing them to oxygen plasma[200,219–223].

In general, the rate of oxygen plasma reduction is a function of the plasma power, accelerating voltage and pressure. Figure 4-10 shows the relationship between the PS size with the duration they were exposed to the oxygen plasma for different initial PS sizes with 20 sccm oxygen flow rate, 100 W plasma power and 200 V accelerating voltage in a Sentech Etchlab 200 system. Table 4-2 shows the PS diameter etching rate for PS on those substrates. The diameter were measured from SEM images using ImageJ (Full detail of analysis steps can be found in appendix). These data are important and useful as a design aids to enable fabrication of nanostructures with different diameters. The results presented here also cover large number of PS sizes which are available in the literature. PS etching rate calculated based on diameter follows a linear relationship and is measured to be around 3.6 ± 0.4 nm/s on silicon, glass, thin gold on silicon, and thin gold on glass substrates. The linear function of the decrease in the PS diameter is consistent with other research groups[200,220,223]. Vogel *et al.* found a

difference in etching rate depending on the type of substrates the PS was on and suggested that the difference in etch rate is attributed to the accumulation of charge on the surface which shield away like charges in the plasma, resulting in slower etching rate for charge insulating substrate[200]. However, this is not the case here as there is no significant deviation between the average PS etching rates between the four different types of substrate. This is likely due to the condition of the oxygen plasma used. In their experiment, the oxygen gas flow rate was between 3 – 10 sccm and plasma power between 15 to 50 W, both are much lower than the condition used here. As such the PS etching rates here are noticeably faster and the shielding effect from the accumulated charges on the substrates become ineffective. The only abnormality comes from the 500 nm sized PS where the etching rate is strikingly higher than all other sizes. The origin of this deviation is unclear but could be due to the molecular structures of this PS was made differently compare to other PS sizes by the manufacturer.

For completeness, the height reduction of the PS on glass and silicon substrate in the oxygen plasma process was measured. The height reduction rate is 3.9 ± 0.2 nm/s on both type of substrates, marginally faster than diameter reduction rate. Knowing the rate at which the PS reduced is beneficial when patterning the nanostructure. In the next subchapter, the reduced PS after oxygen plasma is required to estimate the maximum milling angle to maintain a vertical sidewall.

PS Size / Substrate	210 (nm/s)	290 (nm/s)	400 (nm/s)	500 (nm/s)	620 (nm/s)	Average (nm/s)
Silicon	3.1	3.9	3.5	4	3.5	3.6 ± 0.4
Glass	3.6	3.5	3.3	4.1	3.3	3.6 ± 0.3
Au/Silicon	3.4	3.0	3.7	-	-	3.4 ± 0.4
Au/Glass	3.6	3.8	3.5	-	-	3.6 ± 0.2
Average	3.4 ± 0.2	3.6 ± 0.4	3.5 ± 0.2	4.1 ± 0.1	3.4 ± 0.1	3.6 ± 0.3

Table 4-2 Table showing the PS etching rate by oxygen plasma on different type of substrate. The rates are calculated based on the line of best fit on multiple etching duration and before the PS size is reduced to less than half of its initial size.

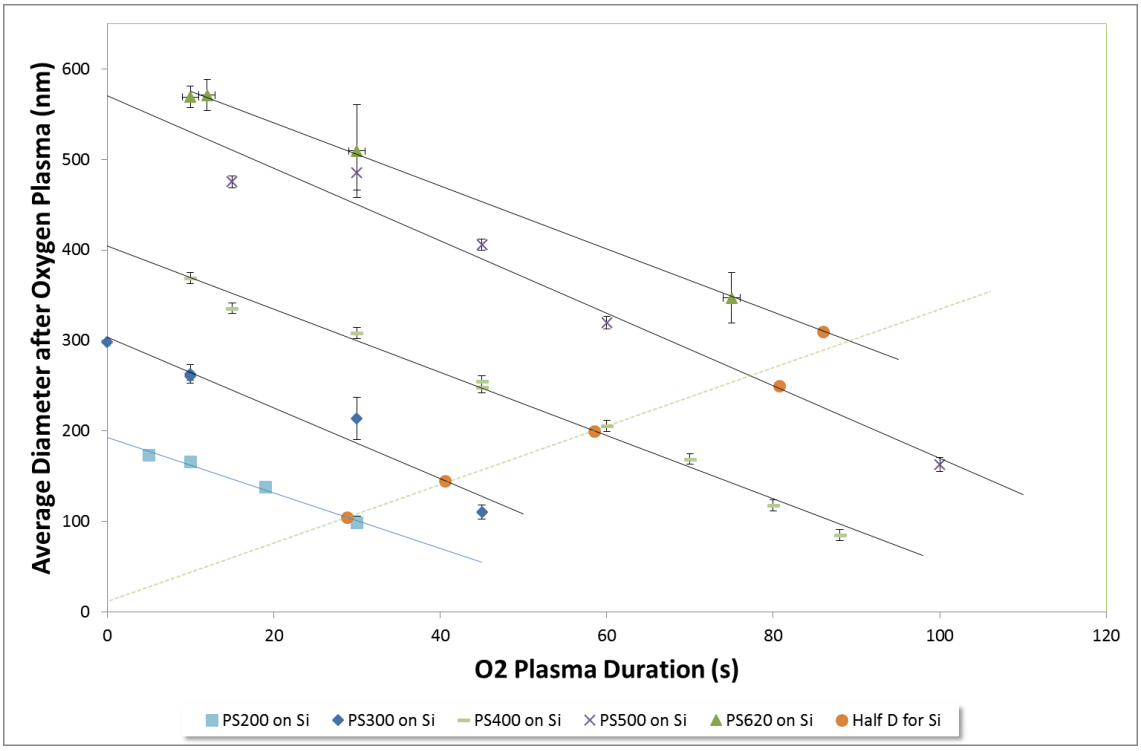
Average Diameter after Oxygen Plasma (nm)
0
100
200
300
400
500
600
0
20
40
60
80
100
120
O2 Plasma Duration (s)
PS200 on Si
PS300 on Si
PS400 on Si
PS500 on Si
PS620 on Si
Half D for Si

(a)

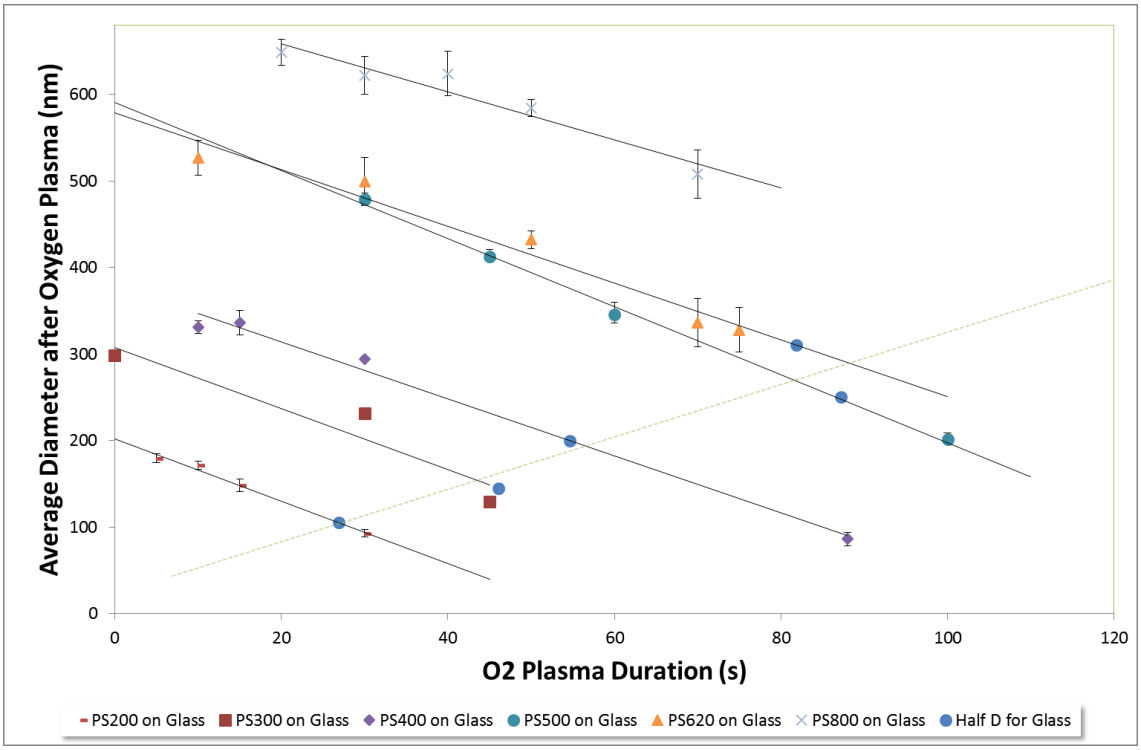
Average Diameter after Oxygen Plasma (nm)
0
100
200
300
400
500
600
0
20
40
60
80
100
120
O2 Plasma Duration (s)
PS200 on Glass
PS300 on Glass
PS400 on Glass
PS500 on Glass
PS620 on Glass
PS800 on Glass
Half D for Glass

(b)

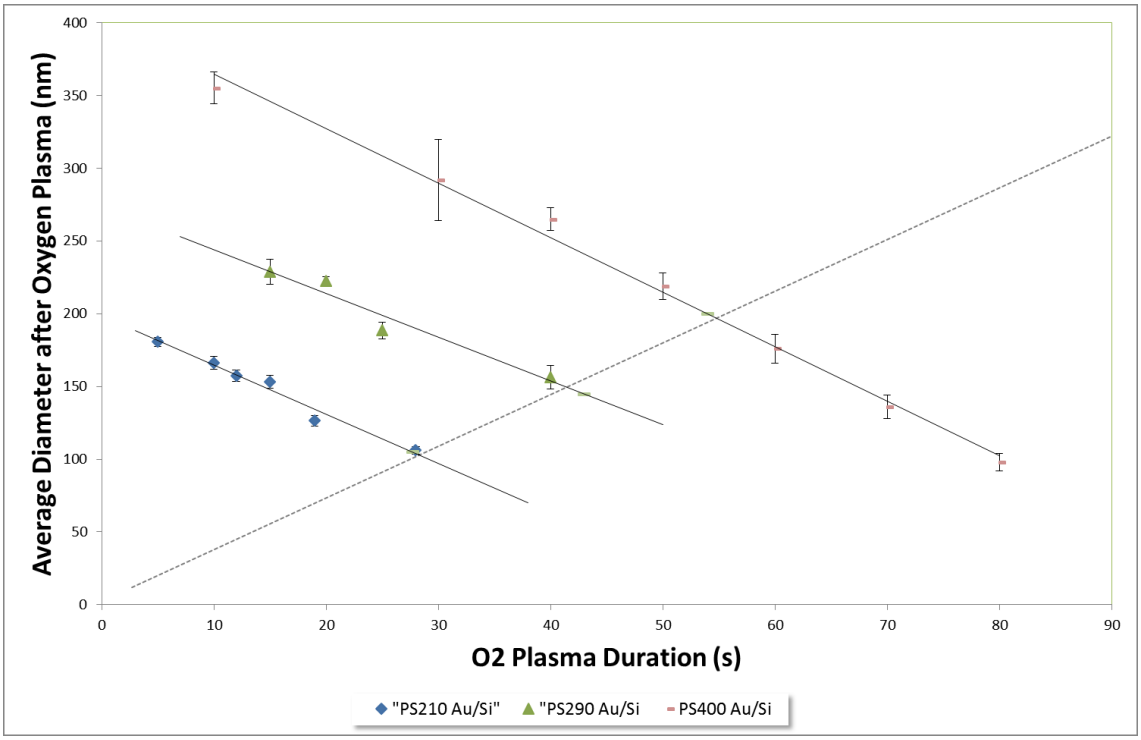

(c)

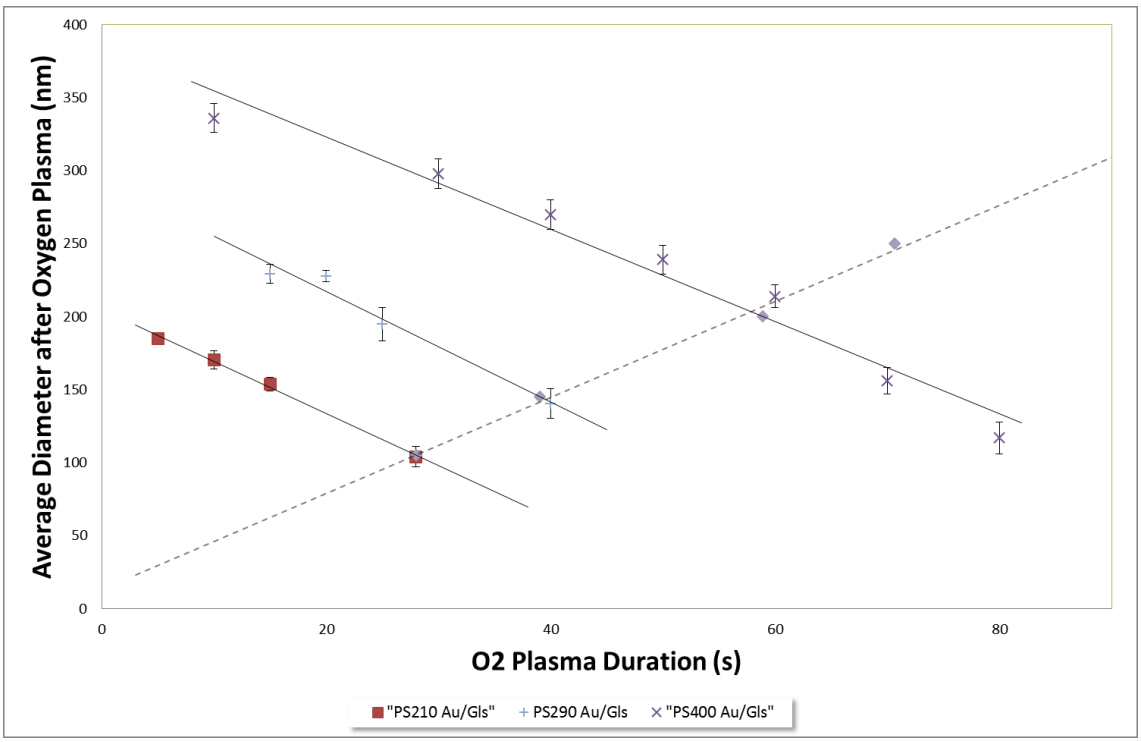

(d)

Figure 4-10 PS Size reduction graph for different initial PS Sizes on different substrates (a)silicon, (b) glass, (c) gold on silicon, and (d) gold on glass. Error bars on the data are derived from statistical data measured from SEM images. The corresponding line of best fit for different PS sizes all have $R^2 > 95\%$. The parameters of these lines are extracted into Table 4-2 below.

Oxygen plasma process is not an isotropic etching process, therefore a linear decrease in PS size may no longer hold after a reduced to a critical sizes. Based on previous publication, a good

approximation of the critical size regime is when then PS is half of its original size[200]. Here, we found that this critical value can be at 30 – 40 % of its original size instead as the line of best fit still produce a high regression factor. It is worth mentioning that shape of the PS also becomes non-spherical during the oxygen plasma process where the materials at the upper hemisphere are constantly being removed by the incoming oxygen plasma. The surface also becomes irregular and rough[218,220,224]. Provided the PS is not overexposed in the oxygen plasma process, it is possible to produce nanostructure arrays of good quality. Figure 4-11 illustrates the systematic decreases in the PS size as the duration in oxygen plasma increased.

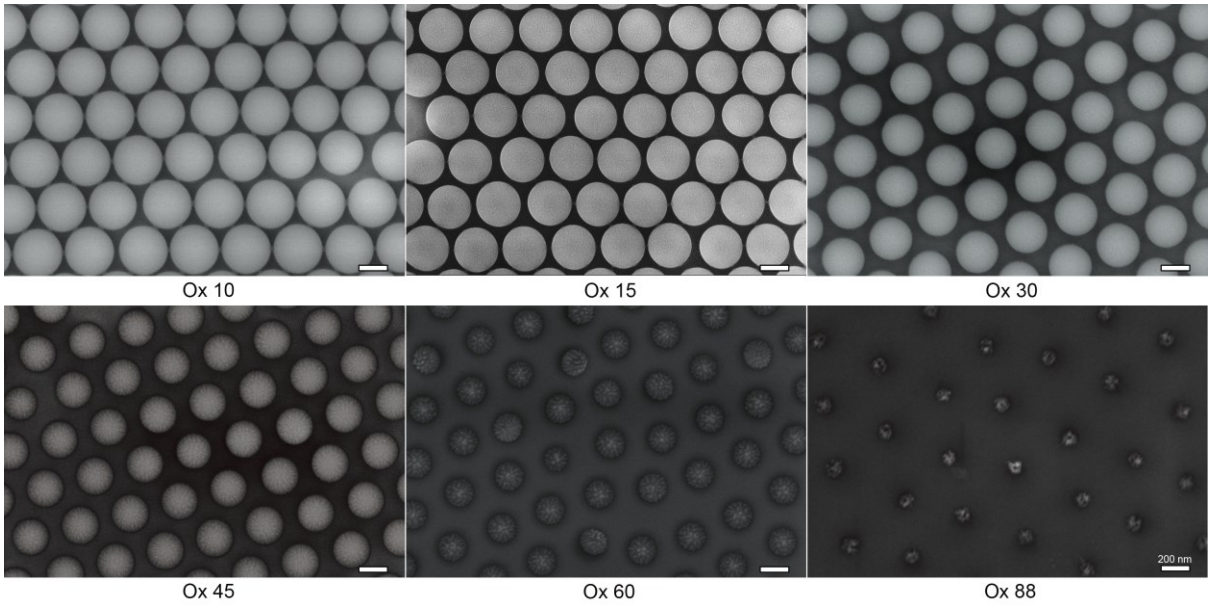

Figure 4-11 Reduction of 400 nm sized PS diameter on silicon substrate after different oxygen plasma exposure duration. Scale bar is 200 nm.

Another complication to the process arises when the PS is exposed to the plasma for long duration. During plasma process, while the PS at the surface are being removed, some PS are also being cross-linked. Cross-linked PS are very difficult to remove because they are insoluble in solvents and can withstand high temperature. Even prolonged oxygen plasma treatment cannot remove cross-linked PS. Details on PS removal process and cross-linked PS are discussed in detail in section 4.6.

4.5 Argon Ion Milling

PS mask can also serve as a protective material in argon ion milling process[225–227]. When high energetic directional argon is bombarding on a material, kinetic energy of the argon is transferred to the collided atoms and can result in ejection and removal of PS from the sample. The rate of the milling depends mainly on the material and argon atoms which determined by the configuration of the system such as the ion flux generated, the angle of the incident argon, and the accelerating voltage[228]. PS has a slower

rate etching rate than some metals such as gold and silver. The differential etching rate allows the PS to protect and pattern material beneath it.

Samples were exposed to argon ion milling in a custom made Oxford Applied Instrument system with 65 – 75 W plasma power to maintain the same ion flux and -200 V accelerating voltage to provide kinetic energy to argon etchants. The system has an angle adjustable and rotatable stage. The angular stage can be adjusted from 0° (normal incidence) to 45° and enable milling of 3D nanostructures and the stage rotation promote a more uniform ion milling of the samples. A screen voltage of 500 V was applied to screen out low energy argon ion and a neutraliser is used to remove the charge on the argon ion so that the effect of electrostatic effect on the sample surface is minimised. If the argon atom is not neutralised, charge build up on the surface will affect subsequent incoming charged argon atom and results in a different type of etching process. The etching rate found for materials used in this project and some published literature results are tabulated in Table 4-3 below.

Material	**Etching Rate (nm/min)**			
	Technics Ion Mill[229] 100 V 80 mA	Micromachining Processing[230] 500 V 1 mA/cm^2	Mathias Kolle[225] 500 V 1 mA/cm^2	Jing Pang** 200 V 22 mA
Silicon, Si	2	38	-	1.4 ± 0.1
Glass*	2.5	39	-	2.1 ± 0.7
Gold, Au	9.0	170	-	6.3 ± 0.2
Silver, Ag	10.0	220	-	-
Aluminium, Al	3.5	-	-	
Aluminium Oxide, Al_2O_3	0.5	-	-	
Nickel, Ni	3.0	-	-	
Polystyrene, PS			20	-

*Table 4-3 Etching rates for different materials from different published resrouces and measured in this project. * Glass substrate is microscope slide obtained from VWR International © and is regarded as SiO_2 for comparison, detail composition can be found in appendix. ** Etching rate measured at with argon ion milling at normal incidence to the sample. The values listed here is found by using marker pen as a positive mask as an alternative to PS and photoresist. This methods not only allows shorter processing time but the residue of the marker pen was also removed completely by sonication in organic solvents (acetone:ethanol in 50:50 mix).*

It is worth mentioning that the etching rate also depends if it is at the interstices or a large area with no PS on top. Etching rate is found to be much faster at area devoid of PS, this is possibly due to (1) the surface interaction between the PS surface and some unneutralised argon atom, and (2) the redeposition of ejected atoms. As such, it was found the best approach to fabricate patterned samples is to trial and error to obtain optimum settings.

Although the PS has a lower etching rate, it is still being etched away during the process. Once depleted, the materials underneath will be left unprotected. As a result, the structure produced will have an angle slope wall instead of vertical wall. It is possible to define the shape by milling the sample at certain angle. Figure 4-12 illustrates three very different nanostructures produced by milling at 0°, 23°, and 45° relative to the normal incidence argon beam. All these samples had same initial gold thickness (100 nm) and PS size (290 nm) exposed to 30 s of oxygen plasma. Here, sample milled at 45° had produced sidewall that is much more vertical compare to the other two samples. However, it was later found that such verticality of the sidewall for this case worked by chance, due to balanced effects from correct material, thickness, and reduced PS size. Same milling parameters did not work for other thickness of gold, etching rate, and different materials. Defects such as irregular base, overetching into substrates, and deformation frequently occur.

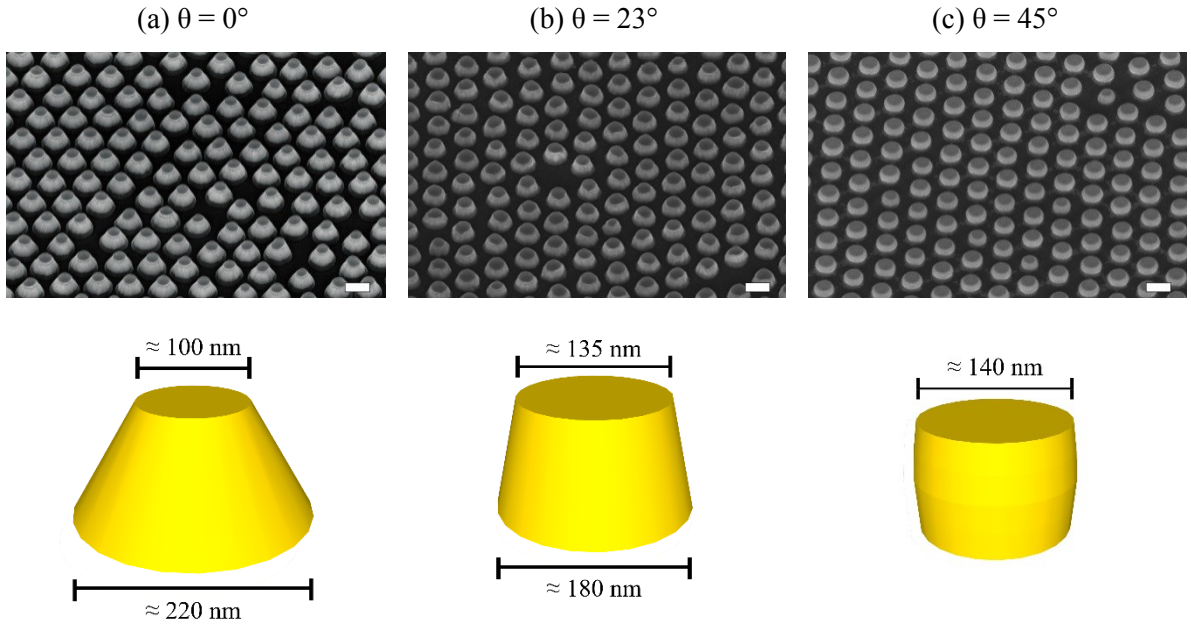

Figure 4-12 SEM images of 100 nm thick nanostructures and illustration of their geometry shape fabricated with sample stage constantly rotated for and tilted at (a) θ = 0° (i.e. stage perpendicular to the neutralized ion beam), (b) θ =23°, (c) θ =45°. (Scale bar = 200 nm). All samples were etched for the same amount of time.

A novel technique was developed in this project to help maintaining high verticality of the sidewall by changing the angle at which the samples are being milled during the process, term "polishing" technique in this project. This technique is applicable to different materials, thickness, and wide range of PS sizes, thus making it possible to fabricate high quality nanodisc and nanohole-disc arrays (chapter 5 and 6). During the ion milling process, the direction of the ion milling is incrementally decreased from maximum usable angle to 0°, or vice versa. The maximum angle is defined by the distance and the size of the polystyrene particles. If the angle used are above this angle, parts of the substrates below will not be etched throughout the process and uneven patterned will be produced. Based on calculation, maximum angle of 45° can be used when the size of the PS is reduced to 60 %

while the centre-to-centre distance remains the same. More details and simulations can be found in appendix.

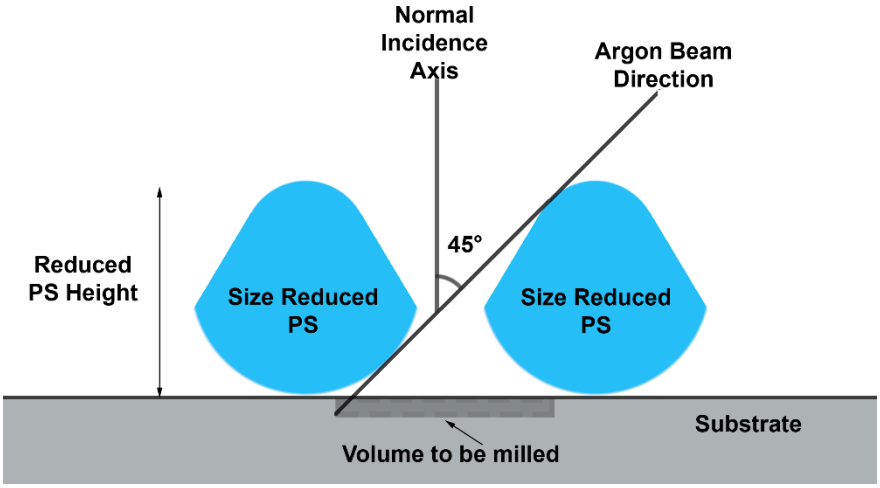

Figure 4-13 Maximum allowed angle, determined by the reduced PS height, initial PS diameter, and the depth of substrate to be removed.

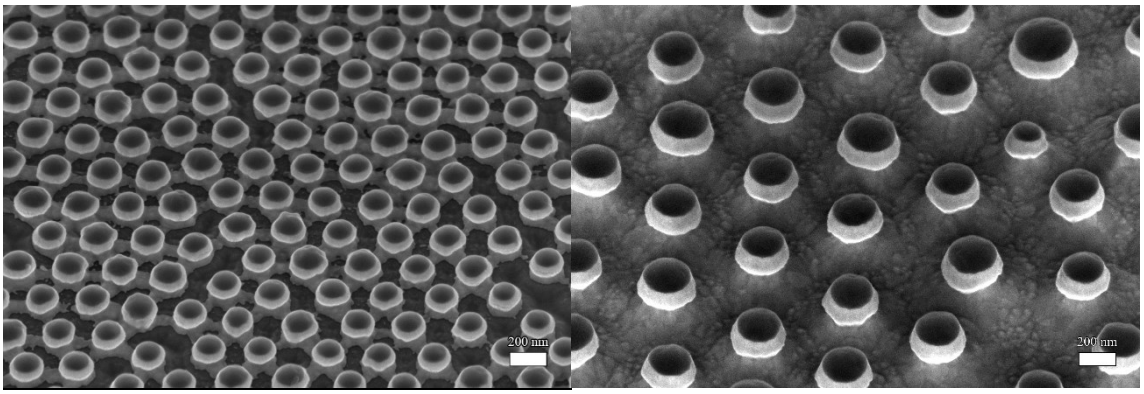

Figure 4-14 Uneven milled pattern on two different metal substrates as part of the metal layer beneath were blocked by the PS due to angle used for the ion milling were too large. (Scale bar = 200 nm).

However, similar to oxygen plasma process, argon ion milling can damage[231] and cross-link[226] PS. This presents a fabrication issue for patterning materials with slow ion milling rate as long exposure time degrades the shape of the PS mask and cross-linked PS can be attached firmly to the material below, which are extremely difficult to remove. Cross-linked PS also has a reduced etching rate[232]. Therefore, if the pattern requires a long exposure to oxygen plasma and ion milling, an alternative strategy will be required in fabrication process. In this project, nanohole-disc arrays requires a long exposure to both processes. A breakthrough in the process was found to overcome this challenge and is described in PS removal section below.

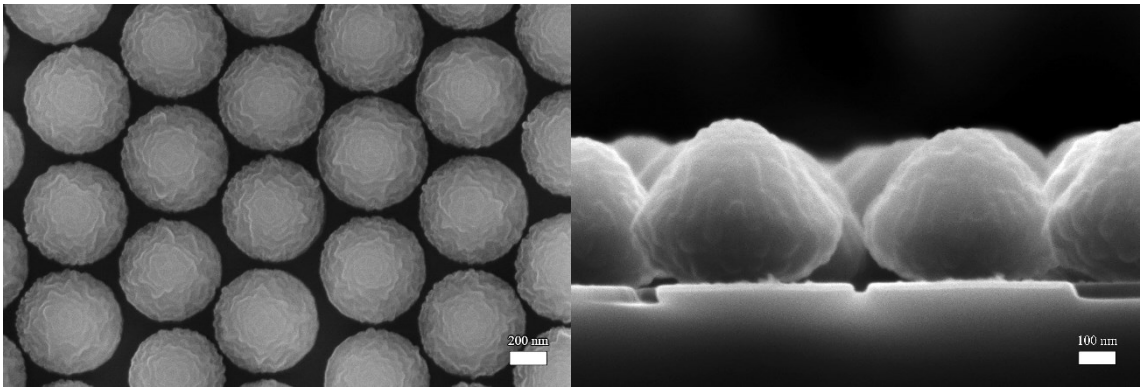

Figure 4-15 Top (left) and cross-section (right) SEM images of PS underwent 10s oxygen plasma and 27 minutes of argon ion milling process. The combined effect of size reduction and milling into the substrates can be seen from the images. Surface roughening caused by the plasma process is also visible on the PS.

4.6 Polystyrene Removal

After the role of PS mask is completed, it should be removed to leave a clean patterned substrate suitable for subsequent characterisations or applications. It was found that PS that have not been exposed to oxygen plasma and argon ion milling process can be removed by common PS removal methods such as high temperature burn-off[233,234], dissolution in organic solvent such as absolute ethanol and toluene, and removal by using tape[7,48,184,194,213,235,236].

However, complication arose if the fabrication of a specific structure involve plasma process. Although the incorporation of oxygen plasma or ion milling process into the fabrication allows a larger variety of nanostructures to be made, exposure to these processes promote cross-linking of PS due to dangling bonds and formation of C-O-C bonds on the surface[226]. Cross-linked PS is very stable and was found to be extremely difficult to remove. It has been found that they remain on the substrates after the following tests: 24 hours 500 °C temperature treatment, immersion in Piranha acid, strong solvents that satisfy Hansen Parameters, 30 minutes oxygen plasma and multiple tape removal. Residues of cross-linked PS remains, leaving incomplete PS removal. Subsequent deposition of metal on top of those surfaces resulted in irregular structures, making it difficult to control the plasmonic effect and reduce the reproducibility. Thus an alternative approach is required.

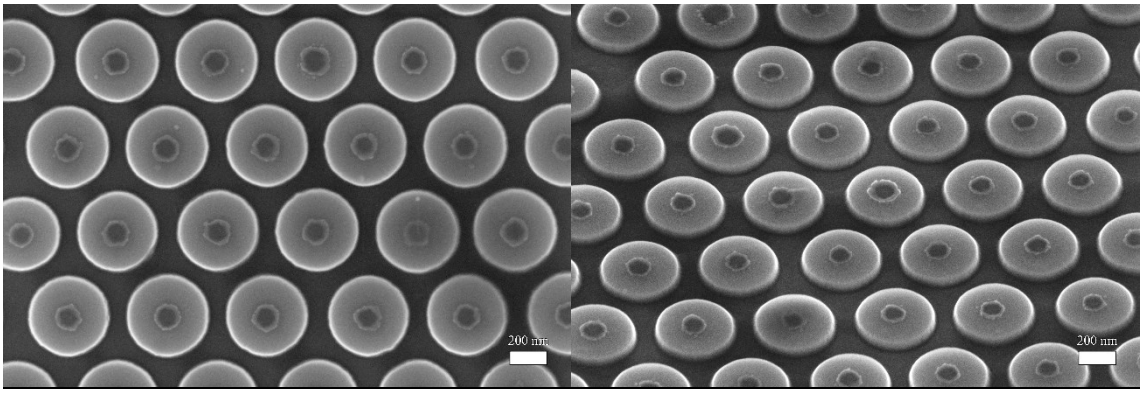

Figure 4-16 Top (left) and 45° view (right) SEM images of a sample processed through oxygen plasma, argon ion milling and standard PS removal steps. An inner circle of PS residual after PS removal is clearly visible on the silicon substrate. Scale bar = 200 nm.

In this project, this problem is solved by a new and novel strategy. We proved that by implementing a sacrificial layer between the required sample pattern and the PS masks, the cross-linked PS residue can be removed completely and no longer presents a problem in the plasmonic array system. The main requirements for the sacrificial layers are (1) sufficient thickness to compensate the diffusion and adhesion of the cross-linked PS, (2) being as thin as possible or very fast etching rate to prevent the longer processing time that may consumed the PS mask before the desired thickness has been etched, (3) being able to be removed together with attached PS without damaging the patterned nanostructures and substrate. According to the reactivity series for metals, two of the main plasmonic materials, silver and gold, are at the bottom of the list and are stable against acids except very strong oxidizing acids such as aqua regia (royal etch). High up in the list are metals that are extremely reactive and can react with water and thus not suitable as a sacrificial layer as nanosphere lithography methods in this project requires water. Therefore, metals that are located at the middle of the reactivity series that are reactive toward acids can be good candidate as a sacrificial material. Among these metals are Al, Cr, and Ni, which are common sputtering targets that can be found in many physical vapour deposition setup and can be deposited on top of another metal *in-situ*.

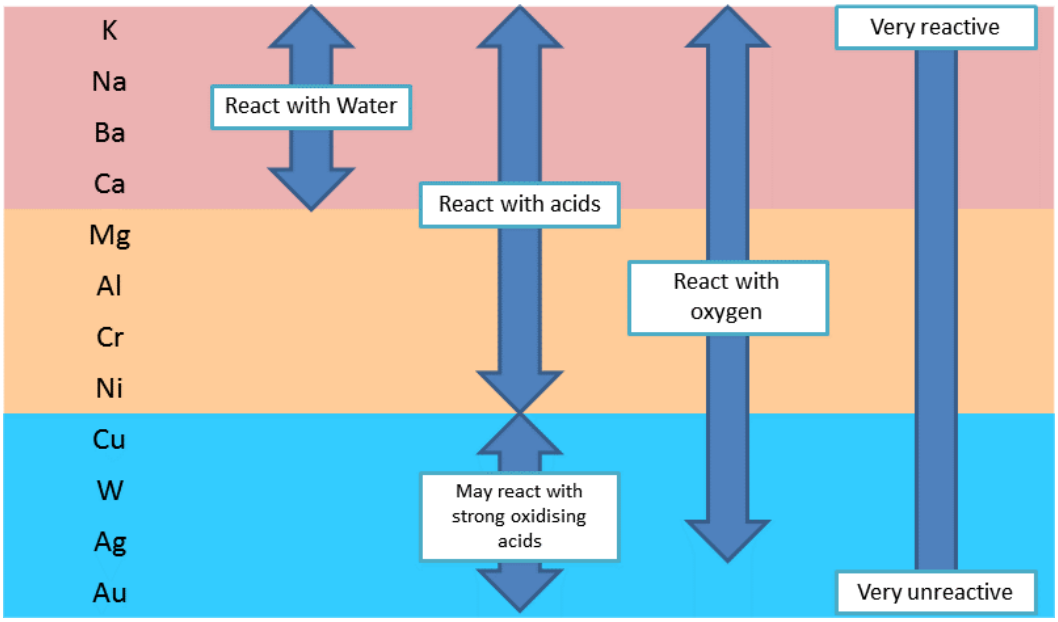

Figure 4-17 Reactivity series of selected metals.

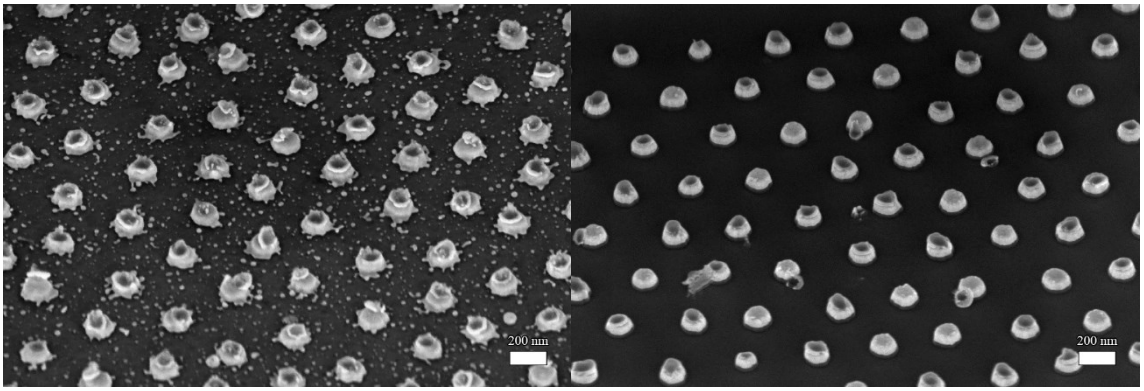

Figure 4-18 SEM images of Au nanodisc arrays on silicon substrates at 45° fabricated using 10 nm Al (left) and Ni (right) sacrificial layer with same oxygen plasma and ion milling process parameters. Samples were immersed in 10 % sulphuric acid for 5 minutes.

A 10 nm thin layer of Al and Ni were tested on nanodisc arrays structure and it was found that Ni outperformed Al as sacrificial material. The results are illustrated in Figure 4-18 where dissolution of the sacrificial metal in acid was stopped when the metal are partially removed to illustrates the process. Ni dissolved faster and preserved the shape of the nanodisc. The removal of Al was found to have become very difficult after exposure to the oxygen plasma and argon ion milling when compared to bare Al immersed in 10 % sulphuric acid. This is most likely due to the formation of aluminium oxide (Al_2O_3) during oxygen plasma process. Although Al_2O_3 can also dissolve in acid, it has very slow ion milling etching rate and affected he patterning process. The small nanoparticles around the nanodisc in the SEM picture is the result of slow Al_2O3 etching and incomplete removal of the gold layer below. For those reasons, Ni is selected as sacrificial material for fabrication of nanostructures that involves plasma process.

4.7 Immobilization of Fluorophore-protein Conjugation Monolayer

Conjugated fluorophore-proteins are attached to nanostructures as a mean to characterise the strength of MEF by those fabricated nanostructures. There are currently a large variety of fluorophores available on the market with different properties for specific purposes[136–138,237] such as those shown in Table 3-2. As the main objective of this project is to establish enhancement effect from different plasmonic nanostructures, the selected protein and fluorophores pair are all of the same category to allow like-for-like comparison with recent studies by our research group[148,150]. Commercially available streptavidin conjugated Alexa Fluor ® (SA-AF) of different wavelengths (Figure 4-19) were purchased from Life Technologies Ltd, which acclaimed to be brightest and has excellent photostability. This fluorophore-protein is very common and have been subjected for biosensing experiments and benchmarking[6,68,136,138,180,182,237–241]. Where possible, Alexa Fluor with low quantum yield is preferred as it helps to demonstrate the effect of MEF by generating greater difference in emission intensity when compare to baseline[150,242].

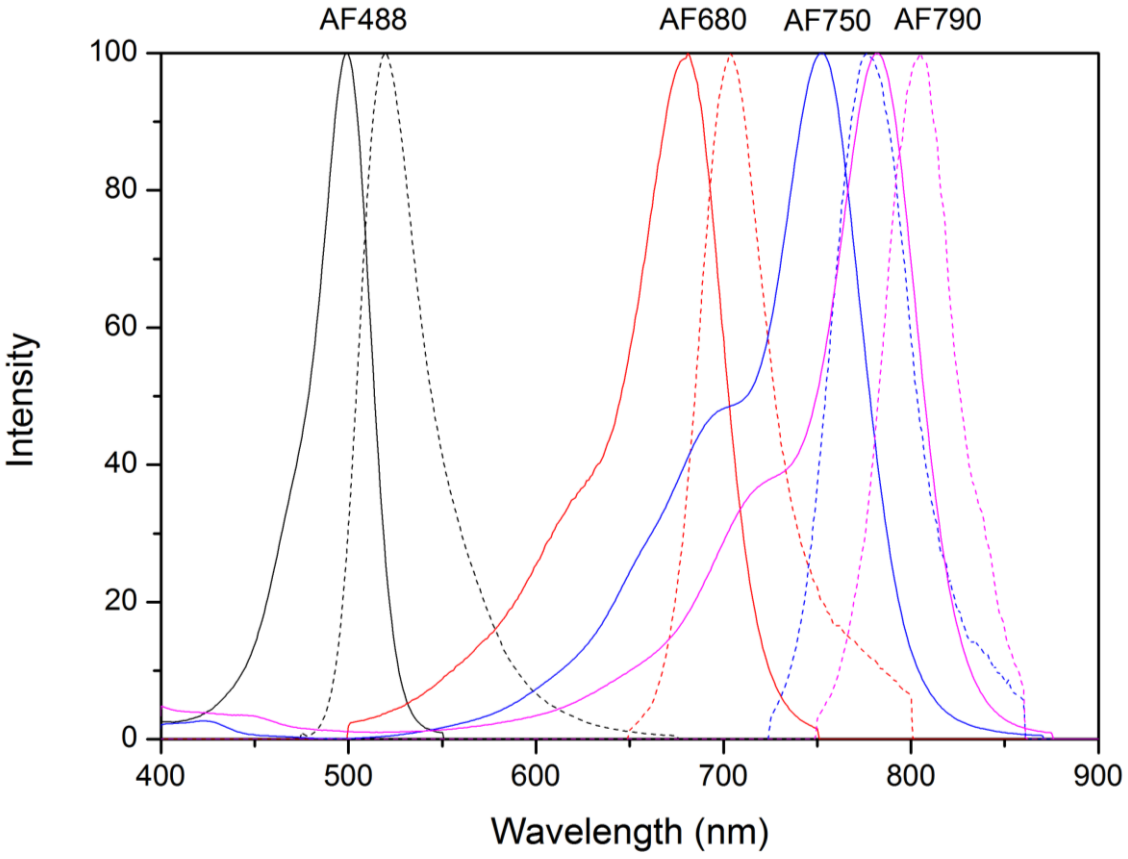

Figure 4-19 Excitation (dash line) and emission (solid line) spectrum of different Alexa-Fluor used in this project.

To facilitate the formation of monolayer of AF and effective distance of approximately 9 nm (bBSA and streptavidin are approximately 5 and 4 nm respectively[150,243]) for good MEF emission and prevent quenching, a monolayer of biotinylated-bovine serum albumin (bBSA) is first deposited on both bare substrates and nanostructure arrays. This is followed by incubation of 25 µg/ml SA-AF on

top for 2 hours to form stable fluorophore-protein conjugations through strong bonding between biotin and streptavidin[244]. The concentration of the solution is chosen to ensure there are sufficient fluorophores for full monolayer coverage on the sample surface. Detail step by step standard operating procedure can be found in appendix.

It is important that reference sample, i.e. bare glass with fluorophore-protein requires same conjugation steps as samples with plasmonic nanostructures for direct comparison and pre-treatment of the substrate surface is vital to obtain correct results. For instance, gold nanodisc arrays are very hydrophobic due to the gold and the geometry of the nanostructure. This made fluorophore-protein attachment very difficult and the gold started to delaminate during the incubation process. Treating those structures with UV-ozone was found to reduce the delamination and increase fabrication yield. On bare glass substrate, it was found that treatment with and without UV-ozone produced a significant difference in the fluorophores emission intensity (see Figure 4-20).

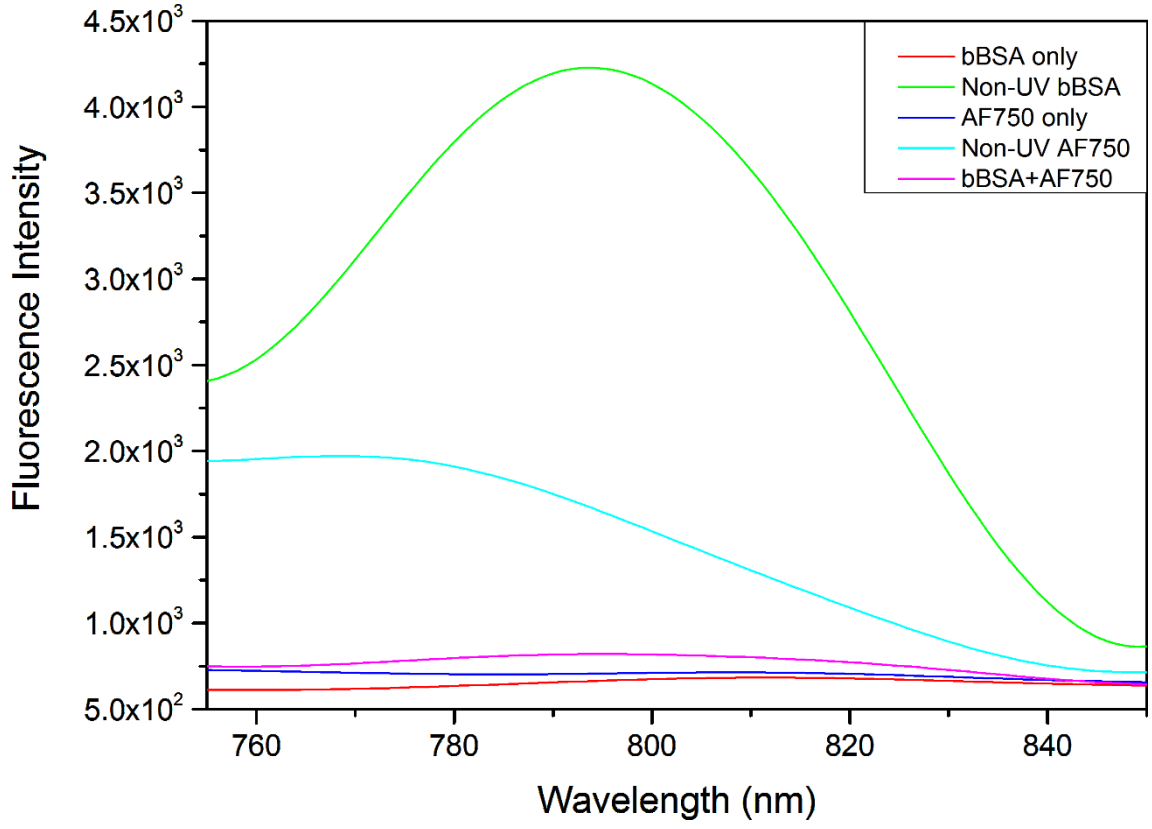

Figure 4-20 Fluorescence emission intensity of bBSA and AF750 on bare glass excited with 740 nm at 30°. Unless specify otherwise, samples are pre-treated with UV-ozone before fluorophore-protein attachment.

4.8 Conclusions

The design criteria to enable fabrication of complex nanostructures for plasmonic arrays, it is crucial to have the ability to produce repeatable good quality area, and precise control over nanoparticle geometries. Modified nanosphere lithography has been developed to produce reproducible and large area PS monolayer mask. Oxygen plasma to reduce the PS size and argon ion milling for nanostructure patterning were incorporated into the process to extend the variety of structures that can be produced. The challenge of removing cross-linked PS has also been circumvented by having a Ni sacrificial layer. Nanotriangular arrays, nanodisc arrays, and complex 3D nanohole-disc arrays were successfully fabricated by modified nanosphere lithography. Their optical properties will be discussed in Chapter 5 and their application in MEF will be demonstrated in chapter 6.

Chapter 5

Nanostructure arrays

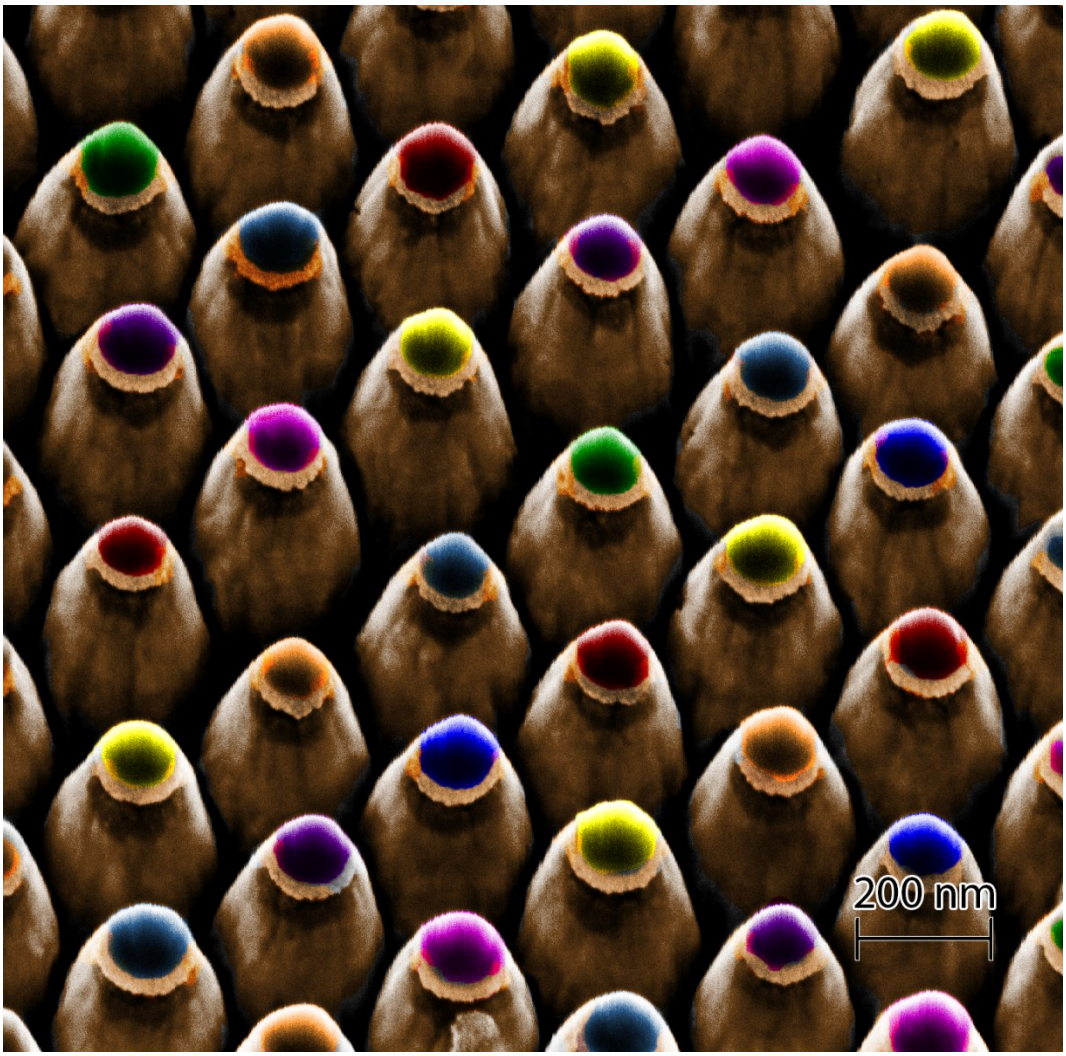

Figure 5 Nanopencil arrays fabricated with nanosphere lithography method. (False colour applied).

Chapter 5 Nanostructure Arrays

Nanosphere lithography is a versatile low cost nanofabrication technique that can be combined with other processes to form large variety of nanostructure in hexagonal close pack arrangement. Three types of arrays were produced in this project: nanotriangles, nanoholes, and nanodiscs. Those nanostructures were studied and this chapter reveals some interesting optical results obtained from those nanostructures.

The nanostructure were imaged using Zeiss LEO-1525 or Carl Zeiss Auriga field emission gun scanning electron microscope (FEG-SEM) system with 5 kV accelerating voltage. Extinction spectrum were measured using Perkin Elmer Lambda 25 or Agilent Cary 5000 system with unpolarised light unless stated otherwise.

5.1 Nanotriangular arrays

Nanotriangle is a basic structure that can be produced by nanosphere lithography. It is straightforward to fabricate by NSL without the need to incorporate many different processing tools. Moreover, the high curvature of the nanotriangle tips helps focusing the electric field strength generated during LSPR resonance. This makes them very attractive to the applications that depend on strong electric field such as SERS and MEF.

The resonance peak is tuneable by changing the geometry parameters of the nanotriangular arrays: thickness, lateral size, shape of the tip, distance between the tip, and the material. These parameters can be controlled by selecting different PS sizes, different metal evaporation thickness, and different exposure time to oxygen plasma. Figure 5-1 and Figure 5-2 show normalised extinction of nanotriangular arrays made of Al, Ag, or Au at different sizes and different thicknesses. The position of their resonance peak is summarised in Table 5-1. Glass substrate is used for all samples except those involved Al as it can have LSPR resonance below 290 nm, which falls into absorption range of a typical microscope glass slide and thus making them unsuitable for UV. Hence, quartz substrate which has high transmittance in UV is used as the substrate for Al based nanostructure. Refractive index of the quartz ($n_{quartz} \approx 1.46$) is also quite close to that of microscope glass ($n_{glass} \approx 1.51$), thus resonance wavelength of those Al are not significantly blue-shifted compare to on glass substrate and thus allows comparison between different metals. The labelling of the samples follows this rule: PS[Sizes of PS][Metal][Thickness of the metal]. For example, PS400Ag50 represents sample nanotriangular arrays fabricated using 400 nm size PS and 50 nm thick Ag. Extinction from different ranges of nanotriangle geometries were gathered as reference database to aid predicting the geometries required for LSPR resonance at desired wavelength.

	Dipole, Quadrupole Resonance Wavelength (nm)				
PS (nm) / Metal	290	400	500	620	800
Al 100	646, 314		>800, 438	>800, 497	>800, 605
Ag 50	772, 470, 406		>1100, 728, 466		
Ag 75	495		680	750, 455	880, 477
Au 50		1203, 710	1500, 856	1622, 976, 625	
Au 75		1125, 762	1408, 845, 614	1498, 1095, 624	

Table 5-1 Plasmonic peak location for nanotriangular arrays consists of different metals, lateral sizes, and thickness. The colour of the text used for each PS sizes are the same as figure 5-1 below.

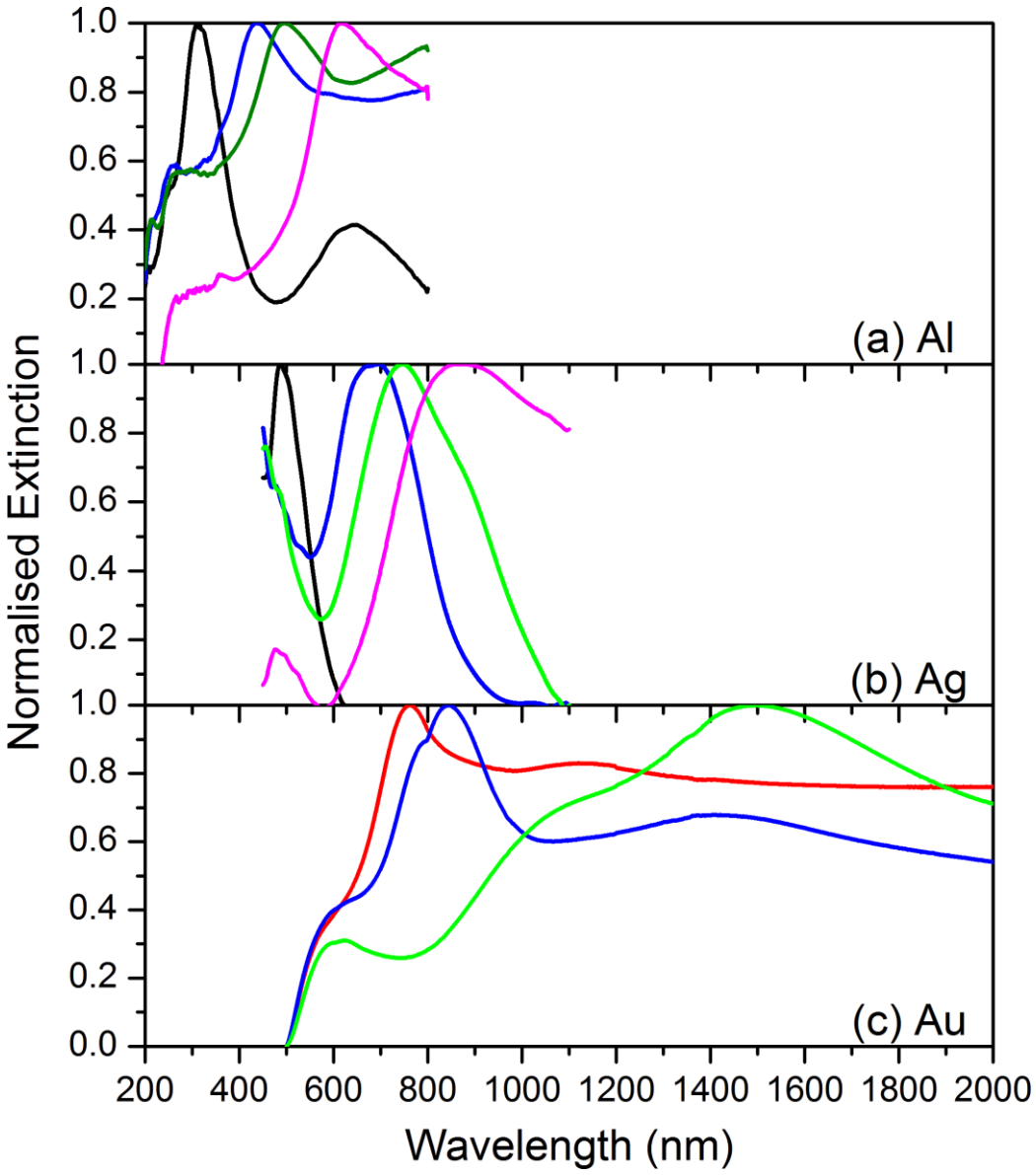

Figure 5-1 Normalised extinction of (a) 100 nm thick aluminium Al, (b) 75 nm thick silver Ag, and (c) 75 nm thick gold Au nanotriangular arrays fabricated through nanosphere lithography. Colour represents the size of PS used: Black (290 nm), red (400 nm), blue (500 nm), green (620 nm), and violet (800 nm).

5.1.1 *Materials*

Since the LSPR resonance is strongly dependent on the dielectric function of the materials (chapter 2.1), the choice of material is usually the first selection criterion. Aluminium (Al), silver (Ag), and gold (Au) are common materials to achieve LSPR resonance in visible wavelength. Figure 5-1 illustrates the location of dipole and quadrupole resonance wavelengths changed according to the plasmonic materials involved. As expected from the dielectric function of the metal (Figure 2-3), for each wavelength at most part of visible spectrum, the real part of dielectric function for Al is most negative, follow by Ag and Au. Hence, to satisfy the LSPR resonance condition $\epsilon_{i,1}(\lambda) = -\chi\epsilon_m$ for different metal with same shape and surrounding medium, the resonance wavelength is pushed toward the UV for Al, with Ag covers the visible wavelength up to NIR. Au, which has lowest $\epsilon_{i,1}(\lambda)$ value among them, resonates above the interband transition around 506 nm and up to NIR-II region.

When reading the plasmonic resonance, one needs to be careful in distinguishing between the dipole resonance and other secondary effects caused by defects such as joined nanotriangles and large metal islands which can cause large changes in resonance[245]. Those secondary effects are hard to discern from the actual plasmonic resonance peak from the structure of interests, especially when then acquisition area from the sample surface during optical measurements cover a large area. For instances, a light spot sizes of 5 mm would covers approximately 16,000 nanotriangles made from 620 nm sized PS. This would require a very high quality fabrication yield and is a challenge for fabrication method based on self-assembly. In addition, the effect of non-homogeneity also broaden the resonance peak.

As such, the limited wavelength in the acquisition due to the experiment setup available at earlier time of the project, measurement were only allowed wavelength up to 1100 nm only. It was difficult to justify if the resonance peak for Al in Figure 5-1 (a) is due to dipole, quadrupole, or from secondary effects unless there are additional information from a different dataset of different thickness or verification through computer modelling. However, it is likely that the dipole resonance has extended further than 800 nm for 100 nm thick Al for all PS sizes except for the smallest 290 nm sized PS, which is around 650 nm. In addition, dipole resonance also has a larger bandwidth than of quadrupole mode, which also appears to be the case here.

A like-by-like comparison of for the effect of dielectric function of the materials with same geometries can be made from 75 nm thick nanotriangular arrays of different sizes between Ag and Au (Figure 5-1 b and c). It can be seen that the resonance peaks for Au have been extended much further into NIR, making it a more suitable material for NIR biosensing application. Higher resonance mode – octupole at 624 and 614 nm for 620 nm and 500 nm sized PS respectively, can also be seen on the extinction spectrum from the Au larger nanotriangular arrays.

A nanotriangle has a long side length and a shorter perpendicular bisector length, an approximate 13.4% difference. Since plasmonic resonance is sensitive to the geometry, it can generate two resonance peaks when excited by unpolarised white light source. However, the plasmon resonance is generated on the same nanoparticle and the difference in lengths is not very different, such phenomena is not easily observed from measurement and often concealed by inhomogeneous size distribution of the nanotriangles in the arrays. For instance, the PS nanospheres solution has a 10% size variation. Nonetheless, provided the quality of the sample is good and the measuring tool has a good spectral resolution, it is possible to measure these double peaks resonance at the dipole peak. In this case, such the Ag nanotriangle arrays in Figure 5-1b shows the existence of such peaks, suggesting the quality of nanotriangular arrays produced.

5.1.2 *Thickness and Size*

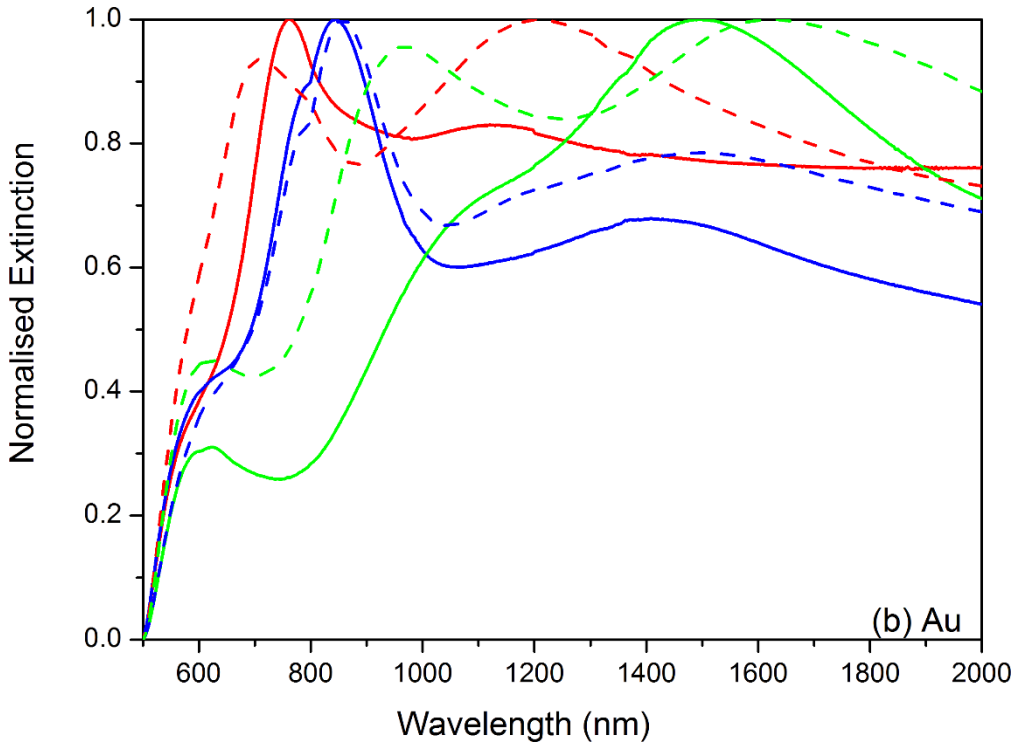

Figure 5-2 Nanotriangular arrays made from Au of same geometries but in 50 nm (dash line) and 75 nm thickness (solid line). Colour represents the size of PS used: Red (400 nm), blue (500 nm), and green (620 nm).

From Figure 5-2, the spectrum also shows blue-shifting of the resonance peak as the thickness increases for both Ag and Au due to increased phase retardation (chapter 2). As the sizes of the PS used increased, the lateral dimensions of the nanotriangle also increased accordingly and red-shift the resonance peak position as expected. A useful quantitative analysis on the change in resonance peak is to calculate their in-plane sensitivity ($\Delta\lambda/\Delta a$)[44]. Table 5-2 summarised the in-plane sensitivity of those nanotriangular arrays with different thicknesses. It indicates that Au has highest sensitivity follow by Ag and Al. Although the dataset is not complete for higher order mode, dipole also appears to be more sensitive than higher resonance mode.

Thickness	Metal	Dipole	Quadrupole	Octupole
50	**Au**	8	5.2	-
75	**Ag**	3.2	-	-
	Au	7.1	6.6	0.36
100	**Al**	2.4	-	-

Table 5-2 In-plane width sensitivity ($\Delta\lambda/\Delta a$) of the nanotriangular arrays.

5.1.3 *Tip to tip distance*

When plasmonic particles get close together, their optical behaviour changed as a result of coupling between them. [150]Here, PS nanospheres of sized 300-, 500- , and 620 nm are exposed to a short duration of oxygen plasma followed by thermal evaporation of 75 nm thick Ag. This forms closely spaced nanotriangular arrays as the tip-to-tip distance between the nanotriangles is reduced. In response to geometry alterations and increased coupling between the adjacent nanotriangles, the resonance peak also changed accordingly. Figure 5-4 shows the change of extinction profile of those samples. Their geometrical parameters and extinction peak are summarised in Table 5-3 below. As can be seen from the extinction spectrum, the arrays are extremely sensitive to slight alteration in the geometrical structure. Small increased in lateral sizes and interparticle coupling results in red-shifted and broadened extinction peak. Peak resonance wavelength, λ_{calc} calculated by FDTD is also included in the table.

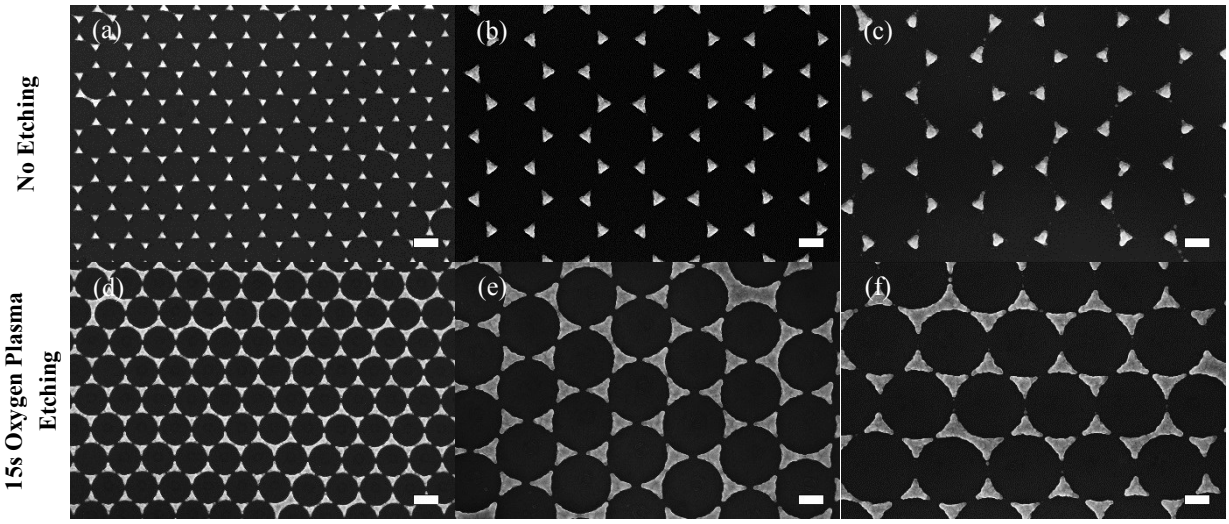

Figure 5-3 FEG-SEM images of Ag nanotriangular-like arrays: (a) 300 nm PS sphere template without oxygen plasma etching (PS300-0s), (b) 500 nm PS sphere template without oxygen plasma etching (PS500-0s), (c) 620 nm PS sphere template without oxygen plasma etching (PS620-0s), (d) 300 nm PS sphere template with 15 seconds oxygen plasma etching (PS300-15s), (e) 500 nm PS sphere template with oxygen plasma etching (PS500-15s), (f) 620 nm PS sphere template with oxygen plasma etching (PS620-15s) [150] (scale bar: 200 nm). (Reprinted from ref 145 with permission from Springer.)

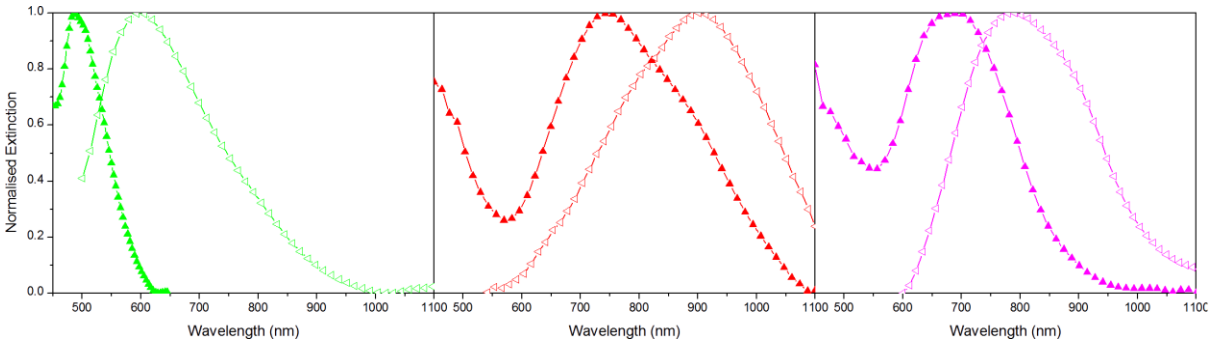

Figure 5-4 Normalised extinction spectrum for nanotriangular arrays fabricated through (a) PS300, (b) PS500, and (c) PS620 with or without oxygen plasma treatment (solid triangle trace: without etching; hollow triangle trace: with 15 s etching) [150]. (Reprinted from ref 145 with permission from Springer.)

Table 5-3 Nanoparticle structural parameters corresponding to the Near- and Mid-Infrared Extinction[a]. a is the length of the perpendicular bisector, s is the measured tip-to-tip distance, D is the size of the PS used, λ_{meas} is the measured extinction peak wavelength, and λ_{calc} is the FDTD simulated extinction peak wavelength based on the geometry of the nanotriangular arrays. [150] (Reprinted from ref 145 with permission from Springer.)

Sample	***PS300-0s***	***PS500-0s***	***P620-0s***	***PS300-15s***	***PS500-15s***	***PS620-15s***
a (nm)	72±4	118±11	137±15	110±8	208±11	227±23
s (nm)	79±8	160±16	218±22	40±4	63±6	80±8
D (nm)	300	500	620	300	500	620
λ_{meas} ***(nm)***	495	680	750	600	800	905
λ_{calc} ***(nm)***	527	666	725	620	770	910

[a]Measurements in Fig. 2 and 3 and FDTD calculations [(a) 300 nm PS sphere template without oxygen plasma etching (PS300-0s), (b) 500 nm PS sphere template without oxygen plasma etching (PS500-0s), (c) 620 nm PS sphere template without oxygen plasma etching (PS620-0s), (d) 300 nm PS sphere template with 15 seconds oxygen plasma etching (PS300-15s), (e) 500 nm PS sphere template with oxygen plasma etching (PS500-15s), (f) 620 nm PS sphere template with oxygen plasma etching (PS620-15s).

It is also worth mention that the FDTD modelling and the experimental data obtained here showed a good agreement. As the plasmonic resonance is known to be very sensitive to the geometry, the simulated and observed plasmonic peak only showed a maximum of ~ 6 % (PS300-0s samples). This suggests the imperfections of the nanostructure are relatively small in our fabricated samples.

5.1.4 *Summary*

An improved modified NSL has been developed and able to reproduce large area quality nanotriangular arrays for optical measurements. Materials and geometrical parameters such as thickness, interparticle gap, and lateral size were all found to influence the plasmonic resonance as expected. Nanotriangular arrays with closer tip-to-tip distance were also fabricated and were found to change the extinction spectrum dramatically. Those samples were then chosen for application in biosensing in the next chapter.

5.1.5 *Future work*

The plasmonic resonance of nanotriangular arrays shown here falls into NIR-I region. Their geometrical structures could be enlarged to tune their resonance into NIR-II region for future biosensing application. Additionally, a limitation of nanotriangular arrays produced by nanosphere lithography is the poor area of coverage. The hot spots only exist at the tip of the nanotriangle and large area of the surface does enhance electric field. Alternative hybrid structure such as nanodiscs filling in the empty space could increase surface area for high electric field throughout the substrate.

5.2 Nanodisc Arrays

5.2.1 *Fabrication of Nanodisc Arrays*

Fabrication of nanodisc is not completely new[221,222,246]. For example, in 2007 Zheng *et al.* published results on long range ordered of Au nanodisc arrays produced from NSL and Ar ion milling[222]. However, a chromium adhesion layer was used in their experiment. Although it helps confine the Au from dewetting and coalescence with the surrounding metal and form a thin island film when undergoes thermal annealing, it was later discovered that such adhesion layer has plasmonic damping effector to the system and increased absorption channel. In addition, although the thermal annealing process can improved the FWHM, it will also cause the nanodisc to lose the sharpness of the sidewall, and can result in reduction in the strength of electric field enhancement.

In this project, a newly developed approach termed "polishing" technique as described in chapter 4.5 was applied to fabricate high quality nanodisc arrays in accordance to the processing steps illustrated in Figure 4-6. The nanodisc arrays produced have their sidewall verticality greatly improved and the process are highly reproducible. The fabrication steps to fabricate nanodisc arrays is illustrated in. The extinction peak also remains clearly visible despite no adhesion layer and thermal treating was used. Figure 5-5 below shows SEM images of some nanodisc arrays fabricated through this process. The centre-to-centre pitch is predetermined by the initial PS sizes and the individual nanodisc diameter is controlled by the exposure of PS to the oxygen plasma and the milling process. However, prolonged PS exposure to the plasma process results in PS bonded to the metal surface and unable to be removed by conventional PS removal methods, especially for smaller PS sizes (b, c, and f).

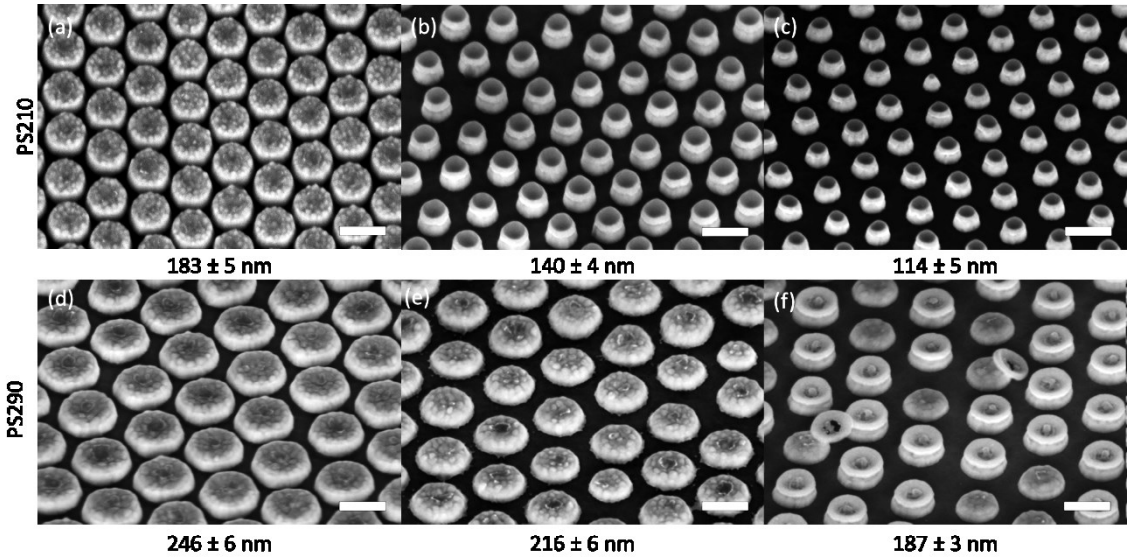

Figure 5-5 Illustration of different nanodisc arrays with centre to centre distance determined by the initial PS size (top: 210 nm, bottom: 290 nm) and nanodisc diameter is controlled by duration of oxygen plasma process. Scale bar = 200 nm.

5.2.2 *Optical Properties of Nanodisc Arrays*

Normalised extinction spectrum acquired from a range of 50 nm Au nanodisc arrays with different diameters and pitches are shown in Figure 5-6. This thickness is chosen as a fixed parameter to explore the influence of other geometrical parameters such as pitch size and nanodisc diameter due to the following reasons: 1) the duration of ion milling needs to be minimised to ensure that the PS mask does not become cross-linked and therefore unable to be removed. Since the milling duration is proportional to the thickness of metal to be etched away, the metal thickness cannot be too thick. 2) the amount of PS mask material is also being etched away during the ion milling process, prolonged ion milling etching will result in reduce sidewall verticality and lose the shape of a nanodisc, 3) As described in chapter 2, the absorption and scattering of the plasmonic material is relevant to the size. Small particle is generally a good absorber (typically less than 30 nm) and bigger nanoparticles are better scatter. Gold nanodisc arrays with 50 nm thickness is thick enough to be consider a good scatterer and reducing this thickness could make the absorption channel dominant. 4) It is also found that for the range of PS sizes and nanodisc diameter under investigation, 50 nm Au nanodisc arrays produce LSPR resonance within the NIR, making this thickness a great choice as a reference thickness. Although scattering can become even more prominent with thicker nanodisc, it will cause blue shift the plasmonic peak, away from the NIR region which is not ideal. 5) Ag and Al were not the main choice of metal for nanodisc arrays study because the LSPR wavelength generated will be located at shorter wavelength. In addition, unlike gold which is inert to oxygen plasma treatment, Ag and Al will be oxidised in the process. Although it is possible to prevent the oxidation by applying a protective layer between the Ag (or Al) and the PS mask, this layer will also increase the milling duration and needs to be removed after the patterning.

For all different pitches, it can be seen that larger nanodisc diameter generates broader extinction spectra, due to increase ramping and effect interparticle coupling. The spectrum also shows the tunability of different pitch size, where resonance are towards more to the NIR for larger pitch sizes. Although interestingly, results from 210 nm pitch size arrays also showed that it is possible to have resonance at NIR for small pitch size provided the gap between the nanodiscs are very close to each other. A resonance peak occurred beyond the 1100 nm for 210 nm arrays with gap of around 10 and 17 nm. This is perhaps not surprising as it has been reported by various research on interparticle coupling that when the nanoparticles gets very close together, the resonance wavelength follows an exponential red-shift as the gap reduced[86,98,99,192,247]. However, the determination of the exact peak location was beyond the limit of Perkin Elmer Lambda 25 at the time of measurement. A better way of analysing the effect of coupling is by plotting the extinction peak against the diameter or gap-to-diameter ratio.

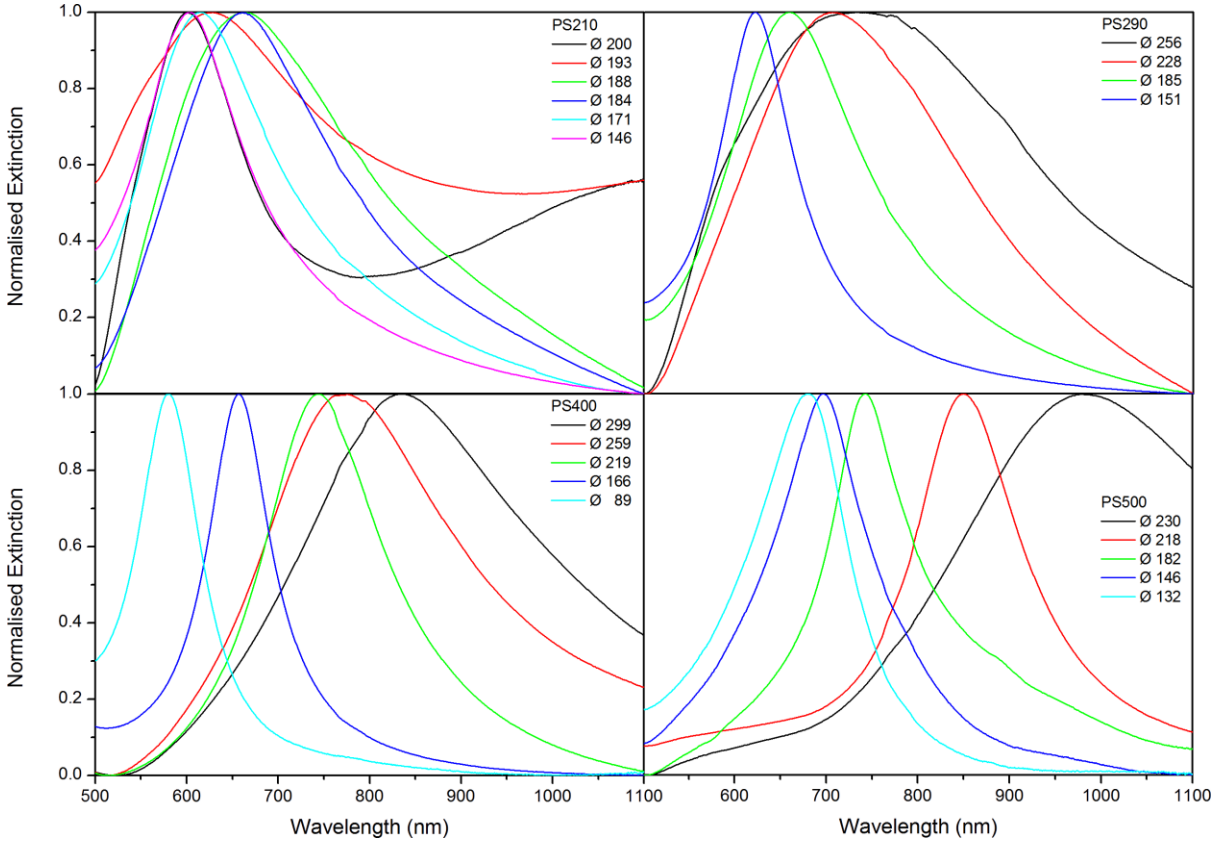

Figure 5-6 Normalised extinction spectrum of 50 nm thick Au nanodisc arrays of different diameters and different hexagonal pitch. Clockwise from top left: 210 nm, 290 nm, 500 nm, and 400 nm. The colour indicates the diameter of the Au nanodiscs.

Figure 5-7 shows that the extinction peak follows a linear trend for all pitch sizes. Larger pitch distance also have a greater tunability range than smaller counterparts. The data also showed that similar nanodisc diameter does not produce extinction peak around the same wavelength. Such phenomena is due the interplay of grating constant, and interparticle coupling effect.

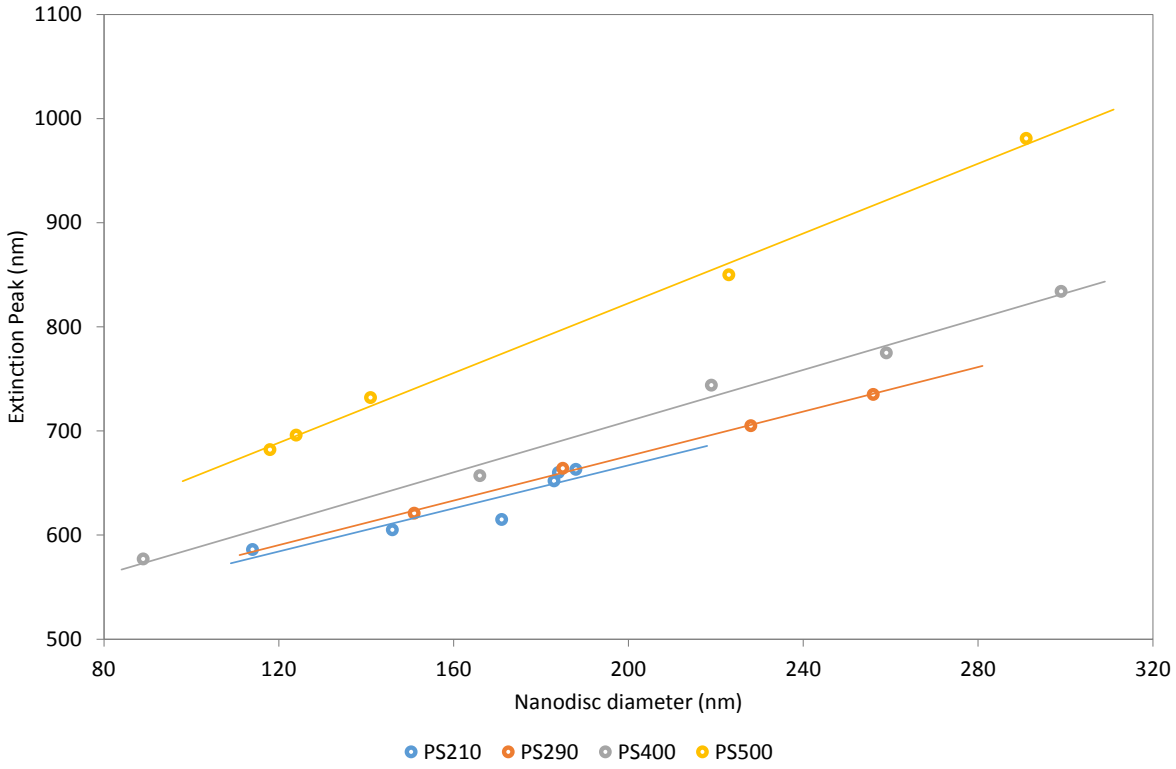

Figure 5-7 Extinction peak of the nanodisc arrays substrates with different pitches and different nanodisc diameters. Solid lines are linear line of best fits.

In general, the LSPR peaks are highly dependent on the size of the particles. For isolated nanoparticles (i.e. near field effect of the nanoparticle does not affect neighbouring nanoparticles), the larger the size the longer the LSPR peak wavelength. However, change in the LSPR shapes and peak locations are more complicated when they are coupled. By combining the results previously published by various research groups, for 2D arrays comprising of individual nanoparticle with same size, I hypothesize there are four distinct grating domains that determine if the LSPR peak red shift or blue shift base on the interparticle distance[71,81,86,98,99,192,247,248]. Starts from arrays with interparticle distance larger than critical grating constant, $c_{crit} = \lambda_{LSPR}/n_{eff}$ where λ_{LSPR} and n_{eff} are LSPR wavelength peak position and effective refractive index respectively, multiple grating orders exist and it is said to be in radiative mode. As the interparticle distance decreases, the LSPR peaks will red shift and a maximum wavelength is reached when first grating order is met (i.e. $C2C = c_{crit}$)[81,86,98,99,247]. Additional reduction in the interparticle distance cause the LSPR peak to blue shift[98,99,192,247,248] and the grating order is evanescence mode. However, when the nanoparticles becomes very close to each other, their near-field effect coupled with neighbouring nanoparticles[71,247,248] resulting in strong SPR peak red shift together with peak broadening. For these reasons, same diameter of the nanodisc but different pitch distances do not generate the same resonance peak. It can be seen that data shown here falls into evanescence mode category as all the resonance wavelengths are above the critical grating constant (Figure 5-9) and therefore no grating effect has been observed.

Change in peak wavelength	Red shift	Blue shift	Red shift	Exponential Red Shift
Decrease in gap	Towards Grating $d > c_{crit}$	After grating $d < c_{crit}$	Coupling	Strong Coupling
	Radiative Mode	Evanescence Mode		

Figure 5-8 Hypothesized four different regions of coupling regime and grating effect based on studying results published in ref [71,81,86,98,99,192,247,248].

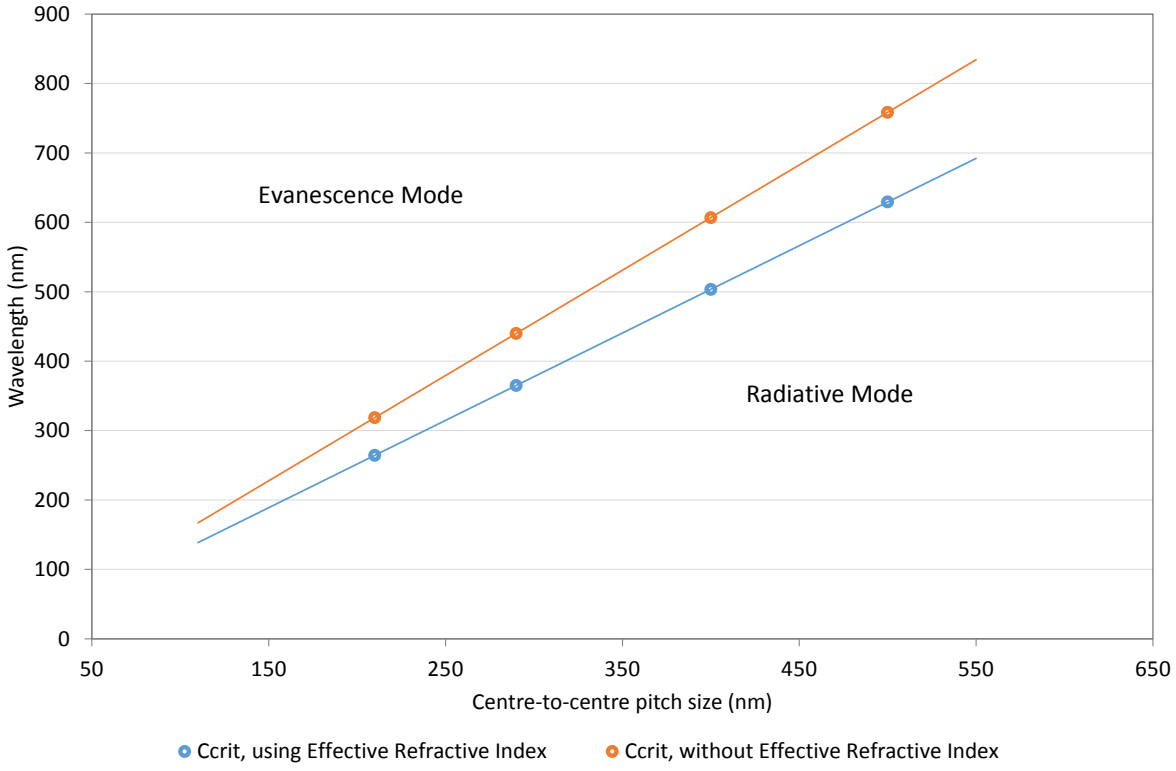

Figure 5-9 Regions where evanescence mode and radiative mode separated by the critical grating constant for different pitch distance.

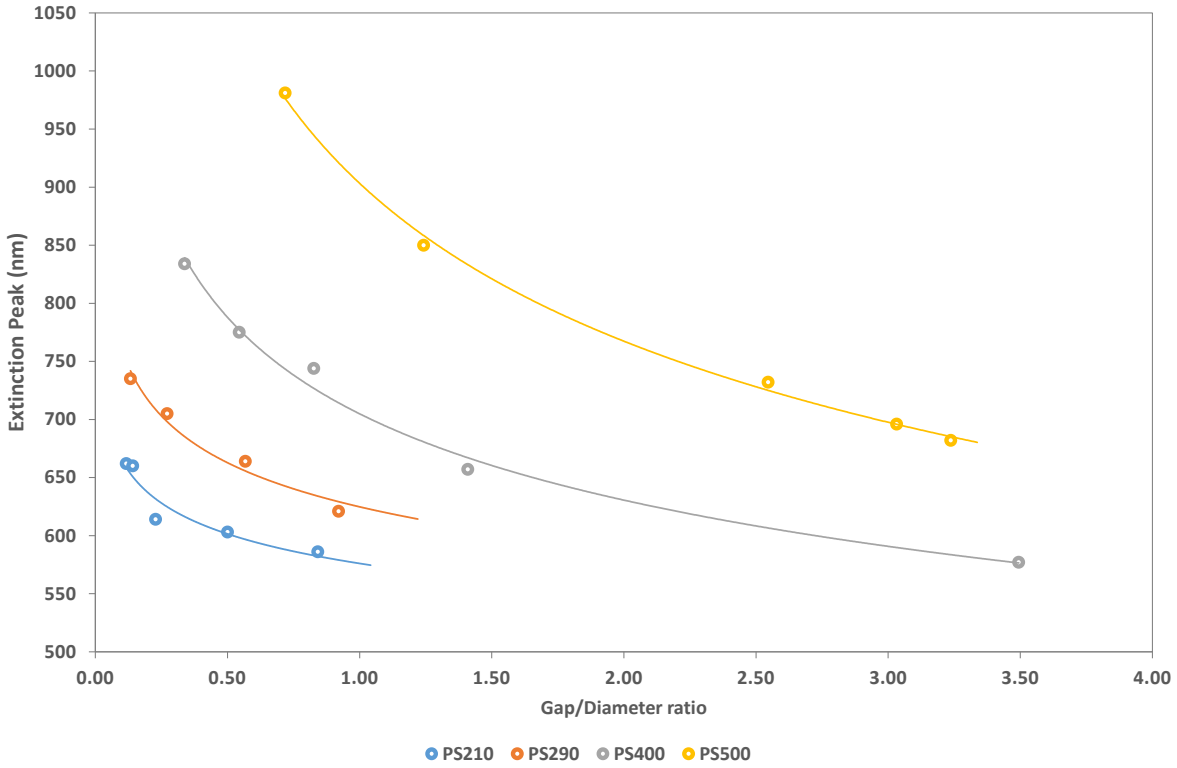

Figure 5-10 Extinction peak of different nanodisc arrays with respect to their gap-to-diameter ratio. Solid lines are line of best fit based on power function. Extinction peak for PS210 arrays with nanodisc diameters of 200 and 193 nm (ratio 0.05 and 0.09 respectively) are not included in this figure.

Another way to interpret the data was suggested by Mostafa *et al.*[86] is to plot the extinction peak in relationship to gap-to-diameter ratio (Figure 5-10). In their experiment, strong interparticle regime started to occur when the red shift in dipole extinction peak increases exponentially as the gap between the dimer falls below a certain threshold. Although the structure here is different from theirs, the nanodisc arrays fabricated here also shown to exhibit a similar behaviour and suggests that some of the samples fabricated are reaching strong interparticle regime, especially for 210 nm pitch with gap-to-diameter ratio of 0.05 and 0.09. In addition, interpreting the figure across horizontally for the same wavelength also showed that stronger coupling is achieved earlier for smaller pitch distance.

Pitch, d (nm)	Gradient (nm wavelength / nm diameter)	Constant (nm)	Regression, R^2
500	1.6762	487.49	0.9963
400	1.2292	463.69	0.9924
290	1.0345	460.16	0.9967
210	1.0345	460.16	0.8567

Table 5-4 Gradient and constant from the linear equation fit obtained from the data shown in Figure 5-7.

From data above, provided the interparticle coupling is not too strong, an empirical expression for equation estimating the extinction peak for different PS can be constructed:

$$\lambda_{ext}(nm) = \left(1.00497 + 0.00272e^{0.01102d}\right)\emptyset + \left(461 + 0.000374e^{0.02233d}\right)$$ *Equation 5-1*

where ϕ is the diameter in nm.This equation provide a useful prediction of the plasmonic resonance location for a 50 nm thick Au nanodisc arrays with specific disc diameter.

5.2.3 *Refractive Index Sensing (RIS)*

The stronger the LSPR mode generated also enhance its sensitivity toward surrounding medium. Refractive index sensing is a crude method to establish and estimate the strength of electric field enhancement by measuring the spectral shift in resonance wavelength per unit change of surrounding refractive index, $\Delta\lambda = \Delta n$.A few nanodisc arrays samples with 290 and 400 nm pitch were chosen. To reduce interferences from the glass substrate below and improve the signal quality, the spectrum is acquired in reflectance mode and collected through an Ocean-Optics 2000+ Fibre Optic Spectrometer (responsive from 200 – 1100 nm) with 5 mm spot size. Reflectance spectrum collected when the samples was in air (n = 1.003) and in ethanol (n = 1.3776) were compared and the red-shift in peaks are shown in Figure 5-11 below.

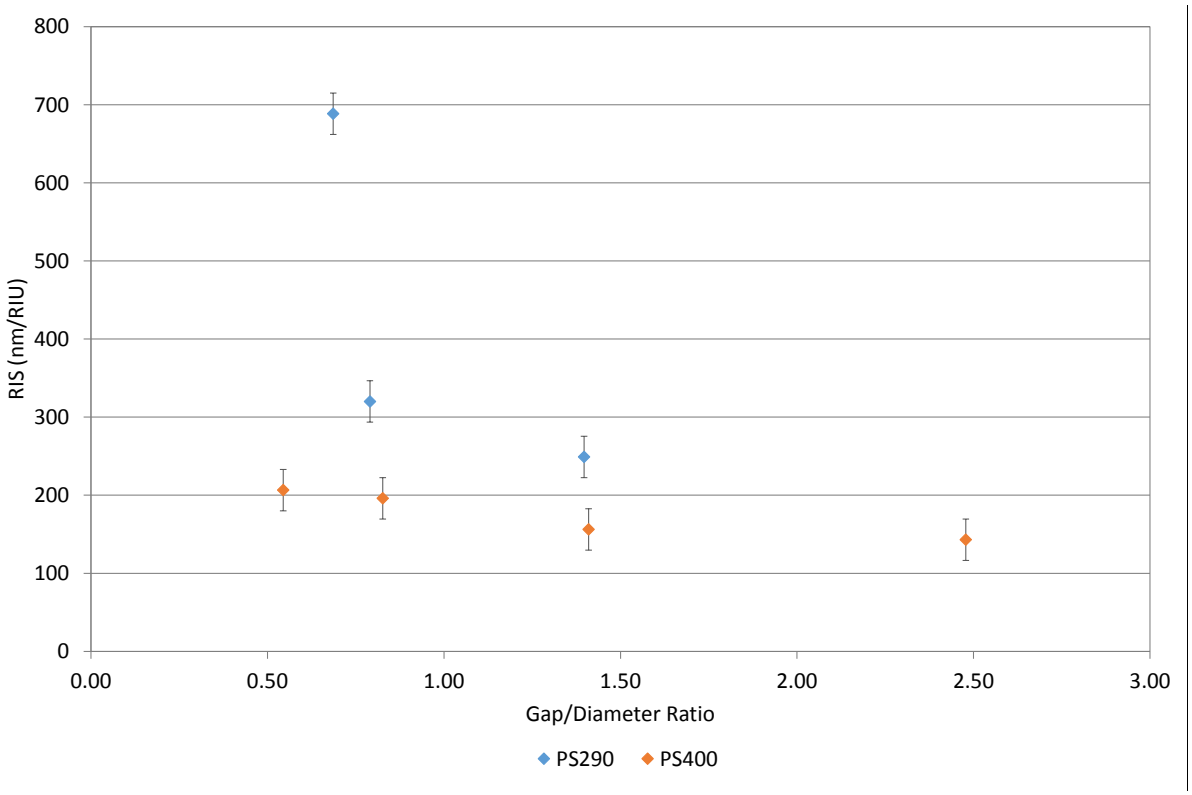

Figure 5-11 RIS of nanodisc arrays with 290 and 400 nm pitch sizes and different gap/diameter ratio. Effective medium approximation is not used in this set of data.

Although there may not have enough data point to fully establish and confirm the trend, the data shows some general idea of the strength of the plasmonic field generated. Nanodisc arrays with

290 nm pitch are found have consistently higher RIS sensitivity when compared to 400 nm pitch size. This suggests that smaller pitch size does indeed produce a stronger plasmonic mode. Also note that the for 290 nm pitch size, below gap/diameter ratio of 0.8, there is sudden increase of RIS, a further indication of presence of strong coupling mode exists.

5.2.4 *Summary*

A range of nanodisc arrays of different pitch distance and nanodisc diameters have been successfully fabricated. Large pitch sizes were found to have larger tunability range than smaller pitch sizes before strong interparticle coupling regime where the dipole resonance experience exponential red-shift. On the other hand, arrays with smaller pitch distance produce a stronger electric field enhancement for plasmon resonance at same wavelength.

5.2.5 *Future work*

Long exposure of PS to plasma results in significant cross-linked of PS onto the substrate surface, making them very difficult to remove and can influence on the location of the resonance peak due to higher refractive index (n_{PS}=1.59) than air. The inhomogeneous quantity of PS residues on each nanodisc also meant that the shift in the resonance peak is also inhomogeneous, leading to a broader peak. This may not be desirable for certain application, for instance in MEF, this translate to reduction in effectiveness in enhancing fluorophores as smaller number of disc matched with the spectrum of the fluorophores. On the bright side, the hot spot generated on the disc are most likely to be around the side wall, thus the effect of PS perhaps not that significant on prohibiting fluorophores from attaching at location of hot spot. Nevertheless, to remove the influence of PS residue, the use of Ni sacrificial layer was also incorporated into those nanodisc arrays fabrication process. It was found to be successful in removing the PS to large extends, although improvement and further testing are required. In addition, the diffusion of the sacrificial material into the main plasmonic nanostructure could also affect the plasmonic property of the structure.

Furthermore, nanodisc arrays with larger pitch distance were not close enough to locate the region where the strong interparticle coupling regime started to occur. Larger pitch which has larger tunability, and capacity to allow larger nanodisc would provide stronger electron density upon resonance mode. This can further give rise to even stronger plasmonic mode than allowed by smaller pitch arrays.

The strong coupling effect has been observed through optical properties of the nanostructures. However, the precise location and intensity of electric field hot spot have not been thoroughly investigated. Such information is also found to be lacking in currently available literature. A possible scenario of the electric field map generated when the nanodisc are highly coupled is illustrated in Figure 5-12. It is unlikely a single dipole can be generated on the nanodiscs and three pair of polarities are

likely to be the minimum requirement for generation of the plasmonic field. However, this is assuming that the nanodiscs are all of perfectly distanced from each other and no defects. In reality, nanodiscs fabricated are not identical and produce asymmetrical configuration, which can result in focusing of the electric in certain region. A computational model in combination with another high resolution technique such as EELS and SNOM would be required to confirm this.

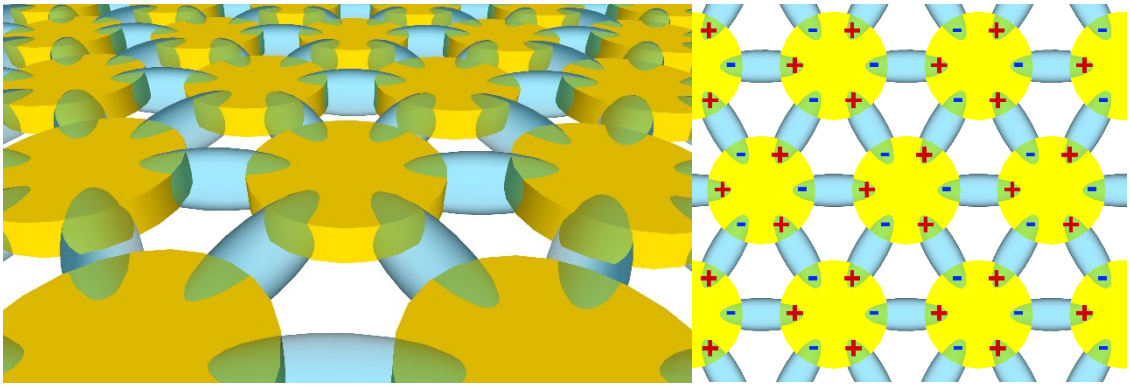

Figure 5-12 Illustration of a scenario upon the plasmon generated electric field (blue colour space) in nanodisc arrays when they are strongly coupled (left) and the polarity signs on each nanodisc (right).

Although the verticality of the side wall was assumed to be a guide to produce good plasmonic resonance effect across the arrays, the properties of truncated nanocones have not been investigated. It is possible that such structure could produce a stronger electric field enhancement due to asymmetrical cross-section than more symmetrical counterpart shown in this case. Provided with correct excitation polarisation and angle, the electrons could be displaced toward a smaller confined region in asymmetrical structure and thus produced a stronger electric field. A good structure that could be tested for high electric field enhancement due to asymmetrical structure could be those nanostructure fabricated without polishing technique or arrays with sharp tips such as nanopencils and nanofins. Such structure would be good initial experiments for future work.

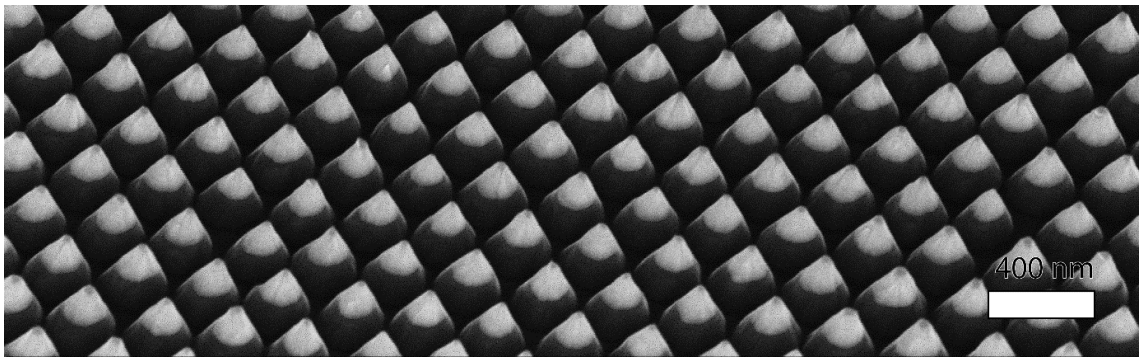

Figure 5-13 SEM image of an aligned nanopencils arrays oriented at a 23° away from the normal angle. Scale bar is 200 nm.

5.3 Nanohole-disc Arrays

To enable further plasmonic enhancement effect, researches are now extending from 2D area structures to more complex 3D architectures. This not only increases the available surface area for functional application but also increase the tunability parameter to achieve stronger plasmonic enhancement. One of such structures is a nanohole-disc coupled arrays, also sometime referred as D2PA (disc-coupled dots-on-pillar arrays) by Chou group[116]. As discussed earlier in chapter 2.4 and 3.2, the idea is to combine the advantages of both the SPP mode and LSPR mode, multiply their plasmonic effects and give rise to an enhancement effect that could not be easily achieved by each type of plasmonic effect alone. In this work, the SPP is generated by nanohole arrays while LSPR is generated by nanodisc arrays, resulting in much stronger plasmonic effects.

The process workflow to produce nanohole and nanohole-disc arrays is illustrated in Figure 4-6. Note that given the flexibility of the process, it is possible to have the nanodisc and nanohole in the structure to have different thickness and even different materials. For instance, using the process flow for fabricating nanodisc arrays of metal A say with thickness X, the milling process can be extended so that it etch deeper into the substrate with depth Y. Before removal of the PS mask, another layer of different metal B can be evaporated on this substrate to produce a nanohole arrays provided this metal thickness Z is less than the depth Y. Finally when the PS mask is removed, a nanohole-disc arrays with nanodisc of metal A thickness X and nanohole of metal B thickness Z are produced. This would be a very fascinating type of plasmonic nanostructures to study by investing the effect arise from LSPR-SPP coupling of different materials and the coupling effect itself can be fine tuned by changing the individual layer thickness. However, due to the limitation of time and resources, this is beyond the scope of this project.

Instead, this section will first show that the extraordinary optical transmission which arise from SPP mode can be achieved by the nanohole arrays fabricated through NSL technique. This is then follow by demonstration of the ability of NSL combined with the new found techniques (i.e. the sacrificial layer and the polishing technique) to produce a wide range of interesting nanohole-disc arrays with different pitch and size.

5.3.1 *Nanohole Arrays*

Hexagonal nanohole arrays can be produced by using NSL. The process is similar to fabrication of nanodisc arrays except no argon milling process is required and the metal is only deposited after the PS size has been reduced, which also determines the diameter of the nanoholes. Figure 5-14 shows 35 nm thick Ag and 50 nm thick gold nanohole arrays with different nanohole diameters fabricated. Their associated transmission spectrum is shown in Figure 5-15.

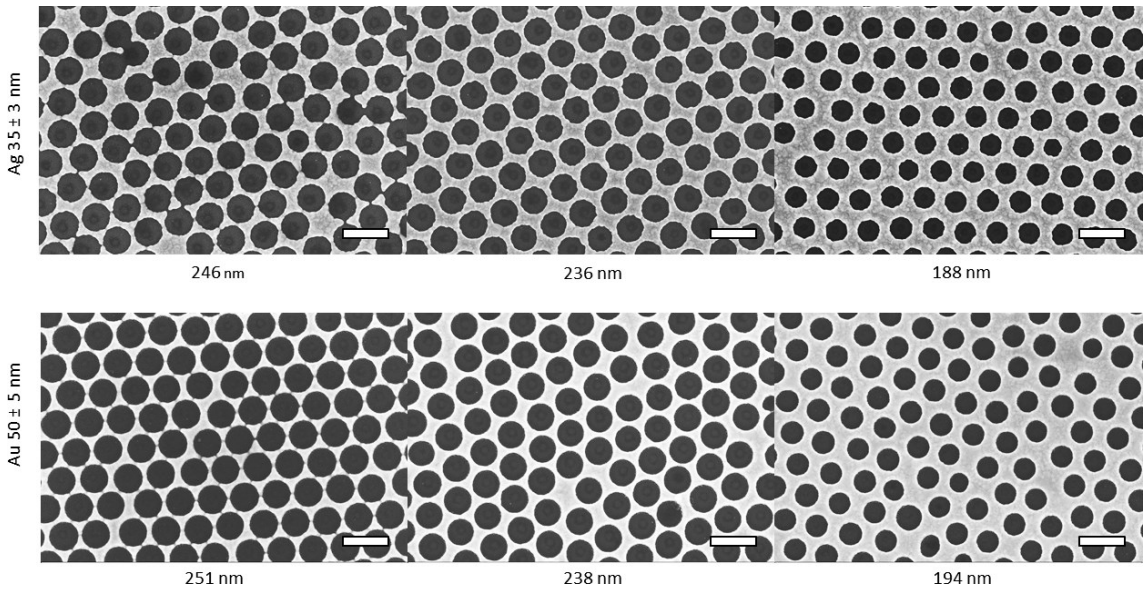

Figure 5-14 SEM images of different hexagonal nanohole arrays fabricated by using NSL as template. (Scale bar: 400 nm).

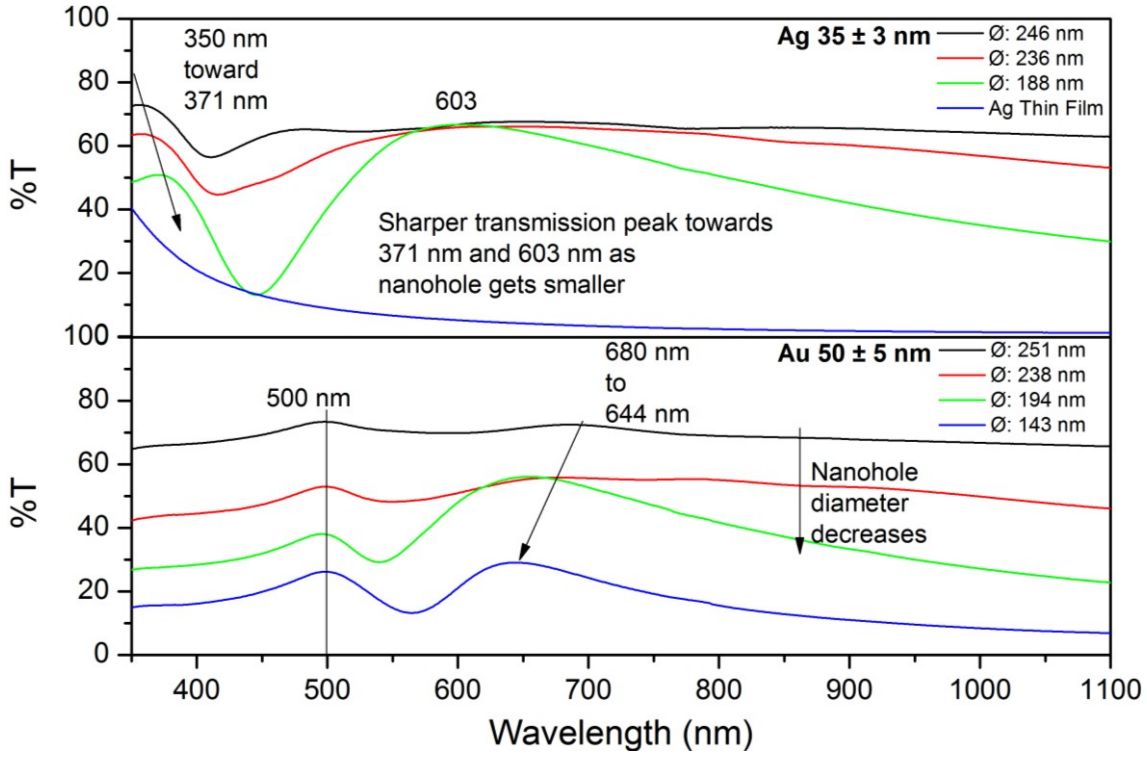

Figure 5-15 Extraordinary optical transmission spectrum exhibited by 35 ± 3 nm Ag (top) and 50 ± 5 nm Au (bottom) with 290 nm pitch size but different hole diameters.

Optically, it can be seen that the type of materials, metal thickness, and nanohole diameter influenced the location of EOT. It can also be seen from the both spectrum that as the nanohole diameter decreases, the percentage transmission also reduced as expected as on average there are less light that can penetrates through the metal film. However, the transmission at the EOT wavelength also becomes more apparent when compare against the transmission baseline. The decrease in hole diameter led to shorter EOT wavelength is also consistent with result obtained by Martin-Moreno *et.al* [249] For gold

samples, the peak around 500 nm is due to interband transition and Wood anomaly has been suggested to be the reason behind the reduction in transmission between the peaks[250]. Equation 2-15 and 2-16 can also be used shows the effect of material dielectric function and the periodicity of the hole determine the peak location. Work published by Li *et al.*.[251] also showed that the thicker metal blue shift the transmission peak, similar to the LSPR case.

However, unlike nanohole arrays, fabrication of nanohole-disc arrays requires a very different process. The optical properties of nanohole and nanodisc arrays are not a simple case of addition and subtraction, because the existing of the plasmonic mode of one influences the other[252]. A precise control of the spacing between the nanodisc and nanoholes are also required to promote strong coupling resonance mode[117]. Next section, fabrication of this complex nanohole-disc array is introduced and their optical properties are also discussed.

5.3.2 *Nanohole-disc Arrays*

Fabrication of nanohole-disc arrays requires an extremely well controlled process. A successful nanohole-disc arrays require very stringent process control to enable a usable high quality structure. Etched depth, metal thickness, sidewall profile, and evaporation angle are all very important in ensuring the successfulness of the nanostructure for optimum result. Here, a novel approach of fabricating high quality nanohole-disc arrays has been developed by combining two newly developed techniques described in chapter 4.5 and 4.6 which found to be absolutely critical to ensure this structure is usable. Polishing technique in milling process to etch into substrate to ensure a good vertical sidewall, an essential requirement to ascertain the metal nanodiscs are isolated from the nanohole arrays below in order to produce both LSPR and SPP effect. A Ni sacrificial layer was added between the substrate and PS mask to produce a clean patterned substrate free from PS residue which would otherwise affect the shape of the nanodisc and complicate the plasmonic effect. Figure 5-16 shows an examples of Si substrate patterned for nanohole disc arrays experiments before metal evaporation. The top of the nanodisc surfaces are smooth and free of PS.

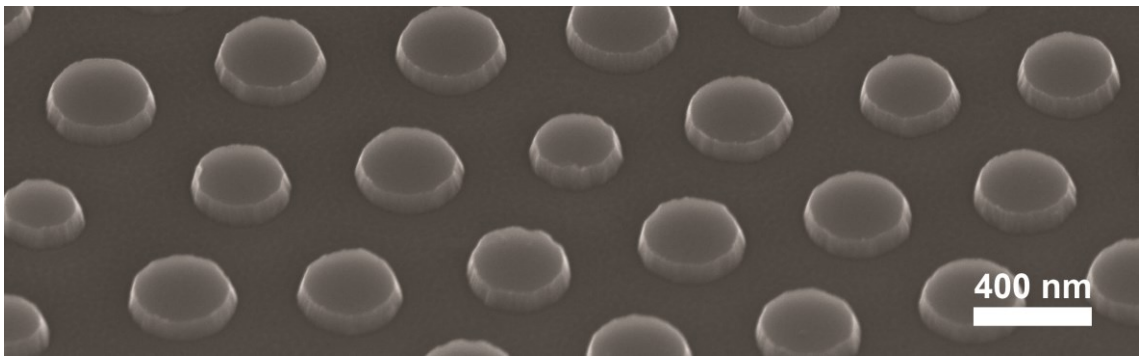

Figure 5-16 SEM image of a patterned silicon substrates with 620 nm pitch size and 40 nm depth. Scale bar: 400 nm.

Metal are then deposited on top of those patterned substrates (in this case silicon and glass) to produce metal nanohole-disc arrays. Figure 5-17 shows a range of arrays produced for different pitch sizes and different nanodisc diameter, showcasing the flexibility and tunability of aforementioned developed technique. A close inspection on the figure shows a gap remained between the nanodisc and nanohole, a crucial requirement for this project. In addition, there are also some small nanoparticles visible inside the gap which Chou group had suggested those small nanoparticles also play an important by enhance and focus the electric field at this region[116]. The milled depth was set to be around 40 nm as this is almost the maximum achievable depth for PS mask with less than 400 nm diameter to undergo all the necessary processing steps. Any further etching results in poor vertical sidewall of the nanodisc and therefore cannot produce a good nanohole-disc array structure. To provide a gap between the nanodisc and nanohole, 30 nm of gold was deposited on the patterned substrate to produce a distance of approximately 10 nm between the two structures. An optimised distance between the nanodisc and nanohole, and their thickness have yet to be determined but this value is chosen because it has been suggested by Wen *et al*. that a 10 nm separation is the optimum distance for the LSPR and SPP coupling to occur[117]. Further distance will result in weaker LSPR-SPP coupling while a shorter distance may increase the coupling strength, the hot spots region can be reduced and the nanodisc and nanohole is likely to connect together. More importantly, the optical characteristic of those fabricated nanohole-disc arrays with 30 nm thick Au layers produced plasmonic resonance within the NIR-I and NIR-II ranges, making them excellent structures suitable for the aim of this project, which is to investigate and develop a highly efficient biosensing platform based on MEF in NIR wavelengths.

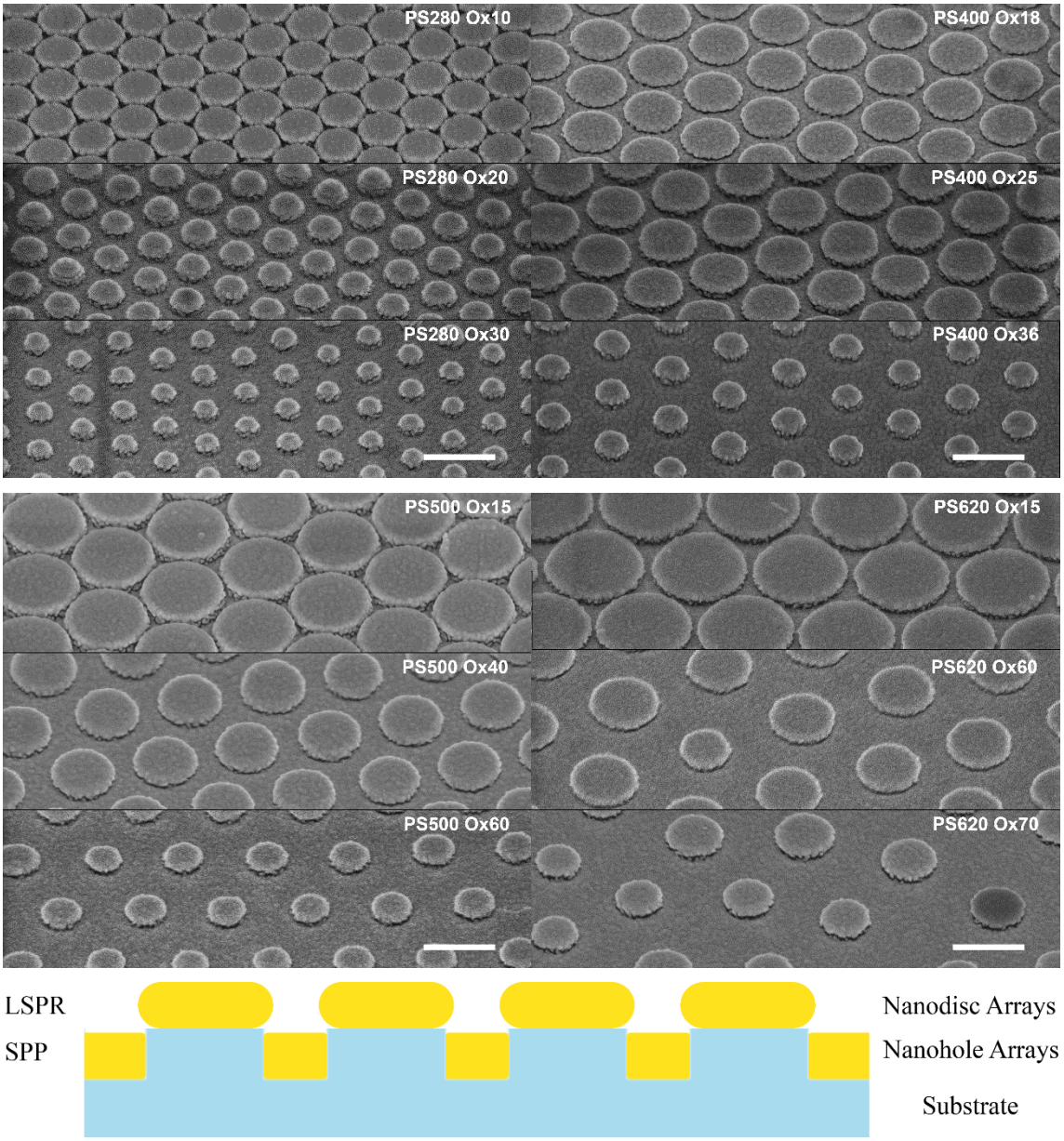

Figure 5-17 SEM images of 30 nm nanohole-disc arrays of different pitch sizes and nanodisc diameters. Scale bar: 400 nm. A schematic illustration of nanohole-disc arrays cross-section is also included.

The extinction spectra of those arrays were measured using a newly acquired Cary 5000 system, which allows measurement from 180 nm to 2500 nm. All the extinction peaks are found to be very broad and fall within in NIR region, suggesting they may be good candidates for NIR biosensing application. Such broad spectrum are also to be expected for highly coupled plasmonic structures. Figure 5-18 is the compilation of extinction spectrum of those samples. The high extinction value at long wavelength is a characteristic of bulk gold absorption, which exists for nanohole arrays itself such as those in Figure 5-15. Interestingly, the occurrence of this trend is apparent when the nanodisc diameter is small compare to the pitch size. The origin of this phenomenon remains unclear and requires further simulation and experiments.

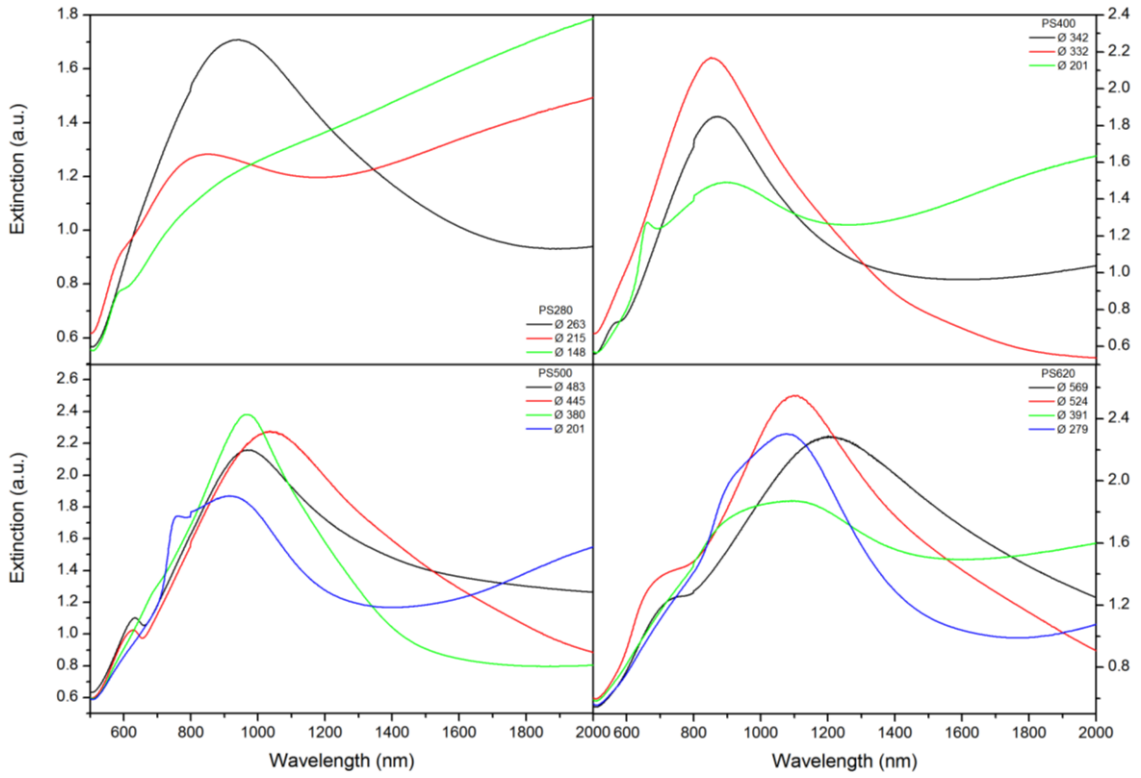

Figure 5-18 Extinction spectrum for 30 nm thick Au nanohole-disc arrays with 210 nm (top left), 400 nm, (top right), 500 nm (bottom left) and 620 nm (bottom right) pitch and various nanodisc diameters.

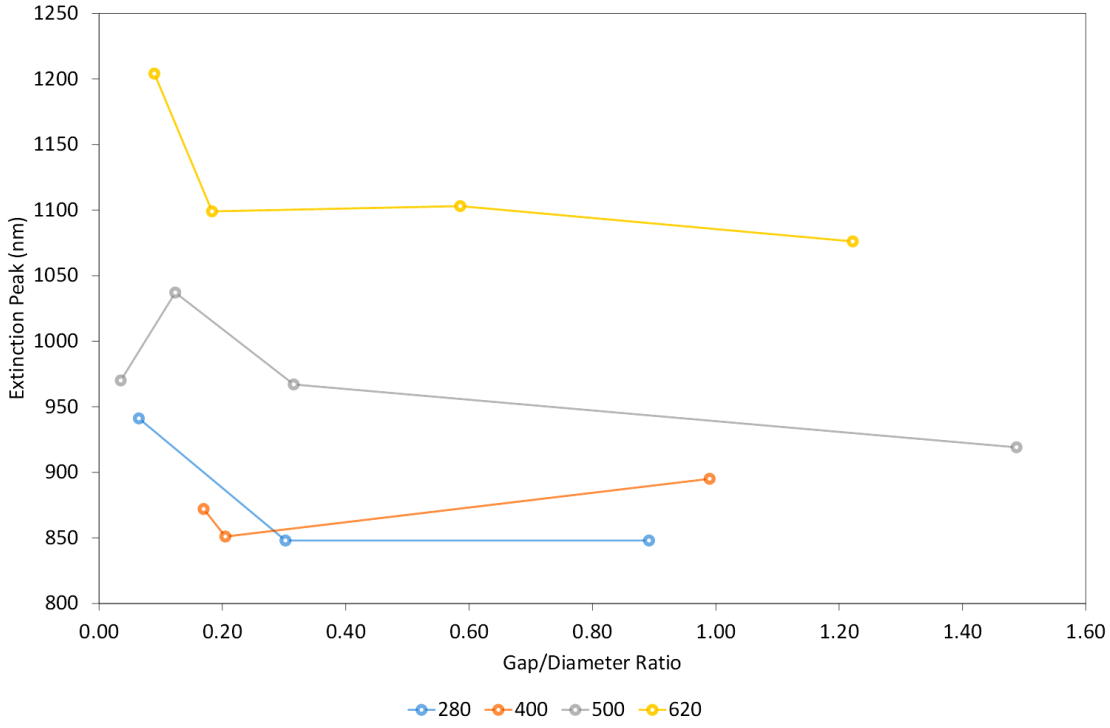

Figure 5-19 Extinction peak of the nanohole disc arrays with respect to nanodisc diameter.

The wavelength of the extinction peaks with respect to gap-to-diameter ratio are also summarised in Figure 5-19. It occurs that although the peak does suggests an exponential increases for

620 nm size pitch, it remains hard to establish for all other data as they are very scattered and does not represent a clear indication of a trend. The inconsistency in the trend of the data could be due to (1) intrinsic complex behaviour of the coupled mode, (2) the extinction peaks in the spectrum are extremely broad, hence the peak location measured directly from the spectrum are the not true location of the plasmonic peak but rather a combination of multiple plasmon excitation mode together. Together with the background absorption of the bulk gold, it becomes hard to distinguish the exact location of the plasmonic peaks. Although what is clear is that larger pitch size does tend to exhibit extinction peak at longer wavelength, a similar characteristic shared by nanodisc arrays.

5.3.3 *Summary*

Nanohole-disc arrays have been successfully fabricated and their resonance peaks are found to fall within the NIR region which may be suitable for NIR biosensing. However, the optical properties of those arrays do not appear to provide a clear indication of a trend and would require further analysis to understand the phenomena better. Nevertheless, these structures are known to exhibit very strong plasmonic resonance and tremendous electric field enhancement. A selected few samples are chosen for MEF experiments and their results are shown in the next chapter.

Additionally, a great benefit of this patterned substrate lies on its reusability. The metal deposited on the patterned substrate can be removed. The patterned dielectric substrate after removing the metal are thus reusable for different type of metals. For instance Au can be removed by aqua regia acid leaving behind patterned surface for other metals such as Ag, Al, or even combination of different materials. This would allow a more repeatable testing of structures and characterise effects of nanodisc arrays from different materials.

5.3.4 *Future Work for Nanodisc-hole Arrays*

The optimum distance between the nanodisc and nanohole has yet to be fully investigated, and could be further explored to locate the optimum thickness for different materials. In addition, the fabrication roadmap allows the control of nanohole and nanodisc thicknesses independently, allowing additional degree of control on the plasmonic generation.

Although a fabrication method to produce nanohole-disc arrays has been established, the observed optical properties remain not understood. As mentioned earlier, it has been suggested that the coupling effect between LSPR and SPP are not commutative. It would be interesting to fabricate structure of individual components, i.e. nanohole arrays only, nanodisc only, and compare their results with nanohole-disc arrays for some experimental indication of their coupling behaviour. Furthermore, the sample could also be subjected to RIS testing to gives some indication of the strength of the electric field generated.

5.4 Chapter Conclusion

In this chapter, the geometry and optical properties of three main plasmonic structures are shown. All of them share the following characteristic: highly tuneable structures, plasmon resonance are extremely sensitive to the geometrical factors, and interparticle coupling produce a broad and red-shifted resonance peak. Such versatility makes those structures highly attractive for many applications such as light management, and energy extraction. In the next chapter, the ability of those structures in MEF were tested and discussed.

Chapter 6

Metal Enhanced Fluorescence (MEF)

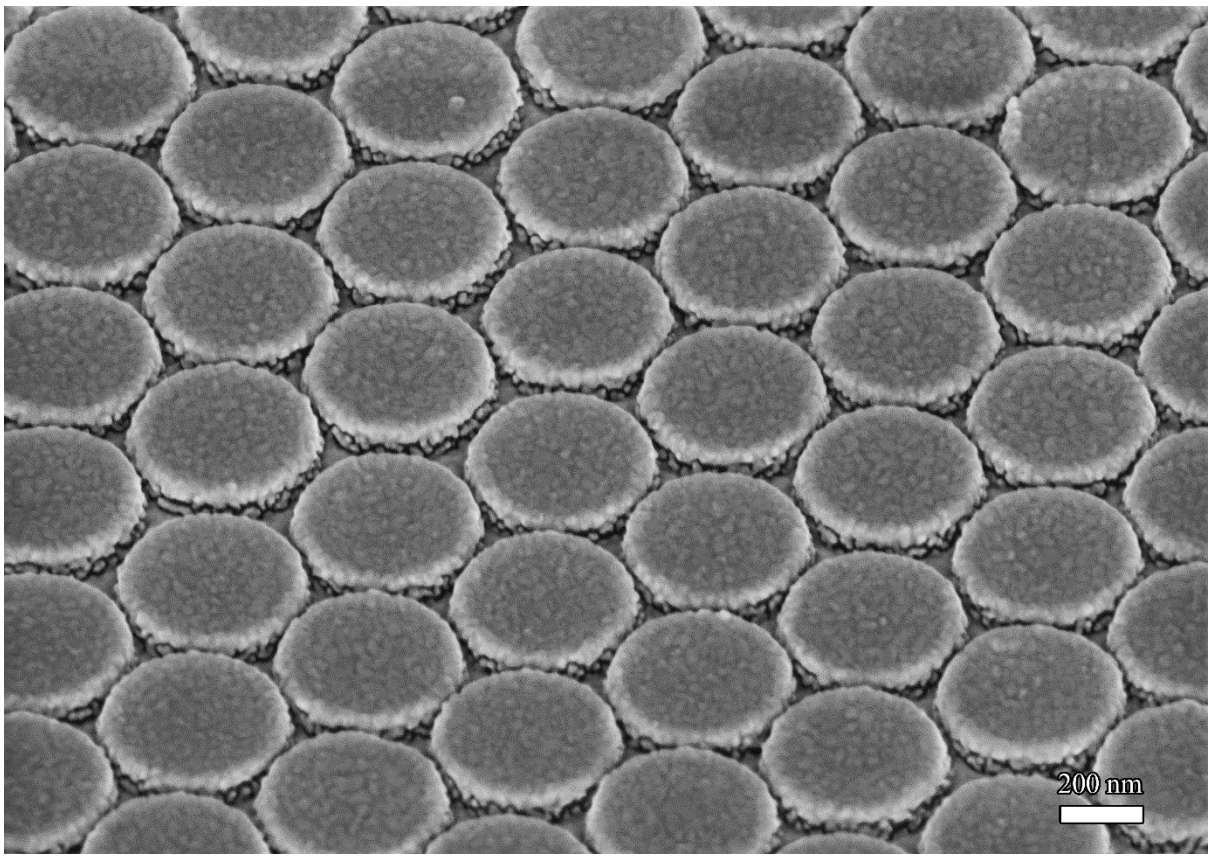

Figure 6 Nanohole-disc arrays with 500 nm pitch distance and 483 nm disc diameter fabricated with modified nanosphere lithography.

Chapter 6 Metal Enhanced Fluorescence (MEF)

The fluorescence emission of fluorophores can be enhanced by attaching them onto materials that exhibit plasmon resonance, commonly known as metal enhanced fluorescence (MEF). The strength of the MEF depends mainly on spectra overlapping of the excitation and emission of the fluorophores to the plasmon resonance wavelength of the metal, location of hot spots, and the metal-fluorophore distance. This chapter aims to focus on the enhancement factors of MEF from three types of nanostructures: nanotriangular arrays, nanodisc arrays, and nanohole-disc arrays. The calculations of fluorescence enhancement factor and lifetime are first introduced before discussing MEF from each structure in details.

6.1 Calculations of Fluorescence Enhancement and Lifetime

Alexa Fluorophores conjugated with streptavidin are chosen as the fluorophores and biotinylated Bovine Serum Albumin (bBSA) as the protein binder for this project (more details in chapter 4.7). The fluorescence emission is detected by using a Fluorolog® Tau 3 system from Horiba Jobin Yvon with a 450 W Xe lamp source. The light emission from samples are collected reflection mode with 20° offset from the excitation light source. The substrate holder allows a range of excitation on the solid-state samples to be measured (25° to 60° relative to the normal of the plane). For accuracy and consistency purpose, the angle of acquisition was set at 30° unless stated otherwise.

For quantitative analysis and comparison, the fluorescence enhancement is typically corrected to adjust the difference in number of fluorophores attached onto the patterned surface and bare glass. Mathematically, it is defined by the following equation[150]:

$$E_F = \left[\frac{I_{AF,PA} - I_{bBSA,PA}}{I_{AF,glass} - I_{bBSA,glass}}\right]\frac{A_{AF,glass}}{A_{AF,PA}} \qquad \textit{Equation 6-1}$$

where I is the fluorescence intensity, A is the surface area available for fluorophore attachment, and the first and second parameters of the subscript represents the stage of the fluorophore-protein conjugation stage and the type of plasmonic arrays (PA) substrate respectively. For instance, $I_{AF,NDA}$ is the fluorescence intensity of bBSA-AF on nanodisc arrays substrate, and $I_{bBSA,glass}$ is the fluorescence intensity of the bBSA on glass substrate. The area ratio term outside the square bracket is needed to account for the changes in amount of fluorophores attached due to increased surface area available for attachment when a plasmonic substrate is used. Alternatively, if a reference control bBSA on plasmonic arrays substrate were used, Equation 6-1 may be re-written as:

$$E_F = \left[\frac{I_{AF,PA} \frac{A_{AF,glass}}{A_{AF,PA}} - I_{bBSA,glass}}{I_{AF,glass} - I_{bBSA,glass}} \right] \qquad \textit{Equation 6-2}$$

For nanotriangular arrays, the fluorescence enhancement factor is calculated using Equation 6-1, whereas Equation 6-2 was used for nanodisc arrays and nanohole-disc arrays. Note that although the area correction factors allow better comparison for fluorescence emission enhancement per fluorophore, the uncorrected fluorescence emission is also relevant for practical applications where signal is measured per acquisition area regardless of number of fluorophores.

Lifetime measurements were carried out by the same method published previously[150]. In brief, time-correlated single photon counting (TCSPC) technique[155] with PicoQuant FluoTime200 spectrometer equipped with a TimeHarp300 TCSPC board and a Hamamatsu photomultiplier (PMA-185). The excitation source was a picosecond pulsed diode laser driven by a PDL800-D driver. The specific laser used depends on the type of fluorophores attached. For instance, AF 700 and AF 750, were excited using 670 nm laser (LDH-P-670B) and AF790 was excited using 730 nm laser (LDH730). The emission was collected at right angles to the excitation laser beam. The emission arm was fitted with a long pass filter to remove the IRF signal. The full width at half maximum (FWHM) of the system's instrument response function (IRF) was 350 ps. The fluorescence decay curves were analysed using the FluoFit software (PicoQuant, version 4.2.1) based on a multi-exponential model which involves an iterative reconvolution process. The quality of the fits was assessed by the value of the reduced χ^2 value and a visual inspection of the distribution of the weighted residuals and their autocorrelation function[253].

The fluorescence lifetime results in this project were calculated based on a widely accepted semi-empirical method[175,242]. Fluorescence lifetime decay can be modelled with a single exponential (SE) term or multiple exponential (ME) terms. A SE model is appropriate for a single fluorophore in a homogeneous environment, while an ME model described contribution of more than one type of fluorophores into their constituent fractional component. In this case, the fluorophores, which are attached to different locations where they experienced the electric field enhancement differently, are best modelled with ME terms to avoid interpreting the data incorrectly. Mathematically, intensity decay as a function of time, $I(t)$, due to multiple fluorophores components is defined as:

$$I(t) = a_1 e^{-t/t_1} + a_1 e^{-t/t_1} + a_2 e^{-t/t_2} + \ \ldots \qquad \textit{Equation 6-3}$$

where a_i and t_i are the weighted fractional component and characteristic lifetime of the associated fluorophore type i. With the reduced fluorescence lifetime known, it becomes possible to estimate the emission enhancement and excitation enhancement by using equation 3-7 and 3-8.

6.2 Nanotriangular arrays

When plasmonic particles are nearby to each other, it is known that the electric field enhancement would be increased. Similarly, the electric field around the tip is also expected to increase when nanotriangles are closer to each other. Such increased electric field should be able to be experienced by the attached fluorophores and increased fluorescence emission. Nanotriangular arrays of same periodicity but with shorter tip-to-tip distance were constructed and their capabilities in MEF were compared.

6.2.1 *Fluorescence Enhancement by Nanotriangular arrays*

Normalised extinction of a selection of nanotriangles arrays fabricated using 300, 500, and 620 nm sized PS are shown in Figure 6-1. Also included in the spectrum are the excitation and emission spectra of the fluorophore used. It is well known that spectral overlapping is a key criteria for MEF. To satisfy this condition, fluorophores are chosen according to their spectral overlapping with the extinction profile of the nanotriangular arrays. In addition, the selected fluorophores are also chosen to have peaks slight to the longer wavelength of the resonance peak to improve emission efficiency. As such, AF488, AF680, and AF750 are chosen for maximum overlapping with 75 nm thick pristine nanotriangular arrays fabricated with 300 (a), 500 (b), and 620 nm (c) PS size mask respectively. To aid differentiating the samples in the data, the following labelling system is used. PS(size)-(oxygen plasma duration)s. For example, PS500-0s implies nanotriangular arrays fabricated with 500 nm size PS and no oxygen plasma process involved.

In (Figure 6-1 d) are normalised extinction of nanotriangular arrays fabricated with PS exposed to 15 s of oxygen plasma treatment to form nanotriangle with closer tip-to-tip distance for all three PS sizes. Note that in this case, instead of using a fluorophore that match the extinction of each closely spaced nanotriangular arrays individually, a NIR I fluorophore - AF790 is used for all three different samples. The idea is to allow two main hypothesises to be tested simultaneously: (1) AF790 spectrum has maximum overlap with PS500-15s, allowing a comparison of MEF strength directly with PS500-0s due to closer tip-to-tip distance. (2) AF790 spectrum are situated further into the red wavelength for PS300-15s and shorter into the blue wavelength for PS620-15s. Comparing the MEF results from those three samples will demonstrate the importance of the spectral overlapping at the right position in the extinction spectrum.

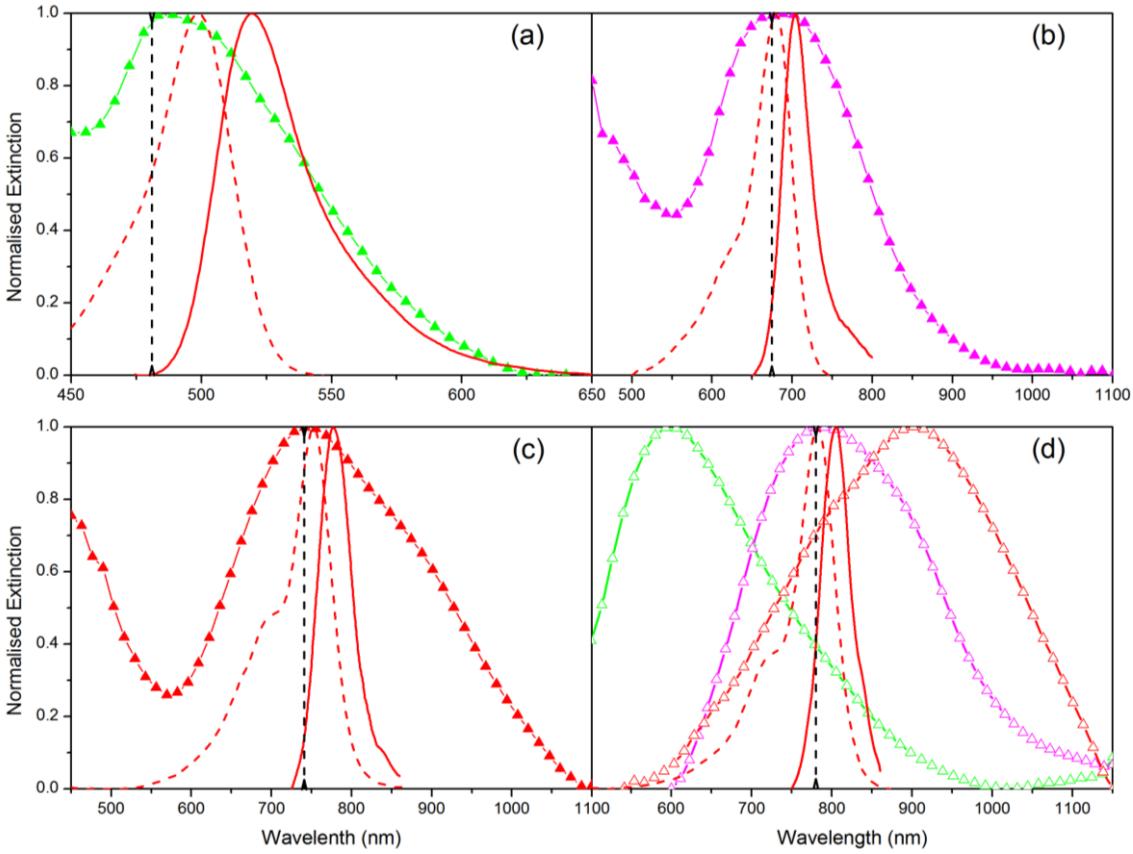

Figure 6-1 Normalized extinction and emission spectra (red dotted and solid line traces, respectively) of Alexa Fluor dyes overlapping with corresponding LSPRs of the set of the samples without oxygen plasma etching: (a) AF488-SA with LSPR of PS300 without etching (green); (b) AF680-SA with LSPR of PS500 without etching (violet); (c) AF750-SA with LSPR of PS620 without etching (red). (d) AF790-SA with LSPRs of Ag triangular arrays from PS300 (green), PS500 (violet), and PS620 (red) templates after 15 second oxygen plasma etching, respectively. The excitation wavelength is indicated by the black dotted line. [150] *(Reprinted from ref 150 with permission from Springer.)*

Figure 6-2 shows the corresponding averaged fluorescence emission intensity measured from attached fluorophores on those samples at three different locations. The emission spectrum closely resemble their well-established shape of Alexa Fluor dyes bounded to proteins. Their enhancement factors are calculated by comparing the emission intensity and corrected for the difference in surface area according to Equation 6-1. The values obtained for all samples together are summarised in Table 6-1. The unmodified quantum yield for the attached fluorophores, and the ratio of tip-to-tip gap to nanotriangle perpendicular bisector length are also included in the table to help interpreting the result.

For all three pristine nanotriangular arrays, the emission intensities have been enhanced with PS620-0s having the highest enhancement factor of 10. Although PS300-0s has the lowest gap to size ratio of 1.10 which suggest highest interparticle coupling among these three pristine nanotriangular arrays, no significant higher enhancement is observed. It could be that such gap to size ratio is insufficient to cause dramatic increase in plasmonic coupling. Another probable explanation is likely due to already very high unmodified quantum yield of AF488 (Q_0= 0.92), making it difficult to significantly further enhanced by the LSPR. Such result is also in agreement with previously reported

result[242]. As such, the enhancement factor is found to be highest for PS620-0s instead which the AF750 fluorophore only has an unmodified quantum yield of 0.12. For PS500-0s, the AF680 fluorophore has a medium range quantum yield while lower interparticle coupling than PS300-0s, results in lowest quantum yield obtained.

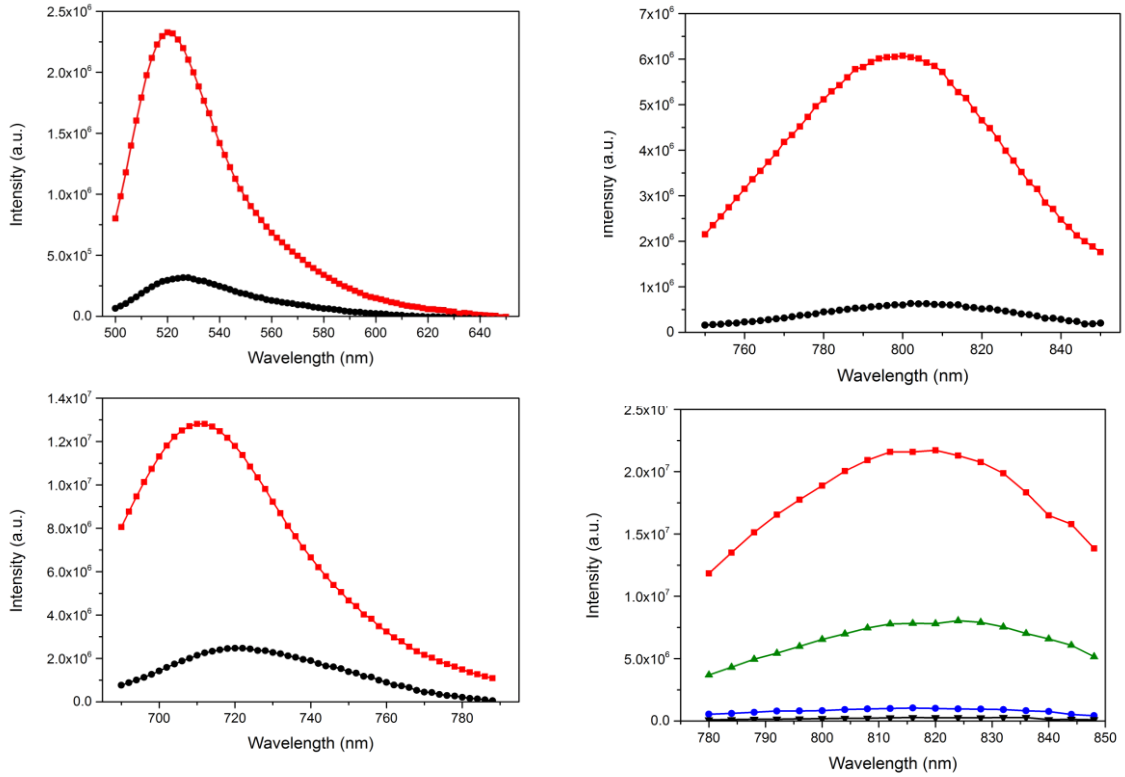

Figure 6-2 Fluorescence spectra of (a) Alexa Fluor 488 monolayer on sample PS300-0s (red) and on glass surface (black), (b) Alexa Fluor 680 monolayer on sample PS500-0s (red) and on glass surface (black), (c) Alexa Fluor 750 monolayer on sample PS620-0s (red) and on glass surface (black), (d) Alexa Fluor 790 monolayer on sample PS300-15s (blue), PS500-15s (red), and PS620-15s (green) as well as on glass as control (black), respectively. [150] *(Reprinted from ref 150 with permission from Springer.)*

Due to the effect arise from closer tip-to-tip distance and partially due to the low quantum yield of AF790, the fluorescence enhancement observed on the closely spaced nanotriangular arrays PS500-15s is dramatically higher (83 times enhanced). In MEF, there are two main enhancement routes: (1) excitation enhancement which depends on the electric field strength around the fluorophores and (2) emission enhancement which due to coupling of the fluorophore to the plasmonic system, results in increased quantum yield and reduced in lifetime. In this case, the short distance of the metal nanotriangles intensified the electric field at the shortest distance between the nanotriangles. The shortest distance also appeared to locate the tip of the nanotriangle, the high curvature of this tip also helps increased the electric field. A combination of optimum condition from both of excitation and enhancement contributed to the high enhancement factor for PS500-15s.

Figure 6-3 shows the simulated electric field at the excitation wavelength for all three closely spaced nanotriangular arrays. From the simulated data, it shows that the electric field enhancement

generated for PS500-15s is 10 or greater when compared with the other two cases. Furthermore, the simulated electric field shows that the enhancement is not only limited to the gap between the tips but also extended onto the sides of the nanotriangle. This allows higher number of fluorophores to benefit from the electric field enhancement. Whereas for PS300-15s and PS620-15s, although they also have a similar ratio of gap to size distance, but due to excitation at wavelength away from the resonance peak wavelength, the electric field enhancement reduced and confined only to the gap between the tips. Hence, very limited fluorescence enhancement is experienced by these two samples.

Table 6-1 Average experimentally measured fluorescence enhancement factors of streptavidin conjugated Alexa Fluor dyes for the samples of PS300, PS500, and PS620 temples, with and without oxygen plasma etching. [150] (Reprinted from ref 150 with permission from Springer.)

Sample	PS300-0s / AF488-SA	PS500-0s / AF680-SA	PS620-0s / AF750-SA	PS300-15s / AF790-SA	PS500-15s/ AF790-SA	PS620-15s/ AF790-SA
Unmodified quantum yield of the attached fluorophores, Q_0	0.92	0.36	0.12	0.1	0.1	0.1
Ratio of Tip distance to perpendicular length, a/s	1.10	1.36	1.59	0.36	0.30	0.35
Fluorescence Enhancement, E_f	7.8	5.7	10	5.5	83	33.8

[a]Data were corrected for variations in streptavidin–dye conjugation surface coverage for different samples.

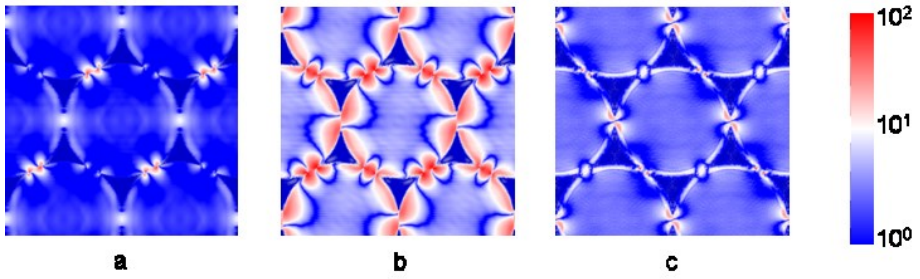

Figure 6-3 Plots of relative electric field enhancement around the metal nanoparticles at 780 nm excitation wavelength, for three templates (a) PS300 (b) PS500 (c) PS620 with 15s etching. [150] (Reprinted from ref 150 with permission from Springer.)

6.2.2 *Fluorophores lifetime reduction due to silver nanotriangular arrays.*

To ascertain that the observed fluorescence enhancement arise from coupling with the LSPR effect of the Ag nanostructures, fluorescence lifetime of those closely spaced nanotriangular arrays were measured. The results provide insights into fluorescence decay rates and deconvolute total fluorescence enhancement into excitation and emission enhancement components. Figure 6-4 depicts the fluorescence lifetime decay spectra of AF790 monolayer on all closely spaced nanotriangular arrays. Also included is an AF790 monolayer on glass as reference and the lifetime on bare glass.

In this experiment, it is found that the fluorescence decay curves can be fitted satisfactory with two exponential terms. This can be seen from the reduced χ^2 value obtained by fitting calculated values

to experimentally obtained parameters by a nonlinear least-square deconvolution method. For AF790 on bare glass, lifetime was measured to be 550 ps. In comparison, fluorescence lifetime for AF790 on PS300-15s, PS500-15s, and PS620-15s were reduced considerably to 238-, 113-, and 177 ps respectively (see Table 6-2). As expected from the fluorescence emission results, the lifetime for the AF790 is shortest when attached onto PS500-15s, follow by PS620-15s and PS300-15s.

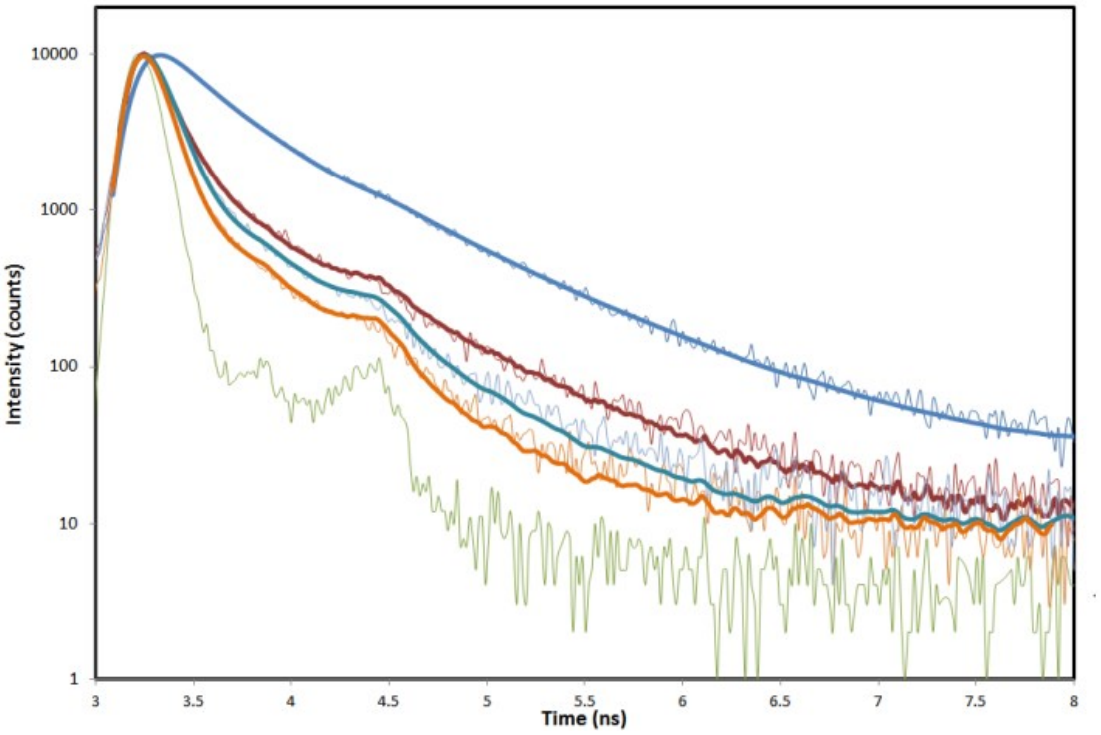

Figure 6-4 Time domain fluorescence decay of AF790-SA monolayer on (a) glass (τ~550 ps), (b) on PS300 template with 15 sec oxygen plasma etching (τ~238 ps), (c) on PS500 template with 15 sec oxygen plasma etching (τ~113 ps), (d) on PS620 template with 15 sec oxygen plasma etching (τ~177 ps). (Reprinted from ref 150 with permission from Springer.)

Table 6-2 Multiexponential analysis of intensity decay of AF790-SA monolayer on glass surface and metallic surface, showing weighting fraction (a_1, a_2), observed lifetime (τ_1, τ_2, ps), intensity weighted lifetime ($<\tau>$, ps), and goodness of fit parameter (x^2_R). [150] (Reprinted from ref 150 with permission from Springer.)

SAMPLE	A_1	A_2	τ_1 (PS)	τ_2 (PS)	τ (PS)	X^2_R
AF790-SA ON GLASS	46.3%	53.7%	264	722	510	1.40
AF790-SA ON PS300-15S	93.3%	6.7%	84	560	238	1.75
AF790-SA ON PS500-15S	96.8%	3.2%	51	374	113	1.70
AF790-SA ON PS620-15S	94.5%	5.5%	77	464	177	1.72

Knowing the reduce lifetime due to LSPR effect, the emission and excitation enhancement can be estimated by assuming the intrinsic radiative and non-radiative decay (Γ_0, k_{nr}) remains unaffected by MEF. Note that this may not be true as the quantum states of the fluorophores is likely to be

perturbed when coupled to the plasmon to achieve MEF. Biagioni *et al.* also suggested that k_{nr} actually increases in MEF although an experimental confirmation has yet to be achieved[254]. Nevertheless, this assumption and estimation provide a figure of merit comparison for the enhancement in excitation and emission achieved through the plasmonic system. Table 6-3 below shows the estimated value for each samples based on this approach. The calculated averaged enhancement values suggests a highest electric field exists for PS500-15s, consistent with the simulated electric field map. The emission enhancement factors also indicates that all samples also coupled with the LSPR of generated by the nanotriangular arrays. Also included in the table is calculated modified quantum yield which showed that a staggering quantum yield of 72.3 % was achieved by PS500-15s structures.

Table 6-3 Estimated values of the excitation enhancement and emission enhancement for each sample. [150] (Reprinted from ref 150 with permission from Springer.)

SAMPLE	E_F	E_{EM}	E_{EX}	Q_M
PS300-15S	5.5	2.1	2.6	21.0%
PS500 -15S	83.0	7.2	11.5	72.3%
PS620-15S	33.8	5.2	6.5	52%

6.2.3 *Summary*

The results above demonstrated that is it possible to use Ag nanotriangle nanostructures produced by NSL to produced significant MEF results. An enhancement factor of 83 times was obtained on NIR-I dyes AF790. This was achieved through correctly matching the spectrum of fluorophores to the extinction spectrum of the nanostructures. The results from the fluorescence intensity, lifetime, and simulated electric field are all consistently supporting the achieved phenomena is indeed due to MEF.

6.3 Nanodisc Arrays

Gold nanodisc arrays produced by using NSL come with a few advantages. The nanodisc diameter and the pitch size can be adjusted independently, allowing a closer examination of the effect of interparticle coupling in MEF mechanism while maximising the best possible enhancement. The arrangement of the nanodisc in hexagonal arrays also meant the excitation of LSPR mode is independent from the polarisation direction of the light source[103], making it an attractive structure for normal unpolarised light source found in many optical apparatus.

In this work, the gold nanodisc arrays have been tuned to achieve LSPR peak around 750 nm in order to match the excitation and emission spectra of the NIR fluorophore - AF750. Another benefit of having hexagonal arrays is that it does not depend on the polarisation of the excitation beam. SEM images of those nanodisc arrays with periodicity of 290-, 400-, and 500 nm are presented in Figure 6-5.

Similar to nanotriangular arrays, the sample labelling also adapt a similar system, PS (hexagonal pitch distance). Note that there are two arrays with the same 400 nm pitch distance but the one labelled with suffix "-65W" represents a slower argon ion milling rate. Interestingly, both PS400 samples exhibit resonance peak around 750 nm, although PS400-65W has a much broader extinction profile and PS400 has a narrow and sharp extinction peak (Figure 6-6 (b), (c)).

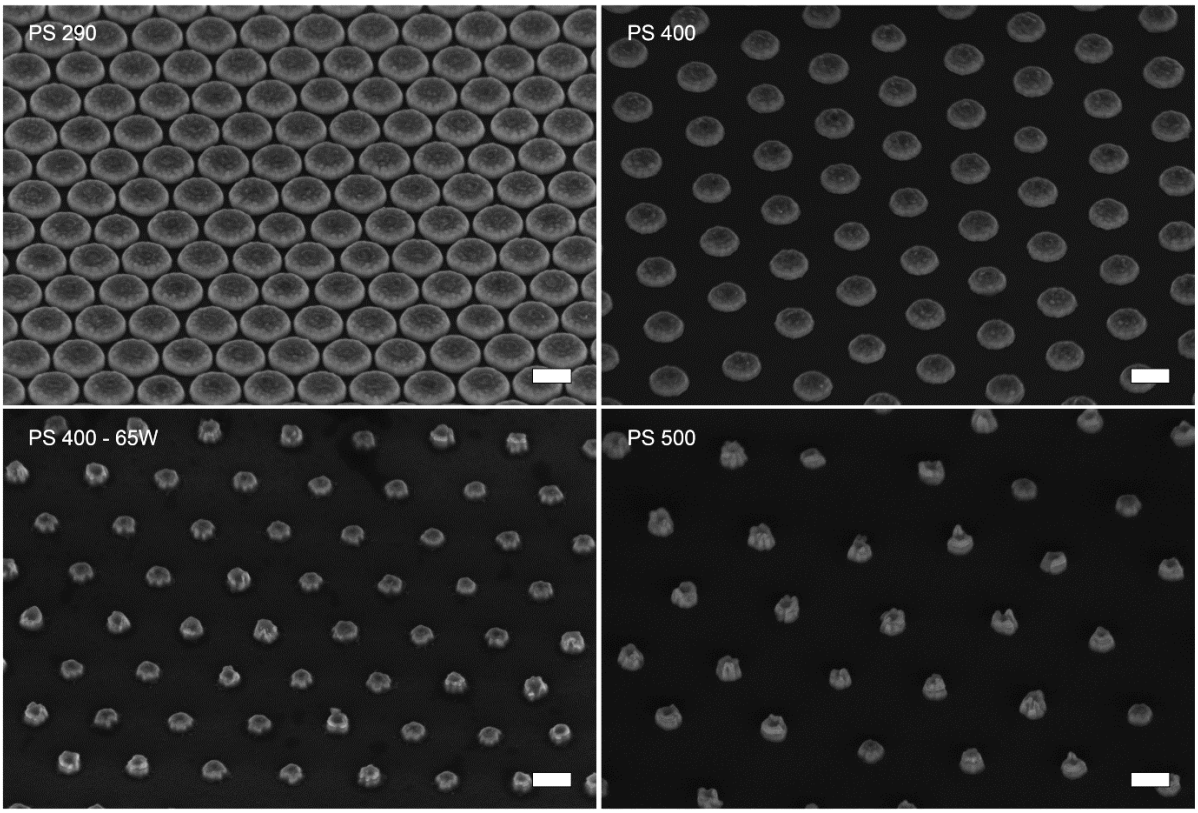

Figure 6-5 SEM images of 50 nm thick gold nanodisc arrays with pitch distance of 290 nm, 400 nm, and 500 nm viewed at 45°. Scale bar is 200 nm.

It is known that the angle of excitation plays a role in influencing the LSPR generated on plasmonic structure[255,256]. To obtain a better perspective of the LSPR behaviour to the setup in the fluorescence emission acquisition chamber used (30°), the extinction profile of the samples were measured at different angles (0° - 45°). The extinction spectra of those samples are shown in Figure 6-6. It can be seen that tilting the samples relative to the excitation light at an angle produced a significant shift in the resonance peak, and changed in shapes for PS400 and 500. Although hexagonal arrays are not affected the polarisation direction of the light source when excited at normal incidence angle, the effect of exciting with unpolarised light source can excites both longitudinal mode and transverse mode of the LSPR. The extinction also decreases with further tilting (figure A6 in appendix) as a result from dephasing of the electron oscillation by adjacent particles induced by the light polarisation in parallel to the substrates. A similar result was also observed by Malynych and

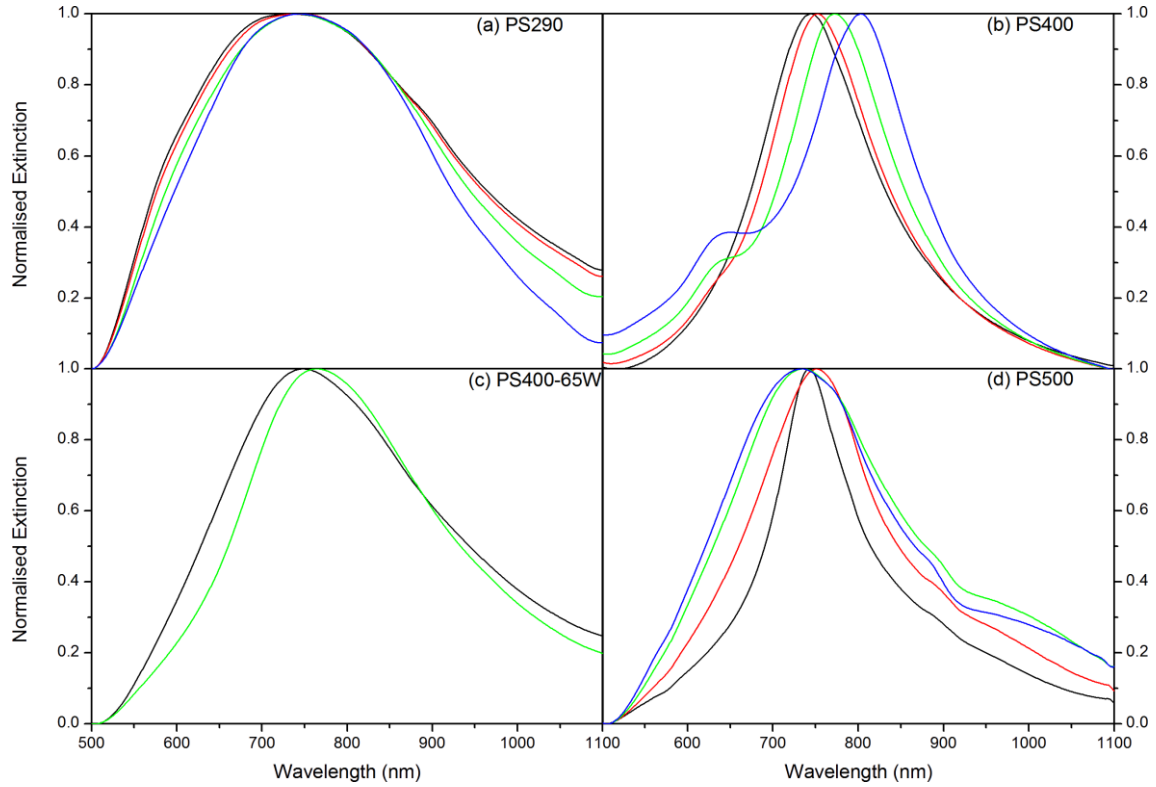

Figure 6-6 Normalised extinction of the nanodisc arrays on glass substrates at different centre to centre distance: a) PS290 b) PS400 c) PS400-65W d) PS500. Legend: black, red, green, blue represents 0°, 15°, 30°, and 45° respectively. Note: due to accessibility to the equipment at the time of measurements, only two angle were measured for PS400-65W sample.

Chuamnov[257]. As can be seen from PS400 extinction spectrum, the resonance peak redshifts significantly and a secondary peak at 649 nm caused by transverse mode is observed when the tilting angle is at 30° and 45°. Interestingly, no noticeable change in shape is observed on PS290. This suggests two possible reasons: i) the coupling in longitudinal mode is very dominant and ii) the density of the nanoparticles is very high and thus prohibits excitation of transverse mode when the sample is tilted relative to the excitation light. For PS500, the peak red shifted slightly at 15° but further increasing the angle results in a broader peak and blue shifted peak. Since the resonance wavelength here is close to the transition between evanescence mode and radiative mode (figure 5-9), the tilting may have contributed toward change in effective grating order. Alternatively, this could be due to secondary plasmonic peak being excited at the longer wavelength by transverse mode as can be seen by the increase in extinction above 900 nm. Additional peak broadening in PS500 may had also caused by the PS residue left on top of the disc and the irregular shape of the nanodisc due to long plasma exposure to the PS mask which roughen the PS surface. Nevertheless, those samples which were selected based on their extinction peak at 30° (green lines in the graphs) remain sufficiently close to AF750 optical profile.

However, the conjugation process in the experiments have proven to be difficult due to delamination of the metal nanoparticles from the substrates. This is likely due to the patterned of the substrate made the surface highly hydrophobic in nature[201] and repelled the protein-fluorophores

solution. In combination of the high meniscus force of the low contact angle and weak adhesion between gold and glass substrate, the gold nanodiscs were peeling off from the substrate surface during protein conjugation. The phenomenon was especially obvious for highly dense nanodisc arrays structure (i.e. more hydrophobic) and around the edge of the protein solutions near the edge of the substrate where meniscus force due to the water based solution is highest. To reduce the delamination effect, the nanodisc arrays samples were exposed to ozone plasma to increase the hydrophilicity of the surface prior to protein conjugation and achieved significant improvement.

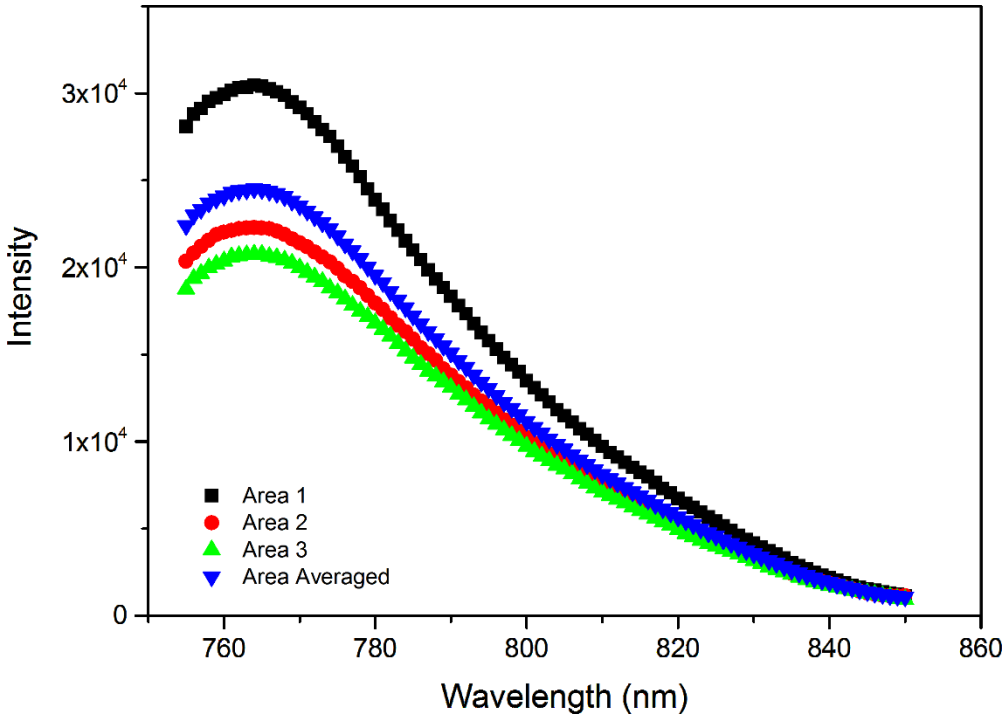

Figure 6-7 Fluorescence intensity of Alexa Fluor 750 monolayer on 50 nm Au nanodisc arrays with 290 nm pitch and 256 nm disc diameter measured at three different locations: Area 1 (black), area 2 (red), area 3 (green), and averaged value (blue).

Similar to previous nanotriangular arrays experiment, the fluorescence intensity is measured at three different locations on the sample (Figure 6-7 shows the individual fluorescence intensity measured at different location for PS290 as an example). Averaged fluorescence emissions of AF750 attached on those samples are shown in Figure 6-8. The shape of emission spectrum closely resembles their well-established profile[258]. By comparing the fluorescence intensity of AF750 on bare glass as control, area averaged fluorescence enhancement factors of 235, 185 and 86, and 77 times were measured on PS290, PS400, PS400-65W and PS500 respectively. In agreement with the hypothesis, the fluorescence enhancement is the highest in PS290 due to very strong interparticle coupling effect with gap/diameter ratio of 0.13. PS500 which has lowest interparticle effect in this set of samples (gap/diameter ratio of 2.5) does not generate strong enhancement. Their fluorescence enhancement factors and geometry parameters of the nanodisc arrays are summarised in Table 6-4. Note that since the value obtained here are averaged over the whole surface area including location where there is no MEF effect. Therefore,

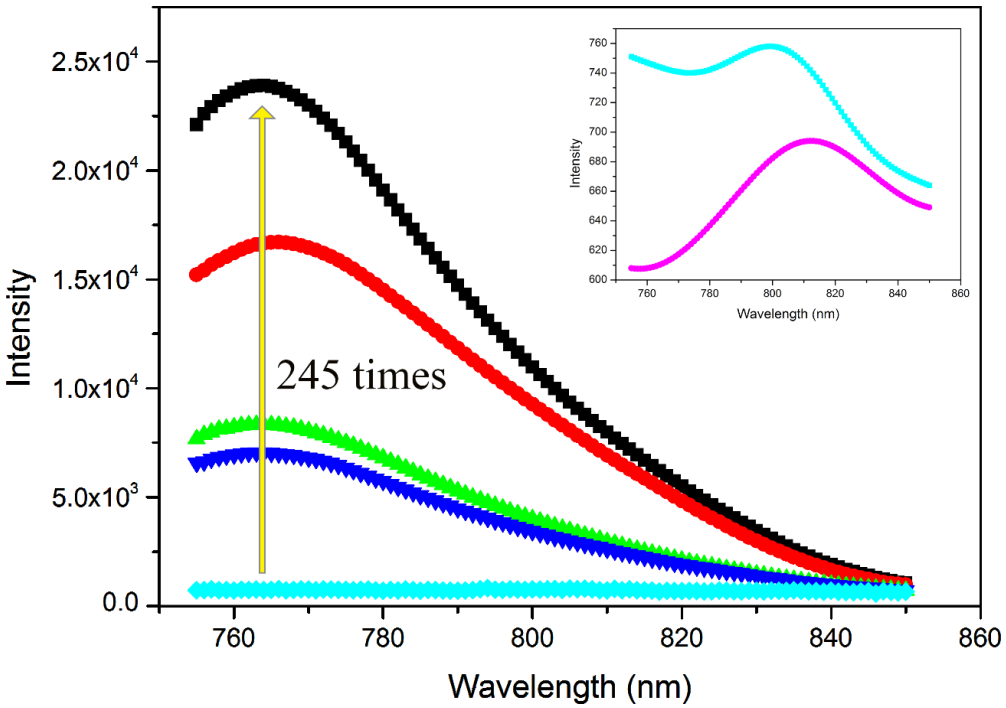

Figure 6-8 Averaged fluorescence spectra of Alexa Fluor 750 monolayer on various 50 nm Au nanodisc arrays on glass substrates: PS290 (black), PS400 (red), PS400-65W (green), PS500 (blue) and as well as on glass as control (cyan). Inset: amplified view of the AF750 (cyan) and bBSA (magenta) emission attached on glass. The peak around 800 nm is an artefact caused by the detector.

Table 6-4 Structural parameters and resonance peak position of nanodisc arrays and their fluorescent enhancement.

Sample	Disc diameter [nm]	Interparticle Gap [nm]	Gap/Diameter Ratio	Area fraction	Extinction Peak at 0° [nm]	Extinction Peak at 30° [nm]	Fluorescence Enhancement, E_f
PS290	256 ± 7	34	0.13	0.71	735	754	235
PS400	219 ± 7	181	0.83	0.27	744	772	185
PS400-65W	132 ± 7	268	2.0	0.10	752	764	86
PS500	141 ± 9	359	2.5	0.07	743	733	77

the actual enhancement factors are higher at region of plasmonic hot spots.

It can be seen that the area fraction of nanodisc surface coverage also increased substantially as the fluorescence enhancement factor increased, it is not the main contributing factor for several reasons: (1) The volume of hot spots generated when strong interparticle coupling occurs are confined to the small space between the nanodiscs[23,81]Hence, only a small fraction of fluorophores benefit from strong interparticle effects. (2) In comparison to strong interparticle coupling for particles in a line, sharing of charge density across multiple locations of the nanodiscs in hexagonal arrays reduced the maximum electric field strength that can be achieved (Figure 5-12). In a hexagonal nanodisc arrays, a single dipole

configuration with one side positive and one side negative is prohibited due to symmetry breaking. Thus charges have to distribute to three different locations in a single nanodisc to produce first order resonance condition. This effectively reduced the amount of charge by a third, and thus reduced the maximum electric field. This theory is consistent with the model proposed by Malynych and Chumanov[257], although in this case, the structure produced is even more uniform. (3) Strong hydrophobicity and could prevent the conjugation solution from covering the sidewall of the nanodisc arrays where the electric hot spots are generated. Therefore, lower number of fluorophores are attached and those attached do not benefit from the full strength of the enhanced electric field.

To confirm the enhancement is origin from MEF, fluorophore lifetime was measured on those samples (Figure 6-9). Since the lifetime acquisition was set to stop measuring when the peak counts reach a fixed number, the intensity of the decay tail can indicates the intensity of the fluorescence emission by the excited fluorophores (i.e. the higher the intensity of the baseline implies a lower intensity from the fluorophores). From the graph, it can be seen that the AF750 attached on the bare glass has significantly lower intensity than the decay profile obtained from nanodisc arrays. In fact, the intensity of AF750 attached on nanodisc arrays was very strong and the lifetime was reduces tremendously to the detection limit where it becomes challenging to deconvolute the lifetime from the internal response function of the system. A ME model[175] was applied to all the samples and a global fit using three to four set of lifetime data per sample were used to improve the accuracy of the calculation. The confidence of the fit are reflected in the reduced χ^2 value. The closer this value to 1, the higher the confidence level that the model has correctly modelled the system. The amplitude weighted reference lifetime of the AF750 on bare glass was measured to be 0.72 ns, in agreement with the value given by the manufacturer. Since a significant large area of the sample surface are bare glass, fluorophores attached to these areas should not experience enhancement. Therefore, the exponential components (Γ_1, Γ_2) from the glass reference are retained in the modelling parameters for nanodisc samples (Table 6-5). It is found that such approach was able to model the lifetime correctly and the reduced lifetime correlate to the fluorescence enhancement factor of each type of array consistently. This suggests the fluorescence enhancement measured was indeed genuine MEF due to coupled LSPR. This is also consistent with other reports that the hot spot generated in the coupling mode are much stronger.

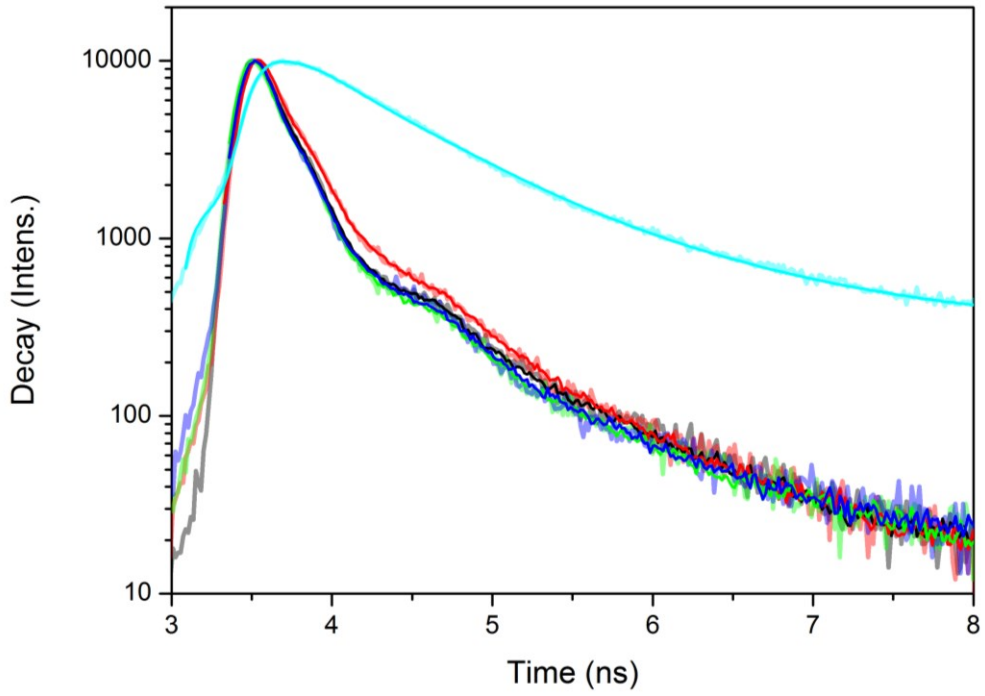

Figure 6-9 Fluorescence lifetime decay profile of the AF750 on different nanodisc arrays. PS290 (black), PS400 (red), PS400-65W (green), PS500 (blue), and on glass (cyan).

Table 6-5 Amplitude weighted multi-exponential decay analysis of AF750 on glass and NDA structures with component percentages (a), lifetime (τ), amplitude weighted lifetime fit (<τ>) and Goodness of Fit parameters (χ_R^2).

Substrate	a_1	a_2	a_3	τ_1 [ns]	τ_2 [ns]	τ_3 [ns]	<τ> [ns]	χ_R^2
Glass	16.5	83.5	-	1.40 ± 0.02	0.59 ± 0.01	-	0.72 ± 0.02	1.275
PS290	1.3	9.7	89	1.40 ± 0.07	0.59 ± 0.02	0.055 ± 0.002	0.12 ± 0.01	1.526
PS400	2.8	23.5	73.7	1.30 ± 0.09	0.59 ± 0.01	0.071 ± 0.003	0.23 ± 0.01	1.370
PS400-65W	12.1	43.4	44.5	1.29 ± 0.06	0.59 ± 0.03	0.54 ± 0.03	0.66 ± 0.03	1.522
PS500	10.1	25.8	64.1	1.34 ± 0.09	0.59 ± 0.03	0.54 ± 0.06	0.64 ± 0.06	1.608

To further understand the insight of this MEF results, the enhancement factor and lifetime results were used to calculate the emission and excitation enhancement, respectively (Table 6-6). For PS280 and PS400, the calculated emission enhancement was found to increase more than 9 times, pushing the modified quantum yield to more than 90%. This suggests the strong interparticle coupling has caused the modified quantum yield close to unity. Interestingly, the excitation enhancement values are close to each other. Since this value suggests the electric field experience by the fluorophore, the

Table 6-6 Measured fluorescence (E_f), estimated emission (E_{em}) and excitation (E_{ex}) enhancement factors for AF750 on different NDA substrates

Sample	E_f	E_{em}	E_{ex}	Modified Quantum Yield
PS290	235	9.3	25.2	0.93
PS400	185	9.1	20.3	0.91
PS400-65W	86	3.3	26.3	0.33
PS500	77	3.3	23.6	0.33

result implies the electric fields generated around the fluorophores are approximately the same. This could be due to the strong coupling between the fluorophore-metal system affected the maximum electric field enhancement experienced by the fluorophores. However, more evidence is required to verify this result.

6.3.1 *Summary*

Gold nanodisc arrays have been tuned to couple with AF750 and enhanced its fluorescence emission. It was found that the strong interparticle coupling effect led to strong MEF. A maximum enhancement factor of 235 was achieved on 50 nm gold nanodisc arrays using PS290 template, where strong interparticle coupling exists. This is much higher than the values obtained from the nanotriangular arrays and higher than those standard of arts results for thin film listed in table 3-2. The calculation of emission and excitation enhancement also suggest the electric field generated in this structure is substantially stronger than nanotriangular arrays.

6.4 Nanohole-disc Arrays

The last structure tested in this project for MEF is nanohole-disc arrays. This structure exploits the capability of LSPR-SPP coupling to achieve a combine effect to produce higher fluorescence enhancement. The distance between the LSPR and SPP structure can also be tuned to achieve interparticle coupling effect to produce even stronger enhancement effect. Similar structure in square arrays has also been fabricated by Chou group through nanoimprint lithography[116] and shown to achieve highest enhancement factor to date. Here, an alternative nanosphere lithography has been used to produce hexagonal type nanohole-disc arrays. As shown previously in chapter 5, the extinction peaks of this structure are very broad and extend into NIR-II region (1100 to 1400 nm) because of the LSPR-SPP hybrid coupling, making it an attractive structure for future biosensing applications.

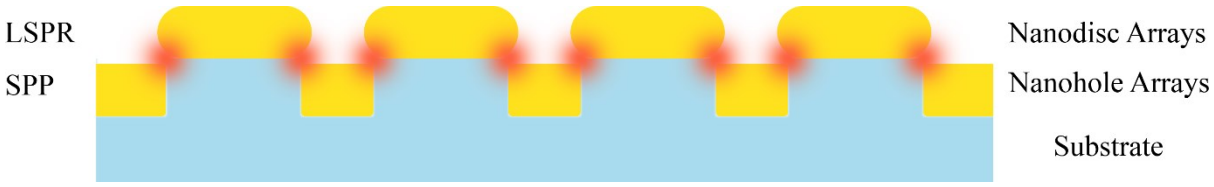

Figure 6-10 Schematic illustration of the nanohole-disc arrays and the location of hotspots (red colour).

Due to unavailability of NIR dye that can match the resonance peaks exhibited by those nanohole-disc arrays perfectly, the fluorophore being chose is AF790, which is also currently the longest wavelength commercially available. Three 30 nm Au nanodisc arrays samples were selected for this experiment from the data set as they have their resonance peak closest to the AF790 optical spectrum – (A) PS280 Ø215 with nanodisc diameter 215, (B) PS280 Ø148, (C) PS400 Ø337. Figure 6-11 shows the normalised extinction of these samples and the optical spectra of AF790. Sample A and C have resonance peak around 848 and 851 nm, respectively. Sample B, which has the same pitch distance as sample A but much smaller disc diameter, does not show a clear visible peak but 1st derivative calculation reveal a small peak exists around 848 nm. Hence, all three samples has almost the same extinction peak location but a significant difference of 45 – 68 nm away from emission-excitation peak of AF790.

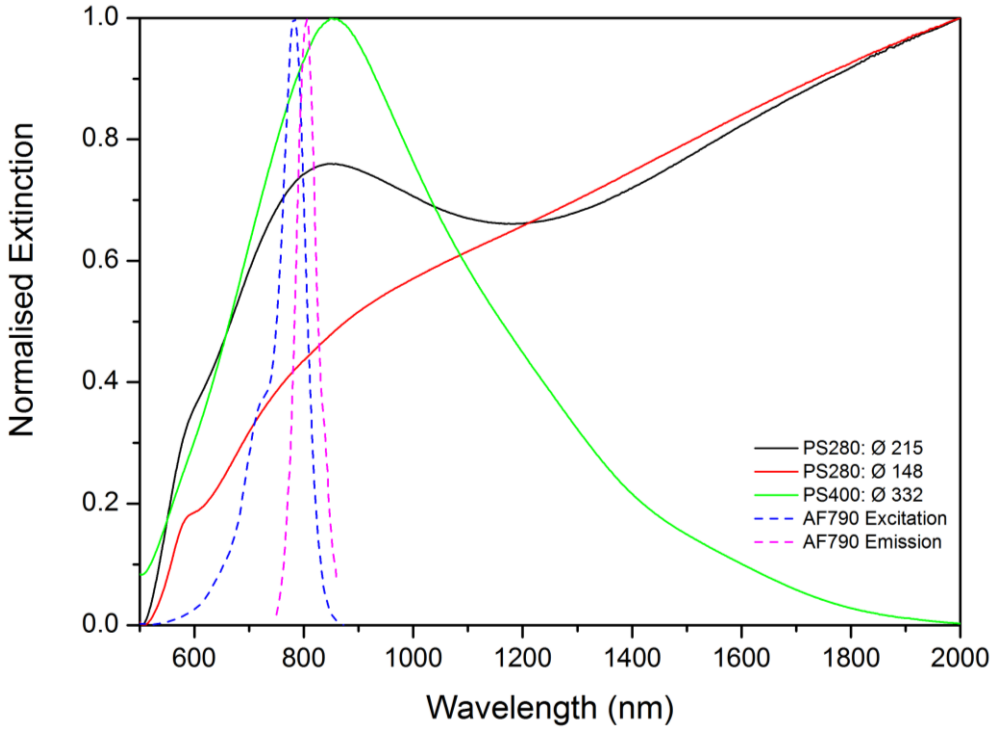

Figure 6-11 Normalised Extinction spectrum of NHDA samples selected for MEF testing. Also included in the figure are the excitation and emission spectra of AF790 fluorophore.

Similar to the previous two MEF experiments, the fluorescence emission intensity were obtain on three different locations on the nanohole-disc arrays samples and AF790 on multiple glass substrates. The fluorescence intensity is then averaged to calculate the enhancement factor. **Error! Reference**

ource not found. shows the fluorescence intensity of those individual components measured from sample B.

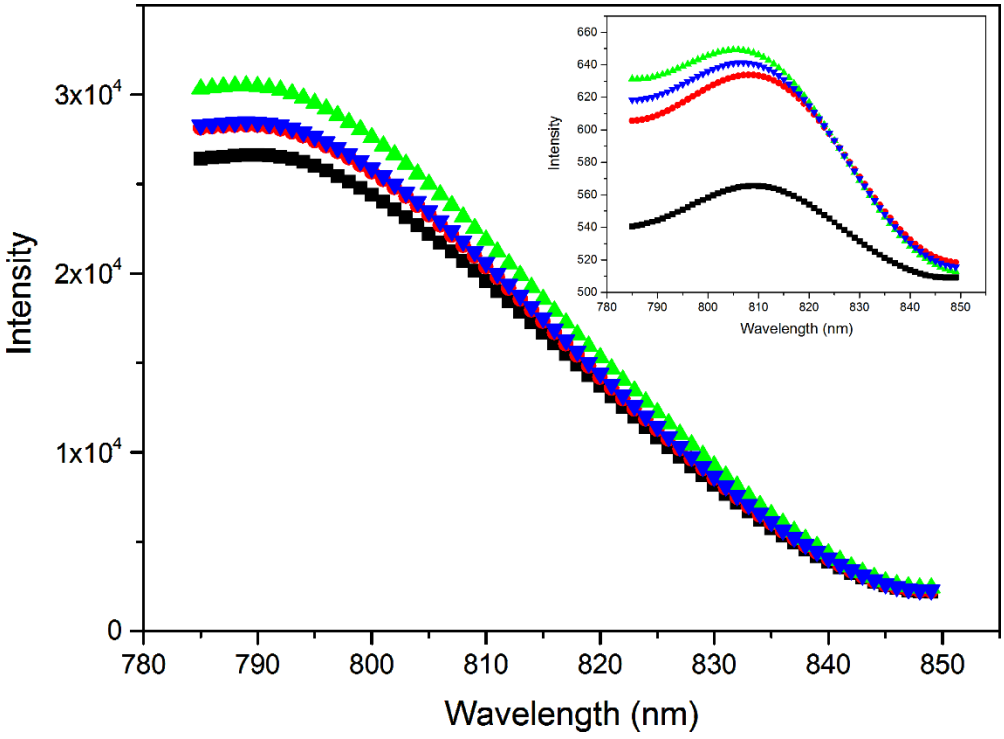

Figure 6-12 Fluorescence intensity of AF790 attached on nanohole-disc arrays sample B measured on different area and on different bare glasses as reference: Sample B - area 1 (black), area 2 (red), area 3 (green), and area averaged intensity (blue). Inset: Fluorescence intensity of bBSA on a bare glass (black), AF790 on two different bare glasses (red and green) and averaged intensity of AF790 on two different glasses (blue).

Fluorescence emission spectra of those samples are shown in Figure 6-13. The results are tabulated in Table 6-7. All samples gave enhancement factors higher than the nanotriangular arrays and nanodisc arrays tested. Among them, sample A enhanced the fluorescence emission tremendously by 411 times. This is the highest value obtained to date in the projects even before the fluorophore-plasmon system is optimized, suggesting this is a very promising structure for NIR-II biosensing application. The huge broadband of nanohole-disc structures also suggest this would be an excellent substrate for multiplex experiment. Highest enhancement obtained in sample A is also likely to be due to closer nanodiscs thus better LSPR interparticle coupling. In comparison, decreasing the diameter while keeping the pitch distance the same (sample B) results in reduction of enhancement. Surprisingly, sample C which has a strong plasmonic peak does not appear to produce enhancement higher than those with smaller pitch size.

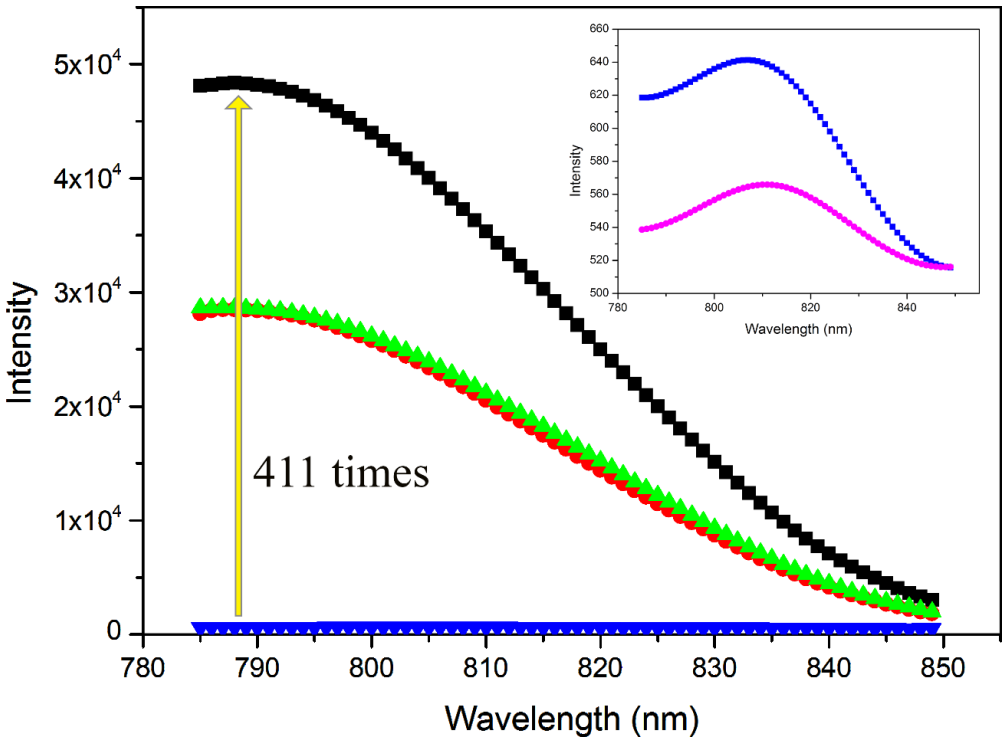

Figure 6-13 Averaged fluorescence intensity of AF790 attached on selected nanohole-disc arrays substrates and on bare glass as reference: PS280 Ø215 (black), PS280 Ø148 (red), PS400 Ø332 (green), and glass as control (blue). Inset: amplified view of fluorescence emission AF790 (blue) and bBSA (magenta) on glass.

Similar to LSPR based structures, excitation angle plays a role in determining the resonance mode for LSPR-SPP coupled system. For instances, Dorpe group explored nanodisc coupled with thin gold film to obtain Fano resonance[252]. The ability to tune the plasmonic mode through changing the excitation angle are useful for many applications. As such, enhancement factors for nanodisc arrays were measured in 30° and 45° as first experimental attempt in understanding the effect of excitation angle on nanohole-disc arrays structure. Increasing the angle to 45° shows the order at which samples have the highest fluorescence enhancement remain the same but the values dropped for both sample A and sample C while a noticeable increase is seen on sample B. This suggests MEF through nanohole-disc arrays are indeed sensitive to the excitation angle and could be exploited for optimization in the future.

Table 6-7 Structural parameters and resonance peak position of nanohole-disc arrays and their fluorescent enhancement.

	Pitch Size (nm)	Disc diameter, Ø (nm)	Extinction Peak at 0° (nm)	Enhancement Factor at 30°	Enhancement Factor at 45°
A - P280 Ø215	280	215 ± 5	848	411	400
B - P280 Ø148	280	148 ± 3	848	298	331
C - P400 Ø332	400	332 ± 5	851	293	256

It is also worth mentioning that it was found the strong photobleaching was observed during the acquisition process. In previous experiments on nanotriangular arrays and nanodisc arrays, the emission intensity from those samples were relatively stable. In this case, the emission intensity decreased significantly after each subsequent scan. In fact, the first measurement performed on sample A showed an enhancement factor of 505 times which degraded to 411 times when being measured 30 minutes later. To verify this was not caused due to the measuring tool, the fluorescence intensity from AF790 on glass reference was re-measured and found to remain at the same intensity level throughout 3 hours of measurements. As such, to compensate with the potential degradation with other samples for a better data comparison, the values shown in Table 6-7 are collected at 30 minutes after first exposure to the excitation light source. Hence, the values listed here are semi-qualitative and is a lower estimation of their full strength MEF since part of the fluorophores have been degraded.

In literature, it has been suggested that the MEF can improve the photostability (i.e. rate of maximum intensity decay per unit time) when the excitation power is decreased so that the emission intensity of the enhanced fluorophores is lowered to match the lower emission intensity of the control samples[166,259]. This photostability is a result of reduced excitation-emission cycle, thus decreased the duration the fluorophores are at the excited state and therefore less likely to photobleach[151]. However, the quenched lifetime of the fluorophores also meant a shorter excitation-emission time. If those enhanced fluorophores were to excite with the same excitation power used for control, the rapid excitation-emission cycle cancels out the effect of photostability per cycle[151]. Since in order to quantitatively determine the fluorescence enhancement, it is necessary to keep the excitation power the same for all samples. Therefore, the decreases in fluorescence intensity during the measurement agrees with the hypothesis. However, such rapid decay in very short time has only been observed from this nanohole-disc arrays plasmonic system and not on previous nanotriangular arrays and nanodisc arrays. This suggests the origin of this strong decay is likely due to very powerful excitation enhancement and emission enhancement generated by a very strong electric field and fast excitation-emission cycle.

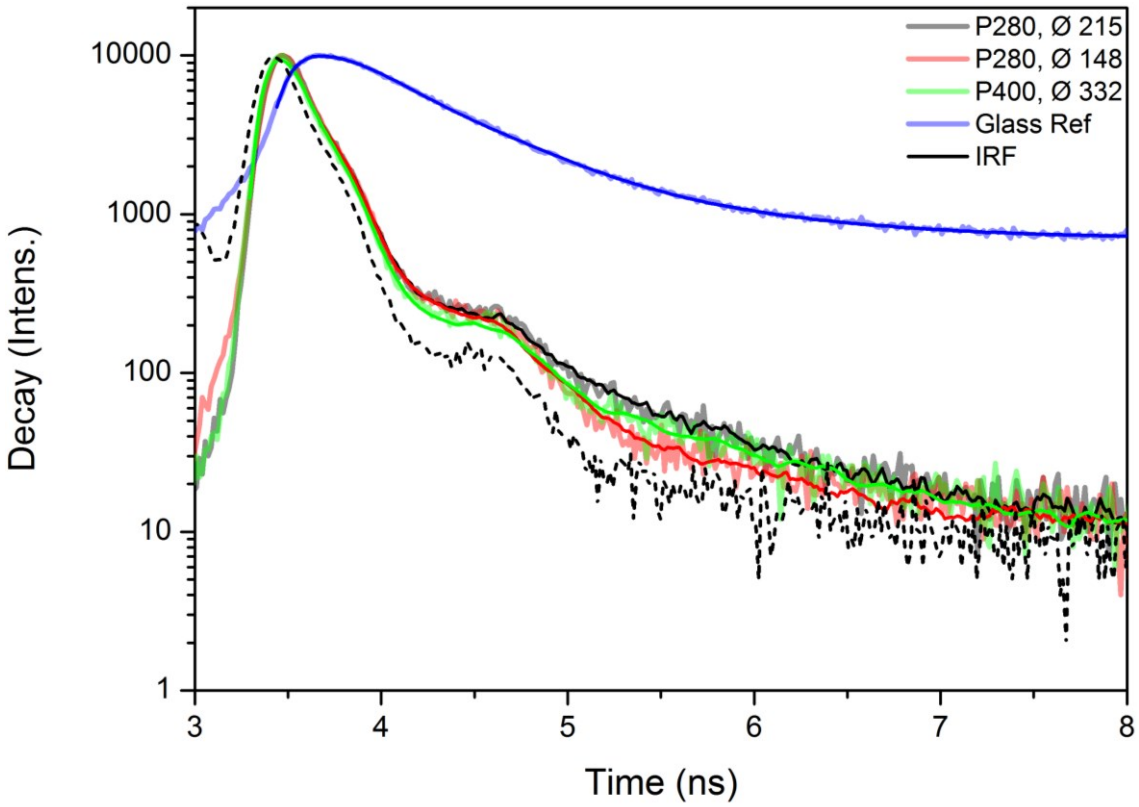

Figure 6-14 Fluorescence lifetime decay profile of the AF790 on different nanohole-disc arrays: A-PS280 Ø215 (black), B-PS280 Ø148 (red), C-PS400 Ø332 (green), glass reference (blue), and IRF of the system (black dash).

Lifetime is measured to verify the enhancement is due to MEF (Figure 6-14). However, the measurement proved challenging as the decay profile from the AF790 attached on nanohole-disc arrays reaching the detection limit of the detector (ca. 50 ps), making it difficult to obtain the true lifetime value for all those highly quenched sample. Modest suggestion based on the ME model fitting for sample A, B, and C are 0.020, 0.022, and 0.040 ns respectively (the uncertainty for those values are all underestimated in this case as the measurements have reached the detection limit). Note the approached used in nanodisc arrays where the lifetime components value obtained from glass reference are not being used in the samples. This is because the surface of nanohole-disc arrays are almost fully covered by Au and thus most fluorophores lifetime would have been modified. In addition, the fractional components for the second lifetime term are very low, suggesting no additional lifetime term is required to improve the modelling.

Table 6-8 Amplitude weighted multi-exponential decay analysis of AF790 on glass and nanohole-disc arrays structures with component percentages (a), lifetime (τ), amplitude weighted lifetime fit (<τ>) and Goodness of Fit parameters (χ_R^2).

Substrate	a_1	a_2	a_3	τ_1 [ns]	τ_2 [ns]	τ_3 [ns]	<τ> [ns]	χ_R^2
Glass	96.79	3.21	-	0.54 ± 0.01	2.5 ± 0.1	-	0.60 ± 0.01	1.13
PS280, Ø 215 ± 5 nm	99.86	00.14	-	0.018 ± 0.001	0.79 ± 0.05	-	0.020 ± 0.001	1.17
PS280, Ø 148 ± 3 nm	99.72	0.28	-	0.021 ± 0.001	0.41 ± 0.02	-	0.022 ± 0.001	1.14
PS400, Ø 332 ± 5 nm	99.82	0.18	-	0.038 ± 0.001	0.91 ± 0.05	-	0.040 ± 0.001	1.84

Table 6-9 Measured fluorescence (E_f), estimated emission (E_{em}) and excitation (E_{ex}) enhancement factors for AF790 on different nanohole-disc arrays substrates.

Sample	E_f	E_{em}	E_{ex}	Modified Quantum Yield
A - PS280, Ø 215 ± 5 nm	411	9.7	42.4	0.97
B - PS280, Ø 148 ± 3 nm	298	9.67	30.8	0.97
C - PS400, Ø 332 ± 5 nm	293	9.4	31.2	0.94

For completion, the emission and excitation enhancement was also calculated (Table 6-9). The results showed the enhancement factors have all been enhanced tremendously and modified the quantum yield to 94 – 97 %, close to unity. The enhancement factor also suggested that the electric fields were strongest for A, follow by B and C, in consistent with the fluorescence enhancement result above and much higher than the nanodisc and nanotriangular arrays tested earlier.

6.4.1 *Summary for Nanohole-disc arrays experiments*

Nanohole-disc arrays explore the possibility of combining the LSPR and SPP modes to provide a greater fluorescence enhancement. It was demonstrated that such structure can be fabricated using NSL. Despite the structures were not optimised for AF790 and suffering from rapid emission decay, an extremely high fluorescence enhancement factor of more than 411 times was obtained, much higher than nanotriangular arrays and nanodisc arrays. In fact, the highest we have measured so far in our lab. Lifetime measurements also showed the result was genuinely due to MEF although the accurate lifetime value was unable to be determined properly due to limitation of the measurement system used.

6.5 Chapter Conclusion

This chapter explored the capability of three different types of nanostructures that can be produced by NSL in MEF. It was found that Au nanohole-disc arrays involving LSPR-SPP coupling mode produced highest fluorescence enhancement, with a staggering value of more than 411 times the value of a control sample. This is of paramount achievement as it is the highest value we have obtained despite the system has not been optimised and suffering from rapid decay. Further optimisation could provide even higher enhancement factor. This suggests that nanohole-disc arrays are an excellent candidate for NIR-II biosensing application. In comparison, Au nanodisc arrays which utilise the property of LSPR interparticle coupling yield enhancement of up to 235 times, which is much higher than closely spaced Ag nanotriangular arrays where only 83 times enhancement was achieved.

Chapter 7

Conclusions and outlooks

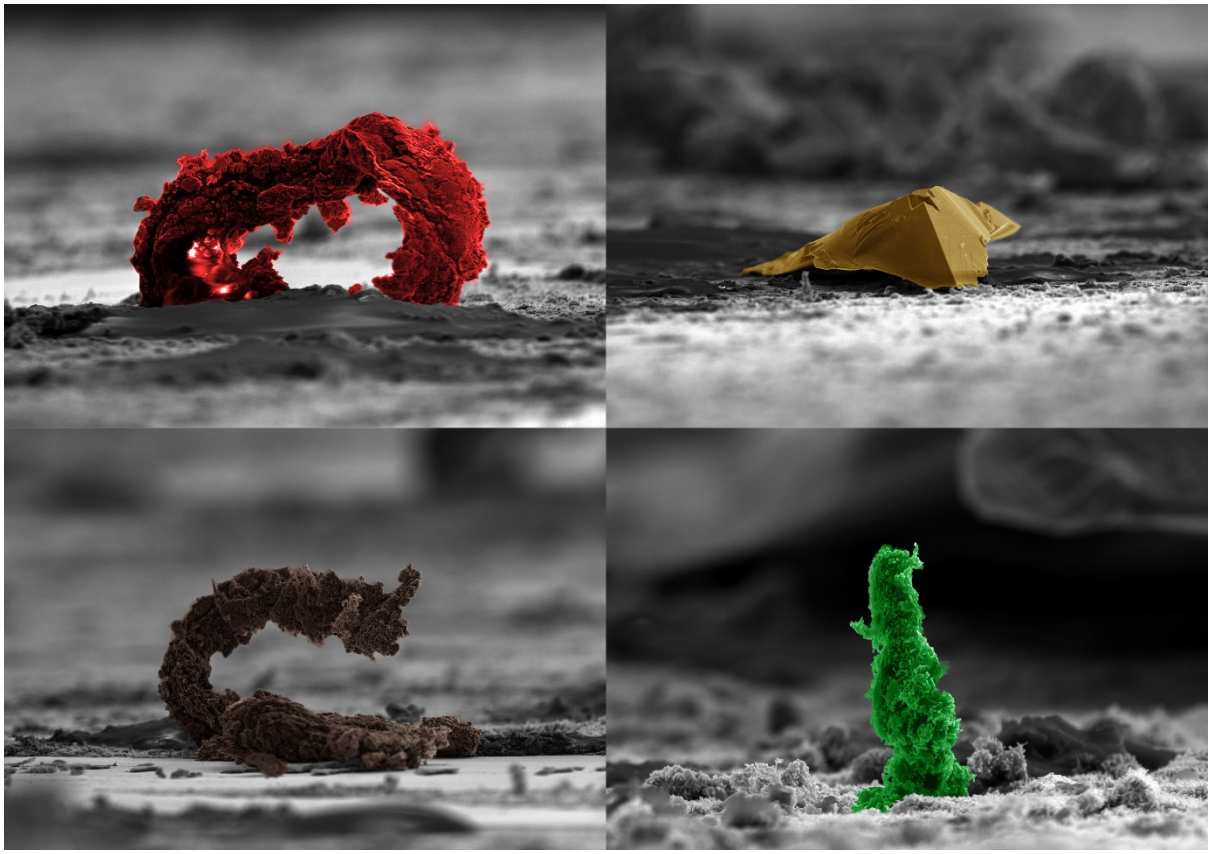

Figure 7 Some bizarre objects stumbled during SEM image acquisition process in this project.

Chapter 7 Conclusions and Outlook

7.1 Summary of Thesis

The discovery of localised surface plasmon resonance and the advancement of nanotechnology generated a myriad of applications and possibilities. In this thesis, the concept of localised surface plasmon resonance and specific application in metal enhanced fluorescence for biosensing has been introduced. Following the trend of development in this branch of nanotechnology, LSPR interparticle coupling between nanoparticles and LSPR-SPP coupling becomes the major focus for this project in order to develop a better nanostructure for biosensing.

In order to fabricate the desired nanostructure, nanosphere lithography was chosen and developed further to fabricate reproducible larger area pattern nanostructure. Throughout the process, novel "polishing" technique in argon ion milling process, and sacrificial layer for removal of cross-linked polystyrene residues were developed to help achieve good quality nanoscale patterned. Many different type of nanostructures have been successfully developed through this project. Among them, closely spaced nanotriangle, nanodisc arrays, and complex nanohole-nanodisc arrays were studied in details for their optical properties and potential in MEF.

The optical properties of the localised surface plasmon resonance of these structures were fine tuned to achieve inter-particle coupling effect. The nature of those mechanisms was studied in details and has been characterised accordingly. In general, when interparticle coupling occurs, the resonance peak was found to be red shifted and broaden, in agreement with many published results. It was also found that the inter-particle coupling effect in nanodisc arrays is highly dependent on the size of the nanodisc and the gap between them. The optical properties of fabricated nanohole-disc arrays were also characterise and documented in this thesis. They are found to resonate well into the NIR and would be a good candidate for application that operates within NIR regime.

Finally, selected few samples were tested with NIR fluorophores to test their capability in metal enhanced fluorescence. All structures were found to be able to enhance the fluorescence emission of the attached fluorophores. Inter-particle coupling was found to be able to enhance the emission greatly. The complex nanohole-disc arrays which explore the property of LSPR-SPP coupling also achieved tremendous enhancement and is the best nanostructure tested to this date even before the structure has been optimised for the attached fluorophores.

As a whole, this thesis aimed to provide some insights into the coupling properties and to provide design and processing criteria to fabricate those structures. The results also suggest that LSPR-SPP effect should be further investigated as it shows a very promising result, albeit some of the mechanism behind remains unclear. The thesis also opened up many questions; below are some

suggested future works that can explore the fabrication technique, plasmonic properties, and applications further.

7.2 Future Work

7.2.1 *Closely spaced nanotriangular arrays*

The optical measurement and simulation shown here were all performed at normal incidence. It is known that angle of excitation can generate different plasmonic modes and the emission could also depends on the angle of detection. It would be a better representation of the results if future experiments includes the angle dependency and could potentially improve the results even further by exciting the LSPR at optimum angle. Furthermore, it is possible that the interparticle coupling could be similar to highly coupled array system such as nanodisc arrays, it would be interesting to see if a similar plasmon ruler equation can be applied to nanotriangular arrays.

7.2.2 *Nanodisc arrays*

The delamination problem during the protein conjugation process presents a problem in experiment as the nanodisc array structure could be destroyed and hamper the results. One of the solutions is to apply an adhesion layer below the metal nanoparticles. However, common adhesion layer such as Ti and Cr need to be avoided as it has been shown that they cause damping of the system, leading to higher energy loss[68,69]. Alternatively, chemical adhesion using MPTMS ((3-Mercaptopropyl)triethoxysilane) has been proven to be a good candidate[69].

Gold was chosen in this experiment because it does not oxidise when exposed to the oxygen plasma process, which is necessary for tuning the diameter of the nanodisc. However, the nanodisc fabrication technique is not restricted to the gold only if a Ni sacrificial layer is used as it can also serve as an oxygen protection layer for the material underneath. This would allow a larger range of material to be tested. An advanced characterisation such as electron energy loss spectroscopy (EELS) for local electric field mapping would help to understand the excitation enhancement while a better resolution of lifetime decay would be needed to better understand the lifetime decay curves.

The detailed mechanism and generation of hot spots in large hexagonal arrays remain unclear and currently unavailable from the literature. It would be necessary to further understand the physics behind generation of plasmonic in those highly coupled nanodisc arrays and their applications in biosensing.

7.2.3 *Nanohole-disc arrays*

Further enhancement for nanohole-disc arrays can be achieved by (1) applying fluorophores that matches the LSPR peaks, (2) a mode complex shape rather than circular nanodisc, preferably those with high curvature corners, (3) optimizing the thickness of the nanohole arrays and nanodisc arrays through

computer simulation to find the best configuration and deposit using the recipe developed in this project, which deposition of nanohole thickness and nanodisc thickness is doable.

It has been shown that effect of excitation angle plays a role in fluorescence enhancement. However, a variable angle transmission measurement stage was unavailable for NIR measurement and thus no correlation between the enhancement factor and the optical properties of the nanohole-disc structure could be made. It would be beneficial to investigate further to optimise the excitation angle for LSPR-SPP coupling mechanism in nanohole-disc arrays.

Although not mentioned earlier, nanohole-disc arrays structures also suffer from delamination issue faced by nanodisc array structure. Similar approach of using MPTMS as an adhesion layer could also be applied here for future investigation.

7.2.4 *Nanosphere lithography*

Currently, there is still room to explore for types of structure that can be obtained from using spherical mask. For instance, bilayer of same sphere sizes and binary arrays from two different sphere sizes gave rise to more complex structure. Creative ideas, testing with the processing parameters and incorporation with other processing technique could produce some fascinating structures in the future.

Patterned substrates could also further improve the quality of the PS monolayer. Notably, works done by Cai *et al.*.[211] and Khanh and Yoon[203] demonstrated by patterning the substrates, not only the PS monolayer quality is improved, but the pattern can also be confined in a specific area of interest. With the help of photoresist patterning, it is possible to confine the patterning of the nanostructures on a small area, thereby reducing the defects and improve the reliability of the measurements.

Although NSL is a scalable technique, large area remains a challenge, especially using PS nanosphere. **Ink-jet printing** which has been used very frequently these days could provide a usable large scale technique to fabricate large area arrays. The volume and the concentration of the polystyrene can be controlled precisely and dropped into specific area of the substrate for subsequent patterning. Combined with pre-photoresist/mask pattern, it is possible to even putting down different sizes of PS mask at different area.

At the moment, the cross-linked PS removal problem is solved by having a sacrificial layer, it is also possible to change the parameters in the process to reach the similar outcome. During the oxygen plasma and argon ion milling process, oxygen and argon atoms bombard on the polystyrene and cause them to cross link by preventing those atoms from reacting with the PS at the PS-substrate interface. For instance, it is possible to increase the kinetic energy of the atoms to become more directional and less diffusive, therefore unable to react with the PS at the base. However, it has also been reported that the greater ion energy could also lead to greater cross-linking in the PS[218,260]. A balance of control

between the accelerating voltage and the plasma power will need to be reached in order to obtain an optimum outcome. Alternatively, it has also been suggested that the H and F atom can suppress cross-linking during plasma etching[261].

Additionally, **charged PS** either by chemical conjugation or additional surfactant could be another novel method to process new type of nanostructure arrays. A lateral manipulation of electric field below substrate surface could determine the pattern at which PS will move around to form a new pattern according to the electric field contour.

7.2.5 *LSPR*

Most of the optical properties of LSPR are examined under wide wavelength light source. The plasmonic mode generated depends on the excitation wave such as polarisation, wavelength, and angle. Thus, the actual plasmon excited on the nanoparticles may not be the same if it is excited at a single wavelength. It would be very interesting to exploit this nature. For instance, one could excite the plasmonic structure through **mixing two or more excitation beams** from different angles and polarisations to squeeze the charge density toward a certain location. The resultant increase in charge density at that region will generate a stronger electric field enhancement. In addition, by doing so allows changing the state of plasmon modes by controlling the light source. Such phenomena could be useful in data communication or selective protein detection in biosensing.

Grating effect is usually being considered when analysing a periodic structure. However, most grating structures being considered in the literature are based on particle in a line or in square lattice. A detailed theory and investigation on the **hexagonal arrays** remain scarcely available. It would be interesting to understand the physics of grating for higher order symmetrical system and to explore the effect when they are being excited in angled.

Recently, it has also been reported that **addition of metal or dielectric**[71,262] nanoparticles into the arrays can induce field confinement. Positioning of carbon nanoparticle in metal clusters was found to induce mixed mode resonance and also intensify the electric field enhancement, without reducing the physical distance between the metal nanoparticles. Similar approach could be applied to highly coupled structures fabricated in this project.

Breaking symmetry in the nanostructure also appears to be a highly attractive route to focus electric field on a specific region[263]. One could design an array of nanostructures that have sharp curvature and use polarised light to focus the electric field into that region.

7.2.6 *Biosensing*

It is known that the **electric field** can enhance the excitation of the fluorophores. However, the detailed mechanism is not very well known and no experiment has been done to investigate this directly. For instance, although the electric field strength is taken at the excited wavelength as this is the wavelength at which the plasmon can be generated by the nanoparticles, the requirement of alternative external electric field is required to give rise to MEF has not been considered and properly explored at all. An external static electric field can also induce high electric field region at metal surface with high curvature too, which could provide an alternative method to enhance excitation of fluorophore. As for the modification of the quantum states of the fluorophores, the fluorophores could have gone through a similar effect to when atom exposed to strong electric and magnetic field in hyperfine splitting, results in changed of internal quantum states. It might be possible to explore this mechanism experimentally by applying direct and alternating electric field generated externally such as capacitor plate across the fluorophores to probe both the existence of electric field enhancement and frequency of alternating electric field on MEF. Although the frequency of the electric field that can be generated in this way is limited, it may still provide some clues on the effect of electric field and its dependency on field frequency through this method.

In most plasmonic structures, the hot spot tends to concentrate around **air/substrate/metal** interface, it is worth evaluating structures that expose this junction to increase the area at which the fluorophore can benefit from high electric field enhancement. For instances, increase the etching into the substrate in nanodisc arrays such that the surface area around the junction beneath the gold disc is increased for fluorophore attachment. Alternatively, one can also produce a dielectric/metal/dielectric structure to achieve similar effect.

It has been suggested that the enhancement of fluorescence is due to the scattering of the LSPR[155], on the other hand direct experimental evidence has yet to be shown. **Quantum dots** have large wavelength gap between emission and excitation. This allows the study of the effect of spectra overlapping on the emission and excitation separately, allowing a better understanding of physical mechanism behind MEF. In addition, they have better resistance against corrosion from ambient environment, better photostability, and large excitation region which is also away from the narrow emission spectra can allow natural excitation of the quantum dots and detect it using an IR detector. In addition, quantum dots such as silver sulphide are non-toxic and biocompatible[264] and emission is around 1100 nm. They would be a great candidate to test on the nanohole-disc arrays nanostructure.

Similar to the strategy in nanohole-disc arrays where two types of enhancement are combined together to gain a better effect, **ZnO** is also able to induce fluorescence enhancement through wave guiding effect. The combination of both effects could also lead to better MEF.

Recently, Goldys group has proposed that the high Purcell factor in core-shell structures could be employed in nanolasers and can be regarded as MEF with virtually unlimited brightness[172] ! It would seem that the potential of plasmonic structures remain bright for many different applications.

Bibliography

(1) μεταλλοί-ωσις, εως, ἡ, change, Plot.3.6.11.
(2) Okamoto, K.; Niki, I.; Shvartser, A.; Narukawa, Y.; Mukai, T.; Scherer, A. *Nat. Mater.* **2004**, *3*, 601–605.
(3) Catchpole, K. R.; Polman, A. *Appl. Phys. Lett.* **2008**, *93*, 191113.
(4) Beck, F. J.; Polman, A.; Catchpole, K. R. *J. Appl. Phys.* **2009**, *105*, 114310.
(5) Jin, Y.; Feng, J.; Zhang, X.-L.; Xu, M.; Bi, Y.-G.; Chen, Q.-D.; Wang, H.-Y.; Sun, H.-B. *Appl. Phys. Lett.* **2012**, *101*, 163303.
(6) Hong, Y.; Huh, Y.-M.; Yoon, D. S.; Yang, J. *J. Nanomater.* **2012**, *2012*.
(7) Dmitriev, A.; Hägglund, C.; Chen, S.; Fredriksson, H.; Pakizeh, T.; Käll, M.; Sutherland, D. S. *Nano Lett.* **2008**, *8*, 3893–3898.
(8) Wu, L.; Bai, P.; Zhou, X.; Li, E. P. *IEEE Photon- J.* **2012**, *4*, 26–33.
(9) Stewart, M. E.; Anderton, C. R.; Thompson, L. B.; Maria, J.; Gray, S. K.; Rogers, J. A.; Nuzzo, R. G. *Chem. Rev.* **2008**, *108*, 494–521.
(10) Okada, N.; Hamanaka, Y.; Nakamura, A.; Pastoriza-Santos, I.; Liz-Marzán, L. M. *J. Phys. Chem. B* **2004**, *108*, 8751–8755.
(11) Kumar, K.; Duan, H.; Hegde, R. S.; Koh, S. C.; Wei, J. N.; Yang, J. K. *Nat. Nanotechnol.* **2012**, *7*, 557–561.
(12) Fakonas, J. S.; Lee, H.; Kelaita, Y. A.; Atwater, H. A. *Nat. Photon-* **2014**, *8*, 317–320.
(13) Altewischer, E.; Van Exter, M. P.; Woerdman, J. P. *Nature* **2002**, *418*, 304–306.
(14) Kreibig, U.; Vollmer, M. *Optical properties of metal clusters*; 1995.
(15) Kelly, K. L.; Coronado, E.; Zhao, L. L.; Schatz, G. C. *J. Phys. Chem. B* **2003**, *107*, 668–677.
(16) Chan, G. H.; Zhao, J.; Schatz, G. C.; Duyne, R. P. V. *J. Phys. Chem. C* **2008**, *112*, 13958–13963.
(17) Maier, S. A. 2007.
(18) Bohren, C. F.; Huffman, D. R. *Absorption and Scattering of Light by Small Particles*; 2008.
(19) Nagel, J. R.; Scarpulla, M. A. *Opt. Express* **2010**, *18*, 139.
(20) Oldenburg, S. J.; Hale, G. D.; Jackson, J. B.; Halas, N. J. *Appl. Phys. Lett.* **1999**, *75*, 1063.
(21) Mie, G. *Ann. der Phys.* **1908**, *330*, 377–445.
(22) Mie, G. *Ann. der Phys.* **1908**, *25*.
(23) Hao, E.; Schatz, G. C. *J. Chem. Phys.* **2003**, *120*, 357–366.
(24) Yang, J.; Rahmani, M.; Teng, J. H.; Hong, M. H. *Opt. Mater. Express* **2012**, *2*, 1407–1415.
(25) Rakic, A. D.; Djurišic, A. B.; Elazar, J. M.; Majewski, M. L. *Appl. Opt.* **1998**, *37*, 5271.
(26) Ehrenreich, H.; Philipp, H. R.; Segall, B. *Phys. Rev.* **1963**, *132*.
(27) Ehrenreich, H.; Philipp, H. R. *Phys. Rev.* **1962**, *128*.
(28) Tauc, J.; Abeles, F. *North-Holland, Amst.* **1972**.
(29) DuJardin, M.-M.; Theye, M.-L. *J. Phys. Chem. Solids* **1971**, *32*, 2033–1.
(30) Zorić, I.; Zäch, M.; Kasemo, B.; Langhammer, C. *ACS Nano* **2011**, *5*, 2535–2546.
(31) Christensen, N. E.; Seraphin, B. O. *Phys. Rev. B* **1971**, *4*.
(32) Reed, J. C.; Zhu, H.; Zhu, A. Y.; Li, C.; Cubukcu, E. *Nano Lett.* **2012**, *12*, 4090–4094.
(33) Knight, M. W.; King, N. S.; Liu, L.; Everitt, H. O.; Nordlander, P.; Halas, N. J. *ACS Nano* **2014**, *8*, 834–840.
(34) Naik, G. V.; Shalaev, V. M.; Boltasseva, A. *Adv. Mater.* **2013**, *25*, 3258–3258.
(35) Naik, G. V.; Schroeder, J. L.; Ni, X.; Kildishev, A. V.; Sands, T. D.; Boltasseva, A. *Opt. Mater. Express* **2012**, *2*, 478.

(36) Fang, Z.; Wang, Y.; Schlather, A. E.; Liu, Z.; Ajayan, P. M.; Abajo, F. J. G. de; Nordlander, P.; Zhu, X.; Halas, N. J. *Nano Lett.* **2014**, *14*, 299–304.
(37) Tassin, P.; Koschny, T.; Kafesaki, M.; Soukoulis, C. M. *Nat. Photon-* **2012**, *6*, 259–264.
(38) Tesler, A. B.; Chuntonov, L.; Karakouz, T.; Bendikov, T. A.; Haran, G.; Vaskevich, A.; Rubinstein, I. *J. Phys. Chem. C* **2011**, *115*, 24642–24652.
(39) Jensen, T.; Kelly, L.; Lazarides, A.; Schatz, G. C. *J. Clust. Sci.* **1999**, *10*, 295–317.
(40) Evanoff, D. D.; Chumanov, G. *J. Phys. Chem. B* **2004**, *108*, 13957–13962.
(41) Yeshchenko, O. A.; Dmitruk, I. M.; Alexeenko, A. A.; Kotko, A. V.; Verdal, J.; Pinchuk, A. O. *Plasmonics* **2012**, *7*, 685–694.
(42) Henson, J.; DiMaria, J.; Paiella, R. *J. Appl. Phys.* **2009**, *106*, 093111.
(43) Jensen, T. R.; Malinsky, M. D.; Haynes, C. L.; Duyne, R. P. V. *J. Phys. Chem. B* **2000**, *104*, 10549–10556.
(44) Haynes, C. L.; Duyne, R. P. V. *J. Phys. Chem. B* **2001**, *105*, 5599–5611.
(45) Haes, A. J.; Haynes, C. L.; McFarland, A. D.; Schatz, G. C.; Duyne, R. P. V.; Zou, S. *MRS Bull.* **2005**, *30*, 368–375.
(46) Wang, H.; Brandl, D. W.; Le, F.; Nordlander, P.; Halas, N. J. *Nano Lett.* **2006**, *6*, 827–832.
(47) Liu, X.; Choi, B.; Gozubenli, N.; Jiang, P. *J. Colloid Interface Sci.* **2013**, *409*, 52–58.
(48) Wu, L. Y.; Ross, B. M.; Lee, L. P. *Nano Lett.* **2009**, *9*, 1956–1961.
(49) Shumaker-Parry, J. S.; Rochholz, H.; Kreiter, M. *Adv. Mater.* **2005**, *17*, 2131–2134.
(50) Kedia, A.; Kumar, P. S. 2013; pp. 232–233.
(51) Khoury, C. G.; Vo-Dinh, T. *J. Phys. Chem. C* **2008**, *112*, 18849–18859.
(52) Rodríguez-Oliveros, R.; Sánchez-Gil, J. A. *Opt. Express* **2012**, *20*, 621.
(53) Tesler, A. B.; Maoz, B. M.; Feldman, Y.; Vaskevich, A.; Rubinstein, I. *J. Phys. Chem. C* **2013**, *117*, 11337–11346.
(54) Johnson, P.; Christy, R. *Phys. Rev. B* **1974**, *9*, 5056–5070.
(55) Trügler, A.; Tinguely, J.-C.; Jakopic, G.; Hohenester, U.; Krenn, J. R.; Hohenau, A. *Phys. Rev. B* **2014**, *89*.
(56) Tinguely, J.-C.; Sow, I.; Leiner, C.; Grand, J.; Hohenau, A.; Felidj, N.; Aubard, J.; Krenn, J. R. *BioNanoScience* **2011**, *1*, 128–135.
(57) Link, S.; El-Sayed, M. A. *J. Phys. Chem. B* **1999**, *103*, 4212–4217.
(58) Mock, J. J.; Smith, D. R.; Schultz, S. *Nano Lett.* **2003**, *3*, 485–491.
(59) Chen, H.; Kou, X.; Yang, Z.; Ni, W.; Wang, J. *Langmuir* **2008**, *24*, 5233–5237.
(60) Miller, M. M.; Lazarides, A. A. *J. Phys. Chem. B* **2005**, *109*, 21556–21565.
(61) Shen, Y.; Zhou, J.; Liu, T.; Tao, Y.; Jiang, R.; Liu, M.; Xiao, G.; Zhu, J.; Zhou, Z.-K.; Wang, X. *Nat. Commun.* **2013**, *4*.
(62) Lublow, M.; Lu, Y.; Wu, S. *J. Phys. Chem. C* **2012**, *116*, 8079–8088.
(63) Haes, A. J.; Zou, S.; Schatz, G. C.; Duyne, R. P. V. *J. Phys. Chem. B* **2004**, *108*, 6961–6968.
(64) Chan, G. H.; Zhao, J.; Hicks, E. M.; Schatz, G. C.; Van Duyne, R. P. *Nano Lett.* **2007**, *7*, 1947–1952.
(65) Sherry, L. J.; Jin, R.; Mirkin, C. A.; Schatz, G. C.; Van Duyne, R. P. *Nano Lett.* **2006**, *6*, 2060–2065.
(66) Malinsky, M. D.; Kelly, K. L.; Schatz, G. C.; Duyne, R. P. V. *J. Phys. Chem. B* **2001**, *105*, 2343–2350.
(67) Ghosh, S. K.; Pal, T. *Chem. Rev.* **2007**, *107*, 4797–4862.
(68) Aouani, H.; Wenger, J.; Gérard, D.; Rigneault, H.; Devaux, E.; Ebbesen, T. W.; Mahdavi, F.; Xu, T.; Blair, S. *ACS nano* **2009**, *3*, 2043–2048.
(69) Habteyes, T. G.; Dhuey, S.; Wood, E.; Gargas, D.; Cabrini, S.; Schuck, P. J.; Alivisatos,

A. P.; Leone, S. R. *Acs Nano* **2012**, *6*, 5702–5709.
(70) Pasquale, A. J.; Reinhard, B. M.; Dal Negro, L. *ACS nano* **2012**, *6*, 4341–4348.
(71) Ye, J.; Wen, F.; Sobhani, H.; Lassiter, J. B.; Dorpe, P. V.; Nordlander, P.; Halas, N. J. *Nano Lett.* **2012**, *12*, 1660–1667.
(72) Luk'yanchuk, B.; Zheludev, N. I.; Maier, S. A.; Halas, N. J.; Nordlander, P.; Giessen, H.; Chong, C. T. *Nat. Mater.* **2010**, *9*, 707–715.
(73) Liu, N.; Mukherjee, S.; Bao, K.; Li, Y.; Brown, L. V.; Nordlander, P.; Halas, N. J. *ACS nano* **2012**, *6*, 5482–5488.
(74) Maier, S. A.; Brongersma, M. L.; Kik, P. G.; Atwater, H. A. *Phys. Rev. B* **2002**, *65*.
(75) Adato, R.; Yanik, A. A.; Wu, C.-H.; Shvets, G.; Altug, H. *Opt. Express* **2010**, *18*, 4526.
(76) Rahmani, M.; Lei, D. Y.; Giannini, V.; Lukiyanchuk, B.; Ranjbar, M.; Liew, T. Y. F.; Hong, M.; Maier, S. A. *Nano Lett.* **2012**, *12*, 2101–2106.
(77) Wang, M.; Cao, M.; Guo, Z.; Gu, N. *J. Phys. Chem. C* **2013**, *117*, 11713–11717.
(78) Halas, N. J.; Lal, S.; Link, S.; Chang, W.-S.; Natelson, D.; Hafner, J. H.; Nordlander, P. *Adv. Mater.* **2012**, *24*, 4842–4877.
(79) Su, K.-H.; Wei, Q.-H.; Zhang, X.; Mock, J. J.; Smith, D. R.; Schultz, S. *Nano Lett.* **2003**, *3*, 1087–1090.
(80) Rechberger, W.; Hohenau, A.; Leitner, A.; Krenn, J. R.; Lamprecht, B.; Aussenegg, F. R. *Opt. Commun.* **2003**, *220*, 137–141.
(81) Tsai, C.-Y.; Lin, J.-W.; Wu, C.-Y.; Lin, P.-T.; Lu, T.-W.; Lee, P.-T. *Nano Lett.* **2012**, *12*, 1648–1654.
(82) Dregely, D.; Hentschel, M.; Giessen, H. *ACS Nano* **2011**, *5*, 8202–8211.
(83) Liu, S.-D.; Yang, Y.-B.; Chen, Z.-H.; Wang, W.-J.; Fei, H.-M.; Zhang, M.-J.; Wang, Y.-C. *J. Phys. Chem. C* **2013**, *117*, 14218–14228.
(84) Hentschel, M.; Dorfmüller, J.; Giessen, H.; Jäger, S.; Kern, A. M.; Braun, K.; Zhang, D.; Meixner, A. J. *Beilstein J. Nanotechnol.* **2013**, *4*, 57–65.
(85) Kottmann, J. P.; Martin, O. J. *Opt. Lett.* **2001**, *26*, 1096–1098.
(86) Jain, P. K.; Huang, W.; El-Sayed, M. A. *Nano Lett.* **2007**, *7*, 2080–2088.
(87) Jain, P. K.; El-Sayed, M. A. *Chem. Phys. Lett.* **2010**, *487*, 153–164.
(88) Jain, P. K.; El-Sayed, M. A. *Nano Lett.* **2008**, *8*, 4347–4352.
(89) Kinnan, M. K.; Kachan, S.; Simmons, C. K.; Chumanov, G. *J. Phys. Chem. C* **2009**, *113*, 7079–7084.
(90) Zou, S.; Schatz, G. C. *J. Chem. Phys.* **2004**, *121*, 12606.
(91) Rahmani, M.; Lukiyanchuk, B.; Ng, B.; Tavakkoli KG, A.; Liew, Y. F.; Hong, M. H. *Opt. Express* **2011**, *19*, 4949–4956.
(92) Rahmani, M.; Luk'yanchuk, B.; Hong, M. *Laser & Photon- Rev.* **2013**, *7*, 329–349.
(93) Lassiter, J. B.; Sobhani, H.; Knight, M. W.; Mielczarek, W. S.; Nordlander, P.; Halas, N. J. *Nano Lett.* **2012**, *12*, 1058–1062.
(94) Lassiter, J. B.; Sobhani, H.; Fan, J. A.; Kundu, J.; Capasso, F.; Nordlander, P.; Halas, N. J. *Nano Lett.* **2010**, *10*, 3184–3189.
(95) Krenn, J.; Dereux, A.; Weeber, J.; Bourillot, E.; Lacroute, Y.; Goudonnet, J.; Schider, G.; Gotschy, W.; Leitner, A.; Aussenegg, F.; Girard, C. *Phys. Rev. Lett.* **1999**, *82*, 2590–2593.
(96) Hohenau, A.; Leitner, A.; Aussenegg, F. R. In *Surface Plasmon Nanophotonics*; 2007; pp. 11–25.
(97) Salerno, M.; Krenn, J. R.; Hohenau, A.; Ditlbacher, H.; Schider, G.; Leitner, A.; Aussenegg, F. R. *Opt. Commun.* **2005**, *248*, 543–549.
(98) Lamprecht, B.; Schider, G.; Lechner, R.; Ditlbacher, H.; Krenn, J.; Leitner, A.; Aussenegg, F. *Phys. Rev. Lett.* **2000**, *84*, 4721–4724.
(99) Jiang, H.; Sabarinathan, J. *J. Phys. Chem. C* **2010**, *114*, 15243–15250.
(100) Wang, X.; Gogol, P.; Cambril, E.; Palpant, B. *J. Phys. Chem. C* **2012**, *116*, 24741–

24747.
(101) Chumanov, G.; Sokolov, K.; Cotton, T. M. *J. Phys. Chem.* **1996**, *100*, 5166–5168.
(102) Nishijima, Y.; Rosa, L.; Juodkazis, S. *Opt. Express* **2012**, *20*, 11466–11477.
(103) Chang, W.-S.; Slaughter, L. S.; Khanal, B. P.; Manna, P.; Zubarev, E. R.; Link, S. *Nano Lett.* **2009**, *9*, 1152–1157.
(104) Benson, O. *Nature* **2011**, *480*, 193–199.
(105) Najiminaini, M.; Vasefi, F.; Kaminska, B.; Carson, J. J. L. *Appl. Phys. Lett.* **2012**, *100*, 043105.
(106) Ebbesen, T. W.; Lezec, H. J.; Ghaemi, H. F.; Thio, T.; Wolff, P. A. *Nature* **1998**, *391*, 667–669.
(107) Gordon, R.; Brolo, A. G.; McKinnon, A.; Rajora, A.; Leathem, B.; Kavanagh, K. L. *Phys. Rev. Lett.* **2004**, *92*.
(108) Elliott, J.; Smolyaninov, I. I.; Zheludev, N. I.; Zayats, A. V. *Opt. Lett.* **2004**, *29*, 1414–1416.
(109) Koerkamp, K. K.; Enoch, S.; Segerink, F. B.; Van Hulst, N. F.; Kuipers, L. *Phys. Rev. Lett.* **2004**, *92*.
(110) Van der Molen, K. L.; Koerkamp, K. K.; Enoch, S.; Segerink, F. B.; Van Hulst, N. F.; Kuipers, L. *Phys. Rev. B* **2005**, *72*.
(111) Ellenbogen, T.; Seo, K.; Crozier, K. B. *Nano Lett.* **2012**, *12*, 1026–1031.
(112) Lovera, P.; Jones, D.; Corbett, B.; O'Riordan, A. *Opt. Express* **2012**, *20*, 25325–25332.
(113) Thio, T.; Ghaemi, H. F.; Lezec, H. J.; Wolff, P. A.; Ebbesen, T. W. *JOSA B* **1999**, *16*, 1743–1748.
(114) Reilly III, T. H.; Tenent, R. C.; Barnes, T. M.; Rowlen, K. L.; van de Lagemaat, J. *ACS nano* **2010**, *4*, 615–624.
(115) Correia-Ledo, D.; Gibson, K. F.; Dhawan, A.; Couture, M.; Vo-Dinh, T.; Graham, D.; Masson, J.-F. *J. Phys. Chem. C* **2012**, *116*, 6884–6892.
(116) Zhou, L.; Ding, F.; Chen, H.; Ding, W.; Zhang, W.; Chou, S. Y. *Anal. Chem.* **2012**, *84*, 4489–4495.
(117) Wen, X.; Xi, Z.; Jiao, X.; Yu, W.; Xue, G.; Zhang, D.; Lu, Y.; Wang, P.; Blair, S.; Ming, H. *Plasmonics* **2013**, *8*, 225–231.
(118) Aslan, K.; Gryczynski, I.; Malicka, J.; Matveeva, E.; Lakowicz, J. R.; Geddes, C. D. *Curr. Opin. Biotechnol.* **2005**, *16*, 55–62.
(119) Zhao, J.; Zhang, X.; Yonzon, C. R.; Haes, A. J.; Van Duyne, R. P. **2006**.
(120) Zhou, Z.; Huang, H.; Chen, Y.; Liu, F.; Huang, C. Z.; Li, N. *Biosens. Bioelectron.* **2014**, *52*, 367–373.
(121) Turner, A. P. *Chem. Soc. Rev.* **2013**, *42*, 3184–3196.
(122) Matoian, M. A.; Sweetman, R.; Hall, E. C.; Albanese, S.; Euler, W. B. *J. Fluoresc.* **2013**, *23*, 877–880.
(123) Qian, X.; Peng, X.-H.; Ansari, D. O.; Yin-Goen, Q.; Chen, G. Z.; Shin, D. M.; Yang, L.; Young, A. N.; Wang, M. D.; Nie, S. *Nat. Biotechnol.* **2008**, *26*, 83–90.
(124) Hong, G.; Lee, J. C.; Robinson, J. T.; Raaz, U.; Xie, L.; Huang, N. F.; Cooke, J. P.; Dai, H. *Nat. Med.* **2012**, *18*, 1841–1846.
(125) Smith, A. M.; Mancini, M. C.; Nie, S. *Nat. Nanotechnol.* **2009**, *4*.
(126) Robinson, J. T.; Hong, G.; Liang, Y.; Zhang, B.; Yaghi, O. K.; Dai, H. *J. Am. Chem. Soc.* **2012**, *134*, 10664–10669.
(127) Bashkatov, A. N.; Genina, E. A.; Kochubey, V. I.; Tuchin, V. V. *J. Phys. D: Appl. Phys.* **2005**, *38*.
(128) Welsher, K.; Liu, Z.; Sherlock, S. P.; Robinson, J. T.; Chen, Z.; Daranciang, D.; Dai, H. *Nat. Nanotechnol.* **2009**, *4*, 773–780.
(129) Aubin, J. E. *J. Histochem. & Cytochem.* **1979**, *27*, 36–43.

(130) Frangioni, J. V. *Curr. Opin. Chem. Biol.* **2003**, *7*, 626–634.
(131) Sordillo, L. A.; Pu, Y.; Pratavieira, S.; Budansky, Y.; Alfano, R. R. *J. Biomed. Opt.* **2014**, *19*, 56004–56004.
(132) Salo, D.; Zhang, H.; Kim, D. M.; Berezin, M. Y. *J. Biomed. Opt.* **2014**, *19*, 086008–086008.
(133) Taik Lim, Y.; Kim, S.; Nakayama, A.; Stott, N. E.; Bawendi, M. G.; Frangioni, J. V. *Mol. Imaging* **2003**, *2*.
(134) Zhang, Y.; Hong, G.; Zhang, Y.; Chen, G.; Li, F.; Dai, H.; Wang, Q. *ACS Nano* **2012**, *6*, 3695–3702.
(135) Tao, Z.; Hong, G.; Shinji, C.; Chen, C.; Diao, S.; Antaris, A. L.; Zhang, B.; Zou, Y.; Dai, H. *Angew. Chem.* **2013**, *125*, 13240–13244.
(136) Pansare, V. J.; Hejazi, S.; Faenza, W. J.; Prud'homme, R. K. *Chem. Mater.* **2012**, *24*, 812–827.
(137) Escobedo, J. O.; Rusin, O.; Lim, S.; Strongin, R. M. *Curr. Opin. Chem. Biol.* **2010**, *14*, 64–70.
(138) Luo, S.; Zhang, E.; Su, Y.; Cheng, T.; Shi, C. *Biomaterials* **2011**, *32*, 7127–7138.
(139) Joseph, R. L.; Lakowicz, R. *Kluwer Acad. Publ. New York* **1999**.
(140) Stokes, G. G. *Philos. Trans. R. Soc. Lond.* **1852**, 463–562.
(141) Purcell, E. M.; Torrey, H. C.; Pound, R. V. *Phys. Rev.* **1946**, *69*.
(142) Giannini, V.; Fernandez-Dominguez, A. I.; Heck, S. C.; Maier, S. A. *Chem. Rev.* **2011**, *111*, 3888–3912.
(143) Loudon, R. *The quantum theory of light*; 2000.
(144) Merzbacher, E. *John Wiler & Sons, New York Zbl0102* **1977**, *42701*.
(145) Xie, F.; Baker, M. S.; Goldys, E. M. *J. Phys. Chem. B* **2006**, *110*, 23085–23091.
(146) Bauch, M.; Toma, K.; Toma, M.; Zhang, Q.; Dostalek, J. *Plasmonics* **2013**, 1–19.
(147) Gandra, N.; Portz, C.; Tian, L.; Tang, R.; Xu, B.; Achilefu, S.; Singamaneni, S. *Angew. Chem.* **2014**, *126*, 885–889.
(148) Xie, F.; Centeno, A.; Ryan, M. R.; Riley, D. J.; Alford, N. M. *J. Mater. Chem. B* **2012**, *1*, 536.
(149) Kühn, S.; Håkanson, U.; Rogobete, L.; Sandoghdar, V. *Phys. Rev. Lett.* **2006**, *97*.
(150) Xie, F.; Pang, J. S.; Centeno, A.; Ryan, M. P.; Riley, D. J.; Alford, N. M. *Nano Res.* **2013**, *6*, 496–510.
(151) Geddes, C. D.; Lakowicz, J. R. *J. Fluoresc.* **2002**, *12*, 121–129.
(152) Kinkhabwala, A.; Yu, Z.; Fan, S.; Avlasevich, Y.; Müllen, K.; Moerner, W. E. *Nat. Photon-* **2009**, *3*, 654–657.
(153) Geddes, C. D. *Metal-enhanced fluorescence*; 2010.
(154) Chen, Y.; Munechika, K.; Ginger, D. S. *Nano Lett.* **2007**, *7*, 690–696.
(155) Lakowicz, J. R. *Anal. Biochem.* **2005**, *337*, 171–194.
(156) Bharadwaj, P.; Novotny, L. *Opt. Express* **2007**, *15*, 14266–14274.
(157) Yuan, H.; Khatua, S.; Zijlstra, P.; Yorulmaz, M.; Orrit, M. *Angew. Chem.* **2013**, *125*, 1255–1259.
(158) Huang, X.; El-Sayed, I. H.; El-Sayed, M. A. 2010; pp. 573–599.
(159) Swathi, R. S.; Sebastian, K. L. *J. Chem. Phys.* **2007**, *126*.
(160) Chatterjee, S.; Lee, J. B.; Valappil, N. V.; Luo, D.; Menon, V. M. *Biomed. Opt. Express* **2011**, *2*, 1727–1733.
(161) Malicka, J.; Gryczynski, I.; Gryczynski, Z.; Lakowicz, J. R. *Anal. Biochem.* **2003**, *315*, 57–66.
(162) Ray, K.; Badugu, R.; Lakowicz, J. R. *Chem. Mater.* **2007**, *19*, 5902–5909.
(163) Ray, K.; Badugu, R.; Lakowicz, J. R. *Langmuir* **2006**, *22*, 8374–8378.
(164) Ray, K.; Badugu, R.; Lakowicz, J. R. *J. Phys. Chem. C* **2007**, *111*, 7091–7097.

(165) Zhang, J.; Fu, Y.; Lakowicz, J. R. *J. Phys. Chem. C* **2007**, *111*, 50–56.
(166) Dragan, A. I.; Bishop, E. S.; Casas-Finet, J. R.; Strouse, R. J.; McGivney, J.; Schenerman, M. A.; Geddes, C. D. *Plasmonics* **2012**, *7*, 739–744.
(167) Mishra, H.; Mali, B. L.; Karolin, J.; Dragan, A. I.; Geddes, C. D. *Phys. Chem. Chem. Phys.* **2013**, *15*, 19538–19544.
(168) Cheng, D.; Xu, Q.-H. *Chem. Commun.* **2007**, 248–250.
(169) Tovmachenko, O. G.; Graf, C.; van den Heuvel, D. J.; van Blaaderen, A.; Gerritsen, H. C. *Adv. Mater.* **2006**, *18*, 91–95.
(170) Stoermer, R. L.; Keating, C. D. *J. Am. Chem. Soc.* **2006**, *128*, 13243–13254.
(171) Zhou, F.; Li, Z.-Y.; Liu, Y.; Xia, Y. *J. Phys. Chem. C* **2008**, *112*, 20233–20240.
(172) Deng, W.; Xie, F.; Baltar, H. T.; Goldys, E. M. *Phys. Chem. Chem. Phys.* **2013**, *15*, 15695–15708.
(173) Hong, G.; Tabakman, S. M.; Welsher, K.; Wang, H.; Wang, X.; Dai, H. *J. Am. Chem. Soc.* **2010**, *132*, 15920–15923.
(174) Xie, F.; Baker, M. S.; Goldys, E. M. *Chem. Mater.* **2008**, *20*, 1788–1797.
(175) Bardhan, R.; Grady, N. K.; Cole, J. R.; Joshi, A.; Halas, N. J. *ACS Nano* **2009**, *3*, 744–752.
(176) Deng, W.; Jin, D.; Drozdowicz-Tomsia, K.; Yuan, J.; Wu, J.; Goldys, E. M. *Adv. Mater.* **2011**, *23*, 4649–4654.
(177) Ayala Orozco, C.; Liu, J. G.; Knight, M. W.; Wang, Y.; Day, J.; Nordlander, P.; Halas, N. J. *Nano Lett.* **2014**.
(178) Ju, J.; Byeon, E.; Han, Y.-A.; Kim, S.-M. *Micro & Nano Lett. IET* **2013**, *8*.
(179) Pompa, P. P.; Martiradonna, L.; Torre, A. D.; Sala, F. D.; Manna, L.; Vittorio, M. D.; Calabi, F.; Cingolani, R.; Rinaldi, R. *Nat. Nanotechnol.* **2006**, *1*, 126–130.
(180) Wong, T. I.; Han, S.; Wu, L.; Wang, Y.; Deng, J.; Tan, C. Y. L.; Bai, P.; Loke, Y. C.; Da Yang, X.; Tse, M. S. *Lab Chip* **2013**, *13*, 2405–2413.
(181) Brolo, A. G.; Kwok, S. C.; Moffitt, M. G.; Gordon, R.; Riordon, J.; Kavanagh, K. L. *J. Am. Chem. Soc.* **2005**, *127*, 14936–14941.
(182) Ray, K.; Lakowicz, J. R. *J. Phys. Chem. C* **2013**, *117*, 15790–15797.
(183) Haynes, C. L.; McFarland, A. D.; Smith, M. T.; Hulteen, J. C.; Duyne, R. P. V. *J. Phys. Chem. B* **2002**, *106*, 1898–1902.
(184) Fredriksson, H.; Alaverdyan, Y.; Dmitriev, A.; Langhammer, C.; Sutherland, D. S.; Zäch, M.; Kasemo, B. *Adv. Mater.* **2007**, *19*, 4297–4302.
(185) Kosiorek, A.; Kandulski, W.; Glaczynska, H.; Giersig, M. *Small* **2005**, *1*, 439–444.
(186) Feng, H. Y.; Luo, F.; Kekesi, R.; Granados, D.; Meneses-Rodríguez, D.; García, J. M.; García-Martín, A.; Armelles, G.; Cebollada, A. *Adv. Opt. Mater.* **2014**.
(187) Chang, Y.-C.; Lu, S.-C.; Chung, H.-C.; Wang, S.-M.; Tsai, T.-D.; Guo, T.-F. *Sci. reports* **2013**, *3*.
(188) Masson, J.-F.; Murray-Méthot, M.-P.; Live, L. S. *Analyst* **2010**, *135*, 1483–1489.
(189) Zhang, X. A.; Elek, J.; Chang, C.-H. *ACS Nano* **2013**, *7*, 6212–6218.
(190) Fischer, U. C. *J. Vac. Sci. Technol.* **1981**, *19*, 881.
(191) Deckman, H. W. *J. Vac. Sci. & Technol. B: Microelectron. Nanom. Struct.* **1983**, *1*, 1109.
(192) Sung, J.; Hicks, E. M.; Duyne, R. P. V.; Spears, K. G. *J. Phys. Chem. C* **2008**, *112*, 4091–4096.
(193) Jensen, T. R.; Duval, M. L.; Kelly, K. L.; Lazarides, A. A.; Schatz, G. C.; Duyne, R. P. V. *J. Phys. Chem. B* **1999**, *103*, 9846–9853.
(194) Hulteen, J. C.; Van Duyne, R. P. *J. Vac. Sci. & Technol.* **1995**, *13*, 1553–1558.
(195) Haes, A. J.; Haynes, C. L.; Van Duyne, R. P. In *MRS Proceedings*; 2000; Vol. 636.
(196) Kosiorek, A.; Kandulski, W.; Chudzinski, P.; Kempa, K.; Giersig, M. *Nano Lett.* **2004**,

4, 1359–1363.
(197) Chang, C.-M.; Shiao, M.-H.; Chiang, D.; Yang, C.-T.; Huang, M.-J.; Hsueh, W.-J. *Met. Mater. Int.* **2013**, *19*, 869–874.
(198) Chang, Y.-C.; Tseng, C.-B. *Plasmonics* **2013**, *8*, 1395–1400.
(199) Li, S.; Yang, Z.; Zhang, Z.; Gao, F.; Du, J.; Zhang, S. *J. Appl. Phys.* **2013**, *113*, 183102.
(200) Vogel, N.; Goerres, S.; Landfester, K.; Weiss, C. K. *Macromol. Chem. Phys.* **2011**, *212*, 1719–1734.
(201) Shiu, J.-Y.; Kuo, C.-W.; Chen, P.; Mou, C.-Y. *Chem. Mater.* **2004**, *16*, 561–564.
(202) Vogel, N.; Weiss, C. K.; Landfester, K. *Soft Matter* **2012**, *8*, 4044–4061.
(203) Khanh, N. N.; Yoon, K. B. *J. Am. Chem. Soc.* **2009**, *131*, 14228–14230.
(204) Chang, Y.-C.; Wang, S.-M.; Chung, H.-C.; Tseng, C.-B.; Chang, S.-H. *Acs Nano* **2012**, *6*, 3390–3396.
(205) Járai-Szabó, F.; A\cstilean, S.; Néda, Z. *Chem. Phys. Lett.* **2005**, *408*, 241–246.
(206) Wang, L.; Wan, Y.; Li, Y.; Cai, Z.; Li, H.-L.; Zhao, X. S.; Li, Q. *Langmuir* **2009**, *25*, 6753–6759.
(207) Choi, Y.; Hong, S.; Lee, L. P. *Nano Lett.* **2009**, *9*, 3726–3731.
(208) Winzer, M.; Kleiber, M.; Dix, N.; Wiesendanger, R. *Appl. Phys.* **1996**, *63*, 617–619.
(209) Hulteen, J. C.; Treichel, D. A.; Smith, M. T.; Duval, M. L.; Jensen, T. R.; Van Duyne, R. P. *J. Phys. Chem. B* **1999**, *103*, 3854–3863.
(210) Chen, J.; Dong, P.; Di, D.; Wang, C.; Wang, H.; Wang, J.; Wu, X. *Appl. Surf. Sci.* **2013**, *270*, 6–15.
(211) Cai, Z.; Teng, J.; Xia, D.; Zhao, X. S. *J. Phys. Chem. C* **2011**, *115*, 9970–9976.
(212) Yu, J.; Yan, Q.; Shen, D. *ACS Appl. Mater. & interfaces* **2010**, *2*, 1922–1926.
(213) Hsu, C.-M.; Connor, S. T.; Tang, M. X.; Cui, Y. *Appl. Phys. Lett.* **2008**, *93*, 133109.
(214) Sirotkin, E.; Apweiler, J. D.; Ogrin, F. Y. *Langmuir* **2010**, *26*, 10677–10683.
(215) Yu, J.; Geng, C.; Zheng, L.; Ma, Z.; Tan, T.; Wang, X.; Yan, Q.; Shen, D. *Langmuir* **2012**, *28*, 12681–12689.
(216) Vogel, N.; de Viguerie, L.; Jonas, U.; Weiss, C. K.; Landfester, K. *Adv. Funct. Mater.* **2011**, *21*, 3064–3073.
(217) Vig, J. R. *J. Vac. Sci. & Technol.* **1985**, *3*, 1027–1034.
(218) Ting, Y.-H.; Liu, C.-C.; Park, S.-M.; Jiang, H.; Nealey, P. F.; Wendt, A. E. *Polymers* **2010**, *2*, 649–663.
(219) Yan, W.-G.; Kong, X.-T.; Li, Z.-B.; Tian, J.-G. *J. Nanosci. Nanotechnol.* **2013**, *13*, 4311–4315.
(220) Luo, H.; Liu, T.; Ma, J.; Wang, W.; Li, H.; Wang, P.; Bai, J.; Jing, G. *Mater. Sci.* **2013**, *31*, 331–337.
(221) Soleimani-Amiri, S.; Gholizadeh, A.; Rajabali, S.; Sanaee, Z.; Mohajerzadeh, S. *RSC Adv.* **2014**, *4*, 12701–12709.
(222) Zheng, Y. B.; Juluri, B. K.; Mao, X.; Walker, T. R.; Huang, T. J. *J. Appl. Phys.* **2008**, *103*, 014308.
(223) Plettl, A.; Enderle, F.; Saitner, M.; Manzke, A.; Pfahler, C.; Wiedemann, S.; Ziemann, P. *Adv. Funct. Mater.* **2009**, *19*, 3279–3284.
(224) Engelmann, S.; Bruce, R. L.; Weilnboeck, F.; Oehrlein, G. S.; Nest, D.; Graves, D. B.; Andes, C.; Hudson, E. A. *Plasma Process. Polym.* **2009**, *6*, 484–489.
(225) Kolle, M. *Photonic structures inspired by nature*; 2011.
(226) Lewicka, Z. A.; Bahloul, A.; Yu, W. W.; Colvin, V. L. *Nanoscale* **2013**, *5*, 11071.
(227) Wang, X.; Lao, C.; Graugnard, E.; Summers, C. J.; Wang, Z. L. *Nano Lett.* **2005**, *5*, 1784–1788.
(228) Lieberman, M. A.; Lichtenberg, A. J. *Principles of Plasma Discharges and Materials Processing*; 2005.

(229) Technics Ion Mill Etch Rates.
(230) Williams, K. R.; Gupta, K.; Wasilik, M. *Microelectromechanical Syst. J.* **2003**, *12*, 761–778.
(231) Bruce, R. L.; Weilnboeck, F.; Lin, T.; Phaneuf, R. J.; Oehrlein, G. S.; Long, B. K.; Willson, C. G.; Vegh, J. J.; Nest, D.; Graves, D. B. *J. Appl. Phys.* **2010**, *107*.
(232) Végh, J. J.; Nest, D.; Graves, D. B.; Bruce, R.; Engelmann, S.; Kwon, T.; Phaneuf, R. J.; Oehrlein, G. S.; Long, B. K.; Willson, C. G. *Appl. Phys. Lett.* **2007**, *91*, 233113.
(233) Usami, R.; Sakamoto, N.; Shinozaki, K.; Suzuki, H.; Wakiya, N. *Sci. Technol. Adv. Mater.* **2011**, *12*.
(234) Lei, Y.; Yang, S.; Wu, M.; Wilde, G. *Chem. Soc. Rev.* **2011**, *40*, 1247–1258.
(235) Rindzevicius, T.; Alaverdyan, Y.; Dahlin, A.; Höök, F.; Sutherland, D. S.; Käll, M. *Nano Lett.* **2005**, *5*, 2335–2339.
(236) Zhao, J.; Frank, B.; Burger, S.; Giessen, H. *ACS nano* **2011**, *5*, 9009–9016.
(237) Berezin, M. Y.; Achilefu, S. *Chem. Rev.* **2010**, *110*, 2641–2684.
(238) Marcello, A.; Sblattero, D.; Cioarec, C.; Maiuri, P.; Melpignano, P. *Biosens. Bioelectron.* **2013**, *46*, 44–47.
(239) Lichtman, J. W.; Conchello, J.-A. *Nat. methods* **2005**, *2*, 910–919.
(240) Wei, Q.; Qi, H.; Luo, W.; Tseng, D.; Ki, S. J.; Wan, Z.; Göröcs, Z.; Bentolila, L. A.; Wu, T.-T.; Sun, R. *ACS nano* **2013**, *7*, 9147–9155.
(241) Zhang, J.; Lakowicz, J. R. *Opt. Express* **2007**, *15*, 2598–2606.
(242) Dragan, A. I.; Geddes, C. D. *Appl. Phys. Lett.* **2012**, *100*.
(243) Liebermann, T.; Knoll, W. *Colloids Surfaces A: Physicochem. Eng. Asp.* **2000**, *171*, 115–130.
(244) Grabar, K. C.; Freeman, R. G.; Hommer, M. B.; Natan, M. J. *Anal. Chem.* **1995**, *67*, 735–743.
(245) Duan, H.; Fernández-Domínguez, A. I.; Bosman, M.; Maier, S. A.; Yang, J. K. W. *Nano Lett.* **2012**, *12*, 1683–1689.
(246) Chang, Y.-C.; Chung, H.-C.; Lu, S.-C.; Guo, T.-F. *Nanotechnology* **2013**, *24*.
(247) Pinchuk, A. O.; Schatz, G. C. *Mater. Sci. Eng.* **2008**, *149*, 251–258.
(248) Haynes, C. L.; McFarland, A. D.; Zhao, L.; Duyne, R. P. V.; Schatz, G. C.; Gunnarsson, L.; Prikulis, J.; Kasemo, B.; Käll, M. *J. Phys. Chem. B* **2003**, *107*, 7337–7342.
(249) Martin-Moreno, L.; Garcia-Vidal, F. J.; Lezec, H. J.; Pellerin, K. M.; Thio, T.; Pendry, J. B.; Ebbesen, T. W. *Phys. Rev. Lett.* **2001**, *86*.
(250) Cheng, K.; Wang, S.; Cui, Z.; Li, Q.; Dai, S.; Du, Z. *Appl. Phys. Lett.* **2012**, *100*, 253101.
(251) Wu, L.; Bai, P.; Zhou, X.; Li, E. P. *IEEE Photon- J.* **2012**, *4*, 26–33.
(252) Lodewijks, K.; Ryken, J.; Van Roy, W.; Borghs, G.; Lagae, L.; Van Dorpe, P. *Plasmonics* **2013**, *8*, 1379–1385.
(253) Danos, L.; Markvart, T. *Chem. Phys. Lett.* **2010**, *490*, 194–199.
(254) Biagioni, P.; Huang, J.-S.; Hecht, B. *Reports Prog. Phys.* **2012**, *75*.
(255) Aslan, K.; Malyn, S. N.; Geddes, C. D. *Analyst* **2007**, *132*, 1112–1121.
(256) Aslan, K.; Malyn, S. N.; Geddes, C. D. *J. Fluoresc.* **2007**, *17*, 7–13.
(257) Malynych, S.; Chumanov, G. *J. Am. Chem. Soc.* **2003**, *125*, 2896–2898.
(258) Lifetechnologies. Fluorescence SpectraViewer https://www.lifetechnologies.com/uk/en/home/life-science/cell-analysis/labeling-chemistry/fluorescence-spectraviewer.html (accessed 2014).
(259) Geddes, C. D.; Parfenov, A.; Roll, D.; Gryczynski, I.; Malicka, J.; Lakowicz, J. R. *J. Fluoresc.* **2003**, *13*, 267–276.
(260) Tead, S. F.; Vanderlinde, W. E.; Marra, G.; Ruoff, A. L.; Kramer, E. J.; Egitto, F. D. *J. Appl. Phys.* **1990**, *68*, 2972–2982.

(261) Végh, J. J.; Nest, D.; Graves, D. B.; Bruce, R.; Engelmann, S.; Kwon, T.; Phaneuf, R. J.; Oehrlein, G. S.; Long, B. K.; Willson, C. G. *J. Appl. Phys.* **2008**, *104*, 034308.
(262) Wen, F.; Ye, J.; Liu, N.; Van Dorpe, P.; Nordlander, P.; Halas, N. J. *Nano Lett.* **2012**, *12*, 5020–5026.
(263) Li, X.; Wang, T.; Zhang, J.; Yan, X.; Zhang, X.; Zhu, D.; Li, W.; Zhang, X.; Yang, B. *Langmuir* **2009**, *26*, 2930–2936.
(264) Jiang, P.; Zhu, C.-N.; Zhang, Z.-L.; Tian, Z.-Q.; Pang, D.-W. *Biomaterials* **2012**, *33*, 5130–5135.
(265) Haes, A. J.; Van Duyne, R. P. *Anal. Bioanal. Chem.* **2004**, *379*, 920–930.
(266) Tanabe, K. *J. Phys. Chem. C* **2008**, *112*, 15721–15728.

Appendix

A. 1 Mind Map

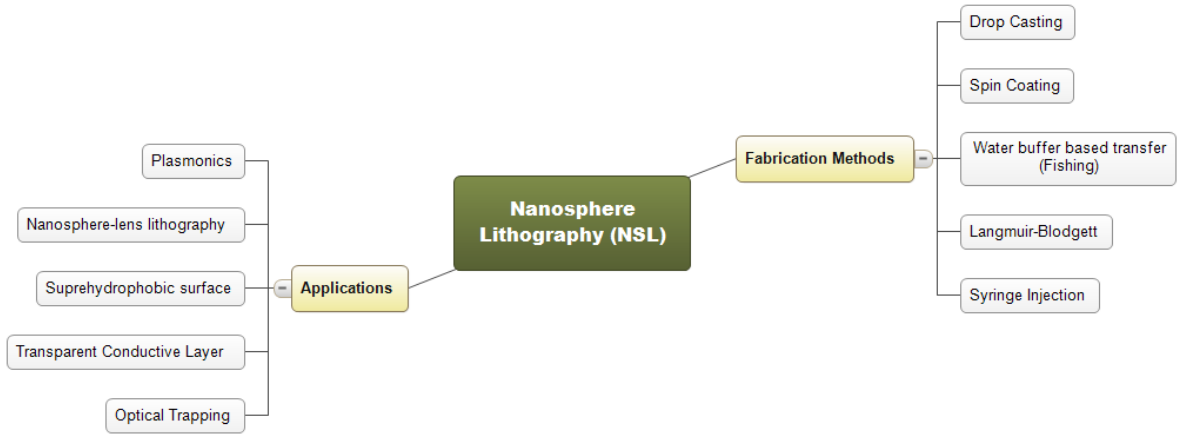

Figure A 1 A mind map diagram showing different variety of nanosphere lithography deposition techniques and some main applications that are currently being researched and developed.

A. 2 Standard Operating Procedure (SOP)

A.2.1 SOP of fishing technique

Steps:

1. Clean transfer substrates (few pieces of medium size silicon wafer) and sample substrates as required. (Sonication in Acetone, DI water, IPA for 10 mins each).
2. Oxygen plasma substrate for 5 – 30 mins. (An initial process time of 30 mins is recommended). Note that if treated substrates are left in air for more than 30 mins, this step needs to be repeated.
3. Stir the PS solution in the source bottle for approximately 2 mins, and then transfer required solution to a clean vial. (Do not sonicate as it may damage the solution).
4. Add equal amount of absolute ethanol into the vial. Sonicate for approx. 30 sec. May repeat this step if the solution has been left in room temp for more than 1.5 hours. Alternatively, keeps the mixed solution constantly stirring.
5. Spreads 6 – 7 µl of mix solution on the transfer substrate by touching the tip on the substrate, dragging it down vertically almost reaching the water surface. Drag a few times over the substrate surface to have big coverage. Note that the larger the coverage, the better the monolayer formation on DI water it will produces, i.e. larger monolayer island. However, too much solution will results in aggregation of the PS.
6. Let the solution dry out while excess PS mixture flow into the first beaker filled with DI water.

7. Once the transfer substrate surface is dried, dip it into the second beaker containing DI water steadily, guided by the circumference of the beaker. Turbulence produced on the surface will cause aggregation or break up the existing PS monolayer. Immersion of the transfer substrate fully into the water helps prevent the PS layer floating on top of the DI water from absorbing back onto the transfer substrate. The transfer substrate can then be removed after transfer of the PS layer.
8. In order to use the transfer substrate again, spray DI water on to the transfer substrate and blow with air to remove PS leftover on top of the substrate.
9. Step 6 – 9 can be repeated many times until a good coverage of PS monolayer formed on the second water beaker.
10. Add 2 – 4 μl of 2% wt. SDS solution on four sides of the beaker to help converging the PS into a bigger grain. Large PS coverage and the surface tension induced by the surfactant can help deposition of PS layer onto the sample. (Otherwise, the PS could slip out from the sample surface when it is being pull up from the DI water bath).
11. Different PS size will produce different colour under different light source. Please see the table X below for colour indication of monolayer formed.
12. Use a narrow tweezer to hold the sample substrate and insert it into an area without PS. Slowly manoeuvre the sample until it is underneath a good area of PS monolayer island. Pull it upward slowly (too fast will cause disturbance across the water surface and break existing PS grains), while maintaining almost horizontal if possible (this is to improve the PS packing on the sample surface).
13. Use a clean paper (preferably clean room grade) to absorb excess water on the sample surface by tapping it gently on a corner while holding the sample substrate and tilt it from horizontal to almost vertical position. Reduce the excess water reduce the effect of coffee stain effects when drying.
14. Leave the samples to dry at approximately 30°-45° relative to horizontal plain.
15. The samples are ready once it is dried.

Colour (On glass and on Silicon):

PS Size (nm)	Estimated Reflectance Wavelength*	Colour Inspected from Silicon Substrate
210	565, 282	Golden
290	780, 390	Purple
400	1076, 538	Green
500	1345, 672	Green
620	1667, 834	
800	2151, 1076	
1050	2824, 1412	-

* calculation based on Macromol. Chem. Phys. 2011, 212, 1719-1734.

Notes:

Further improvement for the process can be done by using higher pH solution bath, e.g. pH9 for PS620 and larger.

A.2.2 SOP for SEM area and disc diameter calculation

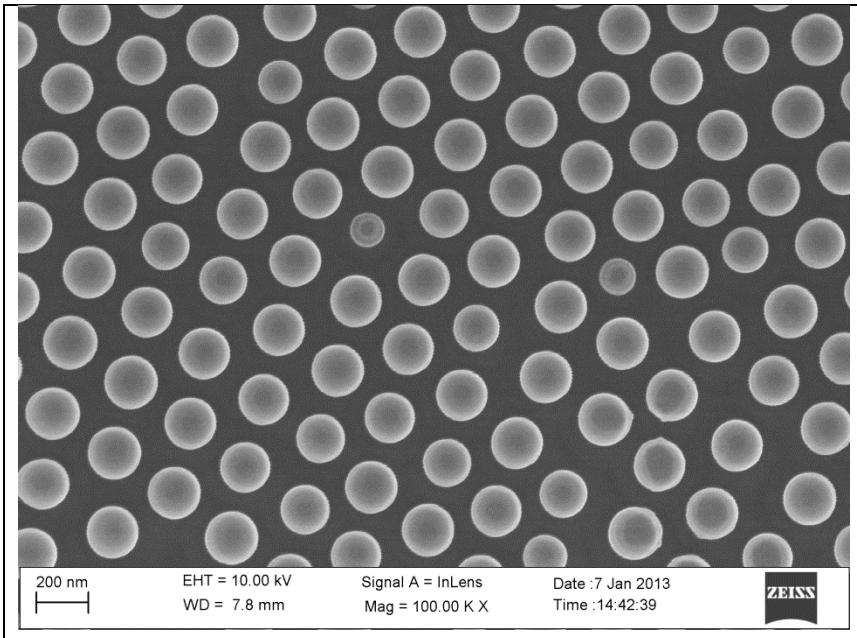	**Original Image** 20130107 PG Expt/1-SiC20sO235mIM-05
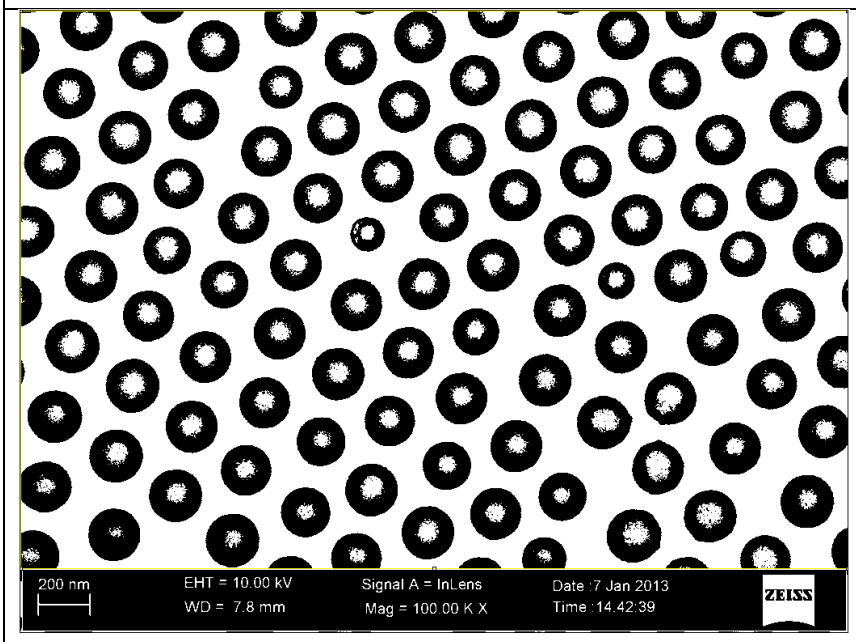	**Convert to a binary image** Steps: Open With ImageJ Smooth Invert (not necessary sometimes) Make 8 – bit (Image -> Type _> 8-bit. Set Measurement Scale (Analyse -> Set Scale) and confirm by drawing a line. Process -> Binary -> Make Binary Optional: Process – Smoothen, Binary options (e.g. watershed, dilated, etc.)

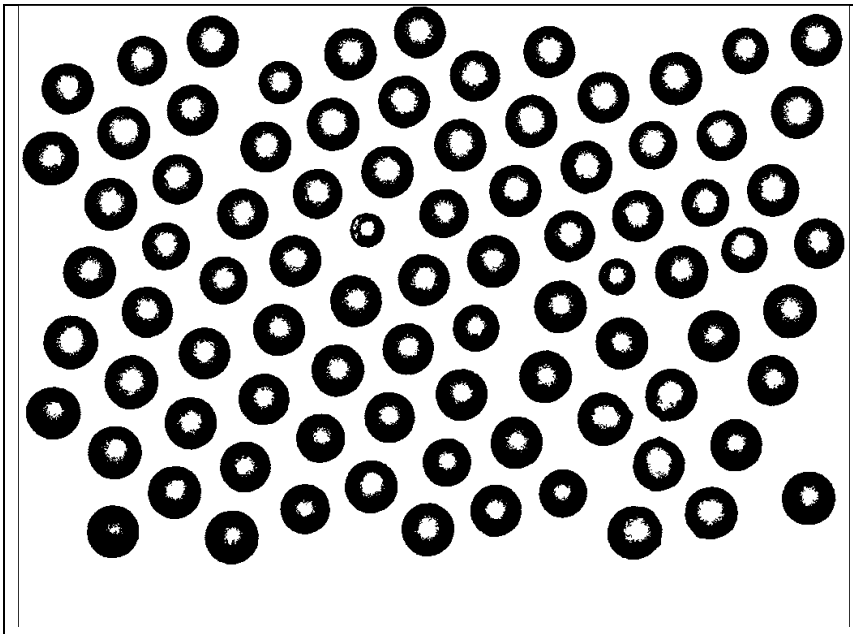	**Analyse** Optional: Set thresehold. Drag and select region of interest (e.g. exclude the information region.) Analyse -> Analyse Particle Check Show outline, exclude on edges, Display Results, Summarize, and Record Stats. (May also need to include holes in certain cases) In this image, circularity of 0.6 – 1.0 size of 100+(nm) – Infinity has been chosen to remove small particles and large defects.

A table of summary (figure below) should appear after the steps above have been executed and provide useful information to user.

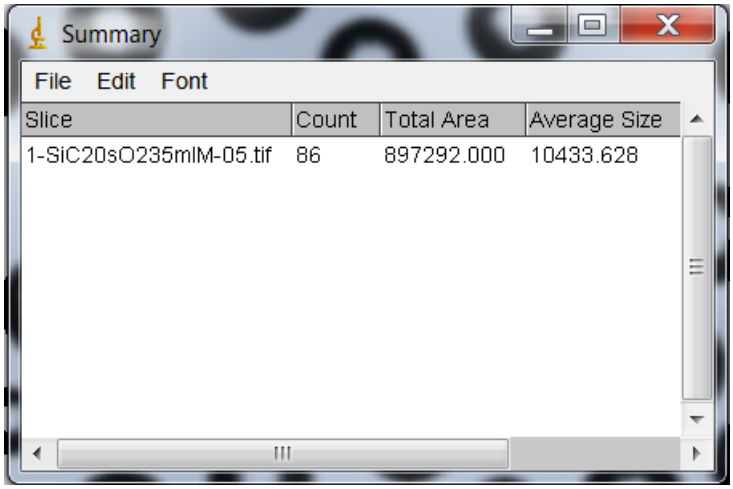

A.2.3 SOP for Oxygen Plasma Process to reduce PS size

	System: Sentech Etchlab 200 Recipe: 1. High Vacuum and hold for 5 minutes. 2. Inject oxygen at 20 sccm flow rate. 3. Hold reactor pressure at 20 Pa for 3 minutes. 4. RF power at 100 W for fixed duration specific to user requirement. 5. High vacuum and hold for 1 munute. 6. Vent reactor.

A.2.4 SOP for protein conjugation

Recipe for **bBSA and AF-SA conjugation** on 1 cm x 1.3 cm substrate (volume of the solutions will need to be adjusted accordingly if the dimension of the substrate is different)

1. Treating the substrate to be hydrophilic
    a. UV-Ozone 10 mins or
    b. Piranha solution
2. bBSA attachment
    a. Drop cast 28 µl bBSA (100 mg/ml mixed in sodium phosphate buffer (PBS), 50 mM, PH 7.2) onto the sample covering almost the whole top surface.
    b. Drop approx. 50 µl of DI water around the samples and cover up the samples and the water together under a petri dish. This is to create a humid environment and prevent formation of multilayer when bBSA dry up on the sample surface.
    c. Incubate for 1 hour.
3. Rinse excess bBSA
    a. Rinse with approx. 50ul PBS and dry with tissues multiple times (I usually repeat 5 – 7 times)
    b. Blow dry (blowing the air in the direction toward the tweezer at the other end helps to prevent excess unbounded bBSA solution from coating additional layer on the sample).
4. AF-SA attachment
    a. Drop cast 40 µl (25 µg/ml) onto the sample covering almost the whole top surface. [Note: This concentration is more than enough for full coverage of monolayer on sample surface. Concentration of streptavidin also has an effect on optical response in the system[265].]

b. Drop approx. 50 µl of DI water around the samples and cover up the samples and the water together under a petri dish. This is to create a humid environment and prevent formation of multilayer when bBSA dry up on the sample surface.
c. Incubate for 2 hours

5. Rinse excess AF-SA (same as step 3)
   a. Rinse with approx. 50 µl PBS and dry with tissues multiple times (I usually repeat 5 – 7 times)
   b. Blow dry (blowing the air in the direction toward the tweezer at the other end helps to prevent excess unbounded bBSA solution from coating additional layer on the sample).

A. 3 Equations

Refractive index	$\tilde{n} = n + ik$
Refractive index of EM radiation	$n = \sqrt{\epsilon_r \mu_r}$
Complex dielectric constant	$\tilde{\epsilon} = \epsilon_1 + i\epsilon_2 = (n + ik)^2$ $\epsilon_1 = n^2 - k^2$ $\epsilon_2 = 2nk$
Relative permittivity	$\epsilon_r(\omega) = \epsilon(\omega)$ $\epsilon_r(\omega) = 1 + \chi_e$ $\epsilon_r(\omega) = \frac{C_x}{C_0}$
Electric field (dipole) outside a metal sphere	$\boldsymbol{E}_{out,dipole} = \boldsymbol{E}_o\hat{x} - \alpha \boldsymbol{E}_o \left[\frac{\hat{x}}{r^3} - \frac{3x}{r^5}(x\hat{x} + y\hat{y} + z\hat{z})\right]$
Dipole Polarizability	$\alpha = g_d a^3$ with $g_d = \frac{\epsilon_i - \epsilon_0}{\epsilon_i + 2\epsilon_0}$
Electrical Field Enhancement for a metal sphere[266]	$\eta(\omega) = \left\lvert 1 + \frac{\alpha(\omega)}{2\pi r^3} \right\rvert^2$
Electric field (quadrupole) outside a metal sphere	$\boldsymbol{E}_{out,quadrupole} = \boldsymbol{E}_o\hat{x} + ik\boldsymbol{E}_o(x\hat{\boldsymbol{x}} + z\hat{\boldsymbol{z}})$ $- \alpha \boldsymbol{E}_o \left[\frac{\hat{\boldsymbol{x}}}{r^3} - \frac{3x}{r^5}(x\hat{\boldsymbol{x}} + y\hat{\boldsymbol{y}} + z\hat{\boldsymbol{z}})\right]$ $- \beta \boldsymbol{E}_o \left[\frac{x\hat{\boldsymbol{x}} + z\hat{\boldsymbol{z}}}{r^5} - \frac{5z}{r^7}(x^2\hat{\boldsymbol{x}} + y^2\hat{\boldsymbol{y}} + xz\hat{\boldsymbol{z}})\right]$
Quadrupole Polarizability	$\beta = g_q a^5$, with $g_q = \frac{\epsilon_i - \epsilon_0}{\epsilon_i + 3\epsilon_0/2}$
Extinction Efficiency	$Q_{ext} = 4xIm(g_d)$, where $x = 2\pi a\sqrt{\epsilon_0}/\lambda$

Scattering efficiency	$Q_{sca} = \frac{8}{3}x^4\|g_d\|^2$, where $x = 2\pi a\sqrt{\epsilon_0}/\lambda$
Skin depth	$k = 1/\delta_s$ $E(z,t) = e^{-\frac{z}{\delta_s}}Re(E_0 e^{i(kz-\omega t)})$ $I(z) = I_0 e^{-2z/\delta_s}$ $\delta_s = 2\delta_p$, where δ_p is penetration depth.
Raman Gains in relationship to E-field enhancement	$G_{SERS} \propto \left\|\frac{E_{loc}(\lambda_{exc})}{E\_inc(\lambda_{exc})}\right\| \left\|\frac{E_{loc}(\lambda_{Raman})}{E_{inc}(\lambda_{Raman})}\right\|^2$
Influence of nanohole coverage on sheet resistance	$f(c) = A(c_{crit} - c)^{\eta}$ where A is a pre-exponential factor, c_{crit} is the critical nanohole coverage, c is the hole coverage, and η is the 2D conductivity exponent.
Energy – photon relationship	$E = hc/\lambda$
Transmission-Extinction Relationship	$\log(\%T) = \log(2 - E)$

A. 4 Mathematical Derivation and Simulation

A.4.1 Case study: dipole and quadrupole electric moment by Maxwell equation and Laplace equation in solving

This case study is adapted from the book written by Uwe Kreibig: Optical Properties of Metal Clusters.

Taking a spherical shape metal particle as an example with the applied electric field in the x direction, it can be shown using Maxwell equation and Laplace equation with angular solution $l = 1$ for dipole moment, the electric field outside the sphere is[15]:

$$\begin{aligned} \boldsymbol{E}_{out,dipole} &= \boldsymbol{E}_o\hat{x} - \alpha\boldsymbol{E}_o\left[\frac{\hat{x}}{r^3} - \frac{3x}{r^5}(x\hat{x} + y\hat{y} + z\hat{z})\right] \\ &= \boldsymbol{E}_o\frac{3\epsilon_m}{\epsilon+2\epsilon_m} \end{aligned} \qquad 2.1$$

where $\boldsymbol{E}_o\hat{x}$ is the applied field, $\alpha\boldsymbol{E}_o$ is the induced dipole moment of the metal sphere, α is the dipole polarizability, and $\hat{x}$, $\hat{y}$, and $\hat{z}$ are the Cartesian unit vector. In case of a sphere, the dipole polarizability is $\alpha = g_d a^3$ where $g_d = \frac{\epsilon_i - \epsilon_0}{\epsilon_i + 2\epsilon_0}$.

Extinction and scattering efficiency: $Q_{ext} = 4xIm(g_d)$; $Q_{sca} = \frac{8}{3}x^4|g_d|^2$, where $x = 2\pi a\sqrt{\epsilon_0}/\lambda$.

Similarly, electric field outside the sphere for quadrupole mode can be found using Laplace solution with angular solution $l = 2$:

$$\begin{aligned} \boldsymbol{E}_{out,quadrupole} = \boldsymbol{E}_o\hat{x} + ik\boldsymbol{E}_o(x\hat{\boldsymbol{x}} + z\hat{\boldsymbol{z}}) - \alpha\boldsymbol{E}_o\left[\frac{\hat{\boldsymbol{x}}}{r^3} - \frac{3x}{r^5}(x\hat{\boldsymbol{x}} + y\hat{\boldsymbol{y}} + z\hat{\boldsymbol{z}})\right] \\ - \beta\boldsymbol{E}_o\left[\frac{x\hat{\boldsymbol{x}} + z\hat{\boldsymbol{z}}}{r^5} - \frac{5z}{r^7}(x^2\hat{\boldsymbol{x}} + y^2\hat{\boldsymbol{y}} + xz\hat{\boldsymbol{z}})\right] \end{aligned}$$

where $\beta = g_q a^5$ is quadrupole polarizability with $g_q = \frac{\epsilon_i - \epsilon_0}{\epsilon_i + 3\epsilon_0/2}$. The factor of 2 and 3/2 in dipole and quadrupole comes from the magnitude of ratio of the exponents, $(l+1)/l$. For example, dipole($l = 1$) and quadrupole($l = 2$), the ratio is 2 and 3/2 respectively.

Extinction and scattering efficiency:

$$Q_{ext} = 4xIm\left[g_d + \frac{x^2}{12}g_d + \frac{x^2}{30}(\epsilon_i - 1)\right] ; Q_{sca} = \frac{8}{3}x^4\left\{|g_d|^2 + \frac{x^4}{240}|g_q|^2 + \frac{x^4}{900}|\epsilon_i - 1|^2\right\}.$$

Condition when the resonance mode occurs[86] is when the denominator becomes minimal, i.e. $\epsilon_i = -2\epsilon_0$ for dipole.

Note that the approach to solution used above are based on classical electrostatic approach. However, it remains valid for quasi-static regime which is applicable to our case. The key is to keep the time frame constant but not constraining on the spatial dependency. Although please note that the dielectric constant are still time dependent in their phase.

[For inclusion of phase retardation effect, see "Multipolar Excitation in Triangular Nanoprisms" written by Kevin *et al.* J. Chem Phys. 123, 114713 (2005)]

A.4.2 Spatial effect from dipole and quadrupole

Assume the E-field strength from dipole and quadrupole is A and B respectively, and probe is in-line with the axis of dipole generated x, then

$$A \approx g_d \left(\frac{a}{x}\right)^3$$

$$B \approx g_q \left(\frac{a}{x}\right)^5$$

$$\therefore \frac{A}{B} = \frac{g_d}{g_q}\left(\frac{x}{a}\right)^2$$

Since $g_q < g_d$, and the contribution of x/a is much more significant, it can be approximate that quadrupole mode is dominant at spatial distance of less than the radius of the sphere, and slowly decreasing at a rate of $1/x^5$. Further distance, the dipole E-field is stronger than quadrupole.

A.4.3 Simulation of ion milling shape and Calculation for maximum allowable angle for angular ion milling

For a PS sphere on a substrate of material type M, the total etched height, $h_t(x,t)$, is given by

$$h_t(x,t) = 2r\left(1 - \frac{R_M}{R_{PS}}\right)\sqrt{r^2 - x^2} + R_M t$$

where r is the PS radius, t is the time in minutes, R_M and R_{PS} are the ion milling etch rate of material M and PS respectively, and x is the lateral distance from the centre axis of the sphere. (Further inclusion of PS after oxygen plasma and additional material can also be included into the equation.)

Reduced height for given incidence angle, A (rad) relative to the normal incidence angle.

$$t_h = D * \tan(A)\left(1 - \tan\left(\frac{A}{2}\right)\right) - h$$

Height of disc, h (nm)	Reduced height, t_h	Diameter of PS, D (nm)						
		130	**210**	**290**	**400**	**500**	**620**	**800**
0		101.2	163.4	225.7	311.3	389.2	482.5	622.6
25		76.2	138.4	200.7	286.3	364.2	457.5	597.6
50		51.2	113.4	175.7	261.3	339.2	432.5	572.6
100		1.2	63.4	125.7	211.3	289.2	382.5	522.6

Experiment data:

15° Rotation vs 45° Rotation (maximum)

A drastic improvement of sidewall can be seen when the initial angle used is maximised.

15° Rotation

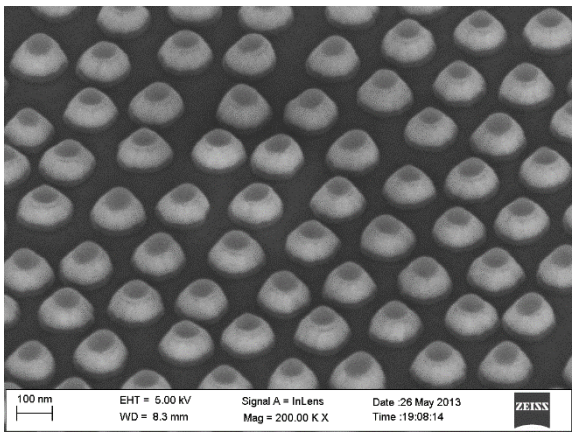

45° Rotation

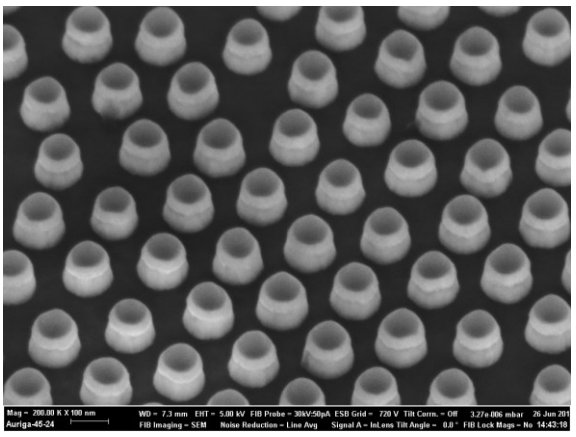

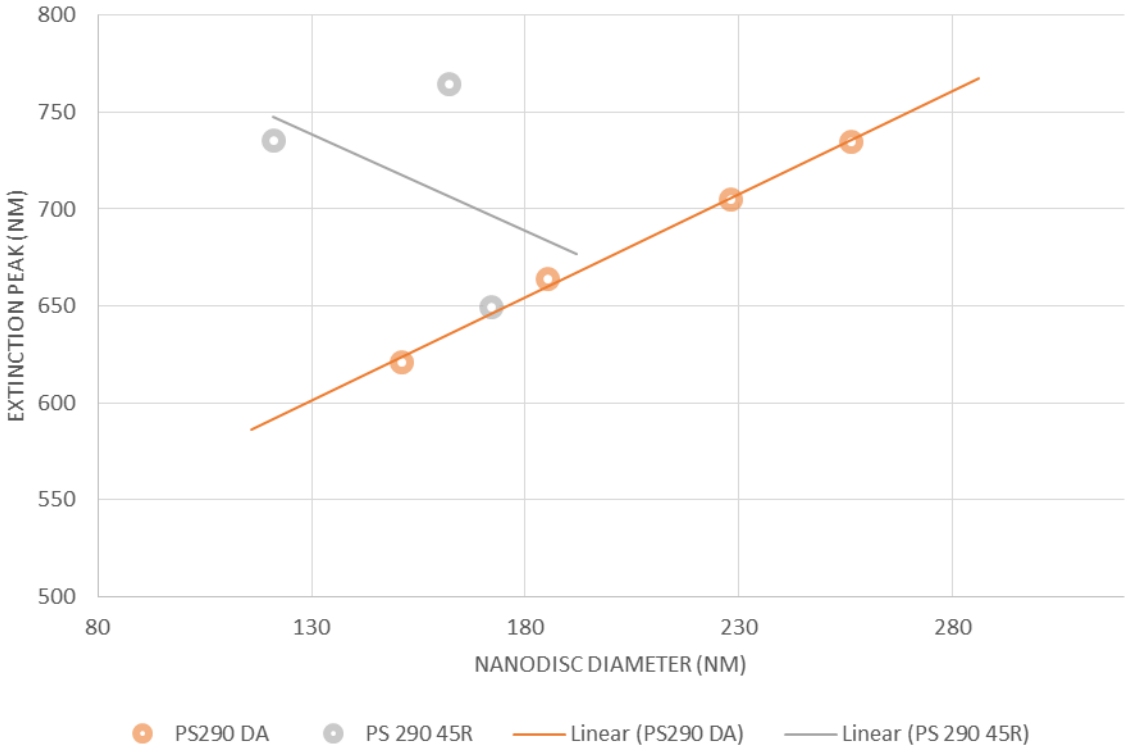

Figure A-2 The relationship between the 50 nm gold nanodisc diameter and resonance wavelength for different PS sizes.

From Figure A-2 above, it can be seen that trend follow a linear relationship using polishing technique. The required nanodisc diameter required to generate resonance wavelength of interest can be estimated from the graph provided the coupling is not too strong. However, fabrication without using polishing method, i.e. fixed 45° only, the shape is hard to control and difficult to estimate the required nanodisc diameter.

A. 5 Materials Information

A.5.1 Silicon substrates

Manufacturer: Si-Mat

Diameter:	100 mm
Type/Dopant:	P/Boron
Orientation:	<100>
Growth Method:	CZ
Resistivity:	1-30 ohm-cm
Thickness:	525 +/- 25 µm
TTV:	< 5 µm
Bow/Warp:	< 30 µm
Front Surface:	polished
Back Surface:	etched
Flats:	2 SEMI

A.5.2 Glass / Microscope Slides

Provider: VWR
Refractive index: 1.5171
Density: 2.479
Mean coefficient of expansion: 90.6 x 10^{-7}/°C (20 – 300 °C)
Strain Point: 513 °C
Softening point: 720 °C

Approximate Chemical Composition	Formula	% composition
Silicon dioxide	SiO_2	72.2
Sodium oxide	Na1O	14.3
Potassium oxide	K1O	1.20
Calcium oxide	CaO	6.40
Magnesium oxide	MgO	4.30
Aluminium oxide	Al_2O_3	1.20
Iron oxide	Fe_2O_3	0.03
Sulphur trioxide	SO_3	0.30

Source: VWR

A.5.3 Quartz Substrates for Aluminium experiments

Manufacturer: CrysTec GmbH
Orientation: (0001)
Edge parallel: (11-20)
Dimension: 10 mm x 10 mm
Thickness: 0,5 mm
Surface: both sides epipolished

A.5.4 Fluorescence Quantum Yields and Lifetime for Alexa Fluor Dyes

Alexa Fluor® dye	Absorption max (nm)	Emission max (nm)	Emission color*	Extinction coefficient**	Quantum yield (QY)†	Lifetime, τ (ns)‡	Measured Lifetime by Fang Group
Alexa Fluor® 350	346	442	Blue	19,000			
Alexa Fluor® 405	401	421	Blue	34,000			
Alexa Fluor® 430	433	541	Green/Yellow	16,000			
Alexa Fluor® 488	496	519	Green	71,000	0.92	4.1	
Alexa Fluor® 532	532	553	Yellow	81,000	0.61	2.5	
Alexa Fluor® 546	556	573	Orange	104,000	0.79	4.1	
Alexa Fluor® 555	555	565	Orange	150,000	0.1	0.3	
Alexa Fluor® 568	578	603	Orange/Red	91,000	0.69	3.6	
Alexa Fluor® 594	590	617	Red	73,000	0.66	3.9	

Alexa Fluor® 610	612	628	Red	138,000			
Alexa Fluor® 633	632	647	Far Red	239,000			
Alexa Fluor® 635	633	647	Far Red	140,000			
Alexa Fluor® 647	650	665	Near-IR***	239,000	0.33	1	
Alexa Fluor® 660	663	690	Near-IR***	132,000	0.37	1.2****	
Alexa Fluor® 680	679	702	Near-IR***	184,000	0.36	1.2	
Alexa Fluor® 700	702	723	Near-IR***	192,000	0.25	1	
Alexa Fluor® 750	749	775	Near-IR***	240,000	0.12	0.7	
Alexa Fluor® 790	784	814	Near-IR***	270,000	0.1		0.5

* Typical emission color seen through the eyepiece of a conventional fluorescence microscope with appropriate filters.
** Extinction coefficient at lmax in cm-1M-1.
*** Human vision is insensitive to light beyond ~650 nm; it is not possible to view near-IR fluorescent dyes.
**** Lifetime measurement was made in pH 7.5 buffer at 20°C by Pierre-Alain Muller, Max Planck Institute for Biophysical Chemistry, Göttingen.
† For Alexa Fluor® 488, Alexa Fluor® 532, Alexa Fluor® 546, Alexa Fluor® 555, Alexa Fluor® 568, Alexa Fluor® 594, and Alexa Fluor® 647 dyes, QY measurements were made in PBS (50 mM potassium phosphate, 150 mM NaCl, pH 7.2) at 22°C relative to fluorescein in 0.01 M NaOH (QY = 0.92). For Alexa Fluor® 660, Alexa Fluor® 680, Alexa Fluor® 700, and Alexa Fluor® 750 dyes, QY measurements were made in PBS at 22°C relative to Alexa Fluor® 647 succinimidyl ester in PBS (QY = 0.33).
‡ Except for the footnoted values, lifetime measurements were made in water at 22°C. Data provided by ISS Inc. (Champaign, IL).

Source: Lifetimetecnologies

A. 6 Other related topics

A.6.1 Hansen Parameters

Hansen solubility parameters indicate how likely a material will be dissolved in a solution or a mixture of solutions. The equation for calculating a material is defined as

$$\delta_t^2 = \delta_d^2 + \delta_p^2 + \delta_h^2$$

Where δ_t^2 is the total Hildebrand parameter, δ_t^2, δ_t^2, δ_t^2 are the dispersion, polar, and hydrogen bonding components respectively. If Hansen parameters of a solvent lies within solubility sphere of the polymers, then that solvent is likely to dissolve this polymer.

$$D_{S-P} = sqrt\left[4(\delta_d s - \delta_d p)^2 + \left(\delta_p s - \delta_p p\right)^2 + 2(\delta_h s - \delta_h p)^2\right]$$

where D_{S-P} is the distance between solvent and center of polymer solubility sphere, and $\delta_x s$ is the Hansen component parameter for solvent.

$\delta_x p$ = Hansen component parameter for polymer

A.6.2 Contact Angle

In equilibrium, the surface tension from each component at the interface balance out.

$$\gamma_{subs/air} - \gamma_{subs/Ag} - \gamma_{air/Ag} \cos\theta_C = 0$$

where γ is surface energy and the subscripts is denote where the interfaces it represents, and θ_C is the contact angle. Rearranging this equation leads to:

$$\cos\theta_C = \frac{\gamma_{subs/air} - \gamma_{subs/Ag}}{\gamma_{air/Ag}}$$

For a perfectly wetting condition, the contact angle is zero. The surface is said to be hydrophobic when the angle is above 90°.

A. 7 Experiment tools

A.7.1 Mantis Sputtering and Evaporation Chamber

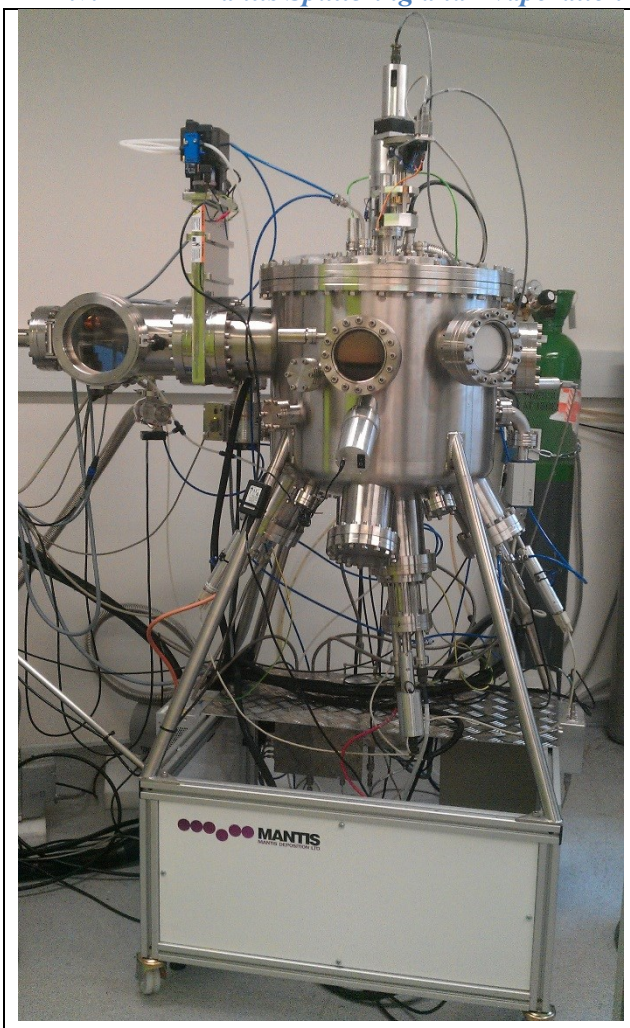

Mantis PVD System

This is a custom made PVD chamber for magnetron sputtering and thermal evaporation of metals. The stage is rotatable and is designed to allow heating up to 500°C or cool down by liquid nitrogen.

A.7.2 Ion Milling System

The ion milling system used in this project is a custom made Oxford Applied Research IM 150 Ion Milling System.

Settings:

Stage angle	**Vary between 0 to 45° depending on the structure required.**
Ion flux	20-30 mA/cm2 controlled by RF power, neutralised before reaching the sample unless specified.
Screen voltage	+500V
Accelerating Voltage	-200V, unless specified
Argon gas flow	20 sccm

A.7.3 Oxygen Plasma system

Please refer to section A.2.3 above.

A. 8 Further Experimental Information

A.8.1 Magnetron sputtering

Compare to thermal evaporation method, magnetron sputtering allows deposition of a more uniform thin film with better roughness. However, due to the kinetics of the sputtering mechanism, the sputtered atoms lost the directionality and can go underneath the PS mask. The results is a connected structures.

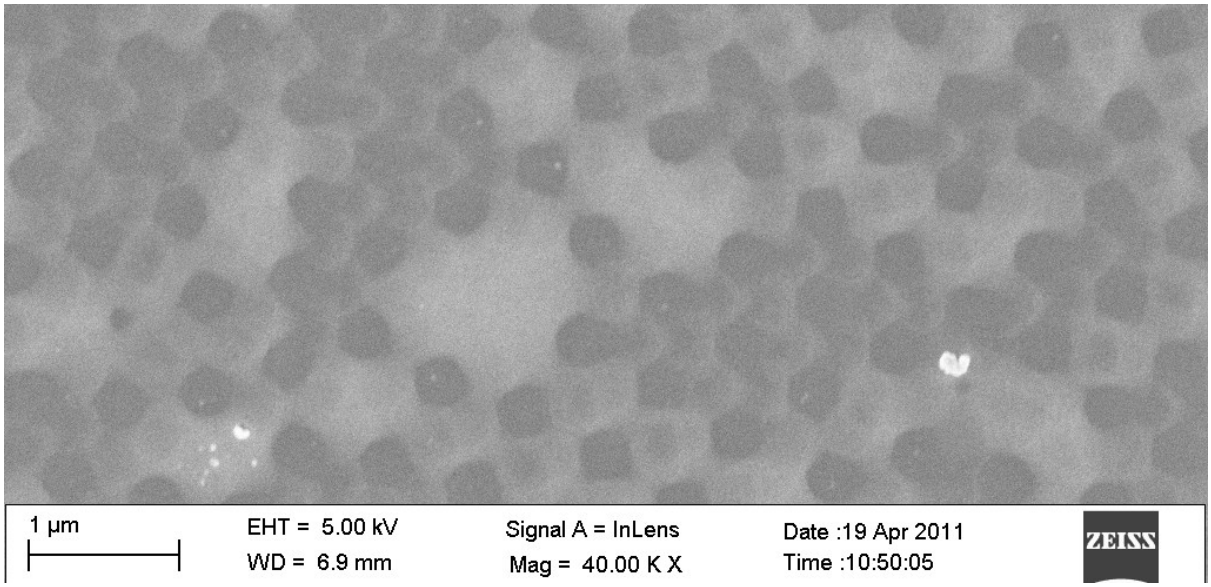

Figure A 3 30 nm gold deposition on 620 nm sized PS mask through magnetron sputtering method produced a connected network of gold.

A.8.2 Thickness profile produced by thermal evaporation without stage rotation

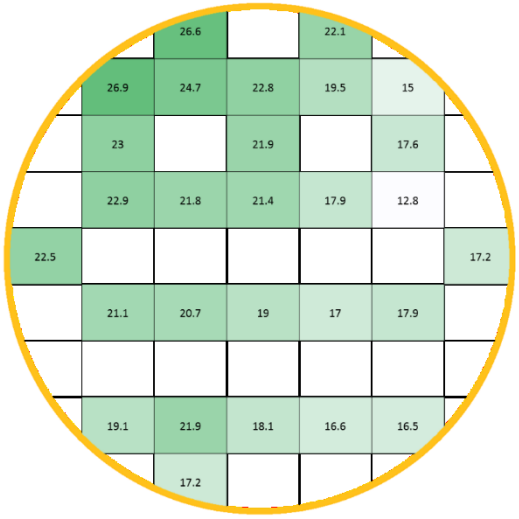

Figure A 4 Variation of deposited gold thickness produced by the Mantis thermal evaporator across the 4" stage holder.

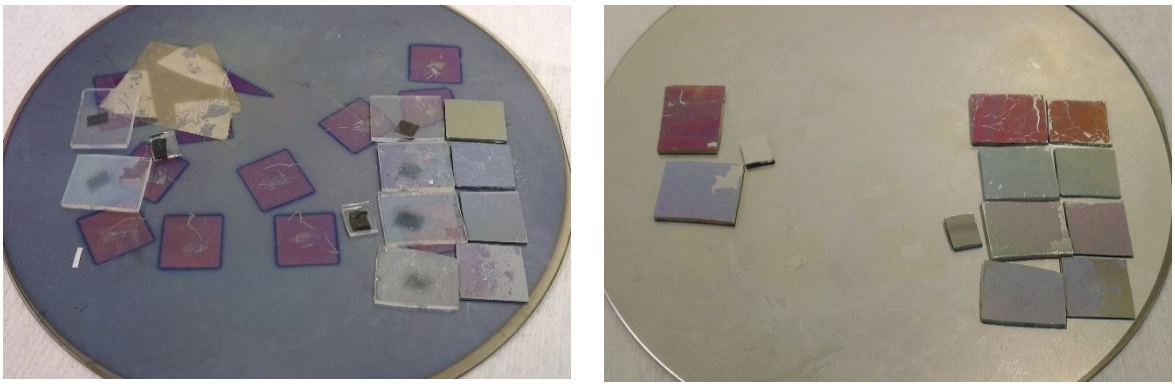

Figure A 5 Samples with different PS diameter monolayer before (left) and after (right) coated with a thin layer of silver through thermal evaporation.

A.8.3 Nanodisc arrays extinction profile

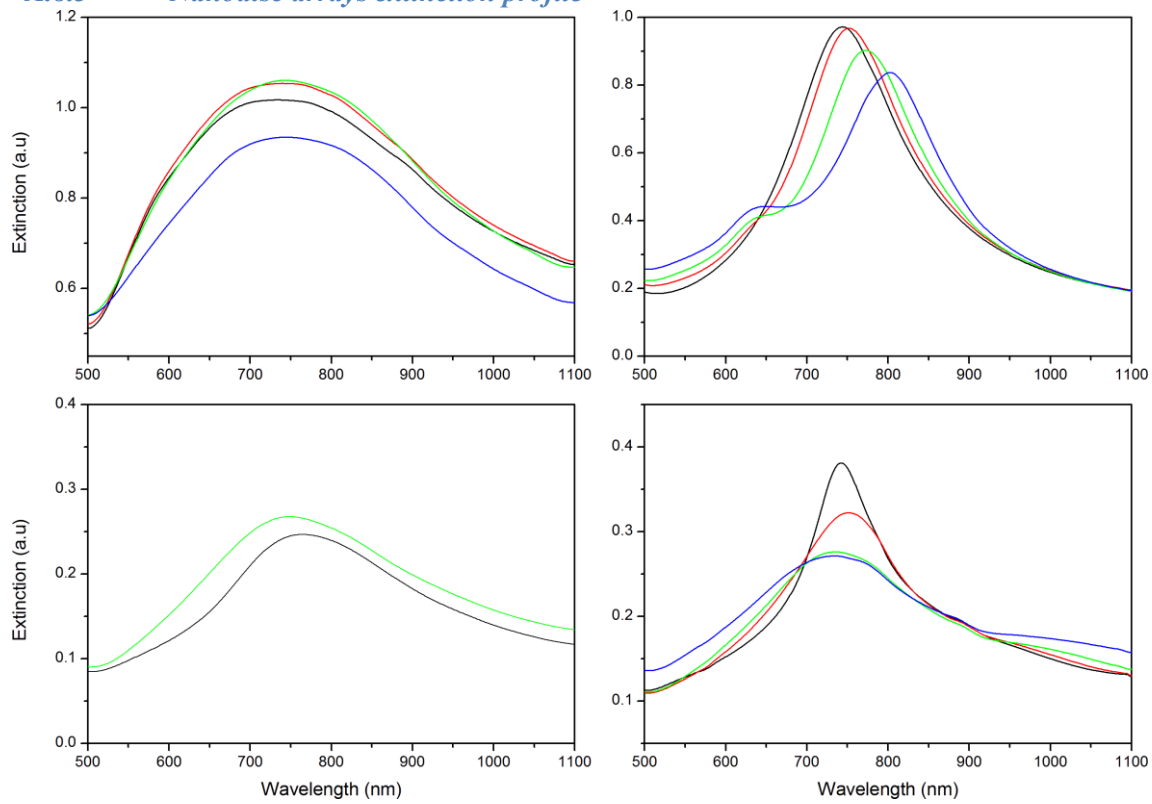

Figure A 6 Extinction of the nanodisc arrays on glass substrates at different centre to centre distance: a) PS290 b) PS400 c) PS400-65W d) PS500. Legend: black, red, green, blue represents 0°, 15°, 30°, and 45° respectively. Note: due to accessibility to the equipment at the time of measurements, only two angle were measured for PS400-65W sample.

A.8.4 Lifetime measurement experiment setup

Time-correlated single photon counting (TCSPC) technique[155]

System: PiciQuant FluoTime 200 spectrometer equipped with a TimeHarp300 TCSPC board and a Hamamatsu photomultiplier (PMA-185). Acquisition of the data is set to stop when the intensity of the peak reach 10,000 counts. Bandpass 2.0 filters were used.
Laser Driver: PDL800-D driver.

The specific laser used depends on the type of fluorophores attached.

Fluorophore	**Laser (nm)**	**Cut-off filter**
AF488	480	LP02-488RU-25 (Semrock)
AF680, 700, 750	670 (LDH-P-670B)	FF01-776/LP-25 (Semrock
AF790	730 (LDH730) / 780	HQ460LP, Chroma)

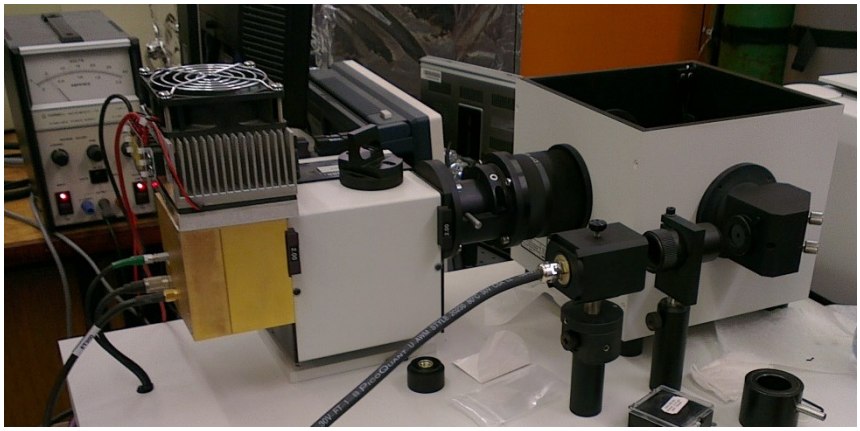

The measured data were analysed using FluoFit software with multi exponential reconvolution fits.

$$I(t) = \int_{-\infty}^{t} IRF(t') \sum_{i=1}^{n} A_i e^{-\frac{t-t'}{\tau_i}} dt'$$

Parameters:

A_i	Amplitude of the i th component in counts at time zero.
τ_i	Lifetime of the i th component.
$Bkgr._{Dec}$	Homogeneous (i.e. time independent) decay background in counts.
$Bkgr._{IRF}$	Homogeneous (i.e. time independent) IRF background in counts.
$Shift_{IRF}$	Time shift between IRF and decay.

Optional Parameters:

A_{Scat}	Scattered light contribution (i.e. multiple of the normalised IRF added to the convolved model curve) in counts.
$Period_{Rep}$	Time period between two consecutive excitation pulses.

Data Curves

Decay	Experimentally measured decay curve.
IRF	Experimentally measured IRF ('lamp function').

A. 9 List of publications

1. Xie F, Pang JS, Centeno A, Ryan MP, Riley DJ, Alford NM, Nanoscale control of Ag nanostructures for plasmonic fluorescence enhancement of near-infrared dyes, ***Nano Research***, 2013, 496-510, Vol 6.
2. Donchev E, Pang JS, Gammon PM, Centeno A, Xie F, Petrov PK, Breeze JD, Ryan MP, Riley DJ, Alford NM, The rectenna device: From theory to practice (a review), *MRS Energy & Sustainability – A Review Journal*, 2014, Pg 1-34, Vol 1.
3. Enhanced Fluorescence of Near Infrared Dye by Gold Nanodisc Arrays, paper in pre-print.
4. Enhanced Fluorescence of Nanohole-disc Arrays for Near Infrared Dye, paper in pre-print.

Conferences

1. Jing S. Pang, Peter Gammon, Evgeniy Donchev, Fang Xie, Anthony Centeno, Peter K. Petrov, Mary P. Ryan, Neil Alford, Nanoantenna for Direct Solar Energy Extraction, MRS Fall 2012.
2. Jing S. Pang, Fang Xie, Anthony Centeno, Peter K. Petrov, Mary P. Ryan, J. Riley, Neil Alford, Optical Absorption of Metal Nanoparticle, Optics for Solar Energy (SOLAR) 2012.